Demonstrating Quantum Speed-Up with a Two-Transmon Quantum Processor

Andreas Dewes

Demonstrating Quantum Speed-Up with a Two-Transmon Quantum Processor

PhD Thesis, 2012

Andreas Dewes

Quantronics Group - CEA Saclay
Université Pierre et Marie Curie
Ecole Doctorale de Physique de la Région Parisienne - ED107

Cover Illustration: King Aegeus asking the priestess Pythia, the Oracle of Delphi, for advice concerning family matters. Analogously, in this work we make use of a quantum Oracle to find the solution to a mathematical problem faster than possible when using classical computing[1]. Similar to the prophecies uttered by the ancient Oracle, the solutions that we obtain also tend to be slightly ambiguous.

[1] Incidentally, we use a language called Python to convey the messages of our Oracle.

Thèse de Doctorat de l'Université Pierre et Marie Curie
Specialité: Physique de la matière condensée
Ecole Doctorale de Physique de la Région Parisienne - ED 107

Demonstrating Quantum Speed-Up with a Two-Transmon Quantum Processor

Présentée par

Andreas Dewes

Pour obtenir le grade de "Docteur de l'Université Pierre et Marie Curie"

Soutenue le 15 novembre 2012 devant le jury composé de:
Prof. Alexey Ustinov (rapporteur)
Dr. Olivier Buisson (rapporteur)
Prof. Jean-Michel Raimond
Prof. David DiVincenzo
Dr. Denis Vion

Thèse préparée au sein du Service de Physique de l'Etat Condensé,
CEA Saclay

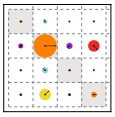

Acknowledgments

This thesis work would not have been possible without the invaluable help of my colleagues at the CEA Saclay. Special thanks go to my advisers **Denis Vion**, **Patrice Bertet** and **Daniel Esteve**, without them this thesis work would simply not exist. Countless times they provided me with invaluable scientific and personal advise and were always patient, optimistic and supportive, even at times when I was not.

In addition, I thank **Florian Ong**, who worked as a Post-Doc in the group during the first year of my thesis and fabricated the original qubit chip with which most of the measurements discussed in this thesis have been made. Also, I want to thank **Agustin Palacios-Laloy**, who introduced me to his setup and helped me to get started with my measurements. Furthermore, I want to thank **Nicolas Boulant**, who, with his experience in quantum state & process tomography, helped me to understand the data of the iSWAP experiment.

Last but not least, I want to thank all of my colleagues for their help and support, as well as for the countless interesting discussions I had with them. They made the Quantronics lab a very special and enjoyable place to work at.

Andreas Dewes

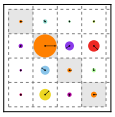

Short Summary

Demonstrating Quantum Speed-Up with a Two-Transmon Quantum Processor

The thesis work discusses the design, realization, characterization and operation of a two-qubit processor implemented using capacitively coupled tunable superconducting qubits of the Transmon type. Each qubit can be manipulated and read out individually using a non-destructive single-shot readout. In addition, a universal-two qubit gate can be implemented using the interaction between the qubits. The processor implements therefore all basic building blocks of a universal two-qubit quantum processor. Using it, we implement the universal $\sqrt{i\mathrm{SWAP}}$ two-qubit gate, characterizing the gate operation by quantum process tomography and obtaining a gate fidelity of 90 %. We use this gate to create entangled two-qubit Bell states and perform a test of the CHSH Bell inequality, observing a violation of the classical boundary by 22 standard deviations after correcting for readout errors.

Using the implemented two-qubit gate, we run the so-called Grover search algorithm: For two-qubits, this algorithm finds among four elements $x \in \{00, 01, 10, 11\}$ the one element y that solves a search problem encoded by a function f for which $f(y) = 1$ and $f(x \neq y) = 0$. Our implementation retrieves the correct answer to the search problem after a single evaluation of the search function $f(x)$, with a success probability between 52 % and 67 %, therefore outperforming classical algorithms that are bound to a success probability of 25 %. This constitutes therefore a proof-of-concept of the quantum speed-up for superconducting quantum processors.

Finally, we propose a scalable architecture for a superconducting quantum processor that can potentially overcome the scalability issues faced by today's superconducting qubit architectures.

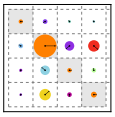

Contents

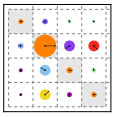

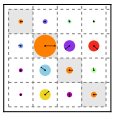

Chapter 1

Introduction & Summary

1.1 Quantum Computing with Superconducting Circuits

This thesis presents experiments performed with a superconducting two-qubit quantum processor. The main goal of this work was to demonstrate a possible quantum computing architecture based on superconducting qubits that follows the canonical blueprint of a quantum processor as sketched in fig. 1.1, in accordance with the five criteria formulated by DiVincenzo [41]. By this definition, a universal quantum computer is a register of well-defined quantum bits (1) with long coherence times (2), on which one can implement any unitary evolution using a universal set of quantum gates (3), fitted with individual high-fidelity readouts of the qubits (4) and with the possibility to reset them to their ground state (5). Implementing this allegedly simple list of requirements in a system of superconducting qubits has been a major research challenge during the last decade, and is part of more general line of research on superconducting quantum circuits briefly summarized below.

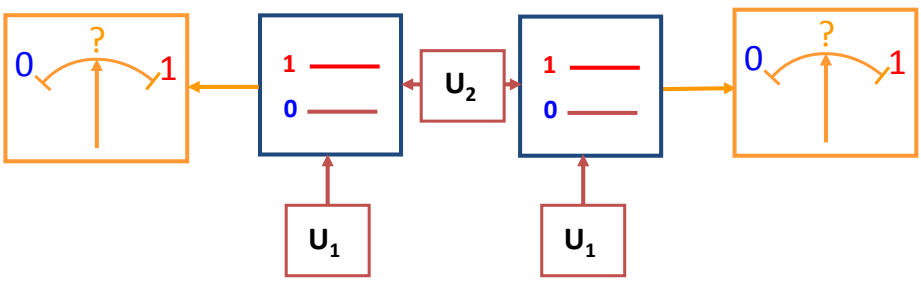

Figure 1.1: Blueprint of a “canonical” two-qubit quantum processor. The two qubits can be individually manipulated (U_1) and a universal two-qubit gate U_2 can be applied to them. Each of the qubits can be read out individually.

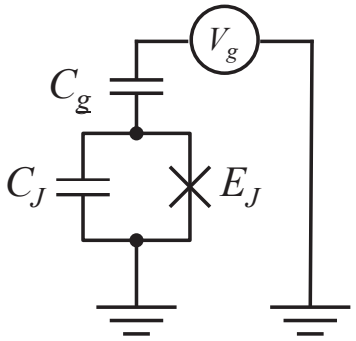

Figure 1.2: Schematic of the simple Cooper pair box (CPB) circuit, consisting of a capacitor C in parallel with a pure Josephson element, capacitively coupled to a voltage source V_g through a gate capacitor C_g.

Context of this thesis work: 25 years of superconducting quantum circuits The observation of quantum tunneling in a current-biased Josephson junction switching out of its zero-voltage state by Devoret *et. al.* [37, 80] first demonstrated that a collective electrical variable such as the superconducting phase difference across a Josephson junction (or the conjugated variable, i.e. the number of Cooper pairs that crossed it) can exhibit quantum properties. The observation of microwave-induced transitions between the quantum states of the junction by Martinis *et. al.* [80] further confirmed the quantum nature of this degree of freedom (See also [80, 81, 28]). A somewhat simpler quantum electrical circuit called the single Cooper Pair Box (CPB), made of a Josephson junction in series with a gate capacitor and a voltage source as shown in fig. 1.2, was later developed in the Quantronics group in the 1990s [18], and its ground state was characterized. With this electrical circuit, Nakamura *et. al.* [89] performed the first superconducting qubit experiment, demonstrating coherent oscillations between its ground and first excited eigenstates. Although the achieved coherence time was quite short, in the 5-10 ns range, this result generated huge interest and triggered the active development of research on superconducting quantum bits.

In the years after, several types of superconducting qubits were proposed using Josephson junctions in different configurations. Different regimes, in which the quantum state of the junctions ranges from almost Cooper pair number states to phase states, were realized. Let us cite here the flux qubit [87, 23] and the phase qubit [82], which are very successful qubits in many aspects. Two-qubit gate operations were demonstrated for the phase qubit [14], flux qubit [96] and charge qubit [123]. On the side of Cooper Pair Boxes, the Quantronics group contributed to the progress by operating a new circuit called the *Quantronium* (Vion *et. al.* [118]), fitted with a strategy for fighting dephasing due to the noise of the electrical control parameters, and with a single-shot readout (although with limited fidelity). The robustness of the quantronium arises from its operation at a so-called *sweet spot* where the qubit frequency is stationary in respect to variations in charge and phase control parameters. The improved coherence of the quantronium allowed to perform all the basic manipulations possible on spins and more

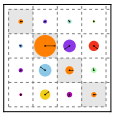

generally on two level systems [30]. Shortly after, another CPB circuit design, inspired from cavity-QED, was developed at Yale by Wallraff *et. al.* [119]. In this so-called circuit-QED (CQED) design, the CPB, embedded in a microwave resonator, can be thought of as an artificial atom in a resonant cavity. The qubit readout is performed dispersively, i.e. through the cavity pull of the resonator frequency controlled by the qubit state. This small frequency change results in a small phase change of a resonant microwave pulse, the measurement of which yields –after sufficient repetition– the probability of the two qubit states [16].

Another great bonus of CQED is that the electromagnetic environment in which the qubit relaxes its energy consists of a microwave resonator with a well-controlled impedance. The modern version of the Cooper Pair Box called *Transmon*, follows this design with an extra feature that makes it insensitive to the charge noise, that has always plagued single electron and single Cooper Pair devices. This feature consists in placing the Cooper Pair Box in the phase regime by adding an extra capacitance in parallel with the junction: the qubit frequency is then totally insensitive to the gate charge, and hence to the charge noise to all orders in charge. This new design, that still leaves sufficient anharmonicity to operate the device as a qubit and drive it, yielded a sizable improvement in coherence times, qubit robustness and usability. The CQED concept was thus rapidly extended to flux and phase qubits [57].

In 2010, a new type of CQED architecture has been developed by Paik *et. al.* [94] that combines Transmon qubits with 3D cavities instead of CPW resonators, resulting again in an impressive increase of qubit coherence times by a large factor, with reported qubit relaxation times approaching 100 μs and dephasing times of the same order. Very recently, these drastically improved coherence times have made possible the realization of elemental quantum feedback schemes with these systems [117].

The progress achieved during the last decade on the Cooper Pair Box and on the phase qubits has benefited quantum processors. So far, superconducting CQED processors with up to three qubits have been realized and two- and three-qubit quantum gates [38, 46], multi-qubit entanglement [39, 3] and simple quantum algorithms [38, 78] as well as quantum error correction [101] have recently been demonstrated.

This Thesis Work At the beginning of this thesis work, CQED processors having demonstrated quantum algorithms did not comply with the rules established by DiVincenzo [41]. In other words, they did not follow the canonical blueprint able to demonstrate quantum speed-up: they were all fitted with a joint readout, which allows to measure the average value of a collective variable of the qubit register, but not each qubit individually. By repeating a given sequence of gates a large number of times, one can nevertheless determine the quantum state of the qubit register at different steps of the

algorithm being run. Since the whole interest of quantum computing is precisely to perform computational tasks more efficiently than with a classical processor, it was essential, in our mind, to demonstrate the quantum speed-up expected from quantum algorithms with a CQED quantum processor fitted with an individual single shot and non-demolishing (QND) readout for each qubit. Such a high fidelity single-shot readout had been developed for a single Transmon during a previous thesis in the Quantronics group [77, 95], and it was natural to use it in the present work.

This thesis discusses therefore the realization of a superconducting two-qubit processor based on Transmon qubits, fitted with individual single-shot readouts. In chapter 2, we present the theoretical building blocks of this work. Chapter 3 outlines the design of the two-qubit processor, whereas chapter 4 presents the most relevant measurement techniques used here. With the two-qubit processor, we implement elementary one- and two-qubit quantum operations, as detailed in chapter 5. We use it to run a simple quantum algorithm that demonstrates probabilistic quantum speed-up: the Grover search algorithm, as explained in chapter 6. Finally, we discuss in chapter 8 the design of a four-qubit quantum processor using a more scalable approach that could possibly be extended to an even larger number of qubits.

Note that during this thesis work, quantum speed-up was also demonstrated for the Deutsch-Josza algorithm with a phase qubit processor using individual single-shot and destructive readouts [122].

1.2 Realizing a Two-Qubit Quantum Processor

The quantum processor implemented in this work is shown in fig. 1.3. It consists of two superconducting quantum bits of the Transmon type, each equipped with its own drive and readout circuit. In order to obtain a high fidelity single-shot readout of the qubit register, we use the Cavity Josephson Bifurcation Amplifier (CJBA) readout method, which is based on the Josephson Bifurcation Amplifier (JBA) readout first developed in the team of Michel Devoret at Yale for the quantronium qubit [109, 116, 108]. During the thesis of A. Palacios-Laloy [95], this method had indeed already been successfully adapted to the Transmon, and yielded a 93 % readout fidelity [77].

Each qubit can be manipulated by driving it with microwave pulses through its readout resonator, allowing robust and fast single-qubit operations. The qubit frequencies can be tuned individually using fast flux lines, allowing us to change the frequency of each qubit over a range of several GHz. The coupling between the two qubits is realized through a fixed capacitance that connects the two top-electrodes of the Transmons and implements a fixed σ_{xx}-type qubit-qubit coupling. This coupling allows us to generate entangled two-qubit states and to implement a two-qubit gate. We use this simple

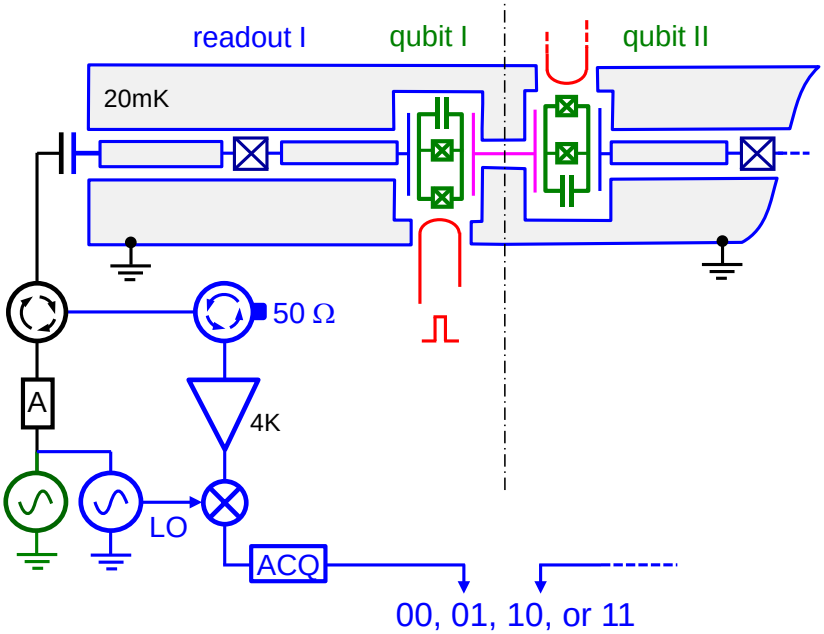

Figure 1.3: Circuit schematic of the two-qubit processor realized in this thesis work, showing the two qubits (in green) coupled by a fixed capacitor (in purple), as well as the fast flux lines (in red) used to tune the qubit frequencies and the qubit readouts (in blue). Each qubit is embedded in its own nonlinear readout resonator and can be driven and read out by microwave reflectometry through an individual microwave line.

processor to generate entangled two-qubit states, test the Bell inequality, implement a universal two-qubit gate and perform a simple quantum algorithm that demonstrates quantum speed-up, as discussed in the following sections.

1.3 Demonstrating Simultaneous Single-Shot Readout

For readout, each qubit is capacitively coupled to a coplanar waveguide resonator made nonlinear by placing a Josephson junction in its central conductor. We exploit the frequency pull of the bifurcation transition that occurs in this resonator when driven at a suitable frequency and power to map the qubit states on the bifurcated and non bifurcated cavity states, which are then discriminated by reflectometry. Here, the hysteretic character of the bifurcation transition allows to reduce the measuring power, to latch the cavity state, and to measure it without being affected by subsequent qubit relaxation. The state of the resonator can thus be determined reliably without being limited by qubit relaxation, thereby providing a high-fidelity single-shot qubit readout. Contrary to previous CQED processors, our processor is fitted with individual readouts, and a simultaneous readout of the full two-qubit register is possible, as requested by the DiVincenzo criteria. For a single-qubit CJBA readout, fidelities up to 93 % have been

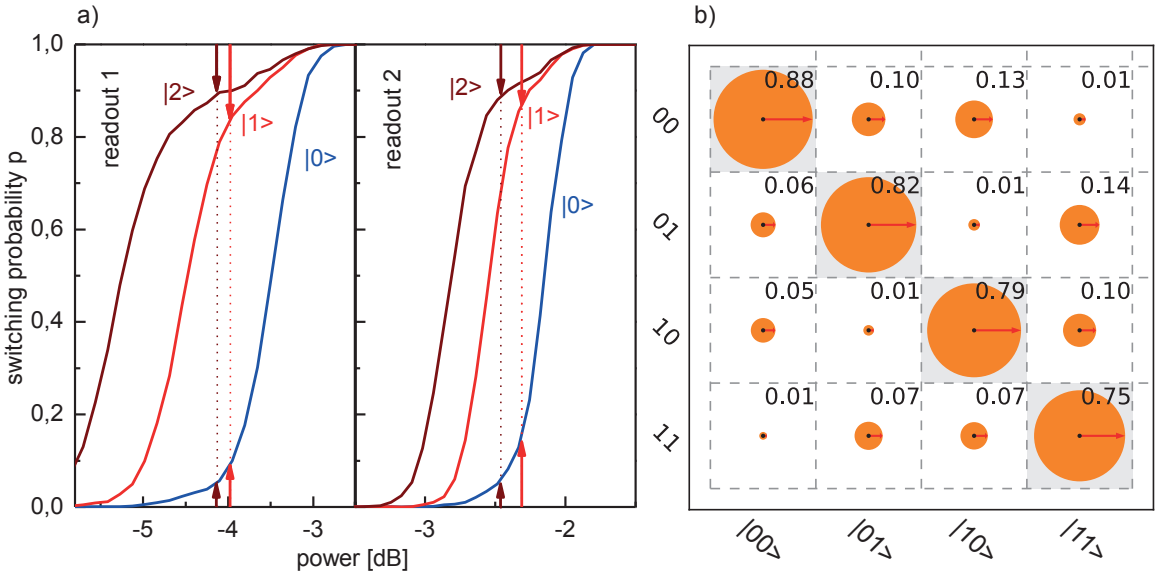

Figure 1.4: a) Switching probabilities of the two readout resonators as a function of the readout drive power at a fixed driving frequency. The measurement is performed after preparing the qubits either in the state $|0\rangle$, $|1\rangle$ or $|2\rangle$. The readout contrast is given as the maximum difference in probability between the curves corresponding to the states $|0\rangle$ and $|1\rangle$ or $|0\rangle$ and $|2\rangle$, respectively (see vertical dotted lines). The highest contrasts of 88 and 89 % for the two qubits are obtained when the qubit is shelved from state $|1\rangle$ to $|2\rangle$. b) Readout matrix of the two-qubit system, giving the probabilities to obtain the different outcomes ij after having prepared the register in the different computational basis states $|kl\rangle$.

achieved [77] by shelving the first excited state of the Transmon $|1\rangle$ to the higher excited state $|2\rangle$. However, due to the higher complexity and design constraints of our system, only 83-89 % fidelity has been achieved for the processor presented here. The full characterization of the readout of our processor is shown in fig. 1.4. Panel a shows the switching probabilities of each individual readout as a function of the drive amplitude, measured at a fixed drive frequency. Individual curves correspond to the qubit being prepared (or shelved) in different states $|0\rangle$, $|1\rangle$ or $|2\rangle$, the difference between either two curves giving the readout contrast between those qubit states. Shelving the qubit from state $|1\rangle$ to state $|2\rangle$ before readout can increase the readout fidelity by more than 10 % and is therefore often used in the experiments presented in this thesis. Panel b shows the full readout matrix of the two-qubit register that relates measured readout switching probabilities with real qubit state occupation probabilities and allows us to correct readout errors when performing quantum state tomography. In chapter 5 we discuss all relevant readout fidelities and errors in detail and analyze different error sources limiting the readout performance in our experiments.

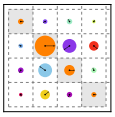

1.4 Generating and Characterizing Entanglement

The capacitive coupling between the two qubits provides a σ_{xx}-type interaction that can be used to generate entangled two-qubit states. Conveniently, this coupling is only effective when the qubit frequencies are near-resonant and can therefore be effectively switched on and off by tuning the qubit frequencies in and out of resonance. For the processor realized in this work, the effective coupling constant g_{qq} of the two qubits has been measured as $2g_{qq}/2\pi = 8.3\ \mathrm{MHz}$. When the two qubits are in resonance, the effective evolution operator of the two-qubit system is:

$$U(t) = \begin{pmatrix} 1 & 0 & 0 & 0 \\ 0 & \cos tg_{qq} & -i\sin tg_{qq} & 0 \\ 0 & -i\sin tg_{qq} & \cos tg_{qq} & 0 \\ 0 & 0 & 0 & 1 \end{pmatrix}_{\{|00\rangle,|01\rangle,|10\rangle,|11\rangle\}} \tag{1.1}$$

in the two-qubit basis $\{|00\rangle, |01\rangle, |10\rangle, |11\rangle\}$. By using fast flux pulses to non-adiabatically tune the qubits in and out of resonance, we can switch on this interaction for a well-defined time. We first characterize the effect of the coupling on the qubit register by preparing the state $|10\rangle$, tuning the qubits in resonance for a given time and measuring the qubit state afterward. The resulting curve is shown in fig. 1.5a and shows swapping oscillations between the two qubits. Analyzing this curve allows us to extract the effective coupling strength between them. Leaving the interaction between the qubits on for a well-defined time allows us to generate entangled Bell states that we characterize by performing quantum state tomography. The experimental reconstruction of the density matrix of such a Bell-state of the type $|\psi\rangle = (|01\rangle + i\,|10\rangle)/\sqrt{2}$ is shown in fig. 1.5c. The measured fidelity of the prepared state of 91 % and the concurrence of 85 % confirm that entanglement is present in the system. We also characterize the entanglement between the two qubits by measuring the average value of the *Clauser-Horne-Shimony-Holt* operator (CHSH) [29], which combines measurements of the state of the two qubits along different axes on the Bloch sphere and provides a test that can distinguish between classical correlations and quantum entanglement in a two-qubit system.

For classical states, the maximum value of the CHSH operator is bound by 2, but for entangled states it can reach a maximum of $2\sqrt{2}$. Figure 1.6 shows the result of such a CHSH-type measurement performed on a state created by the method described above, showing the value of $\langle\mathrm{CHSH}\rangle$ as a function of the angle ϕ of the measurement basis. We observe a violation of the classical boundary 2 of the operator by 22 standard deviations when correcting the readout errors that are present in our system. The raw, uncorrected data fails to exceed the classical threshold because of readout errors mainly caused by qubit relaxation during the readout. Nevertheless, the observed violation in

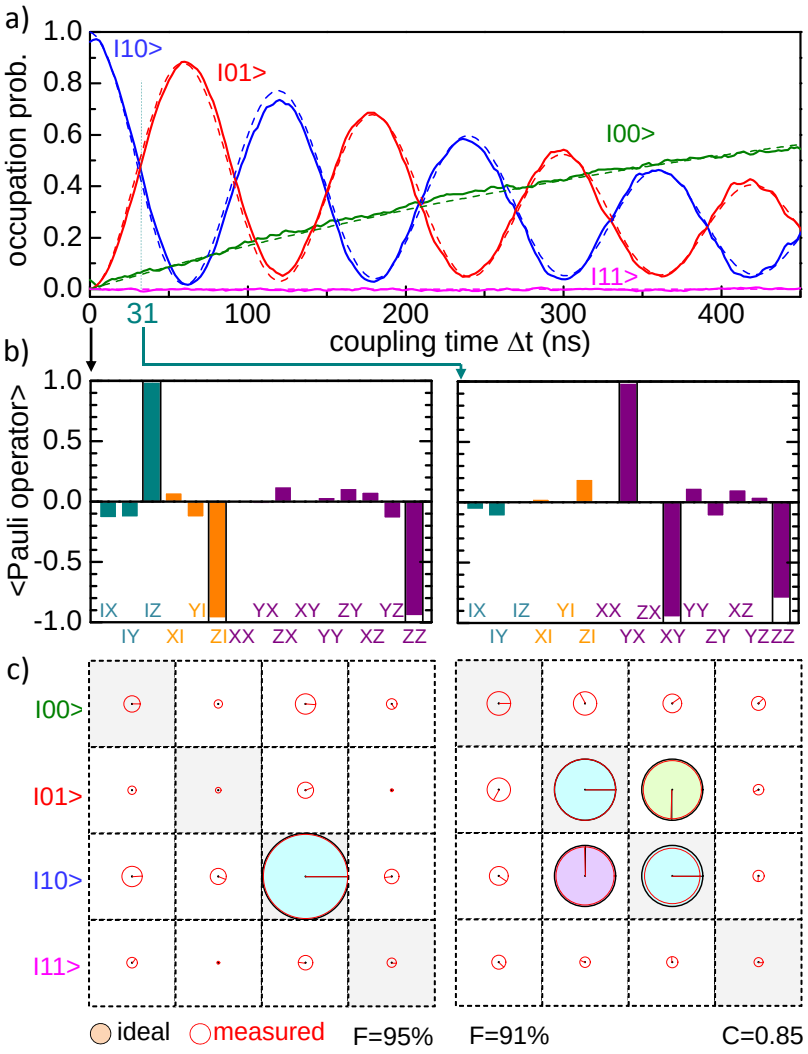

Figure 1.5: Coherent exchange of a single quantum of excitation (swapping oscillations) between the two qubits initially prepared in the register state $|10\rangle$, obtained from the resonant interaction between them. a) Register state probabilities as a function of the swapping time Δt. The frequency of the oscillations corresponds to $2g_{qq}/2\pi = 8.3$ MHz. b) Measured average values of the Pauli operators products $\{I, \sigma_x, \sigma_y, \sigma_z\} \otimes \{I, \sigma_x, \sigma_y, \sigma_z\}$ (Pauli set) for the register states obtained at times 0 ns and 31 ns. c) Corresponding reconstructed density matrices. The area of each circle corresponds to the absolute value of each matrix element and the color and direction of the arrow to the phase of the element. The black circles and arrows correspond to the density matrices of the ideal states $|10\rangle$ and $(|10\rangle + i\,|01\rangle)/\sqrt{2}$, respectively.

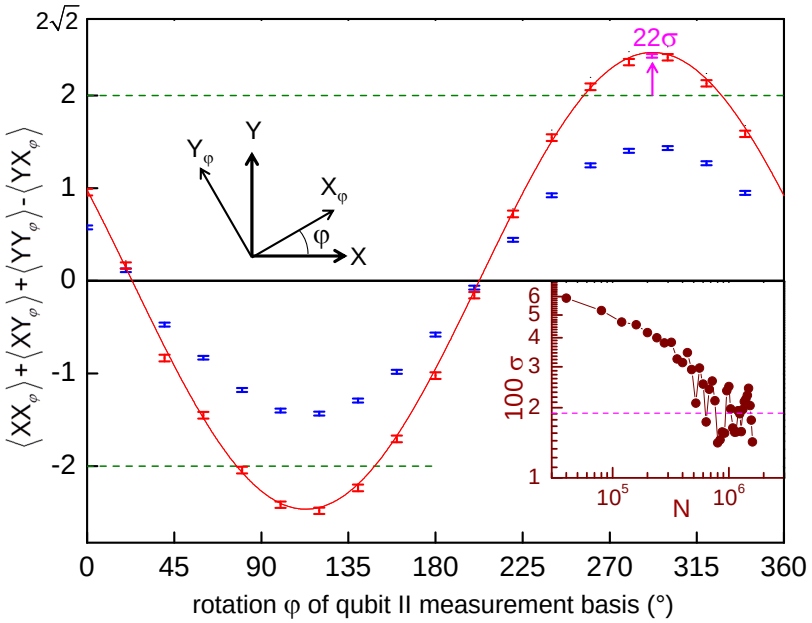

Figure 1.6: Measured average value of the CHSH operator for a prepared Bell state. After readout error corrections, the CHSH expectation value (red points) exceeds the classical boundary of 2. The raw measurement data (blue points) lies below this critical threshold. The inset shows the standard deviation σ at the highest point of the curve as a function of the measurement sample size. For the highest sample count, the classical boundary is exceeded by 22 standard deviations.

the calibrated data is a strong indication of entanglement in the system. A more detailed overview of this experiment can be found in chapter 5.

1.5 Realizing a Universal Two-Qubit Quantum Gate

The swapping evolution given by eq. (1.1) allows not only to prepare entangled two-qubit states but also to implement a universal two-qubit gate: When switching on the interaction for a time $t_{\pi/2} = \pi/4g_{qq}$ one realizes the $\sqrt{i\mathrm{SWAP}}$ gate, represented by the evolution operator

$$U(t) = \begin{pmatrix} 1 & 0 & 0 & 0 \\ 0 & 1/\sqrt{2} & i/\sqrt{2} & 0 \\ 0 & i/\sqrt{2} & 1/\sqrt{2} & 0 \\ 0 & 0 & 0 & 1 \end{pmatrix}_{\{|00\rangle,|01\rangle,|10\rangle,|11\rangle\}} \tag{1.2}$$

which forms together with single qubit gates a universal set of gates, on which any algorithm can be decomposed. We characterize the operation and errors of our implementation of this gate by performing quantum process tomography, obtaining a gate fidelity of 90 % . The 10 % error in gate fidelity is caused mainly by qubit relaxation and

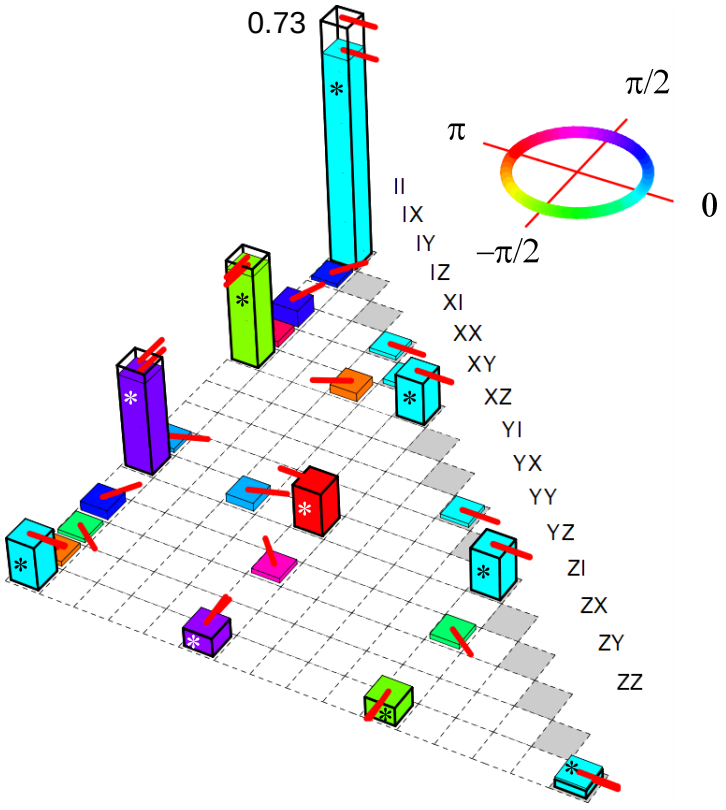

Figure 1.7: Measured χ-matrix of the implemented $\sqrt{i\mathrm{SWAP}}$ gate. The row labels correspond to the indices of the E_i Pauli operators, the height of each bar to the absolute value of the corresponding matrix element, and the color and red arrow direction to the argument of the element. The ideal χ-matrix of the $\sqrt{i\mathrm{SWAP}}$ gate is given by the outlined black bars. The upper half of the positive-hermitian matrix is not shown.

dephasing during the gate operation and only marginally by deterministic preparation errors, as will be discussed in chapter 5. Figure 1.7 shows the measured χ matrix of the gate, that describes its effect in the Pauli basis of two-qubit operators. The χ matrix provides the full information on the unitary and non-unitary action of the gate. The achieved fidelity of the gate operation is sufficient to allow the implementation of simple quantum algorithms with our processor.

1.6 Running a Quantum Search Algorithm

Using a two-qubit quantum gate related to the one described above, we run a simple quantum algorithm on our processor, the so-called *Grover search algorithm* [54]. The version of this algorithm that we implement operates on the two-qubit basis $x_i \in \{|00\rangle, |01\rangle, |10\rangle , |11\rangle\}$ and can distinguish between four different *Oracle functions* $\mathcal{C}_j(x)$ with $x \in x_i$ that give $\mathcal{C}_j(x = x_j) = 1$ and $\mathcal{C}_j(x \neq x_j) = 0$. In the two-qubit case, this algorithm requires only one evaluation of the Oracle function $\mathcal{C}_j(x)$, implemented as a unitary operator, to determine which state among the four possible ones it tags. This case thus provides a simple benchmark of the operation of the quantum processor, and a simple and illustrative example of quantum speed-up in comparison with classical algorithms, as discussed in chapter 6. The diagram of the Grover search algorithm implemented

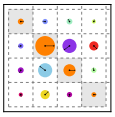

in our processor is shown in fig. 1.8a and involves two $i\mathrm{SWAP}$ gate operations and six single-qubit operations along with a single-shot qubit readout at the end of the algorithm. We measure the success probability of the algorithm from the obtained outcomes, and complete the analysis of its operation by performing the tomography of the quantum state at different steps of the algorithm. We first discuss this evolution that sheds light on how quantum speed-up is achieved.

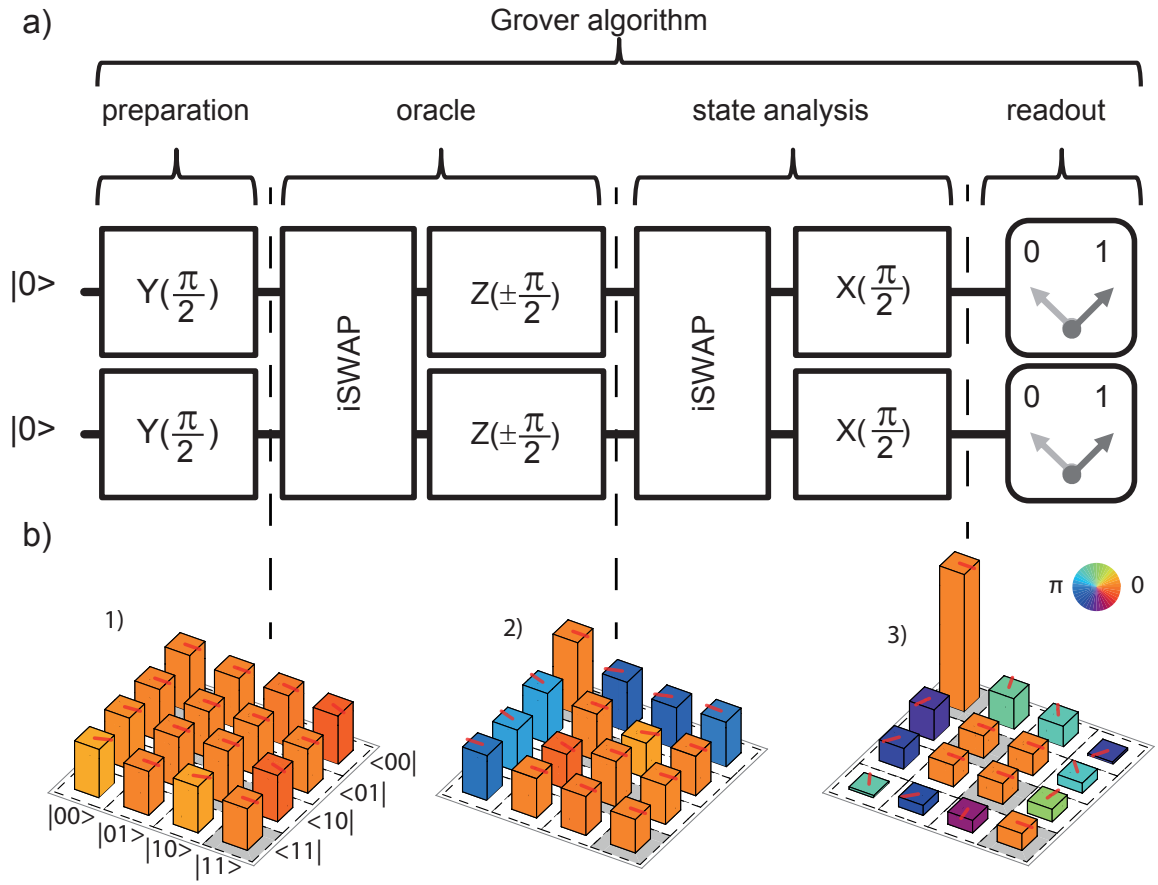

Figure 1.8: a) Two-qubit version of the Grover search algorithm implemented on our quantum processor. The algorithm consists in preparing a fully superposed state, applying a given Oracle operator to it only once, and analyzing the resulting output to determine the quantum state tagged by this Oracle operator. b) Measured density matrices when running the Grover search algorithm with a search oracle marking the state $|00\rangle$. 1) shows the state after the generalized Hadamard transform, 2) after applying the quantum oracle and 3) after the final analysis step of the algorithm.

Fig. 1.8b shows the density matrices determined experimentally when running the Grover search algorithm with the Oracle operator tagging the state $|00\rangle$. State tomography is first shown after preparation with a generalized Hadamard transform applied to the initial state $|00\rangle$. It clearly corresponds to a superposition of all the computational basis states. The quantum state after having applied the quantum Oracle is $-|00\rangle + |01\rangle + |10\rangle + |11\rangle$ and the information on the tagged state is encoded in the

phase of the state $|00\rangle$. After extracting this phase information, the tomography displays a large peak on state $|00\rangle$ at the end of the algorithm, just as expected. The fidelity of the final quantum state of the algorithm is 68%, 61%, 64% and 65% for the four different Oracle operators, respectively. These fidelities, corrected for readout errors, do not quantify the quantum speed-up achieved when running the algorithm. For this, it is necessary to analyze the results obtained after a single run, which does not allow for any corrections of the readout outcomes.

1.7 Demonstrating Quantum Speed-Up

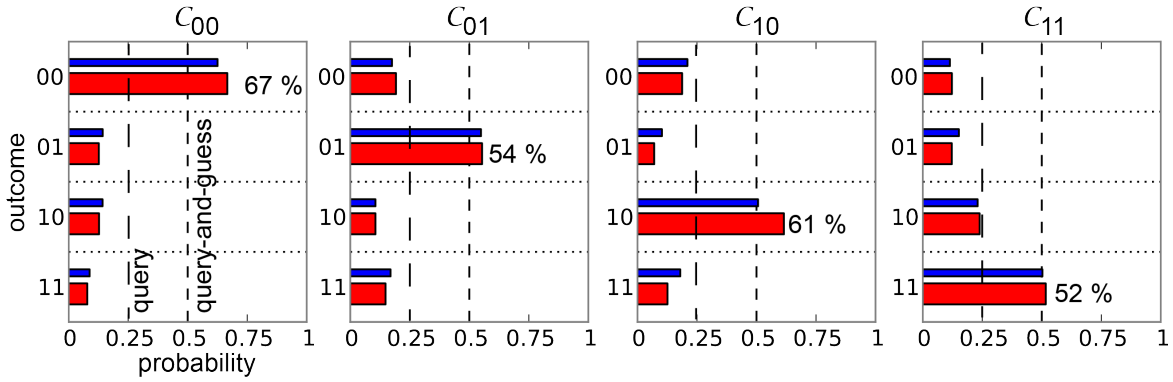

Figure 1.9: Single-run outcomes when running the Grover search algorithm on our two-qubit quantum processor. Shown are the directly (red) or indirectly (blue) measured probabilities of finding the qubit register in state $|i\rangle$ at the end of the algorithm, for each Oracle function $\mathcal{C}_j$ marking the state $|j\rangle$. In all four cases, the success probability of the algorithm is $> 50\%$, thus outperforming any classical "random query" or "query and guess" algorithm using a single Oracle call.

The main interest of running a quantum algorithm is to obtain an advantage in the run-time in comparison to a classical algorithm, the *quantum speed-up*. To characterize this speed-up as obtained with our processor, we run the Grover algorithm for all four possible Oracle functions and directly read out the state of the qubit register after the last step of the algorithm instead of performing quantum state tomography, thus not correcting any readout errors. By averaging the outcomes of many such individual runs with different Oracle functions we obtain the *single-run fidelities*, which –for the four different Oracle functions– have been measured as 66%, 55%, 61% and 52%. The full probability distributions for the four possible cases are shown in fig. 1.9. The achieved success probability is always lower than the theoretically possible value of 100 %, mainly because of relaxation and decoherence of the qubit state during the run time of the algorithm and –to a small degree– errors in the pulse sequence. The measured success probabilities are however larger than the 50% success probability of a

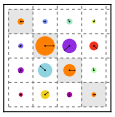

classical query-and-guess algorithm using the outcome of a single query. The algorithm thus demonstrates quantum speed-up, as explained in greater detail in chapter 6.

1.8 Towards a Scalable Multi-Qubit Architecture

The approach to superconducting quantum computing outlined in the previous sections is well suited for the implementation of simple quantum processors with a few qubits. However, due to several design limitations it is not suitable for implementing a large scale quantum computer. As an example, the direct qubit-qubit coupling employed in this thesis work is not suitable for coupling a large number of qubits since it becomes increasingly difficult to deterministically switch on and off the coupling between individual qubits as the number of qubits increases, a problem sometimes referred to as "frequency crowding". Also, fitting each qubit of the processor with individual drive and readout circuitry –as done in this work– is usually not extensible to a large number of qubits due to topological and space constraints on the chip, as well as practical constraints for a cryogenic experimental setup.

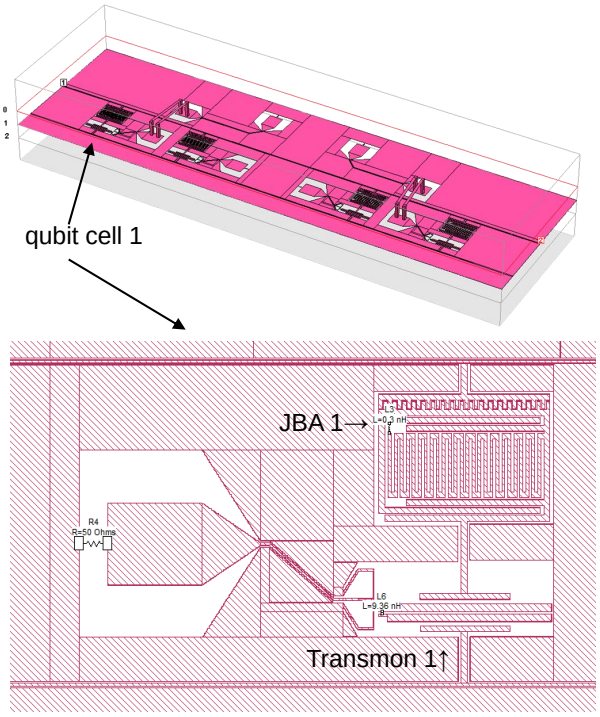

Figure 1.10: Schematic of the four-qubit chip realized in this thesis work. Shown on top is the whole chip with ports for the drive and readout transmission line and for the four fast flux lines. Shown below is a single qubit cell with a Transmon qubit coupled to the quantum bus, a flux line and a JBA readout.

Recently, several research groups have started to address these issues by devising new architectures for superconducting quantum processors that can –in theory– be scaled to a larger number of qubits. Here we will mention only the "Rez-Qu" architecture [50] developed in the Martinis lab and the surface-code approach [42] pursued by IBM. In this thesis work we discuss our own approach towards more scalable superconducting quantum processors, where we develop a revised version of our qubit chip that provides a way to implement a system with a larger –albeit still small– number of qubits. Key elements of this architecture are a quantum bus in form of a high-Q microwave resonator that is used for coupling the qubits and a multiplexed drive and readout cir-

cuit that allows us to measure and manipulate all qubits through one single microwave transmission line.

Figure 1.10 shows the schematic of the first version of this architecture. Our chip contains four Transmon qubits which are capacitively coupled to a distributed high-Q resonator acting as a quantum bus. In addition, each qubit is coupled to a low-Q nonlinear lumped element resonator acting as a CJBA, which is used for reading out the qubit state. Each of these resonators is in turn coupled capacitively to the input transmission line. The resonance frequencies of the readout resonators are arranged in ascending order with a frequency spacing of $\approx 50\ \mathrm{MHz}$ between adjacent resonators. This frequency spacing allows us to address each resonator individually and to read out the state of the full qubit register in parallel using only one single transmission line. Figure 1.11 shows the measured $|S_{12}|$ matrix element of such a chip with four CJBA resonators at frequencies between 6.78 GHz and 6.95 GHz, plotted as a function of the incident microwave power. The "knee" in each of the four resonance curves appearing between -45 and -40 dBm corresponds to the bifurcation point of the resonators.

Still, this approach suffers from a relatively bad ON/OFF ratio in the qubit-qubit coupling. To alleviate this problem, the Transmon qubit used in the current version of this architecture can be replaced by a qubit with a tunable coupling [112]. Alternatively, it is possible to use a fixed-frequency coupling scheme for the qubits, thereby altogether eliminating the need for frequency tuning of individual qubits and also reducing the number of input transmission lines from $n+1$ to 1, with n the number of qubits.

A more detailed discussion of the scalable architecture and the first preliminary measurements performed with a four-qubit chip are presented in chapter 7 of this thesis.

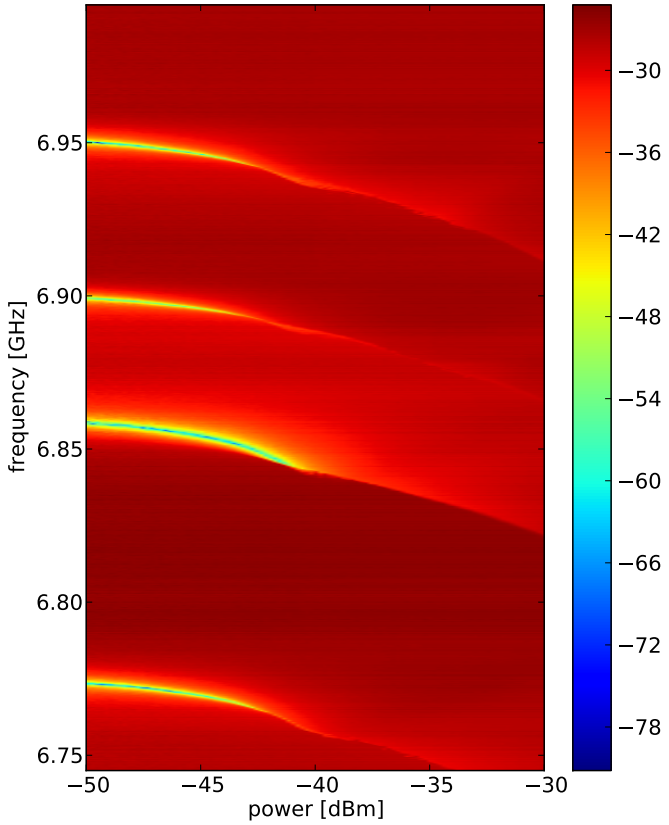

Figure 1.11: Measured $|S_{12}|$ transmission coefficient of drive and readout line of our four-qubit chip, with the four qubits far detuned from the resonators. Clearly visible are the resonances of the four CJBA resonators and their bifurcation at nominal input powers between -42dB and -40 dB.

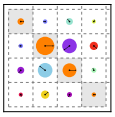

Chapter 2

Theoretical Foundations

In this chapter we provide the reader with the conceptual background and theoretical building blocks necessary to understand our thesis work. We begin our discussion with a general overview of classical and quantum information processing with a Turing machine, followed by an introduction to superconducting quantum circuits. We summarize the method to quantize electrical circuits and apply it to Cooper pair box devices, and in particular to the Transmon that will be used to implement the qubit register of our quantum processor. We then present coplanar waveguide resonators, and introduce circuit quantum electrodynamics on the example of a Transmon coupled to a such a resonator. Finally, we consider the case of a nonlinear resonator used as a Josephson bifurcation amplifier since we use such a readout device in our processor architecture.

2.1 Classical & Quantum Information Processing

By definition, computing designates the activity of using computer hardware and software to process information, or *data*. Classical information processing can be divided in *analog and digital information processing*, the former being based on continuous physical variables whereas the latter is based on discrete variables. The fundamental unit of digital information processing is the *bit*, which represents a Boolean (true/false) information. The discipline of theoretical computer science has been created to investigate the fundamental limits and properties of classical information processing. One of the main foundational theorems of theoretical computer science is the *Church-Turing thesis* which provides a universal computing model by saying (basically) that everything which is computable can be efficiently computed using a *Turing machine*. Such a Turing machine, in turn, is a simple theoretical device which is able to run programs that operate on a discrete set of data using a well-specified set of operations. The Turing machine is universal in the sense that any other classical computing device can be efficiently emulated using a Turing machine with the appropriate program and data.

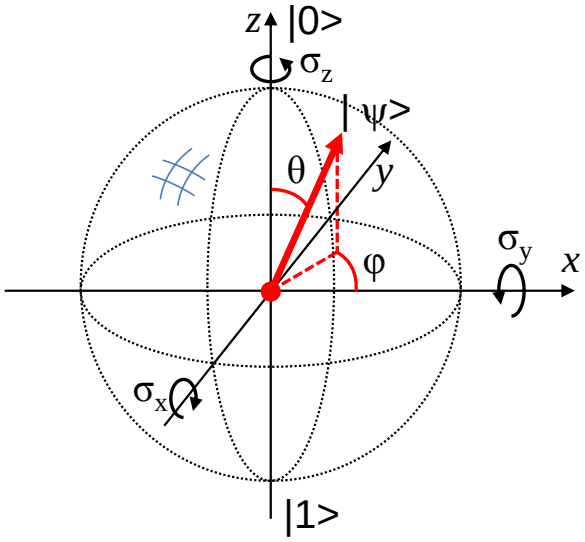

Figure 2.1: Bloch sphere representation of a qubit state $|\psi\rangle = \cos\frac{\theta}{2}|0\rangle + e^{i\phi}\sin\frac{\theta}{2}|1\rangle$. The state is fully characterized by specifying its "latitude" and "azimuth" angles θ and ϕ. Pure quantum states always lie on the surface of the Bloch sphere, whereas mixed quantum states lie inside the sphere.

In the early 1980s, Richard Feynman showed that a classical Turing machine as described above would be unable to efficiently simulate a quantum-mechanical system [47]. He introduced the concept of a *quantum Turing machine* that would be able to simulate quantum-mechanical systems in an efficient manner. Shortly afterwards, Paul Benioff formulated a theoretical description of a quantum Turing machine [10]. Later, David Deutsch developed the theoretical description of an universal information processing framework based on quantum mechanics [35], coining the terms *quantum computing* and *quantum information processing*. He showed that by making use of different properties of quantum mechanics, namely, the superposition principle and entanglement, one could solve certain mathematical problems faster than possible with any classical computer [35]. The work by Deutsch created a large interest in the physics community and led to a huge theoretical and experimental effort aimed at realizing an operational quantum computer and developing quantum algorithms for relevant real-world problems.

2.2 Principles of "Conventional" Quantum Computing

The first scheme imagined for quantum information processing is directly inspired from the classical digital Turing machine: information is stored in a set of quantum two level systems, the *quantum bits* or *qubits*, forming a quantum register, which is manipulated by sequentially applying unitary (and possibly non-unitary) operators to subsets of qubits in the register, typically one or two. As for a classical Turing machine, any arbitrary operation of this quantum processor can be decomposed as a sequence of gate operations chosen from a surprisingly small set of gates, said universal. The power of such a machine comes from the gates operating on superposed states, which provides an intrinsic parallelism in the processing. This *quantum gate* approach is the method relevant to

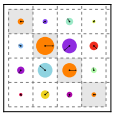

the present thesis work, and we ignore other approaches introduced more recently such as *one-way quantum computing* [100], *adiabatic quantum computing* [45] or *topological quantum computing* [62]. In this section we introduce very briefly quantum bits and quantum gates, as well as some examples of quantum algorithms that are relevant to this work.

2.2.1 Quantum Bits and Registers

As in classical computing, one can define in quantum computing a fundamental unit of information: the qubit. Such a qubit is a quantum-mechanical two-level system that can be put in any superposition

$$|\psi\rangle = \cos\frac{\theta}{2}|0\rangle + e^{i\phi}\sin\frac{\theta}{2}|1\rangle \tag{2.1}$$

of its two states $|0\rangle$ and $|1\rangle$. As can be seen, any state can be described by a pair of real numbers θ and ϕ that characterize the amplitude of each of the two basis states and the phase between them. A useful and intuitive representation of such a single-qubit state is the *Bloch sphere representation*, shown in fig. 2.1. The north and south poles of this sphere correspond by convention to the qubit states $|0\rangle$ and $|1\rangle$ (or vice versa). All states lying on the sphere between those two correspond to pure superposition states, which are characterized by their "latitude" and "azimuth" angles θ and ϕ.

Often it is necessary to describe the qubit not as being in one well-defined pure state but rather being in one of several such states $|\psi_i\rangle$. Usually, we can then associate a classical probability p_i with finding the qubit in either of these states. In this case, we can describe the qubit by a density matrix $\rho = \sum_i p_i \rho_i$, where $\rho_i = |\psi_i\rangle\langle\psi_i|$ is the density matrix of the pure state $|\psi_i\rangle$. All single-qubit density matrices ρ are Hermitian 2×2 matrices with non-negative eigenvalues and can thus be written as

$$\rho = \begin{pmatrix} \rho_{00} & \rho_{01} \\ \rho_{01}^* & \rho_{11} \end{pmatrix} \tag{2.2}$$

in the $|0\rangle, |1\rangle$ basis, with ρ_{00} and ρ_{11} being real numbers and ρ_{01} a complex number. For any state, the matrix has a unity trace $\mathrm{Tr}(\rho) = 1$; for pure states, $\rho = \rho^2$ in addition. The expectation value $\langle A\rangle$ of any operator A acting on the density matrix ρ is given as $\mathrm{Tr}(\rho A)$.

A mixed single-qubit state ρ can also be represented as a 3D vector lying in the *Bloch sphere*. For this, we decompose the density matrix of the state as $\rho = c_i\sigma_I + c_x\sigma_x + c_y\sigma_y + c_z\sigma_z$, where $c_{i,x,y,z}$ are real coefficients and the identity matrix σ_I and Pauli

matrices $\sigma_x, \sigma_y, \sigma_z$ are given as

$$\sigma_I = \begin{pmatrix} 1 & 0 \\ 0 & 1 \end{pmatrix} \quad \sigma_x = \begin{pmatrix} 0 & 1 \\ 1 & 0 \end{pmatrix} \quad \sigma_y = \begin{pmatrix} 0 & -i \\ i & 0 \end{pmatrix} \quad \sigma_z = \begin{pmatrix} 1 & 0 \\ 0 & -1 \end{pmatrix}. \tag{2.3}$$

We can then plot the vector (c_x, c_y, c_z) in a 3D space. The length of it decreases from 1 for a pure state down to 0 for a completely mixed state, hence it will always lie inside a unity sphere.

Quantum states of $n > 1$ qubits cannot be described graphically in an easy way but can be characterized by a density matrix of dimension $2^n \otimes 2^n$ in the computational basis $|q_1 \dots q_n\rangle = |q_1\rangle \otimes |q_2\rangle \dots \otimes |q_n\rangle$, where $|q_i\rangle$ is the state vector of the i-th qubit. For example, a two-qubit Bell state of the form $|\psi_+\rangle = (|01\rangle + |10\rangle)/\sqrt{2}$ can be written as

$$\rho_{\psi_+} = \frac{1}{2} \begin{pmatrix} 0 & 0 & 0 & 0 \\ 0 & 1 & 1 & 0 \\ 0 & 1 & 1 & 0 \\ 0 & 0 & 0 & 0 \end{pmatrix}_{(|00\rangle,|01\rangle,|10\rangle,|11\rangle)}, \tag{2.4}$$

whereas a completely mixed state of 50 % $|01\rangle$ and 50 % $|10\rangle$ is represented by the matrix

$$\rho = \frac{1}{2} \begin{pmatrix} 0 & 0 & 0 & 0 \\ 0 & 1 & 0 & 0 \\ 0 & 0 & 1 & 0 \\ 0 & 0 & 0 & 0 \end{pmatrix}_{(|00\rangle,|01\rangle,|10\rangle,|11\rangle)}. \tag{2.5}$$

Often it is necessary two compare two quantum states to each other. For this, it is useful to define a *quantum state fidelity*, which is a measure of "closeness" between two quantum states. In this work, we will often use the quantum fidelity $F(\rho, \sigma) = F(\sigma, \rho)$ defined as

$$F(\rho, \sigma) = \mathrm{Tr}\left[\sqrt{\sqrt{\rho}\sigma\sqrt{\rho}}\right], \tag{2.6}$$

which can also be written as

$$F(\rho, \sigma) = \left\|\sqrt{\rho}\sqrt{\sigma}\right\|_{tr}, \tag{2.7}$$

where $\|\rho\|_{tr} = \mathrm{Tr}(\rho\rho^\dagger)$ is the Trace norm of the matrix ρ. If we want to compare a density matrix ρ to a pure quantum state $|\psi\rangle$, we can also use the *Trace fidelity* $F_{tr}(\rho, |\psi\rangle)$ defined as

$$F_{tr}(\rho, |\psi\rangle) = \langle\psi| \rho |\psi\rangle. \tag{2.8}$$

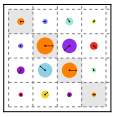

2.2.2 Quantum Gates

Analogously to classical information processing based on logic gates, in quantum computing one uses *quantum gates* that act on individual or multiple qubits and allow to process information. Such a quantum gate can be described as a unitary operator acting on the state of one or several qubits. Theoretically, there is an infinite number of possible quantum gates, however in order to describe all possible quantum operations that can be performed on a qubit register of arbitrary length, it is sufficient to define a *universal set of quantum gates*. Such a set contains a small number of quantum gates that can, by concatenation, produce any arbitrary unitary quantum operator, as shown by the *Solovay-Kitaev theorem* [91, 34]. A universal gate set that will be especially relevant to this work consists of the three single-qubit rotation operators

$$R_x(\theta) = e^{-i\sigma_x \frac{\theta}{2}}, \tag{2.9}$$

$$R_y(\theta) = e^{-i\sigma_y \frac{\theta}{2}}, \tag{2.10}$$

$$R_z(\theta) = e^{-i\sigma_z \frac{\theta}{2}} \tag{2.11}$$

that describe rotations of an angle θ around the X, Y and Z axes of the Bloch sphere, together with the $\sqrt{i\mathrm{SWAP}}$ gate

$$\sqrt{i\mathrm{SWAP}} = \begin{pmatrix} 1 & 0 & 0 & 0 \\ 0 & 1/\sqrt{2} & i/\sqrt{2} & 0 \\ 0 & i/\sqrt{2} & 1/\sqrt{2} & 0 \\ 0 & 0 & 0 & 1 \end{pmatrix}_{(|00\rangle,|01\rangle,|10\rangle,|11\rangle)} . \tag{2.12}$$

By applying the $\sqrt{i\mathrm{SWAP}}$ operation twice we obtain the $i\mathrm{SWAP}$ quantum gate, which is, by itself, **not** a universal quantum gate but which is nevertheless used in some practical quantum algorithms:

$$i\mathrm{SWAP} = \begin{pmatrix} 1 & 0 & 0 & 0 \\ 0 & 0 & i & 0 \\ 0 & i & 0 & 0 \\ 0 & 0 & 0 & 1 \end{pmatrix}_{(|00\rangle,|01\rangle,|10\rangle,|11\rangle)} . \tag{2.13}$$

This universal set it not minimal, since in principle two single-qubit gates with a fixed rotation angle (e.g. $R_x(\pi/4)$ and $R_y(\pi/4)$) together with a universal two-qubit gate would be sufficient to form a universal set of gates [34]. However, it is often advantageous if one can use single-qubit rotations with arbitrary rotation angles around all three axes of the Bloch sphere since it can significantly reduce the number of gates required to implement a given unitary operation.

2.2.3 Quantum Algorithms

The interest in quantum computing is mainly due to the fact that certain problems can be solved faster on a quantum computer than on a classical one. By faster we mean here that the order $\mathcal{O}$ of the run time of the algorithm increases faster on a classical computer than on a quantum computer as a function of the problem size, i.e. the number of bits needed to encode the problem. Up to this day it has not been demonstrated that a quantum computer can perform all tasks faster than a classical computer. However, a small number of real-world problems have been found that can be solved exponentially to polynomially faster on a quantum computer than with known classical algorithms on a classical computer. Here we cite only the two most "famous" ones:

1. **The Shor Factorization Algorithm** Developed by Peter Shor in 1994 [106, 107]. This algorithm can factorize a binary number of length N into its prime factors in $\mathcal{O}(\log N)^3$ steps, therefore exponentially outperforming any known classical factorization algorithm. There is large interest in this algorithm since the security of many asymmetrical cryptographic key exchange protocols rely on the assumption that it is difficult to factorize large numbers into their prime components. Hence, realizing a polynomial-time method for number factorization would undermine the security of these algorithms.

2. **The Grover Search Algorithm**: Discovered by Lov Grover in 1996 [53], this search algorithm can find a single well-defined state in an unsorted database of size N in $\mathcal{O}(\sqrt{N})$ steps, being hence $\sqrt{N}$ faster than a classical search algorithm. Recently, similar algorithms using quantum random walks on graphs have been found that provide similar speed-up [105].

2.2.4 Quantum Simulation

Another domain of interest for quantum computers is the so called *quantum simulation* [72]. Here the goal is to simulate the behavior of an arbitrary quantum system using a quantum computer by either engineering the quantum computer in direct analogy with the system being modeled (so called *analog quantum simulation*) or by numerically simulating the Hamiltonian of the quantum system on a general-purpose quantum computer (so-called *digital quantum simulation*). Since no classical computer can simulate a quantum system efficiently, there is a large interest in quantum simulation, especially in the fields of biology & chemistry [6], quantum field theory [52, 48] and many-body physics [111].

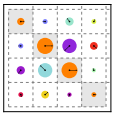

2.2.5 Realization of a Quantum Computer

To realize a working quantum computer, it is necessary to implement highly coherent qubits that can be manipulated, read out and coupled with high fidelity. So far, no fully working quantum computer has been experimentally demonstrated. However, larger progress towards its realization has been achieved in the last decade. Promising approaches for its realization include, among others, ions trapped in magnetic and electric fields [86, 26], nuclear magnetic resonance of organic molecules [59, 114], cold atomic gases [21], photonic circuits [63], semiconductor circuits [74] and, last but not least, superconducting circuits, on which we focus our attention.

2.3 Superconducting Quantum Circuits

In this section we discuss several types of superconducting circuit elements that are most relevant to this work. First, we introduce the reader to the Josephson junction, which is the key device for realizing superconducting qubits and amplifiers. Then, we present a general method for the quantization of arbitrary electrical circuits that we use afterwards to perform canonical quantization of our circuits. We use this method to derive the Hamiltonian of the Cooper pair box and treat the Transmon qubit as a special case. Afterwards, we discuss the properties of transmission lines and transmission line resonators that we use extensively for implementing readout and coupling elements in our qubit design. Then we give a short overview of the field of circuit quantum electrodynamics, which describes the interaction of a superconducting qubit capacitively coupled to a resonator. Finally, we introduce the reader to the Josephson and cavity bifurcation amplifiers that we use for our qubit readout.

2.3.1 The Josephson Junction

The core element used to construct superconducting quantum circuits is the *Josephson junction*. A Josephson junction is based on the Josephson effect [60], which states that between two superconductors connected through an insulating barrier, a supercurrent

$$I_{12} = I_c \sin \varphi \tag{2.14}$$

will flow, depending on the difference $\varphi = \varphi_1 - \varphi_2$ between the gauge-invariant superconducting phases φ_1 and φ_2 on each side of the link. I_c, the *critical current* of the Josephson junction, is the maximum super-current that it can support. φ is related to

the instantaneous voltage between the electrodes of the junction as

$$V = \varphi_0 \frac{\partial \varphi}{\partial t}, \tag{2.15}$$

where $\varphi_0 = \hbar/2e \approx 2.05/2\pi \times 10^{-15}$ Wb. These two simple equations yield a system exhibiting a wealth of interesting physical phenomena which are used today in applications as varied as the detection of weak magnetic fields [27], voltage standards [70], generation of Terahertz radiation [93] and quantum limited amplifiers [116]. The energy associated with the phase difference across the Josephson junction is

$$E = E_J \cdot (1 - \cos \varphi) \tag{2.16}$$

where $E_J = I_c \varphi_0$ is the *Josephson energy*. In addition, the junction usually has an electrostatic energy associated to the capacitance formed by its two electrodes given as $E_C = Q^2/2C$, with $\pm|Q|$ being the charge accumulated on each of the electrodes of the junction.

For currents $I \ll I_c$, the Josephson junction behaves approximately like a nonlinear inductance

$$L_J(\varphi) = \frac{\varphi_0}{I_c \cos \varphi} \approx L_{J0} \left[1 + \frac{\varphi^2}{2} + \mathcal{O}(\varphi^4) \right], \tag{2.17}$$

where $L_{J0} = \varphi_0/I_c$ is the *Josephson inductance*.

Using the potential and capacitive energies of the Josephson junction alone, we can formulate the quantum Hamiltonian of the junction, which is

$$\hat{H} = \frac{1}{2C} \hat{Q}_{tr}^2 + E_J(1 - \cos \hat{\varphi}), \tag{2.18}$$

where $\hat{Q}_{tr}$ is the charge transferred between the two electrodes of the junction and $\hat{\varphi}$ and $\hat{Q}_{tr}$ are conjugate quantum operators that, in analogy to a classical pendulum, play the role of position and momentum for the Josephson junction. In the limit of small angles φ, the Hamiltonian becomes that of a harmonic LC oscillator. The nonlinearity present in the system is a key ingredient for realizing a Josephson qubit since it makes it possible to drive transitions between the first two quantum states of the device without also exciting higher quantum states, as would be the case when driving a harmonic oscillator.

2.3.2 Quantization of Electrical Circuits

In this section we outline a general method to treat arbitrary electrical circuits as the ones discussed before within the framework of quantum-mechanics, hence *quantizing*

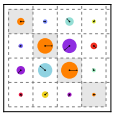

them. This introduction on circuit quantization is based on a seminal article by B. Yurke [124] and an article by M. Devoret [36]. A more specific example of circuit quantization can be found in [22].

An electrical circuit is fully characterized by the parameters of its elements and its topology. The latter can be described as a set of nodes j connected by a number of branches i that are formed by dipolar circuit elements. In classical circuit theory, each branch is described by a voltage V_i between its ends and a current I_i flowing through it. The Kirchhoff laws demand that the sum of the branch voltages V_i along any closed path in the circuit must be zero and that the sum of currents flowing in and out of each node must be zero. For quantization it is usually more convenient to replace voltages and currents with branch charges and fluxes that are defined as

$$\Phi_i(t) = \int_{t_{ref}}^{t} V_i(t')dt', \tag{2.19}$$

$$Q_i(t) = \int_{t_{ref}}^{t} I_i(t')dt', \tag{2.20}$$

where t_{ref} is an arbitrarily chosen reference time. The Kirchhoff laws now write

$$\sum_i Q_i = Q_c \quad , \quad \sum_i \Phi_i = \Phi_c \tag{2.21}$$

with Q_c and Φ_c constants, where the first sum is over charges Q_i of all elements connected to a certain node c and the second one is over all branches forming a closed loop in the circuit. We can obtain a complete set of node and branch equations for any given circuit by constructing a *spanning tree* of the circuit, which is a tree in which all nodes are connected to an arbitrarily chosen *ground node* by one unique path [36]. From the spanning tree we obtain a complete set of branches and the corresponding Kirchoff equations for the fluxes Φ_i around them. Together with the set of Kirchhoff equations for the charges at each node, we can use this system of equations to eliminate unnecessary circuit variables and obtain a description of the circuit using a minimal set of degrees of freedom. Now, to quantize a circuit made up of non-dissipative elements we can follow the method given in [124], writing the Lagrangian (using the reduced set of variables) as

$$\mathcal{L}(\Phi_1, \ldots, \Phi_n, \dot{\Phi}_1, \ldots, \dot{\Phi}_n) = \sum_i \mathcal{V}_i - \sum_i \mathcal{T}_i, \tag{2.22}$$

where the sum i runs over all circuit elements and $\mathcal{V}_i$ and $\mathcal{T}_i$ are the potential and kinetic energies associated to the i-th element. Here, linear inductances contribute only to the potential energy as $\mathcal{V}_{L_i} = \Phi_i^2/2L_i$, whereas linear capacitances contribute only to the ki-

netic energy as $\mathcal{T}_{C_i} = C_i\dot{\Phi}_i^2/2$. Resistors can be described within the Lagrangian formalism by modeling them as semi-infinite transmission lines with a characteristic impedance matching their resistance [124]. We can also include general nonlinear capacitances and inductances that obey the relations $\dot{\Phi} = f_C(Q)$ and $\dot{Q} = g_L(\Phi)$ between their node flux and charge, and whose energies are given as

$$E_C = \int_0^Q f_C(Q')dQ', \tag{2.23}$$

$$E_L = \int_0^\Phi g_L(\Phi')d\Phi'. \tag{2.24}$$

A Josephson junction, for example, can be described as a nonlinear inductance with $g_L^{JJ}(\Phi) = I_c \sin(\Phi/\varphi_0)$, having an associated energy

$$E_L^{JJ} = \int_0^\Phi I_c \sin(\Phi'/\varphi_0)\, d\Phi' = E_J\left(1 - \cos\left[\frac{\Phi}{\varphi_0}\right]\right). \tag{2.25}$$

Transmission lines can be quantized by a similar approach, as shown e.g. in [124]. Externally imposed charges and fluxes can be modeled as "pre-charged" capacitors and inductors with infinite charge or flux and infinite capacitance or inductance that get renormalized at the end of the quantization process [36]. Externally imposed voltages and currents can be treated like this as well by converting them to corresponding fluxes or charges. From the Lagrangian as given by eq. (2.22) we can obtain the classical equations of motion of the system by variation of the action

$$\frac{\partial}{\partial t}\left(\frac{\partial \mathcal{L}}{\partial \dot{\Phi}_i}\right) - \frac{\partial \mathcal{L}}{\partial \Phi_i} = 0. \tag{2.26}$$

For each flux Φ_i we obtain its canonically conjugate momentum Q_i by the equation

$$Q_i = \frac{\partial \mathcal{L}}{\partial(\dot{\Phi}_i)}, \tag{2.27}$$

where $\dot{\Phi}_i = d\Phi_i/dt$. Having obtained Φ_i and Q_i, we can calculate the Hamiltonian $\mathcal{H}$ of the system by applying the transformation

$$\mathcal{H}(\Phi_1, \ldots, \Phi_n, Q_1, \ldots, Q_n) = \sum_j \dot{\Phi}_i Q_i - \mathcal{L}(\Phi_1, \ldots, \Phi_n, \dot{\Phi}_1, \ldots, \dot{\Phi}_n). \tag{2.28}$$

This Hamiltonian, written in generalized coordinates, yields the full set of equations of motion of the electrical circuit and depends only on the canonically conjugate variables $\Phi_1, \ldots, \Phi_n$ and $Q_1, \ldots, Q_n$. First quantization of the circuit can then be done by simply

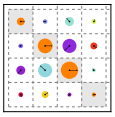

replacing the classical variables by quantum observables such that $\Phi_i \rightarrow \hat{\Phi}_i$ and $Q_i \rightarrow \hat{Q}_i$ and imposing commutation relations between them:

$$\left[\hat{Q}_i, \hat{Q}_j\right] = 0, \tag{2.29}$$

$$\left[\hat{\Phi}_i, \hat{\Phi}_j\right] = 0, \tag{2.30}$$

$$\left[\hat{\Phi}_i, \hat{Q}_i\right] = i\hbar\delta_{ij}. \tag{2.31}$$

In the following sections we apply this quantization method to the Cooper pair box circuit that we use to implement a superconducting qubit and to the simple LCR resonator circuit that we use as a qubit readout and coupling bus.

2.3.3 The LCR Resonator

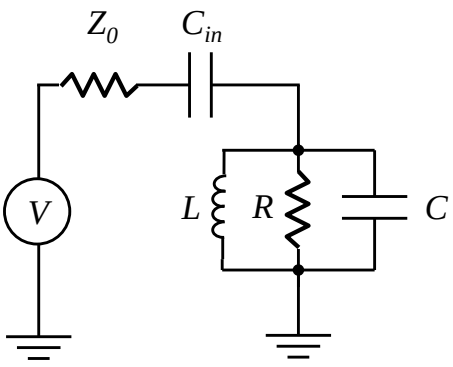

Figure 2.2: An LCR resonator coupled to a voltage source V with internal impedance Z_0 through an input capacitance C_{in}.

The LCR resonator is the circuit element that forms the basis of our qubit readout. The schematic of a LCR resonator coupled to a voltage source through an input capacitance C_{in} is shown in fig. 2.2. The impedance of the resonator alone is

$$Z_{LCR} = \frac{1}{\frac{1}{R} + i\omega C - \frac{i}{\omega L}}, \tag{2.32}$$

yielding a resonance frequency $\omega_r = 1/\sqrt{LC}$ and an *internal quality factor* $Q_{int} = R/Z_r$ with $Z_r = \sqrt{L/C}$ the characteristic impedance of the resonator. To probe the resonator we couple it through a gate capacitance C_{in} to an input transmission line with characteristic impedance Z_0. We can model the resulting circuit as a modified LCR resonator with a frequency-dependent, effective resistance R' such that

$$\frac{1}{R'(\omega)} = \frac{1}{R} + \frac{1}{R_{ext}(\omega)}, \tag{2.33}$$

with

$$\frac{R_{ext}(\omega)}{Z_0} = \frac{1}{C_{in}^2 Z_0^2 \omega^2} + 1, \tag{2.34}$$

and a new capacitance

$$C'(\omega) = C + \frac{C_{in}}{1 + (C_{in}\omega_r Z_0)^2}, \tag{2.35}$$

yielding a shifted resonance frequency $\omega_r' = 1/\sqrt{LC'}$ and a modified quality factor

$$Q_r^{-1} = Q_{int}^{-1} + Q_{ext}^{-1}, \tag{2.36}$$

where $Q_{ext} = R_{ext}/Z_r$. As can be seen, the external quality factor increases $\propto 1/C_{in}^2$. We can define a coupling or decay rate $\kappa = \omega_r/Q_r$, which corresponds to the rate at which energy leaks out of the resonator. For frequencies close to the resonance frequency of the resonator, we can write its impedance as

$$Z_{LCR}(\Delta) = \frac{\omega_r Z_r}{\kappa + 2i\Delta} \tag{2.37}$$

where $\Delta = \omega_r - \omega$ and $Z_r = \sqrt{L/C}$ is the characteristic impedance of the resonator. This approximation is useful when e.g. experimentally fitting resonance data to obtain the quality factor of the resonator.

Before quantizing the LCR resonator, we will first show how we can map a transmission line resonator to the LCR model presented here.

Coplanar Waveguide Resonators

Due to practical reasons we use *coplanar waveguide resonators* instead of lumped elements LCR resonators in our experiments. We will therefore briefly discuss them and show how we can map them to the simple LCR resonator model. A coplanar waveguide is a flat structure with a central conductor that is separated by a gap from a ground plane on either side, as shown in fig. 2.3c. In general, it can be treated as a *transmission line*. A detailed treatment of the physics of transmission lines can be found e.g. in [98]. If we regard a transmission line of finite length l, the voltages and currents at both ends are related through [98]

$$\begin{pmatrix} V_1 \\ I_1 \end{pmatrix} = \begin{pmatrix} \cos\gamma l & iZ_r \cos\gamma l \\ iY_r \sin\gamma l & \cos\gamma l \end{pmatrix} \cdot \begin{pmatrix} V_2 \\ I_2 \end{pmatrix}, \tag{2.38}$$

where $\gamma = \alpha + i\beta = \sqrt{(R + i\omega L)(G + i\omega C)}$ is the *propagation constant* which describes the dispersion and damping of electromagnetic waves along the waveguide, ω is the angular frequency of the electromagnetic wave, L, C, R and G are the characteristic inductance, capacitance, resistance and conductance of the transmission line per unit length (for a superconducting, lossless line $G = R = 0$), $Z_r = \sqrt{L/C}$ is the characteris-

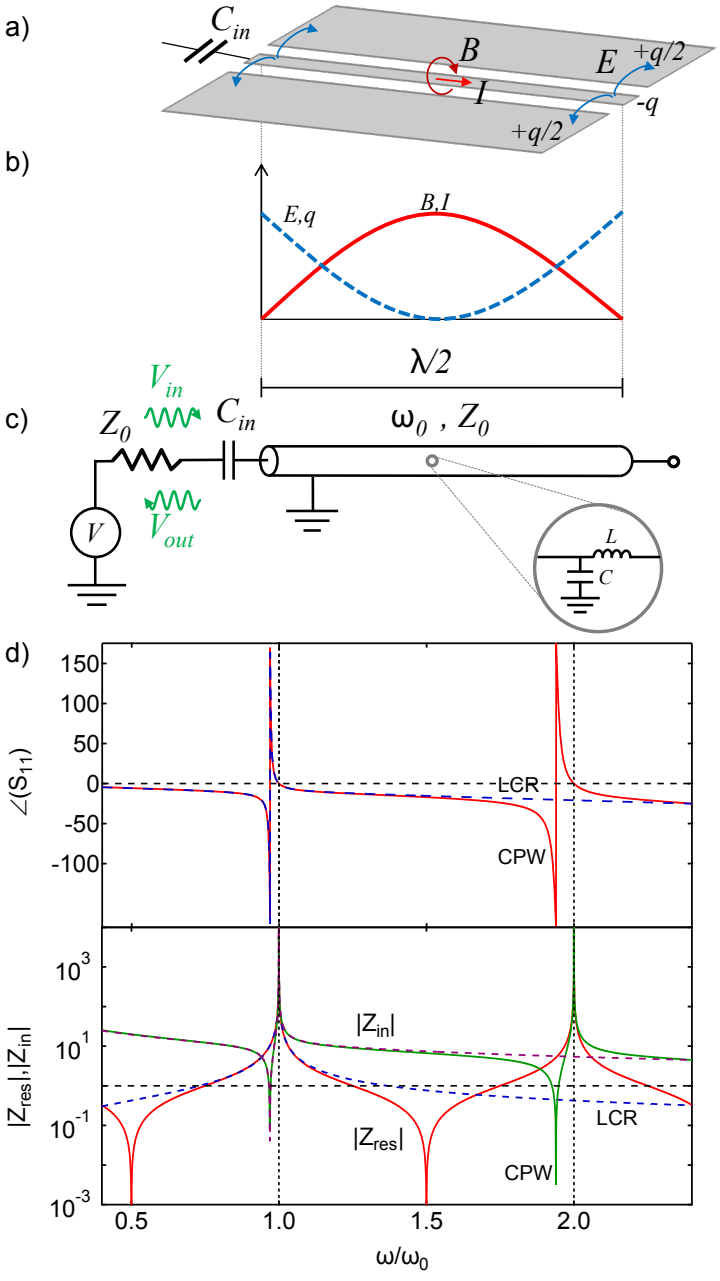

Figure 2.3: Frequency response of an open-terminated $\lambda/2$ coplanar waveguide resonator. a) 3D schematic of the resonator showing the electric field E, the line charge q, the magnetic field B, and the current I configuration. b) Distributions of E or q (blue) and of B or I along the resonator.c) Circuit model of the resonator capacitively coupled to a drive circuit with voltage source V and source impedance Z_0. The (lossless) resonator can be modeled as a series of infinitesimal sections of LC elements (inset). The reflection coefficient $S_{11} = V_{out}/V_{in}$ has a constant amplitude of 1 at all frequencies if the resonator is lossless d) Reflected phase $\arg(S_{11})$ and absolute values of the input impedance $|Z_{in}|$ and resonator impedance $|Z_{res}|$ (see text) as a function of the reduced frequency $\omega_r = \omega/\omega_0$, for a $\lambda/2$ resonator with $\omega_r = Z_r = Z_0 = 1$ ($C_r = \pi/2$) and $C_{in} = 0.1$ (red solid line). With the chosen parameters, the first resonance frequency of the loaded resonator is shifted down to $\omega_r^{\text{loaded}} \approx 0.969$ with respect to that of the uncoupled one. For this first resonance, $\arg(S_{11})$, $|Z_{in}|$, and $|Z_{res}|$ are very close to those of a lumped element $L_r C_r R_r$ resonator with the same ω_r, Z_r and C_{in} (blue dashed lines).

tic impedance of the waveguide and $Y_r = 1/Z_r$ the corresponding admittance.

Let us now consider the open-ended $\lambda/2$ CPW resonator that we use in our experiments to realize the qubit readout resonator, as shown in fig. 2.3b-c. To realize the resonator, we terminate the transmission line at one end by an open gap and connect

the other end to a drive line through an input capacitance C_{in}. We can then make use of eq. (2.38) to calculate the end voltages and currents of the resonator,demanding that $I_2 = 0$ (since the resonator is open-ended). We obtain for the voltage V_1 and current I_2 the relation

$$V_1 = \cos\gamma l V_2, \tag{2.39}$$

$$I_1 = iY_r \sin\gamma l V_2. \tag{2.40}$$

The impedance of the resonator is thus given as $V_1/I_1 = -iZ_r \cot\gamma l$. We can approximately model this distributed CPW resonator as a lumped element parallel LCR resonator by equating their impedances close to their resonance frequency ω_r. This yields an effective inductance, capacitance and resistance for the CPW resonator

$$L_r = \frac{2Z_r}{\omega_r \pi}, \tag{2.41}$$

$$C_r = \frac{\pi}{2\omega_r Z_r}, \tag{2.42}$$

$$R_r = \frac{2Z_r Q}{\pi}. \tag{2.43}$$

Using this mapping, we can calculate all relevant resonator properties using the theory of the lumped element LCR resonator, disregarding however the internal multi-mode structure of the resonator.

Quantization of the Resonator

We can quantize the LCR resonator by following the procedure outlined in the last section. The circuit in fig. 2.2 contains two active nodes. If we disregard for now the input voltage source V, the input capacitance C_{in} and the resistance R, we can directly obtain the Hamiltonian of the non-dissipative part of the LCR resonator as

$$H = \frac{1}{2C}Q^2 + \frac{1}{2L}\Phi^2, \tag{2.44}$$

where Q is the charge accumulated on the capacitor and Φ the flux in the inductance of the resonator. This Hamiltonian corresponds to that of a harmonic oscillator given in second quantization as

$$\hat{H} = \omega_r \hbar \left(\hat{a}^\dagger \hat{a} + \frac{1}{2}\right), \tag{2.45}$$

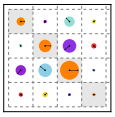

with the *creation and annihilation operators*

$$\hat{a}^\dagger = \sqrt{\frac{1}{2\hbar Z_r}}\left(\hat{\Phi} + iZ_r\hat{Q}\right), \tag{2.46}$$

$$\hat{a} = \sqrt{\frac{1}{2\hbar Z_r}}\left(\hat{\Phi} - iZ_r\hat{Q}\right). \tag{2.47}$$

By inverting these relations we obtain the flux and charge operators $\hat{\Phi}$ and $\hat{Q}$. Calculating their time derivatives gives us the voltage and current operators $\hat{V} = i[\hat{H}, \hat{\Phi}]/\hbar$ and $\hat{I} = i[\hat{H}, \hat{Q}]/\hbar$:

$$\hat{V} = V_{rms}\left(\hat{a}^\dagger + \hat{a}\right), \tag{2.48}$$

$$\hat{\Phi} = \frac{V_{rms}}{\omega_r}\left(\hat{a}^\dagger + \hat{a}\right), \tag{2.49}$$

$$\hat{I} = i\omega_r C V_{rms}\left(\hat{a}^\dagger - \hat{a}\right), \tag{2.50}$$

$$\hat{Q} = iCV_{rms}\left(\hat{a}^\dagger - \hat{a}\right), \tag{2.51}$$

where $V_{rms} = \sqrt{\hbar\omega_r/2C}$ is the root-mean-square voltage corresponding to one photon in the resonator. Using the modified values given by eqs. (2.43), these equations also give the maximum values of $\hat{V}$, $\hat{\Phi}$, $\hat{I}$ and $\hat{Q}$ of the fundamental mode in a transmission line resonator.

2.3.4 The Cooper Pair Box

The LC resonator discussed in the last section is one of the key elements for building quantum circuits. However, it is not possible to implement a superconducting qubit using such a linear resonator since the transition frequencies between all adjacent energy levels are equal, which makes it impossible to drive e.g. the $|0\rangle \rightarrow |1\rangle$ transition of the system without also exciting higher energy states. Therefore, to realize a qubit, we need to introduce a non-linear element in the circuit. One way of doing this is to replace the linear inductance of the LC resonator by a non-linear one. A Josephson junction conveniently provides such a non-linear inductance. The resulting circuit, called a *Cooper pair box (CPB)* contains thus a Josephson junction in parallel with a capacitance and is coupled to an input voltage source through a gate capacitance C_g, as shown in fig. 2.4a. Often one also uses two junctions in a loop instead of a single one, as shown in fig. 2.4b, which allows one to tune the effective Josephson energy of the system by changing the flux inside the junction loop. Finally, in our experimental setup, we can separate the bottom electrode of the CPB capacitively from the ground, as shown in fig. 2.4c. In this section we discuss only the circuit a), since b) can be mapped to the

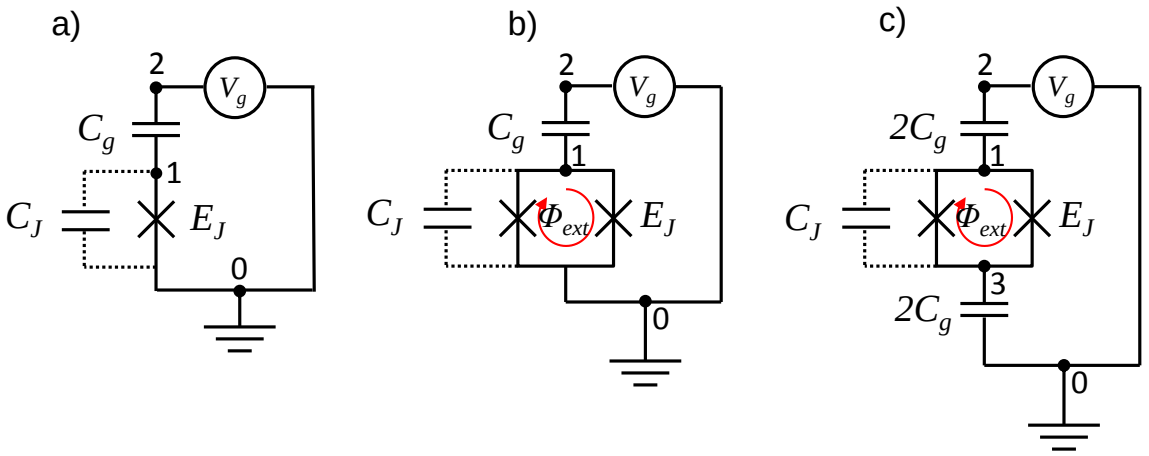

Figure 2.4: a) Circuit schematic of a Cooper Pair Box (CPB). The device consists of a Josephson junction with Josephson energy E_J capacitively coupled to a voltage source V_g through a gate capacitor C_g. The extra capacitance of the Josephson junction as well as any added parallel capacitance is modeled by a capacitor C_J. Charges can accumulate on the island 1 (the box). b) *Split Cooper pair box*, where two junctions with Josephson $E_J/2$ are arranged in a loop, to make the total Josephson energy $E_J|\cos(\Phi_{ext}/\phi_0)|$ tunable with the external flux Φ_{ext} applied to the loop. c) Schematic of a split CPB with C_g split in two series capacitor $2C_g$ to decouple the bottom electrode of the box (3) from the ground. This last geometry is the one used in this thesis work.

simpler version a) and the topology of c) is mathematically equivalent to that of b). The simple CPB circuit 2.4a consists of three nodes (including ground) and two branches. The flux Φ_2 is not independent since it is set by the voltage source V_g, so we can directly eliminate it from the equations. This leaves us with only one remaining active node Φ_1. Using these specifications, the Lagrangian of the circuit is given as

$$\mathcal{L} = \frac{1}{2}C_J\dot{\Phi}_1^2 + \frac{1}{2}C_g\left(\dot{\Phi}_1 + V_g\right)^2 - E_J\left(1-\cos\phi_1\right), \tag{2.52}$$

where $\phi_1 = \Phi_1/\varphi_0$. The canonical momentum Q_1 associated to the flux Φ_1 is given as

$$Q_1 = \frac{\partial\mathcal{L}}{\partial\dot{\Phi}_1} = C_J\dot{\Phi}_1 + C_g(V_g + \dot{\Phi}_1). \tag{2.53}$$

From this, we can directly calculate the Hamiltonian by using eq. (2.28) and substituting Q_1 as given by eq. (2.53) for $\dot{\Phi}_1$, which yields

$$\mathcal{H} = E_J\left(1-\cos\phi_1\right) + \frac{(Q_1 - C_gV_g)^2}{2(C_J+C_g)} - \frac{1}{2}C_gV_g^2. \tag{2.54}$$

Quantization of the Hamiltonian is completed by replacing $Q_i \to \hat{Q}_i$ and $\phi_1 \to \hat{\phi}_1$ and imposing the commutation relations given by eqs. (2.31). If, in addition we introduce reduced operators for the charge $\hat{n} = \hat{Q}/2e$ and discard the energy stored in the volt-

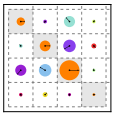

age source (which is irrelevant), we obtain the Hamiltonian of the Cooper pair box, as formulated e.g. in the thesis of V. Bouchiat [18],

$$\hat{H} = E_C \left(\hat{n} - n_g\right)^2 - E_J \cos\hat{\theta}, \tag{2.55}$$

with $\hat{\theta} = \hat{\phi}_1$, $E_C = (2e)^2/(C_J + C_g)$ the charging energy of the Cooper pair box and $n_g = C_g V_g/2e$ the reduced gate charge.

For the split Cooper pair box as shown in fig. 2.4b, the treatment is slightly modified [31]. First of all, we write the Josephson energies of the two junctions as $E_{J1} = (1 + d)E_J/2$ and $E_{J2} = (1 - d)E_J/2$, where $d \in [0, 1]$ is the energy asymmetry between the junctions. When imposing an external phase $\phi_{ext} = \Phi_{ext}/\varphi_0$ in the loop, the potential energy of the two junctions can be written as

$$\mathcal{V}_J = -\frac{E_J}{2}\left[(1+d)\cos\left(\phi_1 - \phi_{ext}/2\right) + (1-d)\cos\left(\phi_1 + \phi_{ext}/2\right)\right] \tag{2.56}$$

$$= -E_J\left[\cos\phi_1 \cos\frac{\phi_{ext}}{2} + d\sin\phi_1 \sin\frac{\phi_{ext}}{2}\right]. \tag{2.57}$$

The remaining part of the quantization process proceeds as above, yielding a Hamiltonian of the split Cooper pair box of the form

$$\hat{H}_{split} = E_C(\hat{n} - n_g)^2 - E_J\left[\cos\hat{\phi}_1 \cos\frac{\phi_{ext}}{2} + d\sin\hat{\phi}_1 \sin\frac{\phi_{ext}}{2}\right]. \tag{2.58}$$

This Hamiltonian can be recast in the form [31]

$$\hat{H}_{split} = E_C(\hat{n} - n_g)^2 - E'_J(d, \phi_{ext})\cos\left[\hat{\phi}_1 + \gamma(\phi_{ext})\right], \tag{2.59}$$

with

$$E'_J(d, \phi_{ext}) = E_J\sqrt{\frac{1 + d^2 + (1 - d^2)\cos\phi_{ext}}{2}}, \tag{2.60}$$

$$\tan\gamma(\phi_{ext}) = -d\tan\frac{\phi_{ext}}{2}. \tag{2.61}$$

It is therefore possible to map the Hamiltonian of the split CPB to that of the single-junction one by defining $\hat{\theta} \to \hat{\phi}_1 + \gamma(\phi_{ext})$ and $E_J \to E'_J(d, \phi_{ext})$.

Using the Hamiltonian (2.55), we can calculate the eigen wave functions of the simple Cooper pair box. The variables $\hat{n}$ and $\hat{\theta}$ are conjugate such that $[\hat{\theta}, \hat{n}] = i\hbar$, the corresponding wave function $\Psi_k(\theta) = \langle\theta, k\rangle$ will therefore satisfy a Schrödinger equa-

tion of the form

$$E_k\Psi_k(\theta) = E_C\left(\frac{1}{i}\frac{\partial}{\partial\theta} - n_g\right)^2\Psi_k(\theta) - E_J\cos(\theta)\Psi_k(\theta). \tag{2.62}$$

Since the potential $-E_J\cos(\theta)$ is 2π periodic, the solution will be of the form

$$\Psi_k(\theta) = \Psi_k(\theta + 2\pi), \tag{2.63}$$

which allows us to map eq. (2.62) to the *Mathieu equation*

$$\frac{d^2y}{dx^2} + [a - 2q\cos(2x)]\,y = 0. \tag{2.64}$$

The *Floquet theorem* states that all solutions to this equation can be written in the form

$$F(a,q,x) = \exp(i\mu x)P(a,q,x), \tag{2.65}$$

and the most general solutions are [31]

$$\Psi_k(r,q,\theta) = \mathcal{C}_1\exp(in_g\theta)\mathcal{M}_C\left(\frac{4E_k}{E_C}, -\frac{2E_J}{E_C}, \frac{\theta}{2}\right) + \mathcal{C}_2\exp(in_g\theta)\mathcal{M}_S\left(\frac{4E_k}{E_C}, -\frac{2E_J}{E_C}, \frac{\theta}{2}\right), \tag{2.66}$$

with

$$E_k = \frac{E_C}{4}\mathcal{M}_A\left(r_k, -\frac{2E_J}{E_C}\right). \tag{2.67}$$

Here, $\mathcal{M}_C$, $\mathcal{M}_S$ are the cosine and sine *Mathieu functions* and $\mathcal{M}_A$ corresponds to the Mathieu characteristic value of each solution. Following the convention in [31] we order the E_k such that the energy increases with increasing k, yielding [64]

$$\begin{aligned} r_k(n_g) &= \sum_{l\pm1}[\mathrm{int}(n_g + l/2)\mathrm{mod}\ 2] \\ &\quad\times\left\{\mathrm{int}(n_g/2) + l(-1)^k[(k+1)\mathrm{div}\ 2]\right\}, \end{aligned} \tag{2.68}$$

where $x\ \mathrm{div}\ y$ denotes the integer part of x/y.

We denote the energy differences between individual energy levels i, j by $E_{ij} = E_j - E_i$. We also define the absolute and relative anharmonicities of the first two energy levels as $\alpha \equiv E_{12} - E_{01}$ and $\alpha_r \equiv \alpha/E_{01}$. An in-depth treatment of the Cooper pair box can be found in [31]. Using the basis states $|i\rangle$ of the CPB, we can rewrite its Hamiltonian in the form

$$\hat{H} = \hbar\sum_{i=0}\omega_i\left|i\right\rangle\left\langle i\right|, \tag{2.69}$$

where $\hbar\omega_i$ is the energy associated to the i-th CPB state. Disregarding CPB levels $i \geq 2$,

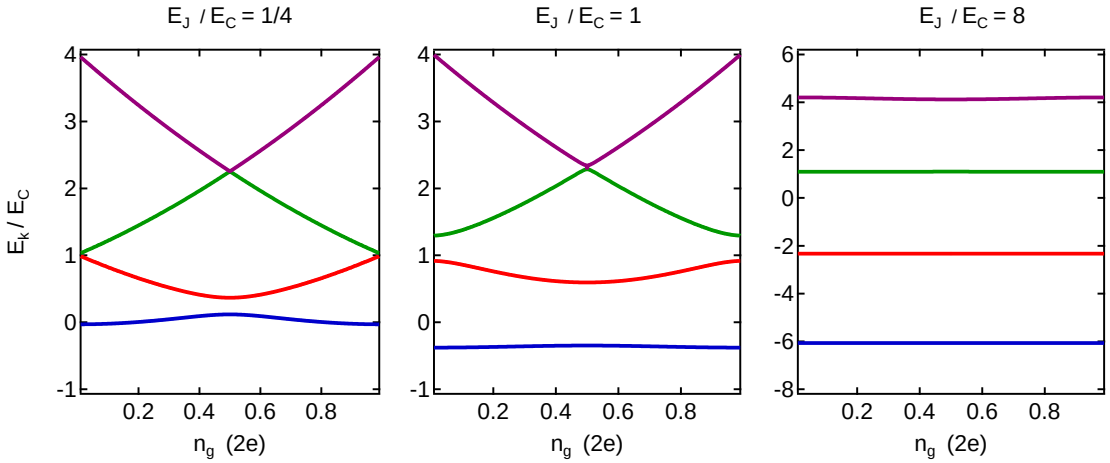

Figure 2.5: First four energy levels of the Cooper pair box as a function of the reduced gate charge n_g, for E_J/E_C ratios equal to 1/4, 1, and 8 (left to right). As can be seen, for $E_J \gg E_C$, the charge-dispersion curve becomes almost completely flat.

we can also formulate an approximate qubit Hamiltonian of the CPB of the form

$$\hat{H} = -\frac{\hbar\omega_{01}}{2}\hat{\sigma}_z, \tag{2.70}$$

where $\omega_{01} = \omega_1 - \omega_0$ is the frequency of the transition $|0\rangle \rightarrow |1\rangle$.

The Transmon Qubit

The Transmon qubit as developed in R. Schoelkopf's lab [64, 119] is a Cooper pair box whose charging energy is strongly reduced by putting a large capacitance in parallel to the Josephson junction, such that the device is in the regime $E_J \gg E_C$. As shown in fig. 2.5, in this regime the charge dispersion of the energy levels of the Cooper pair box becomes extremely weak, thus rendering the transition frequency E_{01} practically insensitive to the value of the gate charge n_g. This reduced sensitivity to charge noise is highly advantageous in experiments since it increases the coherence time of the qubit. However, when increasing the ratio E_J/E_C, one also reduces the anharmonicity α_r of the qubit, therefore limiting the speed of gate operations that can be realized with this system (driving errors related to weak anharmonicity will be discussed more thoroughly chapter 5). In the limit $E_J \gg E_C$, the qubit anharmonicity is well approximated by $\alpha \simeq -E_C/4$, $\alpha_r \simeq -(2E_J/E_C)^{-1/2}$. In this limit we can also approximate the transition frequency of the Transmon as $\hbar\omega_{01} \approx \sqrt{2E_J E_C}$. α_r decreases only geometrically with E_J/E_C, whereas the sensitivity of the qubit to charge noise decreases exponentially with the ratio of Josephson and charging energy.

Decoherence of the Transmon

An in-depth derivation of the decoherence of the CPB and the Transmon can be found e.g. in [31, 64]. Here, we give the relevant expressions that we use to estimate the coherence of the qubits in our quantum processor. Fundamentally, *relaxation* and *dephasing* are the relevant decoherence mechanisms of the qubit, each one characterized by relaxation and dephasing rates Γ_1 and Γ_ϕ and corresponding coherence times $T_1 = \Gamma_1^{-1}$ and $T_\phi = \Gamma_\phi^{-1}$. Following the treatment by Cottet *et. al.* [31], the perturbation of the CPB Hamiltonian by fluctuations of the Hamiltonian can be written as $\delta\hat{H}_\lambda = -\hbar/2(\hat{\mathbf{D}}_\lambda \cdot \sigma)\delta\lambda$, where $\hat{\mathbf{D}}_\lambda = 1/\hbar \cdot \partial\hat{H}/\partial\lambda$ describes the sensitivity of the Hamiltonian to a noise source λ. In the operator $\hat{\mathbf{D}}_\lambda = \vec{D}_\lambda \cdot \vec{\sigma} = D_{\lambda,x} \cdot \hat{\sigma}_x + D_{\lambda,y} \cdot \hat{\sigma}_y + D_{\lambda,z} \cdot \hat{\sigma}_z$ we can distinguish between transversal parts $\vec{D}_{\lambda,\perp}$ (in the XY plane) that describe relaxation processes and longitudinal parts $\vec{D}_{\lambda,z}$ that describe dephasing processes. For the relaxation processes,we can calculate the relaxation rate from the sensitivity $\vec{D}_{\lambda,\perp}$ and spectral density of the noise channel $S_\lambda(\omega_{01})$ using Fermi's golden rule:

$$\Gamma_{S,\lambda}^{rel} = \frac{\pi}{2} D_{\lambda,\perp}^2 S_\lambda(\omega_{01}). \tag{2.71}$$

Similarly, for the dephasing processes $\hat{\mathbf{D}}_{\lambda,z}$ we can calculate the dephasing rates using the corresponding sensitivities and spectral densities as

$$\Gamma_{S,\lambda}^{\phi} = \pi D_{\lambda,z}^2 S_\lambda(\omega = 0). \tag{2.72}$$

Here, the spectral density of the noise is to be evaluated at $\omega = 0$ or at a natural cutoff frequency defined by the experimental protocol if $S_\lambda(\omega = 0)$ diverges [31]. In the case of fluctuations of a control parameter with a $1/f$ spectrum of amplitude A, dephasing is furthermore not exponential $\propto \exp(-\Gamma_\phi t)$, but Gaussian $\propto \exp(-\Gamma_\phi^2 t^2)$ with an effective rate.

$$\Gamma_\phi = 3.7A \left| \frac{\partial\omega_{01}}{\partial\lambda} \right|. \tag{2.73}$$

In the Transmon, the parameters that modulate the Hamiltonian are the gate charge n_g and the flux ϕ_{ext} through the junction loop. The relevant coupling terms are

$$D_{n_g,z} = 2\frac{E_C}{\hbar} \left(\langle 0| \hat{n} |0\rangle - \langle 1| \hat{n} |1\rangle \right), \tag{2.74}$$

$$D_{\phi_{ext},z} = \frac{2E_J}{\hbar} \left| \left(\langle 0| \cos\hat{\theta} |0\rangle - \langle 1| \cos\hat{\theta} |1\rangle \right) \sin\frac{\phi_{\text{ext}}}{2} \right|, \tag{2.75}$$

$$D_{n_g,\perp} = 4\frac{E_C}{\hbar} \left| \langle 0| \hat{n} |1\rangle \right|, \tag{2.76}$$

$$D_{\phi_{ext},\perp} = \frac{E_J}{2\hbar} d \left| \langle 0| \sin\hat{\theta} |1\rangle \cos\frac{\phi_{\text{ext}}}{2} \right|, \tag{2.77}$$

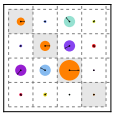

where we have neglected matrix elements that nearly vanish due to wave-function parity reasons. Using these sensitivities and the spectral density of the corresponding noise parameter, we can calculate the relevant dephasing or relaxation rate.

Two decoherence channels involving two types of degrees of freedom Relaxation and dephasing arise from the coupling of the qubit to its environment through the charge and flux channels. The environment degrees of freedom can be either macroscopic, such as those of an electromagnetic impedance, or microscopic, such as charge fluctuators in insulators. Note that, although a given impedance in the environment can couple to the qubit through both the charge or the flux channel, one of them is usually a dominant. Whereas the contribution to decoherence of electromagnetic impedances is amenable to calculation, the contribution of the microscopic degrees of freedom is not. In particular, their contribution to relaxation is uncontrolled, which does not imply however it is negligible. For dephasing, previous measurements on single electron/single Cooper pair devices and on SQUIDs provide estimates of the low frequency charge and flux spectral densities which allows to estimate the induced dephasing.

Relaxation through the Charge Channel Relaxation through the charge channel involves the electromagnetic impedance in the gate circuit, but also in the flux-tuning line because of the residual capacitive coupling of the common mode of this line to the qubit. This latter contribution can be made small by design, and can be treated if necessary along the same lines as for the gate impedance. The spectral density of the charge noise seen by the qubit through its gate circuit is

$$S_{V_g}(\omega) = \frac{\hbar\omega}{2\pi}\left[\coth\left(\frac{\hbar\omega}{2k_BT}\right)+1\right]\mathrm{Re}\left[Z_g(\omega)\right]. \tag{2.78}$$

At low temperatures $k_BT \ll \hbar\omega$, $\coth\left(\hbar\omega/2k_BT\right) \approx 1$, so the resulting relaxation rate as given by eq. (2.71) simply becomes

$$\Gamma_1^{n_g} = 16\pi\beta^2\omega_{01}\frac{\mathrm{Re}[Z_g(\omega_{01})]}{R_K}\left|\langle 0|\,\hat{n}\,|1\rangle\right|^2, \tag{2.79}$$

where $R_K = h/e^2$, $\beta = C_g/C_\Sigma$, $C_\Sigma = C_g + C_J$ and Z_g is the impedance of the gate line in series with C_g.

Relaxation through the Flux Channel Relaxation through the flux channel involves the flux line impedance. The spectral density of magnetic flux fluctuations, as induced by current fluctuations in the flux line coupled to the qubit by a mutual inductance M is

given as

$$S_{\phi_{ext}}(\omega) = \left(\frac{M}{\Phi_0}\right)^2 S_I(\omega) = \left(\frac{M}{\Phi_0}\right)^2 \frac{\hbar\omega}{2\pi}\mathrm{Re}\left(\frac{1}{Z_{fl}(\omega)}\right)\left[\coth\left(\frac{\hbar\omega}{2k_BT}\right)+1\right], \quad (2.80)$$

where $Z_{fl}(\omega)$ is the impedance of the flux line coupled to the qubit. As before, the resulting relaxation rate is thus given as

$$\Gamma_1^{\phi_{ext}} = \frac{\hbar\omega_{01}}{4}\left(\frac{E_J dM}{\Phi_0}\right)^2 \mathrm{Re}\left(\frac{1}{Z_{fl}(\omega_{01})}\right)\left|\langle 0|\sin\hat{\theta}\,|1\rangle\cos\left(\frac{\phi_{ext}}{2}\right)\right|^2 \quad (2.81)$$

Dephasing through the Charge Channel Noise in the gate charge n_g randomly changes the transition frequency of the CPB and induces dephasing. First, the low frequency charge noise arising from the gate impedance is negligible because it is vanishingly small at low temperature as shown by eq. (2.78). We thus only consider here the microscopic charge noise for which a $1/f$ spectrum has been observed in numerous experiments. Even though dephasing is non gaussian for a a $1/f$ noise spectrum, one can define an effective dephasing rate [31, 113]

$$\Gamma_\phi^{\delta n_g} \simeq 3.7A\left|\frac{\partial\omega_{01}}{\partial n_g}\right|, \quad (2.82)$$

where $A \approx 10^{-5}$ is a measured parameter that describes the amplitude of the microscopic gate charge fluctuations. In the limit $E_J \gg E_C$ this rate can be written analytically as

$$\Gamma_\phi^{\delta N_g} \simeq 3.7\frac{A\pi}{\hbar}\left|(\epsilon_1-\epsilon_0)\sin(2\pi N_g)\right| \leq 3.7\frac{A\pi}{\hbar}|\epsilon_1|, \quad (2.83)$$

where ϵ_i is the energy modulation amplitude of the i-th CPB level, given as [64]

$$\epsilon_m \simeq (-1)^m E_C \frac{2^{4m+3}}{m!}\sqrt{\frac{2}{\pi}}\left(\frac{2E_J}{E_C}\right)^{\frac{m}{2}+\frac{3}{4}}\exp\left(-\sqrt{\frac{32E_J}{E_C}}\right). \quad (2.84)$$

This formula shows that the sensitivity to charge noise decreases exponentially with the ratio E_J/E_C for $E_J \gg E_C$ and can thus be very small, which is the rationale for this regime.

Dephasing through the Flux Channel As for dephasing through the charge channel, and for the same reason, dephasing through the flux channel is mainly due to microscopic fluctuators with similarly a $1/f$-type flux noise spectrum in the junction loop. The effective dephasing rate is

$$\Gamma_\phi^{\delta\phi_{ext}} \simeq 3.7A\left|\frac{\partial\omega_{01}}{\partial\phi_{ext}}\right| \quad (2.85)$$

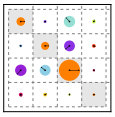

where again $A = 10^{-5}$ is a measured noise amplitude [64]. For the general, asymmetric CPB in the limit $E_J \gg E_C$ we obtain a dephasing rate

$$\Gamma_{\phi}^{\delta\phi_{ext}} \approx \frac{1}{2} A \omega_{01}^{max} \left| \sin(\phi_{ext})(1-d^2) \left(\frac{1 + d^2 + (1-d^2)\cos(\phi_{ext})}{2} \right)^{-3/4} \right| \tag{2.86}$$

where $\omega_{01}^{max} = \sqrt{2E_C E_J}/\hbar$ is the maximum transition frequency of the qubit.

2.4 Circuit Quantum Electrodynamics

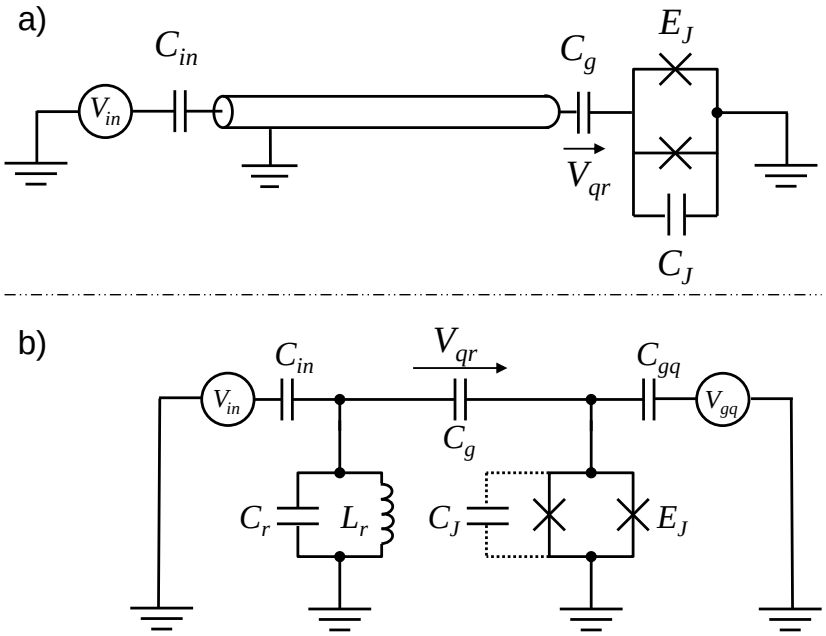

Figure 2.6: a) Schematic of a typical CQED circuit, consisting of a Transmon qubit capacitively coupled to a transmission line resonator. b) Equivalent lumped element circuit.

All experiments reported in this thesis rely on the coupling between a superconducting qubit and a resonator, where the latter serves either for reading out the qubit state and/or for coupling several qubits. The corresponding research field is today referred to as *circuit quantum electrodynamics* (CQED), a term coined in reference to *cavity quantum electrodynamics*, a field that investigates the physics of atoms interacting with a cavity (see e.g. [76, 120] for a review of cavity QED). In circuit QED, qubits that act as "artificial atoms" interact with coplanar or lumped elements resonators on a chip, where the qubit-resonator system can be represented as in fig. 2.6. There, a Transmon qubit is capacitively coupled to a $\lambda/2$ resonator which itself is capacitively coupled to an input transmission line. The Hamiltonian of the resonator and the qubit are given by eqs. (2.45) and (2.70). Due to the capacitance between the qubit and the resonator, a coupling energy between the two arises. The full Hamiltonian of the qubit-resonator system

can therefore be written as

$$\hat{H}_{cqed} = \hat{H}_r + \hat{H}_q + \hat{H}_{qr}, \tag{2.87}$$

where $\hat{H}_r$ and $\hat{H}_q$ are the Hamiltonians of the resonator and the qubit as given by eqs. (2.45) and (2.55), respectively, and $\hat{H}_{qr}$ is the interaction Hamiltonian between them. For small couplings $C_g \ll C_{in}, C_r, C_\Sigma$, we can estimate the coupling energy between the qubit and the resonator simply as

$$\hat{H}_{qr} = \frac{1}{2} C_g \hat{V}_{qr}^2 = \frac{1}{2} C_g \left(V_{rms}(a^\dagger + a) - \hat{V} \right)^2, \tag{2.88}$$

where $\hat{V}_{qr}$ is the voltage across the coupling capacitance C_g and $\hat{V} = 2e/C_\Sigma \cdot (n_g - \hat{n})$ is the voltage across the Transmon electrodes. A rigorous treatment of the coupling energy, which is necessary for large coupling capacitances $C_{qr} \simeq C_r, C_\Sigma$, would require a full quantization of the coupled qubit-resonator circuit, as performed e.g. in [90]. The coupling energy in eq. (2.88) can be rewritten as

$$\begin{aligned} \hat{H}_{qr} &= \frac{1}{2} C_g \left[V_{rms}(a^\dagger + a) - \frac{2e}{C_\Sigma} (n_g - \hat{n}) \right]^2 \\ &= 2e\beta V_{rms} \hat{n}(a^\dagger + a) + \dots \end{aligned} \tag{2.89}$$

in the limit $\beta = C_g/C_\Sigma \ll C_\Sigma$. The terms omitted in eq. (2.89) correspond to energy shifts of the qubit and the resonator which are not directly relevant for the coupling between them. In the limit where the resonator capacitance $C_r \gg C_\Sigma$, we can write the effective Hamiltonian of the qubit-resonator system using the uncoupled basis states $|i\rangle$ of the Transmon as

$$\hat{H} = \hbar \sum_{j=0} \omega_j |j\rangle \langle j| + \hbar \omega_r \hat{a}^\dagger \hat{a} + \hbar \sum_{i \neq j} g_{ij} |i\rangle \langle j| (\hat{a} + \hat{a}^\dagger), \tag{2.90}$$

where the coupling energies g_{ij} are given as

$$\hbar g_{ij} = 2\beta e V_{rms} \langle i| \hat{n} |j\rangle . \tag{2.91}$$

When the coupling between the resonator and the Transmon is such that $g_{ij} \ll \omega_r, E_{01}/h$, we can ignore the terms in eq. (2.90) that describe simultaneous excitation or de-excitation of the Transmon and the resonator and obtain the *rotating wave approximation*, yielding the Hamiltonian

$$\hat{H} = \hbar \sum_{j=0} \omega_j |j\rangle \langle j| + \hbar \omega_r \hat{a}^\dagger \hat{a} + \hbar \sum_{i=0} g_{i,i+1} \left(|i\rangle \langle i+1| \hat{a}^\dagger + |i+1\rangle \langle i| \hat{a} \right). \tag{2.92}$$

The term $|i\rangle \langle i+1| \hat{a}^\dagger$ describes the creation of a photon in the resonator accompanied

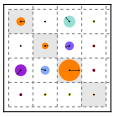

by the de-excitation of the n-level system by one energy level and the term $|i+1\rangle \langle i| \hat{a}$ describes the opposite process.

2.4.1 Qubit Driving

When driving the qubit with a classical signal we can model the drive as a voltage $V_d(t)$ coupled to the qubit gate charge. The coupling Hamiltonian in this case is given as

$$\hat{H}_d = 2\beta e V_d(t)\hat{n} \tag{2.93}$$

In the reduced $\{|0\rangle, |1\rangle\}$ basis, this Hamiltonian can be written as

$$\hat{H}_d = 2\beta e V_d(t) \begin{pmatrix} 0 & n_{01}^* \\ n_{01} & 0 \end{pmatrix}, \tag{2.94}$$

where $n_{01} = \langle 0| \hat{n} |1\rangle$. Usually, we apply the drive voltage through the resonator coupled to the qubit. The resonator filters then the voltage seen by the qubit. For an input drive signal at a fixed frequency ω_d, $V_{in}(t) = V_{in} \cdot \cos \omega_d t$, the voltage $V_d(t)$ seen by the qubit at its gate capacitance is given as

$$V_d(t) = V_{in}(t) 2\sqrt{2} \sqrt{\frac{Z_r}{Z_0}} \frac{Q_r/\sqrt{Q_{ext}}}{\sqrt{1 + 4Q_r^2(\omega_d/\omega_r - 1)^2}}. \tag{2.95}$$

2.4.2 Dispersive Limit & Qubit Readout

When the qubit frequency is far detuned from the resonator frequency such that $\Delta_{ij} = |\omega_{ij} - \omega_r| \gg g_{ij}$, direct energy exchange between the qubit and the resonator is completely suppressed, and only a dispersive shift of the transition frequency of both systems remains as an effect of the coupling between them. This effect has been discussed e.g. in [16, 64] and yields the effective Hamiltonian

$$\hat{H}_{eff} = \frac{\hbar\omega_{01}'}{2}\hat{\sigma}_z + (\hbar\omega_r' + \hbar\chi\hat{\sigma}_z)\hat{a}^\dagger\hat{a}, \tag{2.96}$$

where we have used the two-level qubit Hamiltonian as given by eq. (2.70). Here, the resonance frequencies of the qubit and the resonator are shifted as $\omega_{01}' = \omega_{01} + \chi_{01}$ and $\omega_r' = \omega_r - \chi_{12}/2$ and the dispersive shift is given as $\chi = \chi_{01} - \chi_{12}/2$ [64], where $\chi_{ij} = g_{ij}^2/(\omega_{ij} - \omega_r)$. As can be seen, for a state with n photons, the qubit transition frequency ω_{01} is given as

$$\omega_{01}^n = \omega_{01}' + 2\chi n. \tag{2.97}$$

Thus, there is a dispersive shift of the qubit transition frequency that is proportional to the number of photons in the resonator. Likewise, the resonance frequency of the resonator gets also shifted by $\pm\chi$ depending on the state of the qubit. This *cavity pull* is very useful since it allows us to read out the state of the qubit by measuring the state-dependent frequency displacement of the resonator, as we explain now.

2.4.3 The Josephson Bifurcation Amplifier

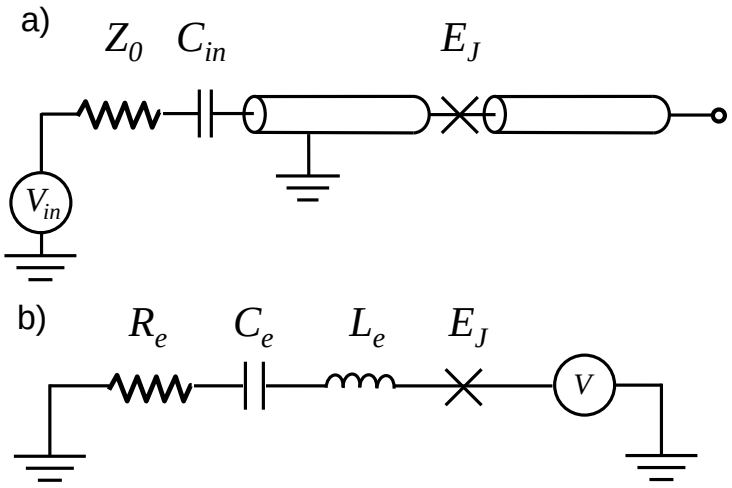

Figure 2.7: a) Circuit schematic of a driven cavity Josephson bifurcation amplifier (CJBA), consisting of two sections of transmission line joined by a Josephson junction, forming a nonlinear, open-end $\lambda/2$ resonator. b) Equivalent lumped elements circuit model.

In this section we discuss the physics of superconducting nonlinear bifurcation amplifiers, which we use to realize a single-shot readout scheme for our qubits. Most notably, we discuss the *cavity Josephson bifurcation amplifier (CJBA)*, as shown in fig. 2.7a. A detailed discussion of the CJBA can be found e.g. in [95]. The device consists of a transmission line resonator with a Josephson junction embedded in its central conductor. We can model the whole circuit as a lumped elements resonator, as shown in fig. 2.7b. The Hamiltonian of the resonator, disregarding the resistor and the voltage source, is

$$H = \frac{\Phi_1^2}{2L_e} - E_J \cos\left(\frac{\Phi_2 - \Phi_1}{\varphi_0}\right) + \frac{Q_2^2}{2C_e}. \tag{2.98}$$

By using the current-phase relation of the Josephson junction we obtain the current

$$I = \frac{\Phi_1}{L_e} = I_0 \sin\left(\frac{\Phi_2 - \Phi_1}{\varphi_0}\right). \tag{2.99}$$

We can hence write $\Phi_1 = g(\Phi_2)$. When we develop this equation to second order in Φ_2

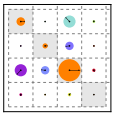

and insert in eq. (2.98), we obtain

$$H = \frac{\phi_2^2}{2L_t} + \frac{Q_2^2}{2C_e} - \frac{1}{24}p^3\frac{\Phi_2^4}{L_t\varphi_0^2}, \tag{2.100}$$

where $L_t = L_J + L_e$ and $p = L_J/L_t$ is the *participation ratio*. Quantizing this Hamiltonian and writing Φ_2 and Q_2 in terms of creation and annihilation operators yields, up to second order, the Hamiltonian

$$H_{N_L} = \hbar\omega_r\left(\hat{a}^\dagger\hat{a} + \frac{K}{2}\hat{a}^{\dagger 2}\hat{a}^2\right), \tag{2.101}$$

where $\omega_r = 1/\sqrt{L_tC_e}$, $R_K = h/e^2$ and

$$K = -\pi p^3 Z_e/R_K \tag{2.102}$$

is the *reduced Kerr constant*. When subjecting the resonator to a classical drive signal

$$H_p/\hbar = \epsilon_p e^{-i\omega_p t}\hat{a}^\dagger + \text{h.c.}, \tag{2.103}$$

the complex amplitude of the intra-resonator field α will satisfy the equation

$$i\left(\Omega\frac{\kappa}{2}\alpha + K|\alpha|^2\alpha\right) + \frac{\kappa}{2}\alpha = -i\epsilon_p, \tag{2.104}$$

where $\Omega = 2Q\left(1 - \omega_p/\omega_r\right)$. For certain drive parameters, this equation has one or two stable solutions for α. Fig. 2.8a shows the current in the resonator as a function of Ω, plotted for several values of the drive power $P_p \propto |\epsilon_p|^2$. Fig. 2.8b shows the different regimes of the resonator as a function of the input power and the detuning Ω. For drive frequencies with $\Omega > \Omega_c = \sqrt{3}$, a bistable region exists in the phase diagram, in which we typically operate the resonator when using it as a CJBA readout of our qubit. For this, we make use of the dispersive shift of the resonance frequency ω_r caused by the qubit, which allows us to map the qubit state to one of the bistable resonator states.

Operation Principle

We can use the CJBA to read out the qubit state using the dispersive interaction between the qubit and the resonator as given by eq. (2.96). Due to this interaction, the frequency of the resonator gets shifted depending on the qubit state by $\pm\chi$. Fig. 2.9b shows again the phase diagram of the CJBA, indicating the stability regions of the different solutions L (low-amplitude) and H (high-amplitude) of the driven system for two different qubit states. If we drive the resonator at a frequency ω_m and ramp the drive power up to point A as indicated in the diagram, the resonator will remain in the low-amplitude state L if the qubit is in state $|0\rangle$, whereas it will switch to the high-amplitude state H if it is in

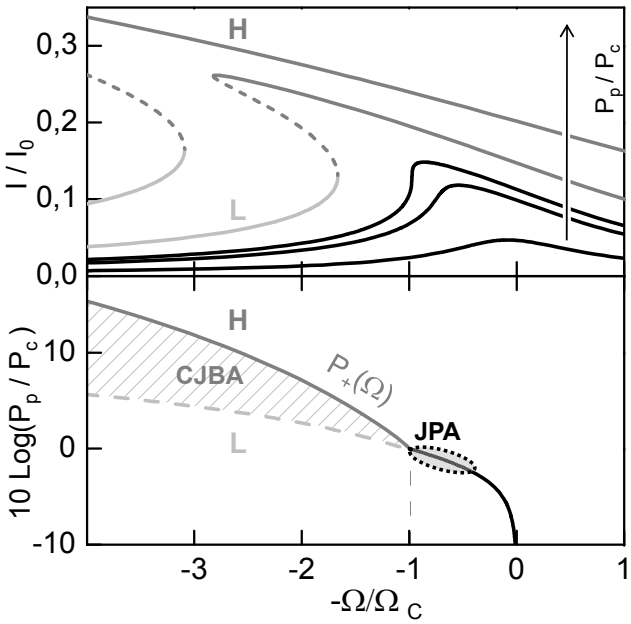

Figure 2.8: a) Current in a driven non-linear resonator as a function of the reduced drive detuning Ω (see text), plotted for various drive powers P_p. For drive detunings Ω larger than a threshold value Ω_c, the resonator becomes bistable above a certain power threshold $P_p > P_c$. b) Phase diagram in the $\Omega - P_p$ plane, showing the region of low amplitude internal oscillations (L), the region of high amplitude internal oscillations (H), and the bistable region (dashed) where both L and H dynamical states can exist and where the non-linear resonator can be operated as a CJBA.

$|1\rangle$. We can thus map the state of the qubit to one of the two states of the resonator, and since these two states can be easily distinguished by measuring the phase of the reflected resonator drive signal, we can obtain a single-shot readout of the qubit state. The measurement of the phase of the reflected drive signal has to be carried out during a long time interval (typically $1 - 2$ μs) to distinguish between the two oscillator states with certainty. To avoid further switching processes during the measurement of the phase, we reduce the drive power of the resonator down to point B in fig. 2.9b. There, the switching probability of the resonator regardless of the qubit state is very small, thus virtually no switching events will occur and we can hence measure the phase of the reflected drive signal for an arbitrarily long time without being limited by spurious switching events. This part of the readout is usually referred to as *latching*.

In theory, the CJBA readout method is able to achieve perfect readout fidelity. However, in reality several factors degrade its performance:

- Since the switching of the resonator is a stochastic process, the associated switching probability will exhibit a s-shaped dependence on the drive power, as shown in fig. 2.9. Now, if the shift of this distribution along the power axis which is induced by the shift of the resonator frequency that depends itself on the state of the qubit is less than the width of the distribution, there cannot be perfect mapping between the qubit and resonator states.

- If the qubit state changes during the measurement step at point A, e.g. due to qubit relaxation or excitation, the resonator state will, with high probability, also fall to the state corresponding to the new qubit state, producing a wrong readout signal.

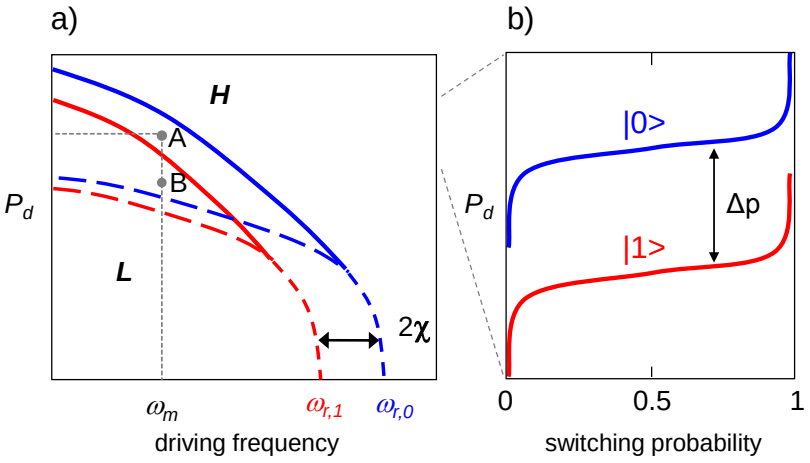

Figure 2.9: a) Same CJBA phase diagram as on Fig. 2.8 for a CJBA embedding a qubit that shifts the diagram by $\pm\chi$ when being in its $|0\rangle$ and $|1\rangle$ states, respectively. b) Probability of switching from L to H as a function of the CJBA input drive power P_d, shown for an embedded qubit in state $|0\rangle$ (blue) or $|1\rangle$ (red).

- The resonator state can switch back from H to L during the latching phase of the readout (so-called *retrapping*), producing a wrong readout value.

With the CJBA, a single-shot readout contrast of 93 % has been achieved in past experiments [77].

2.4.4 Qubit-Qubit Interaction

In this section we discuss possible qubit-qubit coupling schemes. We regard a direct coupling scheme involving a capacitive coupling between two qubits and an indirect scheme involving the coupling of multiple qubits to a resonator which acts as a *quantum bus*.

Direct Capacitive Coupling

A direct capacitive coupling C_{qq} between two qubits yields a coupling Hamiltonian of the form

$$\hat{H}_{qq} = \frac{1}{2}C_{qq}\hat{V}_{qq}^2 = \frac{1}{2}C_{qq}\left[\frac{2e}{C_{\Sigma 1}}(n_{g1}-\hat{n}_1) - \frac{2e}{C_{\Sigma 2}}(n_{g2}-\hat{n}_2)\right]^2 \tag{2.105}$$

$$= \frac{4e^2 C_{qq}}{C_{\Sigma_1}C_{\Sigma_2}}\hat{n}_1\hat{n}_2 + \ldots \tag{2.106}$$

Again, this equation is valid in the limit where $C_{qq} \ll C_{\Sigma 1}, C_{\Sigma 2}$. For larger capacitances C_{qq} the coupling gets renormalized by a factor $\alpha = 1/(1-C_{qq}^2/[C_{\Sigma 1}C_{\Sigma 2}])$ [90]. Rewriting this coupling in the basis of uncoupled qubit states yields the effective Hamiltonian

$$\hat{H}_{qq} = \hbar g_{qq}\left(\sigma_1^+\sigma_2^- + \sigma_1^-\sigma_2^+\right), \tag{2.107}$$

where $\sigma^+ = |1\rangle\langle 0|$ and $\sigma^- = |0\rangle\langle 1|$ and $\sigma_1^\pm = \sigma^\pm \otimes \mathrm{I}$, $\sigma_2^\pm = \mathrm{I} \otimes \sigma^\pm$ and where we have defined the effective qubit-qubit coupling as $\hbar g_{qq} = 4e^2 C_{qq}/C_{\Sigma 1} C_{\Sigma 2}$. Full energy exchange between the qubits is achieved when the qubit frequencies are on resonance. For the more general case of two coupled n-level Transmons, the coupling Hamiltonian takes a slightly more complicated form, as discussed in section A.1. The time evolution operator of the Hamiltonian (2.107) yields a swapping interaction of the form

$$i\mathrm{SWAP}(t,\Delta) = \begin{pmatrix} 1 & 0 & 0 & 0 \\ 0 & \cos t g_e - i\frac{\Delta}{g_e}\sin t g_e & i\frac{g_{qq}}{g_e}\sin t g_e & 0 \\ 0 & i\frac{g_{qq}}{g_e}\sin t g_e & \cos t g_e + i\frac{\Delta}{g_e}\sin t g_e & 0 \\ 0 & 0 & 0 & 1 \end{pmatrix}, \tag{2.108}$$

where $\Delta = \omega_{01}^2 - \omega_{01}^1$ is the detuning between the qubits and $g_e = \sqrt{4g_{qq}^2 + \Delta^2}$ is the effective swapping frequency. Using this interaction, it is straightforward to implement e.g. an $\sqrt{i\mathrm{SWAP}}$ or $i\mathrm{SWAP}$ quantum gate by tuning the qubits non-adiabatically from an off-resonant condition $\Delta \gg g_{qq}$ to a resonance-condition $\Delta = 0$ and letting them interact there for a well-defined time before re-establishing the large detuning, after $t = \pi/4g_e$ for the $\sqrt{i\mathrm{SWAP}}$ gate and $t = \pi/2g_e$ for the $i\mathrm{SWAP}$ gate.

Coupling Bus

For this particular coupling scheme, which was first proposed by Zheng *et. al.* [126, 125, 92], we consider two (or more) Transmon qubits coupled to the same resonator. Blais *et. al.* [15] showed that extending the single-qubit rotating-wave Hamiltonian as given in eq. (2.92) to the case of two qubits coupled to a resonator yields an effective qubit-qubit coupling Hamiltonian of the form

$$\hat{H}_{2q} = \hbar\frac{g_1 g_2(\Delta_1 + \Delta_2)}{2\Delta_1\Delta_2}(\sigma_1^+\sigma_2^- + \sigma_1^-\sigma_2^+). \tag{2.109}$$

This approximation is valid in the limit of large qubit-resonator detuning $\Delta_1 \gg g_1, \Delta_2 \gg g_2$, with $\Delta_{1,2} = \omega_{01}^{1,2} - \omega_r$ the detuning of the $|0\rangle \to |1\rangle$ transition frequency of each qubit. Full energy-exchange between the qubits is achieved when the qubit frequencies are on resonance. By detuning the qubits from the resonator, the effective coupling constant can be varied, which is often advantageous. The time evolution operator resulting from eq. (2.109) is identical to eq. (2.108) when taking into account a modified coupling constant

$$g_{qq,r} = g_1 g_2 \frac{(\Delta_1 + \Delta_2)}{2\Delta_1\Delta_2}. \tag{2.110}$$

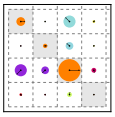

2.4.5 Qubit Decoherence in CQED

In this section we discuss relaxation and dephasing mechanisms specific to the CQED architecture.

Relaxation In CQED, the qubit is coupled capacitively to a resonator, which itself is coupled to a transmission line. The qubit can relax into this transmission line through the gate circuit. The resulting relaxation rate is given by eq. (2.79). If we assume that the Transmon sees only the impedance of the readout resonator through its gate capacitance, as given by eq. (2.37), we can insert the impedance of the resonator in the equation and obtain the resulting relaxation rate:

$$\begin{aligned} \Gamma_1^{Purcell} &= 2\pi \frac{\omega_{01}}{Z_0 \omega_r^2} g_{01}^2 \mathrm{Re}\left[Z(\omega_{01})\right], \\ &= \kappa \cdot \frac{g_{01}^2}{\Delta^2 + \kappa^2/4}. \end{aligned} \tag{2.111}$$

As can be seen, the rate is proportional to $(\Delta^2 + \kappa^2/4)^{-1}$ ($\approx \Delta^{-2}$ for $\Delta \gg \kappa$). The relaxation (or emission) rate of the Transmon compared to the relaxation rate of a qubit get thus modified by the presence of the resonator, which is the *Purcell effect* [99]. For our processor, this effect is advantageous since it shields the qubit from the low impedance environment presented by the input transmission line and increases thus its relaxation time compared to a direct gate coupling to the input line. For a real-world qubit chip, we have to take into account further capacitive couplings of the qubit to e.g. the fast flux line, which will also contribute to the relaxation rate.

Dephasing Besides the usual mechanisms discussed above, dephasing can also occur due to photon-number fluctuations that occur when the resonator is not in state $|0\rangle$, e.g. due to thermal noise or during readout. These fluctuations affect the qubit frequency through an induced AC-Stark shift (2.97) [12, 11, 102].

The sensitivity of the qubit to fluctuations of the photon number n can be derived in the dispersive limit from the Hamiltonian (2.96) as

$$\delta \hat{H}_{\bar{n}} = \hbar \delta\bar{n} \chi \hat{\sigma}_z = -\frac{\hbar}{2} \left(D_{\bar{n}} \cdot \hat{\sigma}_z\right) \cdot \delta\bar{n}, \tag{2.112}$$

where $D_{\bar{n}} = -2\chi$. Photon number fluctuations δn will randomly change the transition frequency of the qubit through the AC Stark effect and cause the qubit phase $\phi(t)$ to diffuse. The dephasing rate of the qubit induced by this noise can be calculated from the correlator

$$\langle \hat{\sigma}_-(t) \hat{\sigma}_+(0) \rangle = \left\langle e^{-i\delta\phi(t)} \right\rangle. \tag{2.113}$$

In the limit where $\kappa \gg \gamma$, we can model the dephasing $\delta\phi(t)$ according to the equation

$$\delta\phi(t) = 2\chi \int_0^t d\tau \; \delta n(\tau). \tag{2.114}$$

For a resonator driven to a coherent state $|\alpha\rangle$, the correlator of the photon-number noise $\delta n(t)$ with intra-cavity mean photon number $\bar{n} = |\alpha|^2$ can be shown to be

$$\langle \delta n(t_1)\delta n(t_2)\rangle = \bar{n} e^{-\frac{\kappa}{2}|t_1 - t_2|}. \tag{2.115}$$

Inserting this in eq. (2.113) yields a dephasing rate in the limit $t \gg \kappa$ of

$$\Gamma_\phi^{\bar{n}} = \frac{8\chi^2}{\kappa}\bar{n}. \tag{2.116}$$

As expected, the dephasing rate depends on the dispersive shift χ and the resonator photon loss-rate κ.

For thermal photon noise, the correlator given above in eq. (2.115) is slightly modified to

$$\langle \delta n(t_1)\delta n(t_2)\rangle = \bar{n}_{th}(\bar{n}_{th} + 1) e^{-\kappa|t_1 - t_2|}, \tag{2.117}$$

yielding a modified dephasing rate

$$\Gamma_\phi^{\bar{n}_{th}} = \frac{4\chi^2}{\kappa}\bar{n}_{th}(\bar{n}_{th} + 1). \tag{2.118}$$

The dephasing induced through photon number shot-noise during the readout is relevant when performing measurements of the qubit state. Thermal photon-noise induced dephasing can be relevant when the thermal photon distribution in the resonator is not negligible. We will take both dephasing mechanisms into account in the design of our processor, as discussed in chapter 3.

2.5 Master Equation Formalism

As already explained, the qubits that we use in this work are subjected to decoherence. This means that their quantum state will at least partially evolve in a non-unitary way, making it impossible to model their evolution using a Schrödinger equation approach alone. In this work we will therefore employ the *master equation approach*, which is a more powerful formalism that can treat the qubit register as an *open quantum system*, which interacts with its environment.

A detailed introduction to the master equation formalism can be found e.g. in [56].

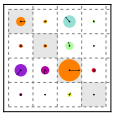

Here we give only a brief overview of the most relevant concepts and results. A quantum system A, described by its density matrix ρ_A defined in a Hilbert space $\mathcal{H}_A$, interacts with an environment E that induces a non-unitary evolution of the density operator ρ_A.

In general, any evolution of the quantum system ρ_A between two points in time can be described by a *quantum map*. Such a quantum map transforms ρ_A into a new matrix $\mathcal{L}_A(\rho_A)$ and can be described as a linear *super-operator* acting in the space of operators defined in $\mathcal{H}_A$. To be a valid quantum operator, $\mathcal{L}_A$ must fulfill the following conditions:

- **Linearity**: The operator $\mathcal{L}_A$ must be linear, i.e. $\mathcal{L}_A(p\rho_A + q\rho'_A) = p\mathcal{L}_A(\rho_A) + q\mathcal{L}_A(\rho'_A)$ with $p + q = 1$.
- **Preservation of** $\mathrm{Tr}(\rho_A)$: The operator $\mathcal{L}_A$ must preserve the unity trace of ρ_A, i.e. $\mathrm{Tr}(\mathcal{L}_A(\rho_A)) = 1$.
- **Complete Positivity**: $\mathcal{L}_A(\rho_A)$ must be positive, i.e. $\left\langle \phi^{(A)} \right| \mathcal{L}_A(\rho_A) \left| \phi^{(A)} \right\rangle \geq 0$ for all $\left| \phi^{(A)} \right\rangle$ in $\mathcal{H}_A$. In addition, for any composite quantum system $A \otimes B$, the quantum map $\mathcal{L}_A \otimes 1_B$ (where 1_B is the identity super-operator acting in $\mathcal{H}_B$) must be positive, i.e.
$$\left\langle \phi^{(AB)} \right| \mathcal{L}_A \otimes 1_B(\rho_{AB}) \left| \phi^{(AB)} \right\rangle \geq 0$$
for all $\left| \phi^{(AB)} \right\rangle$ in $\mathcal{H}_{AB}$.

Under these conditions it can be shown that any quantum map $\mathcal{L}_A$ can be expressed as a sum of operators [65]

$$\mathcal{L}_A(\rho_A) = \sum_i^{N_k} E_i \rho_A E_i^\dagger, \tag{2.119}$$

where $N_k \leq N_A^2$ with N_A the dimension of the Hilbert space $\mathcal{H}_A$, and E_i the *Kraus operators* of the quantum map. These operators satisfy the normalization condition

$$\sum_{i=0} E_i^\dagger E_i = 1. \tag{2.120}$$

Now, we can also use a quantum map $\mathcal{L}_\tau$ to describe the evolution of a density matrix $\rho_A(t)$ during an infinitesimal time τ. In this case, we approximate the time derivative of $\rho(t)$ as

$$\frac{d\rho_A(t)}{dt} = \frac{\mathcal{L}_\tau\left[\rho_A(t)\right] - \rho_A(t)}{\tau}. \tag{2.121}$$

This *Markovian approximation* is valid if τ is longer than the "memory time" of correlations between the system A and its environment but smaller than the characteristic evolution time of system A [56]. In general, since $\mathcal{L}_\tau \to \mathbb{1}$ for $\tau \to 0$, the Kraus operators E_i of the process $\mathcal{L}_\tau$ will depend on τ and can be usually written as $E_i = \sqrt{\tau} L_i$,

where the L_i are the time-independent *Lindblad operators*. By developing eq. (2.121) up to first order in τ, we obtain the *Lindblad master equation*

$$\frac{d\rho_A}{dt} = -\frac{i}{\hbar}[H_A, \rho] + \sum_{i=1}\left(L_i\rho_a L_i^\dagger - \frac{1}{2}L_i^\dagger L_i\rho_A - \frac{1}{2}\rho_A L_i^\dagger L_i\right). \tag{2.122}$$

This equation describes the evolution of quantum system under a Hamiltonian H_A and coupled to an environment that is simulated by the non-unitary action of the operators L_i. Often these operators can be guessed or derived from the relevant decoherence mechanisms present in the quantum system. We will use eq. (2.122) in this work to simulate the dynamics of the qubit register of our quantum processor and fit experimental data to a master equation model of our system.

The relevant case for this work is a qubit subjected to relaxation and dephasing. In general, dephasing is not a Markovian process since it is often caused by slowly fluctuating (e.g. $1/f$) noise, nevertheless it is often useful to describe it using a Markovian process with a phenomenological dephasing rate. The Markovian dephasing and relaxation operators for a single qubit are given as $L_{01}^r = \sqrt{\Gamma_{01}^r}\hat{\sigma}_{01}^-$ and $L_{01}^\phi = \sqrt{\Gamma_{01}^\phi/2}\hat{\sigma}_{01}^z$, where Γ_{01}^r and Γ_{01}^ϕ are the effective relaxation and dephasing rates, respectively, and $\hat{\sigma}_{01}^-$ and $\hat{\sigma}_{01}^z$ are matrices

$$\hat{\sigma}_{01}^- = \begin{pmatrix} 0 & 1 \\ 0 & 0 \end{pmatrix}, \qquad \hat{\sigma}_{01}^z = \begin{pmatrix} 1 & 0 \\ 0 & -1 \end{pmatrix}, \tag{2.123}$$

that describe a relaxation or dephasing process, respectively.

2.5.1 Simulation of the Two-Qubit Processor

To simulate our two qubit processor using the master equation formalism, we will normally use a model that takes into account only the levels $|0\rangle$ and $|1\rangle$ of each qubit. However, in order to e.g. quantify the effect of the finite qubit anharmonicity, we are forced to take into account the state $|2\rangle$ of the Transmon as well, which leads to a slightly more complicated Hamiltonian that we discuss in section A.1. For the simple two-level variant, the Hamiltonian of the two-qubit system can be written as

$$\hat{H} = \hat{H}_1^d \otimes \mathrm{I} + \mathrm{I} \otimes \hat{H}_2^d + \hat{H}_{qq} \tag{2.124}$$

where $\hat{H}_1^d$ and $\hat{H}_2^d$ are the drive Hamiltonians of the first and second qubit, respectively, and are given as

$$\hat{H}_{1,2}^d = \alpha_{1,2}(t)\hat{\sigma}_x + \beta_{1,2}(t)\hat{\sigma}_y + \gamma_{1,2}(t)\hat{\sigma}_z, \tag{2.125}$$

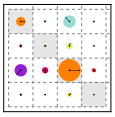

where $\alpha_{1,2}(t)$ and $\beta_{1,2}(t)$ are complex functions and $\gamma_{1,2}(t)$ are real-valued functions. The interaction Hamiltonian in the frame rotating at the average qubit-frequency $(\omega_{01}^1 + \omega_{01}^2)/2$ is given as

$$\hat{H}_{qq} = \begin{pmatrix} 0 & 0 & 0 & 0 \\ 0 & -\frac{\Delta(t)}{2} & g_{qq} & 0 \\ 0 & g_{qq} & +\frac{\Delta(t)}{2} & 0 \\ 0 & 0 & 0 & 0 \end{pmatrix}, \tag{2.126}$$

where $\Delta(t) = \omega_{01}^2(t) - \omega_{01}^1(t)$ is the time-dependent frequency detuning between the two qubits. Inserting the Hamiltonian in eq. (2.124) into eq. (2.122) we can simulate the operation of the two qubit Hamiltonian. The relaxation and dephasing rates depend on the qubit frequency and can be adapted in the simulation according to the chosen qubit frequency working point. Since the master equation approach does not allow to accurately simulate all relevant physical dephasing processes, we will often choose a phenomenological value for the dephasing rate of the qubit, as discussed above. Single-qubit gate sequences are fully described by the three functions $\alpha_{1,2}(t)$, $\beta_{1,2}(t)$ and $\gamma_{1,2}(t)$, a two-qubit swap gate can be modeled by changing the parameter $\Delta(t)$.

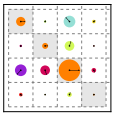

Chapter 3

Realizing a Two-Qubit Processor

This chapter discusses the design and fabrication processes of the two-qubit processor used in this thesis work. We start by introducing the general constraints faced when designing our two-qubit processor, followed by a component-wise discussion of its elements and of the associated parameters we need to choose for them.

3.1 Introduction & Motivation

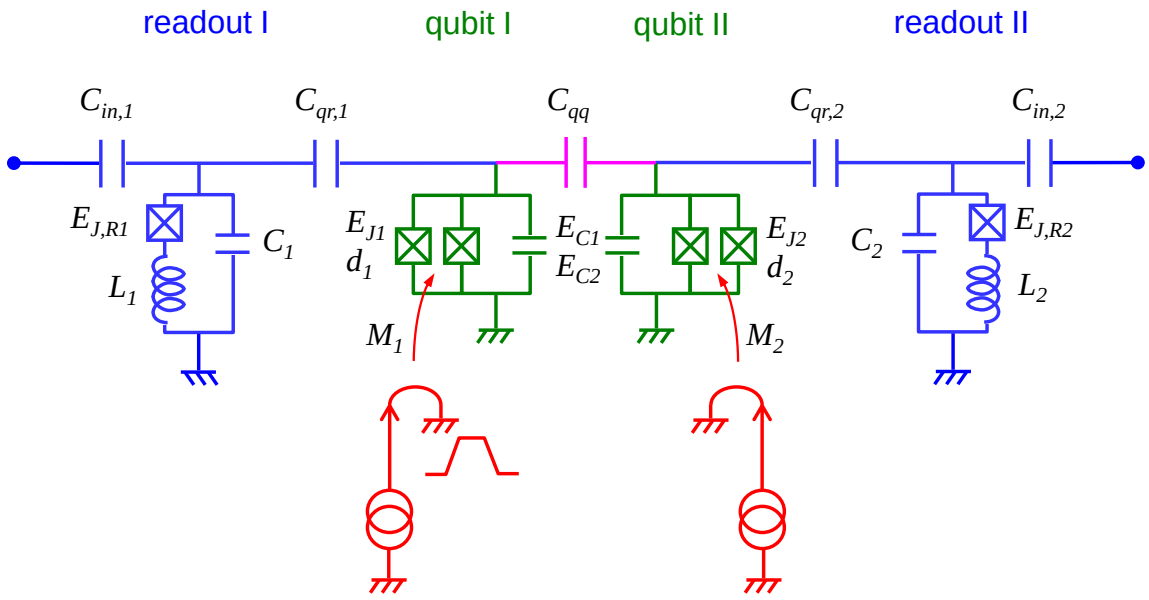

Figure 3.1: Circuit schematic of the two-qubit processor used in this work, together with all the parameters to be chosen. Shown are the two Transmon qubits in green, the drive and readout circuit in blue, the fast flux lines in red and the coupling capacitance in magenta.

As discussed in the introduction, the simplest imaginable quantum processor consists of two qubits that can be manipulated and read out individually, and between which

one can realize a universal two-qubit gate. We implement such a two-qubit processor using two Transmon qubits that are coupled by a fixed capacitor and that can be read out individually by a pair of cavity Josephson bifurcation amplifiers (CJBAs). Figure 3.1 shows the circuit diagram of our processor with all relevant design parameters.

3.1.1 Processor Operation

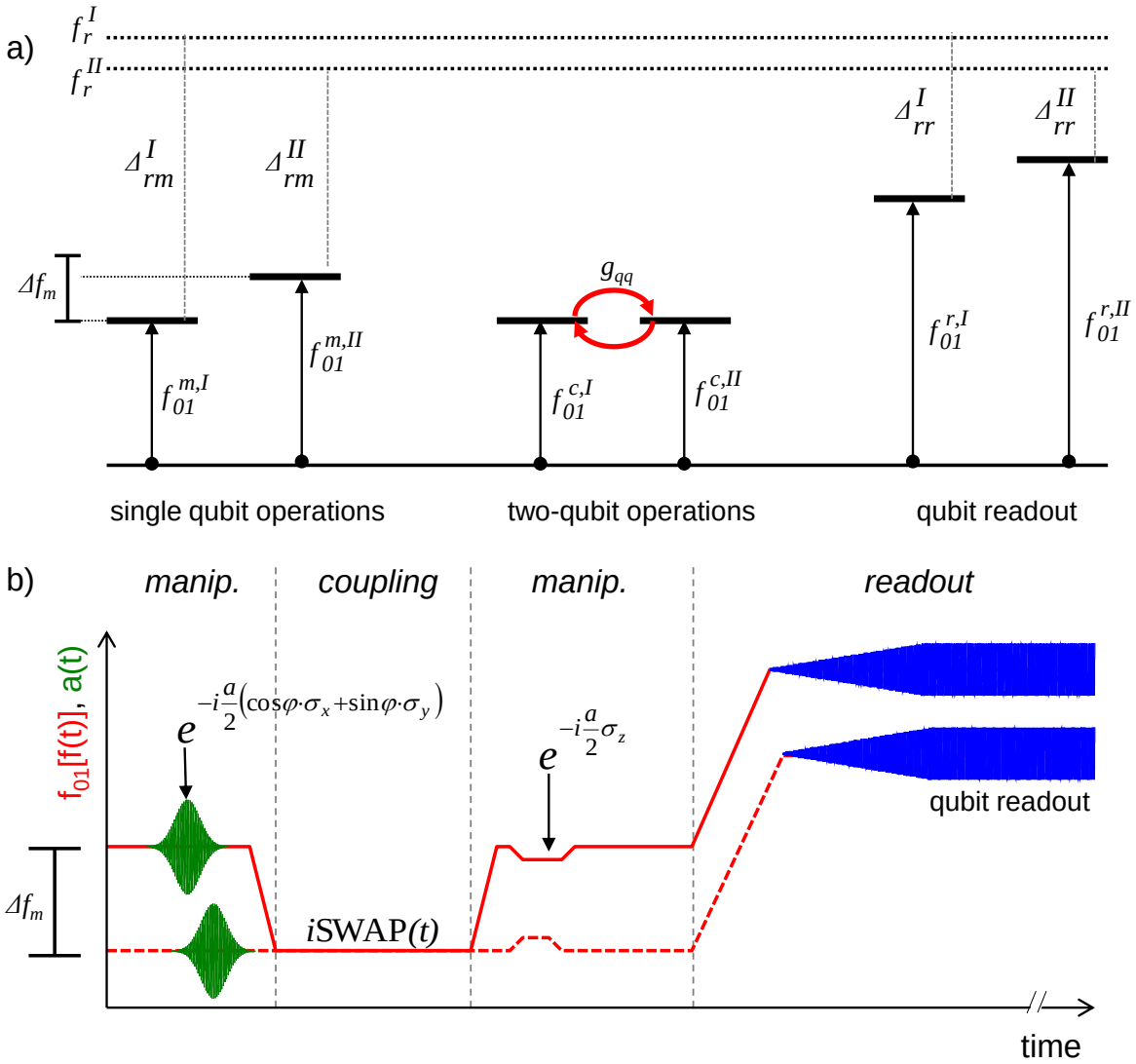

Figure 3.2: Operation principle of the two-qubit processor. a) Frequencies of qubits I and II during the different operations: single-qubit manipulation or parking (index m), two-qubit resonant coupling (index c), and qubit readout (index r). the readout resonator frequencies $f_r^{I,II}$ are also indicated. The smaller the detuning between qubits (resp. between a qubit and its readout), the larger the corresponding coupling 2g (resp. $\chi_r^{I,II}$. b) Typical gate sequence consisting of two single-qubit XY-gates, a two-qubit $i\mathrm{SWAP}(t)$ gate, two single-qubit Z-gates, and qubit readout.

We want to perform three basic operations with the quantum processor:

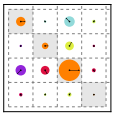

- **Single-qubit gates**: Manipulating a single qubit by rotating its Bloch vector around the X, Y or Z axis of the Bloch sphere.
- **Two-qubit gate**: Performing two-qubit gates, in this work in particular the universal $\sqrt{i\mathrm{SWAP}}$ and $i\mathrm{SWAP}$ gates.
- **Qubit readout**: Performing single-shot readout of the state of each qubit, possibly simultaneously for both of them.

The parameter requirements for each of these operations are usually conflicting: For single-qubit manipulation, no interaction between the qubits must be present, hence the qubit frequencies need to be strongly detuned. However, to implement the two-qubit gates, strong resonant interaction between the qubits is required, hence the two qubit frequencies should be equal. Furthermore, during qubit manipulation the relaxation of the qubit state through the readout resonator should be negligible, hence the frequency detuning Δ between each qubit and its readout resonator should be large, as shown by eq. (2.111). On the other hand, to obtain a high state fidelity during the readout of the qubit state, the interaction between the qubit and its readout resonator should be large, which requires a small frequency detuning Δ between the two.

We solve these conflicting requirements by dynamically changing the qubit frequencies during the operation of the processor using fast on-chip flux lines. Fig. 3.2 illustrates this basic operating principle of the two-qubit processor: For each of the three basic operations (single-qubit manipulation, two-qubit gate and readout), we choose a different set of qubit frequencies $f_{01}^{I,II}$. For the single-qubit gates, the two frequencies $f_{01}^{m,I}$ and $f_{01}^{m,II}$ are detuned by $\Delta f_m = f_{01}^{m,II} - f_{01}^{m,I}$. This tuning is chosen such that only negligible qubit-qubit interaction is present when performing single-qubit manipulations or no operation. Furthermore, at this working point the detuning between each qubit and its readout resonator is such that the qubit lifetime is not limited by relaxation through the gate circuit. To realize a two qubit gate, the two qubits get tuned in resonance such that $f_{01}^{c,I} = f_{01}^{c,II}$. At this point, the qubits experience a swapping interaction as given by eq. (2.107) with an effective swapping frequency $2g$. For the readout, we change the qubit frequencies to $f_{01}^{r,I}$, $f_{01}^{r,II}$, reducing the qubit-resonator detuning such that the corresponding dispersive shift $\chi^I(f_{01}^{r,I})$ and $\chi^{II}(f_{01}^{r,II})$ of the resonator during readout assures an optimal readout fidelity. The displacement of the qubit frequency between the different working points has to be performed on a time scale faster than all relevant qubit manipulation and coupling frequencies but not as a fast as to induce transitions of the qubit state.

We discuss now the parameters of each component of the processor in greater detail, explaining each time the relevant design goals and possible conflicts and presenting the parameter choice or compromise we arrive at.

3.2 Qubit Design

The main design goals for the qubits are large coherence times, good frequency tunability and the possibility of fast single-qubit driving. Good frequency tunability is important since we need to move the qubits to different frequency working points for single-qubit and two-qubit manipulation as well as qubit readout. The maximum qubit drive frequency should be large compared to the decoherence rate of the qubit, so that one is able to perform a large number of gate operations on the qubit before its coherence is destroyed, which is crucial when running quantum algorithms.

3.2.1 Qubit Frequency & Junction Asymmetry

The choice of the maximum qubit frequency is influenced by several requirements:

- The density of thermal photons at the qubit frequency should be sufficiently low at the operating temperature of the circuit (typically 20-100 mK) such that the thermal excitation of the qubit into higher energy levels is negligible.
- Robust equipment for signal generation and measurement in the frequency range of the qubit should be available. This includes microwave sources needed to generate the charge drive pulses as well as room-temperate and cryogenic microwave components such as mixers, splitters, circulators and amplifiers.
- The design of microwave circuits is all the more easy, the lower the required frequency range.

In addition, the choice of the qubit frequency also influences the choice of the readout resonator frequency. For our qubits, we choose a minimum transition frequency of $\omega_{01}^{1,2}/2\pi = 4\ \mathrm{GHz}$, which ideally yields a negligible excited state occupation probability of $p(|1\rangle) = 1/[1 + \exp(\hbar\omega/k_B T)] = 2.1\%$ at $T = 50\ \mathrm{mK}$. In addition, in the frequency range $2 - 18\ \mathrm{GHz}$, commercial microwave equipment and components are available for both room-temperature as well as cryogenic applications. A qubit frequency tunability bandwidth of 3 GHz being sufficient for the operation of the processor, we choose a maximum qubit frequency $\omega_{01}^{max}/2\pi = 7\ \mathrm{GHz}$.

As described in chapter 2, we use a split Josephson junction geometry as shown in fig. 2.4b to make the Josephson energy of the qubit tunable by an external flux Φ_{ext}. The modulation depth of $E_J(\Phi_{ext})$ is given by eq. (2.61): A finite asymmetry reduces the manipulation depth of the Josephson energy and therefore diminishes the sensitivity of the Transmon to flux-noise. Hence we chose an asymmetry $d \approx 0.35$ so that the minimum qubit frequency coincides with our lower boundary frequency of $4\ \mathrm{GHz}$, reducing the sensitivity of the qubit to flux noise at its working point.

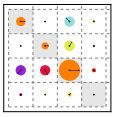

3.2.2 Single-Qubit Gates

We distinguish between single-qubit rotations around the X and Y axes and around the Z axis of the Bloch sphere. The latter are implemented by changing the qubit frequency using a fast on-chip flux line, whereas the former are implemented by driving the qubit with an oscillatory electrical drive signal at its resonance frequency. For the X/Y gates, it is necessary to capacitively couple the qubit to an external charge driving circuit.

Charge Driving The maximum drive frequency of the qubit is limited by its anharmonicity: Since the Transmon qubit is only weakly anharmonic, when driving the qubit at a frequency comparable to the qubit anharmonicity, transitions to higher Transmon levels are induced: This yields a leakage of the qubit state out of the computational basis, and hence unitary drive errors. This effect can be partially alleviated by increasing the anharmonicity of the qubit. However, by increasing the anharmonicity, one also increases the sensitivity of the qubit to charge noise. Hence it is necessary to find a compromise for the value of the qubit anharmonicity which allows sufficiently fast qubit driving but which does not incur too much dephasing.

To estimate quantitatively the drive error arising due to the finite anharmonicity of a Transmon, we model its driving using a simple three-level Hamiltonian in the rotating-frame, as used e.g. in [88]:

$$\hat{H} = \alpha \begin{pmatrix} 0 & \epsilon^*(t)/\alpha & 0 \\ \epsilon(t)/\alpha & \delta/\alpha & \sqrt{2}\epsilon^*(t)/\alpha \\ 0 & \sqrt{2}\epsilon(t)/\alpha & 2\delta/\alpha + 1 \end{pmatrix} \tag{3.1}$$

Here, $\epsilon(t) = \epsilon_x(t) + i\epsilon_y(t)$ is the complex drive IQ amplitude in the rotating qubit frame, δ is the detuning of the microwave drive from the Transmon ω_{01} transition frequency and α is the Transmon anharmonicity. Due to the presence of the third energy level, the effective $|0\rangle \rightarrow |1\rangle$ transition frequency will get shifted with respect to the bare frequency ω_{01} when driving the qubit. For $\delta = \alpha = 0$ (and $\delta/\alpha \rightarrow 1$), the characteristic polynomial of $\hat{H}$ is given as $E(E^2 - 3|\epsilon|^2/4) = 0$ with the two eigenvalues $E = \pm|\epsilon|\sqrt{3}/2$. Thus, for weak anharmonicities this frequency shift is given approximately as $\Delta_{ac} = \sqrt{3}|\epsilon|/2$. To estimate the leakage to the Transmon level $|2\rangle$ when driving the system, we calculate the eigenvalues and eigenvectors of the Hamiltonian (3.1). We then decompose an initial state $|0\rangle$ in the eigenbasis of $\hat{H}$, and calculate its subsequent evolution under the operator $U_d(t, \delta, \epsilon_0)$ with a constant drive amplitude ϵ_0. By numerically maximizing the occupation probability of the state $|1\rangle$ as a function of the evolution time t and the drive detuning δ we obtain the ideal gate time, gate error and frequency shift for a π-pulse at a given drive frequency/anharmonicity ratio. In

fig. 3.3 we show these quantities as a function of ϵ/α. As can be seen, the gate error due to leakage into the level $|2\rangle$ increases with the drive frequency. For very large drive frequencies, the gate fidelity saturates at a value of $F \approx 0.86$ (the numerically obtained maximum π-pulse fidelity for ultra-strong driving of the three-level system is $F_{max} \approx 0.895$). We can make use of fig. 3.3 to estimate the minimum required qubit anharmonicity given the desired gate fidelity and gate time. If we demand a maximum Rabi frequency $\epsilon/2 = \Omega_{Rabi}^{max} = 2\pi \cdot 100$ MHz, which corresponds to a gate time for a single-qubit π-pulse of $T_\pi = 5$ ns small compared to the targeted relaxation and dephasing times of the qubit of $T_1, T_\phi \simeq 1$ μs, and a maximum π-gate error of $1 - F_\pi = 0.04$, we need an absolute anharmonicity $\alpha > 250$ MHz.

In our experiments, we use Gaussian-shaped drive pulses, which already reduce the leakage to the state $|2\rangle$ compared to the continuous pulses that we analyze here. Furthermore, it is possible to correct leakage errors using optimized DRAG drive pulses [75, 24], thereby eliminating leakage to the third qubit level. In this work, we did not use such techniques, and we will include possible errors arising due to leakage to higher Transmon levels in our error models when discussing experimental data.

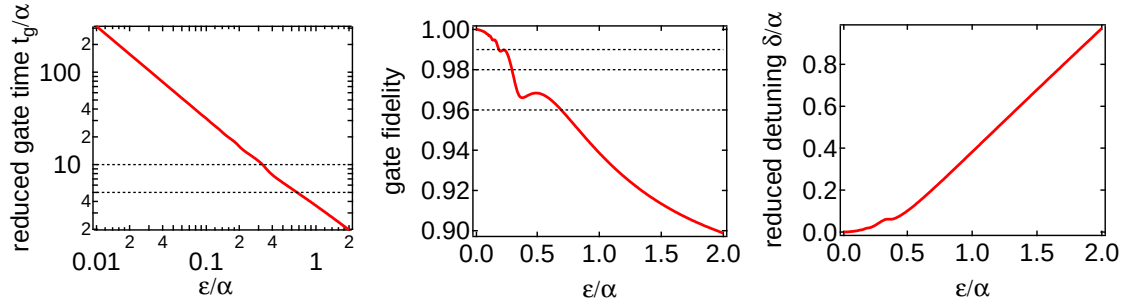

Figure 3.3: Gate duration, gate fidelity, and shift in driving frequency of a π single-qubit gate applied to the three-level Transmon, as a function of the driving strength ϵ/α. As the drive strength increases, the gate duration decreases as α/ϵ whereas the gate fidelity decreases non-monotonously.

Furthermore, charge driving of the qubit is done through the readout resonator on the chip, as shown in fig. 3.1. The Rabi frequency of the qubit in eq. (2.94) is given as $\Omega_{Rabi} = 2\beta e V_d \langle 0| \hat{n} |1\rangle$, where the drive voltage V_d seen at the qubit gate capacitance depends on the input voltage V_{in} at the input capacitance of the resonator as given by eq. (2.95). Since the resonator acts as a band-pass filter for the input drive signal, the more the drive frequency ω_d is detuned from the resonator frequency ω_r, the smaller the gate voltage seen by the qubit is. A Rabi frequency of $\Omega_{Rabi}^{max}/2\pi = 100$ MHz at $\omega_{01}/2\pi = 4$ GHz corresponds to $V_{in} = 0.4$ mV for the resonator parameters that we will choose below, $\omega_r/2\pi = 6.7$ GHz, $g_{01}/2\pi = 50$ MHz and $Q = 800$. With 60 dB attenuation in the cryostat input lines, this corresponds to an injected power of $P \approx 5$ dBm at room temperature, which is compatible with our microwave setup .

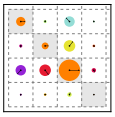

Flux Driving To rapidly change the flux in the qubit loop, we couple each qubit inductively to a fast flux line. The flux induced in the qubit loop by this line is given as $\Phi_{ext} = MI_{fl}$, where I_{fl} is the current in the line and M is the mutual inductance between the flux line and the qubit loop, which can be estimated as $M = \mu_0 l \ln\left[(d_f + w)/d\right]/2\pi$, where l is the length of the qubit loop parallel to the flux line, d_f the distance of the loop to the line and w the width of the qubit loop perpendicular to the flux line. In order to avoid sample heating through the flux line, we demand a maximum current for inducing one flux quantum Φ_0 in the loop not in excess of $I_{\Phi_0}^{max} = 10\ \mathrm{mA}$, corresponding to an electrical input power of $P_{in}^{max} = 50\ \mathrm{mW}$ on a $50\ \Omega$ transmission line with 20 dB attenuation and $P_{out}^{max} = 500\ \mu\mathrm{W}$ on the output transmission line, which can be easily dissipated on the 1 K stage of the cryostat. This yields a minimal value of the mutual inductance $M \geq 0.23\ \mathrm{pH}$, which can easily be achieved with a qubit loop of $l = w = 4\ \mu\mathrm{m}$ at a distance $d_f = 12\ \mu\mathrm{m}$ to the flux line. The coupling of the qubit to the flux line also induces decoherence that we will take into account later when confirming our choice of M.

When passing a current through the flux line, superconducting shielding currents build up in the superconducting ground plane around the line. Therefore, we usually remove the ground plane between the center pin of the flux line and the qubit loop, since otherwise the induced shielding currents would modify the effective flux seen by the qubit and lead to unwanted distortions in the shape of the applied flux signal. However, removing this ground plane also leads to stronger capacitive coupling of the qubit to the flux line, thereby increasing qubit relaxation, which we also have to take into account.

3.2.3 Qubit-Qubit Coupling

We use a direct capacitive coupling between our qubits to create an interaction between them suitable to implement a two-qubit gate. The full interaction Hamiltonian is given by eq. (2.108), and the coupling strength g_{qq} between the two qubits can be calculated with eq. (2.106). This coupling strength must be chosen such that the interaction between the qubits is sufficiently strong to realize two-qubit gate operations with adequate fidelity, but not too strong in order to still allow to suppress the coupling by detuning the qubit frequencies, as needed. By diagonalizing the Hamiltonian (2.107) we find for the eigenenergies $E_{qq}^{\pm}$, the swapping frequency f_{qq} and the swap amplitude a_{qq} of the two coupled

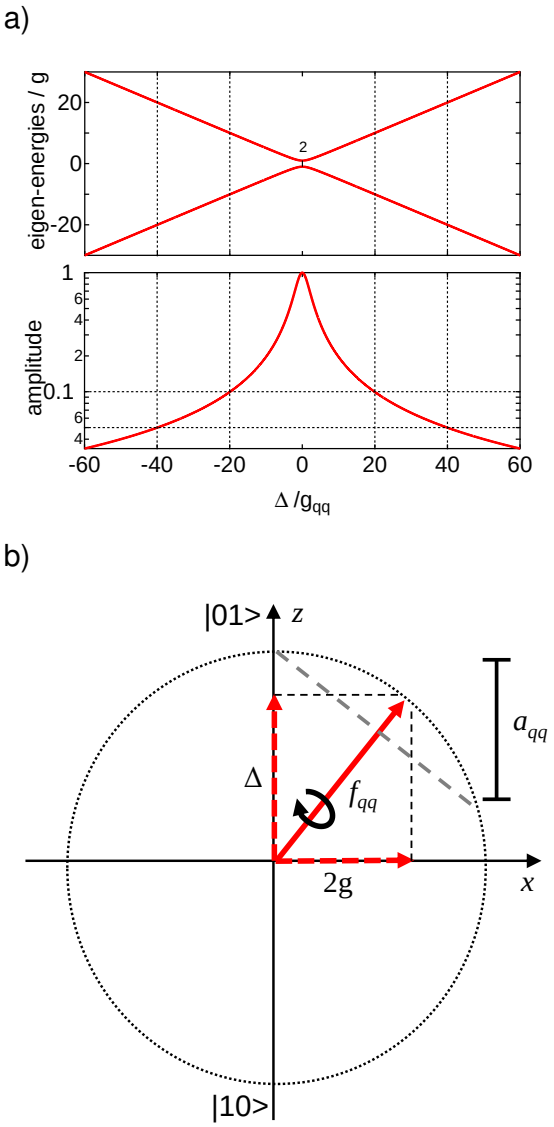

Figure 3.4: a) Two-qubit eigen-energies $E_{\pm}$ and swapping amplitude a_{qq} given by eqs. (3.2) as a function of detuning Δ between qubits. For $\Delta \gg g$, the amplitude of the swap decreases $\propto 1/\Delta$ and the frequency increases $\propto \Delta$. To effectively switch off the swapping interaction to $a_{qq} = 0.1$, a detuning of $\Delta = 20g$ is required. b) Illustration of the swapping amplitude and frequency on a "Bloch sphere" representing the $(|01\rangle,|10\rangle)$ register's subspace: The rotation axis depends on the ratio Δ/g; it coincides with the x axis when $\Delta = 0$ and asymptotically approaches the z axis when for $\Delta \gg g$. At the same time, the rotation frequency around this axis increases with Δ.

qubits as a function of the qubit-qubit detuning $\Delta/2\pi = f_{01}^{I} - f_{01}^{II}$ the values

$$\begin{aligned} E_{qq}^{\pm} &= \pm\frac{1}{2}\sqrt{4g_{qq}^2 + \Delta^2}, \\ f_{qq} &= \sqrt{4g_{qq}^2 + \Delta^2}, \\ a_{qq} &= \frac{2g_{qq}}{\sqrt{4g_{qq}^2 + \Delta^2}}. \end{aligned} \tag{3.2}$$

Figure 3.4 shows the the eigen energies and qubit-qubit swapping amplitude as a function of the normalized qubit-qubit detuning Δ/g. As can be seen, for $\Delta \gg g$ the swap amplitude decreases $\propto 1/\Delta$ whereas the swap frequency increases $\propto \Delta$. For our processor, we demand that the residual swapping amplitude $a \leq 0.1$ when the qubits are "parked" for single-qubit gates and readout, hence it is necessary to de-

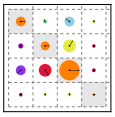

tune the qubits by $\Delta \approx 20g$. At this detuning, the swapping frequency is given as $f_{qq}(20g) \approx 20g$. For our processor, we choose $2g/2\pi = 10\ \mathrm{MHz}$, corresponding to a qubit-qubit detuning of $200\ \mathrm{MHz}$ at $a_{qq} = 0.1$ and an associated swapping frequency $f_{qq} = 100\ \mathrm{MHz} = (10\ \mathrm{ns})^{-1}$. The required frequency displacement is easily achievable with the on-chip fast flux lines. On resonance, the swap frequency of $10\ \mathrm{MHz}$ allows us to realize an $\sqrt{i\mathrm{SWAP}}$ gate in $25\ \mathrm{ns}$ and an $i\mathrm{SWAP}$ gate in $50\ \mathrm{ns}$, which is sufficiently fast compared to the estimated relaxation and dephasing times of the qubits. The residual swapping between the qubits at their parking position is usually small enough to be irrelevant for most experiments performed in this work. However, when executing long gate sequences, as required for certain algorithms, the induced error may be too large, hence a larger detuning should be chosen for these cases.

To estimate the error due to finite rise times for the flux pulse before the $i\mathrm{SWAP}$ gate, we numerically solve the Schrödinger equation of the 2-qubit system in the $|01\rangle, |10\rangle$ basis, which is given as

$$i\hbar \begin{pmatrix} \dot{\psi}_{01} \\ \dot{\psi}_{10} \end{pmatrix} = \begin{pmatrix} -\frac{\Delta(t)}{2} & g_{qq} \\ g_{qq} & \frac{\Delta(t)}{2} \end{pmatrix} \cdot \begin{pmatrix} \psi_{01} \\ \psi_{10} \end{pmatrix} \tag{3.3}$$

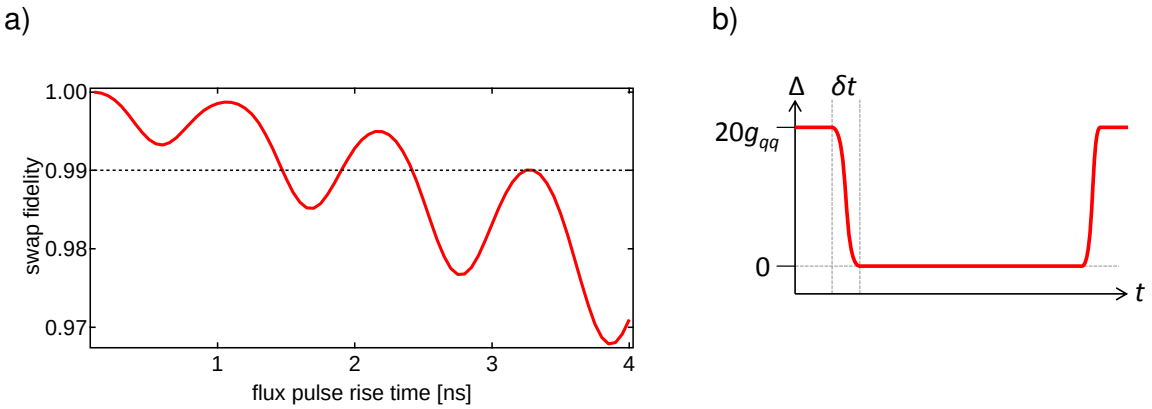

Figure 3.5: a) Numerically obtained maximum fidelity of a two-qubit $i\mathrm{SWAP}$ gate realized by changing the detuning Δ in eq. (3.3) from $\Delta = 20g_{qq}$ to $\Delta = 0$ using a Gaussian pulse of width δt. b) Pulse shape used in the simulation.

To estimate the error, we go from a detuning $\Delta = 20g_{qq}$ at $t = 0$ to a detuning $\Delta = 0$ using a Gaussian waveform with a rise time δt. We then numerically determine the maximum SWAP amplitude between the qubits and plot the resulting value against δt. The result of this simulation is shown in fig. 3.5. As can be seen, the fidelity of the gate decreases in a non-monotonous way as a function of the flux pulse rise time. In order to obtain $F > 0.99$, a flux pulse rise time of $\delta t \leq 1.5\ \mathrm{ns}$ is required.

3.2.4 Relaxation and Dephasing

In this section we discuss the relaxation and dephasing channels of the Transmon qubit which are most relevant to our experiment. We analyze the relaxation and dephasing rates as a function of the Transmon parameters and optimize these parameters to achieve maximum qubit coherence times.

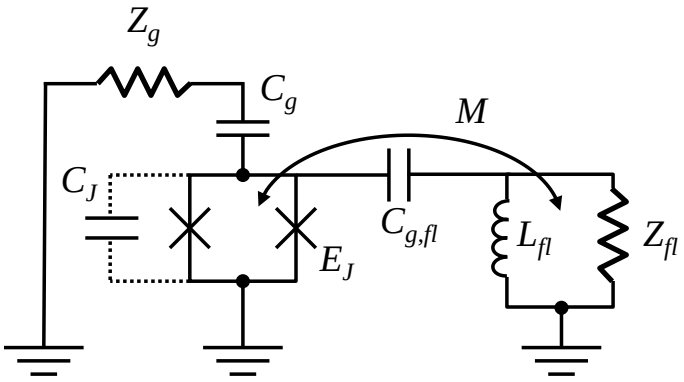

Figure 3.6: Model of the coupling between the qubit (C_J, E_J) and the rest of the circuitry: C_g and Z_g represents the gate line whereas $L_{fl}$and Z_{fl} represents the flux line, both capacitively and inductively coupled to the qubit through C_g, fl and M.

Qubit Relaxation

Relaxation of the qubit can occur either through the charge channel or the flux channel. The qubit has a capacitive coupling to both the flux line and the readout resonator, hence charge relaxation through both of them is possible. On the other hand, the only relevant relaxation channel through the flux channel is through the inductive coupling to the external flux line.

Relaxation through the Gate Charge Channel Since the CPB is coupled to an external impedance (in this case the readout resonator that is coupled to a lossy input transmission line) through a gate capacitance C_g, as shown in fig. 3.6, relaxation into modes of the input impedance seen by the qubit can occur. The relaxation time of similar Transmon qubits used in previous experiments was found to be limited to $T_1^{int} = 1-4\ \mu\mathrm{s}$ independent of the circuit [110, 79]. Consequently, we require the relaxation time associated to charge relaxation through the gate circuit to be significantly longer than this intrinsic relaxation time, i.e. $\Gamma_1^{Purcell} \ll 1\ \mathrm{MHz}$. This requirement influences the choice of the coupling of the qubit to the readout resonator g_{01}, the quality factor and associated loss rate κ of this resonator and the qubit-resonator detuning Δ for the different processor operations. The relaxation rate due to the coupling of the qubit to the input resonator is given by eq. (2.111). For the qubit parameters chosen above, a resonator quality factor $Q = 800$ and a resonator-qubit coupling of $g_{01}/2\pi = 50\ \mathrm{MHz}$ chosen below, the relaxation rate is $\Gamma_1^{Purcell} \approx 0.25\ \mathrm{MHz}$ at $\Delta/2\pi = 2\ \mathrm{GHz}$ (for qubit manipulation)

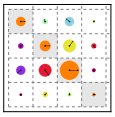

and $\Gamma_1^{Purcell} \approx 1\ \mathrm{MHz}$ at $\Delta/2\pi = 1\ \mathrm{GHz}$ (for qubit readout). This rate is comparable or larger than the typical intrinsic relaxation rate of the qubit and thus compatible with our design goals.

In addition to the capacitive coupling to the input impedance Z_g, the qubit is also coupled to its flux line by $C_{g,fl}$, which can lead to relaxation through the charge channel of the flux line [58]. Assuming that the flux line is terminated by a 50 Ω load and that $C_{g,fl} \leq 10\ \mathrm{fF}$, one calculates a relaxation rate $\Gamma_1^{\mathrm{fl},n_g} \leq 260\ \mathrm{kHz}$ for the qubit parameters discussed above, which is well compatible with our design requirements.

Relaxation through the Flux Channel On the two-qubit chip, each Transmon is equipped with a fast magnetic flux line. These flux lines are coupled to the qubits through a mutual inductance M, as shown in fig. 3.6. The sensitivity of the qubit to relaxation through the flux channel via the mutual inductance M is given by eq. (2.77). For the mutual inductance discussed above, $M \approx 0.23\ \mathrm{pH}$, a characteristic impedance of the flux line of $Z_{fl} = 50\ \Omega$, a qubit frequency $\omega_{01}/2\pi = 7\ \mathrm{GHz}$ and anharmonicity $\alpha = -250\ \mathrm{MHz}$ and an asymmetry $d = 0.35$, we obtain a maximum relaxation rate of $\Gamma_1^{fl} = 0.28\ \mathrm{MHz}$, which is small compared to all other relevant relaxation rates.

Qubit Dephasing

Dephasing of the qubit can occur due to coupling to external charge or flux noise. Here we will calculate the associated rates for both cases for our designed qubit parameters.

Dephasing through the Flux Channel For the qubit parameters discussed in the last paragraph, using eq. (2.85) we obtain a maximum dephasing rate $\Gamma_\phi^{\delta\phi_{ext}} = 0.3\ \mathrm{MHz}$ in the relevant frequency interval $\omega_{01}/2\pi = 4 - 7\ \mathrm{GHz}$. This rate is thus smaller than the relaxation-limited dephasing rate of the qubit at all relevant working frequencies of our processor. Our choice of qubit parameters is thus compatible with the demanded dephasing time.

Dephasing through the Charge Channel We can use eq. (2.84) to calculate the charge-induced dephasing rate of our Transmon qubit. This rate depends exponentially on the ratio E_J/E_C. The highest dephasing rate occurs thus at the smallest qubit frequency that we operate our qubit at, in our case $\omega_{01}/2\pi = 4\ \mathrm{GHz}$. The chosen maximum tolerable dephasing rate of $\left(\Gamma_\phi^{\delta N_g}\right)^{-1} \approx 1\ \mu\mathrm{s}$ at $\omega_{01}/2\pi = 4\ \mathrm{GHz}$ is obtained for a qubit anharmonicity of $\alpha \approx -500\ \mathrm{MHz}$, which is thus the upper bound for the anharmonicity. However, for this work we choose $\alpha = -250\ \mathrm{MHz}$, since it allows already for sufficiently fast driving of the qubit, as discussed in section 3.2.2. For this parameter choice, we obtain a negligible maximum dephasing rate $\left(\Gamma_\phi^{\delta N_g}\right)^{-1} \approx 1\ \mathrm{ms}$ at $\omega_{01}/2\pi = 4\ \mathrm{GHz}$.

As mentioned in section 2.4.5, the coupling of the qubit to the readout resonator can induce dephasing trough the AC-Stark shift of the qubit induced by photon-number fluctuations in the resonator. The resulting relaxation rate is given by eq. (2.118). For the qubit parameters discussed above and a qubit-resonator coupling $g_{01}/2\pi = 50$ MHz, this dephasing rate is $\Gamma_\phi^{\bar{n}} = 0.95 \cdot \bar{n}$ MHz at the minimum chosen qubit-resonator detuning $\Delta = 1$ GHz. When choosing $T_{ph} = 100$ mK as an upper bound for the photon temperature at the 20 mK base stage of the cryostat, the average number of photons in a resonator with $\omega_r/2\pi = 6.7$ GHz is given as $\bar{n} = [\exp(\hbar\omega_r/k_B T) - 1]^{-1} \approx 0.05$, yielding an effective dephasing rate $\Gamma_\phi^{\bar{n}} \approx 38$ kHz, which is small compared to the flux-induced dephasing rate at all working points of the qubit.

3.3 Readout Design

As explained in section 2.4.3 of chapter 2, the readout fidelity is influenced by three sources of errors: Finite overlap between the switching probability distributions for different qubit states, relaxation of the qubit during the measurement phase of the readout and retrapping of the resonator state during the latching phase of the readout. In order to minimize these errors, the following constraints should be met for the readout resonator:

1. The state-dependent dispersive shift of the resonator frequency should be large enough that the switching probability distributions of the resonator corresponding to the qubit states $|0\rangle$ and $|1\rangle$ do not overlap.

2. The measurement phase of the readout should be completed in a time T_{meas} short compared to the relaxation time of the qubit, i.e. $T_{meas} \ll T_1$.

3. There should be no retrapping of the resonator state during the latching period of the readout.

In order to maximize the dispersive shift, we can either increase the coupling g_{01} between the resonator and the qubit or reduce the frequency detuning Δ between them. However, increasing g_{01} or decreasing Δ will also increase the relaxation rate of the qubit through the Purcell effect, thereby reducing the readout fidelity. There is thus an optimum choice for g_{01} and Δ [77]. To counteract the qubit relaxation through the cavity, we can simply increase the quality factor of the resonator. However, usually the maximum relaxation time of the Transmon qubit used in this work is limited to $T_1 \approx 1 - 4\ \mu$s due to intrinsic relaxation processes. Therefore, increasing the quality factor of the resonator does not necessarily increase the readout fidelity because a higher quality factor also increases the time required to excite the readout resonator by the drive pulse and hence the measurement time of the qubit state. Therefore, if the qubit relaxation

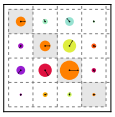

time is intrinsically limited, a longer measurement time at a constant relaxation rate implies a higher probability for the qubit to relax during the measurement, hence actually reducing the readout fidelity. We therefore need to find a compromise for the values of g_{01}, χ and Δ that will maximize the readout fidelity under the given constraints.

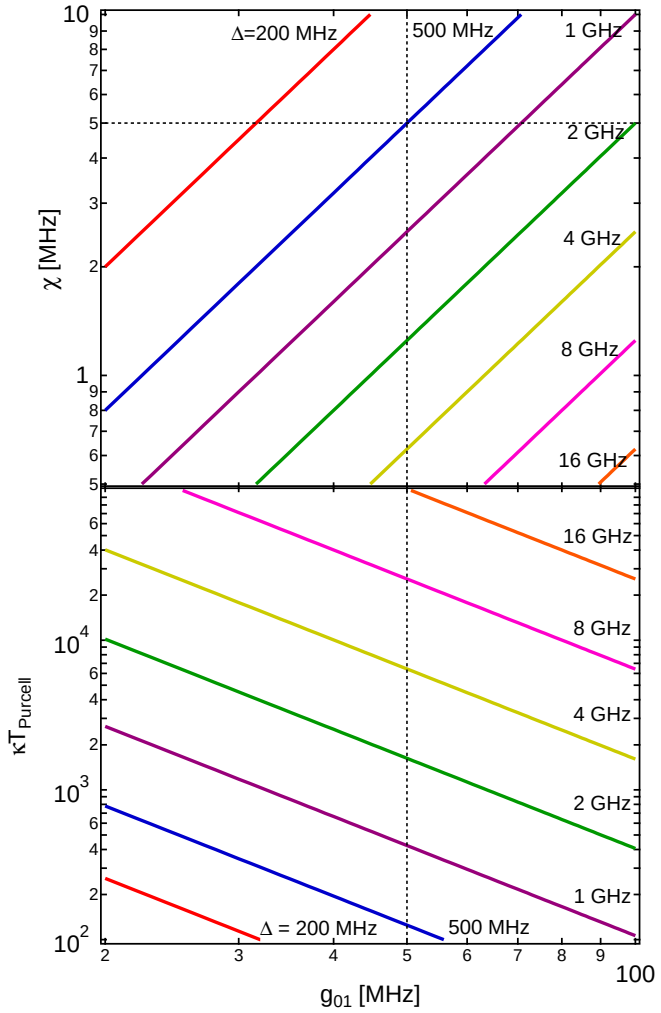

Figure 3.7: Dispersive coupling χ and Purcell relaxation time $T_{Purcell}$ versus qubit-resonator coupling strength g_{01} and detuning $\Delta = \omega_r - \omega_{01}$. The relaxation time is normalized to the resonator decay time $1/\kappa = Q/\omega_r$).

To illustrate the effect of g_{01} and Δ on the relaxation time T_1 and the dispersive shift χ, fig. 3.7 shows both quantities as a function of g_{01}, plotted for several choices of Δ. Now, criterion 1 above demands that the dispersive shift be large enough to completely separate the switching probability distributions for different qubit states. The width of these probability curves can be calculated theoretically, however for this discussion we rely on experimentally measured values and assume that a dispersive shift of $2\chi/2\bar{n} \approx 5\ \mathrm{MHz}$ suffices to fully separate the two distributions. This assumption limits the range of possible values for g_{01} and Δ to the region above the horizontal line in fig. 3.7a. On the other hand, criterion 2 demands that the time required to map the qubit state to the oscillator state should be small compared to the relaxation time of the qubit. For the CJBA parameters relevant to this work, this time is given as $T_{meas} \approx 50 - 100\ \mathrm{ns}$. In

order to have negligible qubit relaxation during the readout, we therefore demand that $T_1 \geq 1\ \mu\mathrm{s}$, which corresponds to a 5 % relaxation probability during the measurement interval. This again limits the choice of possible values of g_{01} and Δ.

Another important design parameter of the CJBA is the Kerr constant K. This constant characterizes the non-linearity of the resonator and determines the power at which the resonator becomes bistable. In particular, the number of photons in the low- and high-amplitude solution of the resonator increases with increasing K. Since the dispersive shift of the qubit frequency caused by the resonator is proportional to the number of these photons, choosing a too high K should be avoided since it can induce large displacements of the qubit frequency, thereby recoupling the two qubits of the processor during the readout operation.

Taking these constraints into account, for the final choice of parameter values we rely on a set of optimized CJBA parameters that have been obtained in an earlier experiment by Mallet *et. al.* [77]. For our processor we choose readout resonator frequencies $\omega_r^1/2\pi = 6.7\ \mathrm{GHz}$ and $\omega_r^2/2\pi = 6.85\ \mathrm{GHz}$, quality factors $Q^{1,2} = 800$, Kerr constants $2\pi K^{1,2}/\omega_r^{1,2} = -2.5 \times 10^{-5}$ and qubit-resonator couplings $g_{01}^{1,2}/2\pi = 50\ \mathrm{MHz}$. In addition, we choose a detuning $\Delta/2\pi = 500\ \mathrm{MHz}$ for reading out the qubits, yielding a relaxation rate $\Gamma_1^{Purcell} \approx 0.5\ \mathrm{MHZ}$ during readout.

3.4 Summary: Qubit and Readout Parameters

Having discussed the relevant properties of all building blocks of our processor and their dependence on the sample parameters, we choose a full set of these parameters, summarized in table 3.1. The left column contains the processor parameters, the right column the related sample parameters.

3.5 Processor Layout & Fabrication

After having chosen a set of sample parameters, it remains to find a physical implementation of the design that we can realize. In this section we discuss therefore the layout design of the qubit processor. From the beginning, we restrict our discussion to lithographically fabricated circuits on a chip, disregarding recent approaches to the realization of superconducting qubits and resonators using 3D microwave cavities [94].

The readout resonator can be realized as a lumped-elements LC resonator or as a transmission line resonator. In the original approach to CQED [119], a coplanar waveguide (CPW) resonator was used. Distributed microwave resonators such as CPW resonators are often advantageous since they can be fabricated with a high intrinsic quality

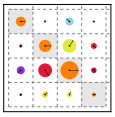

Parameter	Value	Related Parameters
E_J	$h \cdot 28.4$ GHz	$f_{01} = 7$ GHz, $\alpha = -250$ MHz
E_C	$h \cdot 0.92$ GHz	$C_q = 42$ fF, $I_c = 57.4$ nA
d	0.35	
$M_{1,2}$	0.25 pH	
g_{qq}/π	10 MHz	$C_{qq} = 0.45$ fF
$g_{01}/2\pi$	50 MHz	$C_{qr} \approx 62.8$ fF
$\omega_r^1/2\pi$	6.7 GHz	$L_r^1 = 756$ pH, $C_r^1 = 497$ fF
$\omega_r^2/2\pi$	6.85 GHz	$L_r^2 = 739$ pH, $C_r^2 = 486$ pF
$Q_r^{1,2}$	800	$C_{in}^{1,2} \approx 17$ fF
$K_r^{1,2}$	-2.5×10^{-5}	$I_{J,r} \approx 1.0$ μA

Table 3.1: Sample parameters chosen for our two-qubit processor, see fig. 3.1. The left column lists a set of all independent parameters whereas the right columns contains parameters derived from the first set.

factors [83, 32, 121, 5], although recently large progress has been made concerning the quality factors of discrete LC resonators as well [61]. Also, the isolation between the input port of the distributed resonator and the qubit electrode to which the open end of the resonator is coupled is high, whereas for a discrete LC resonator a significant capacitive coupling between the input port of the resonator and the qubit can exist, which is unwanted since it would cause additional relaxation. For this work, we therefore chose a distributed design using a $\lambda/2$ CPW resonator. The open port of the resonator is capacitively coupled to one of the qubit electrodes to achieve the desired coupling factor g_{01}. Figure 3.8 summarizes the layout of the qubit chip.

The flux lines can be realized in several ways. For our processor, we choose a simple 50 Ω CPW transmission line passing nearby the qubit SQUID at a distance of $d \approx 12$ μm. We eliminate the unwanted shielding currents in the ground planes by removing the ground plane between the qubit and the central conductor of the flux line, as shown in figs. 3.10b and 3.9a. By doing this, we also increase the capacitive coupling between the line and the qubit electrodes, thereby increasing the charge relaxation rate through the flux line. However, as discussed in section 3.2.4, this effect is negligible. The flux line can be terminated either directly at the 20 mK stage by wire-bonding it to the ground plane of the chip, or by connecting it to a matched impedance at the 4 K stage of the cryostat. Alternatively, we can also feed back the flux signal to room temperature, which is useful for e.g. measuring the response function of the line.

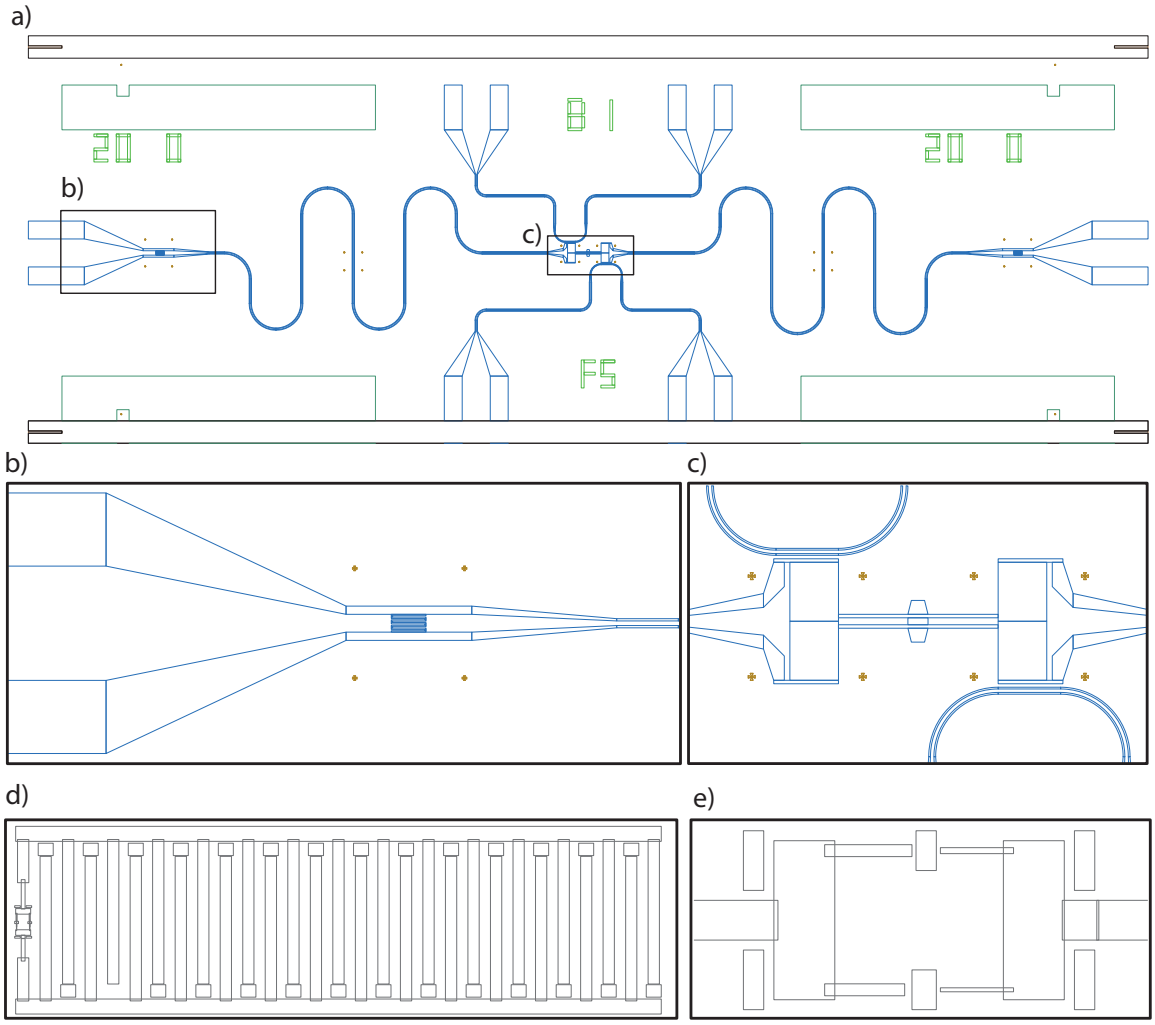

Figure 3.8: CAD layout of the implemented two-qubit processor, showing (a) the two CPW readout resonators and the two qubits with their adjacent fast flux lines, (b) the input capacitor of a resonator, (c) the two Transmon housings in the center of the chip and the active section of the flux lines, (d) a Transmon pattern for e-beam lithography, and (e) a more detailed view of the Transmon's SQUID pattern.

For the Transmon qubit itself, we need to fabricate a large shunt capacitance C_J in order to achieve the desired charging energy. We implement this capacitance as an interdigitated planar capacitor that we pattern together with the qubit junctions using electron-beam lithography. The Josephson junctions of the qubit are realized in a SQUID geometry with a loop area of $A \approx 16\ \mu\mathrm{m}^2$ and are fabricated using double-angle shadow-evaporation of Aluminium.

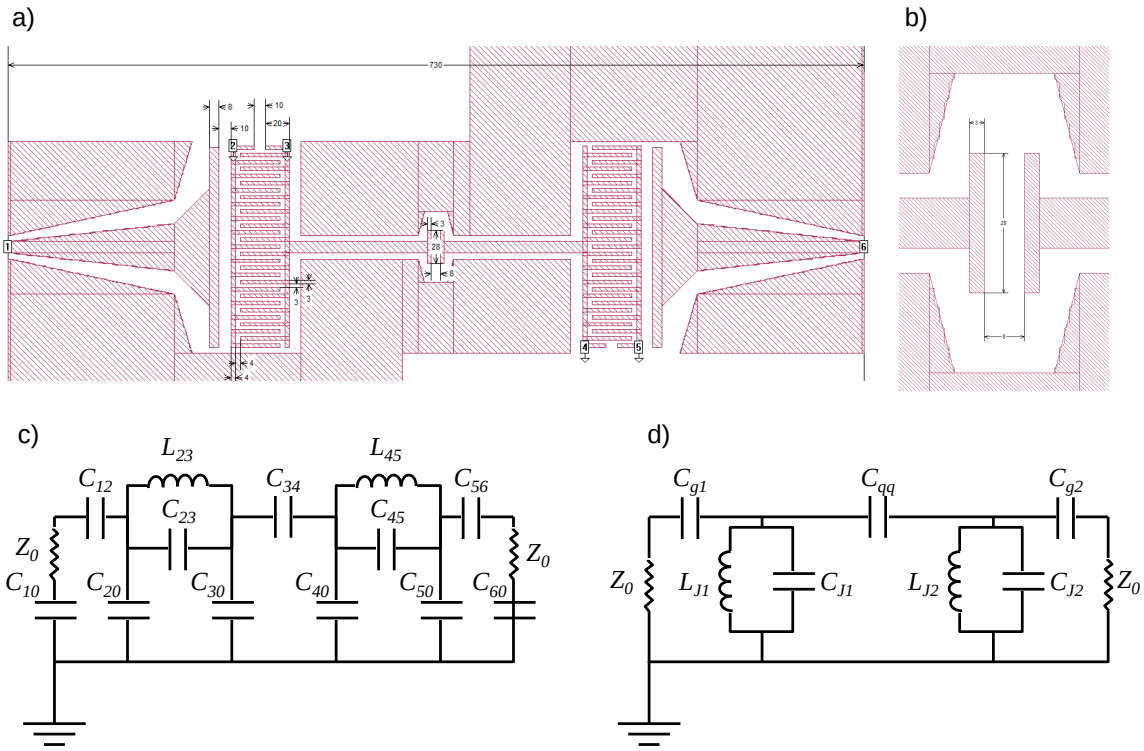

Figure 3.9: a) Schematic of the simulated chip geometry, showing the two coupled Transmon capacitances and the couplings to the readout resonators. b) Detailed view of the qubit coupling capacitance. c) SONNET generated equivalent model of the simulated geometry. d) Equivalent coupled Transmon circuit model. For the geometry shown, the obtained circuit parameters are $C_{g1} = C_{g2} = 13.8$ fF, $C_{qq} = 0.13$ fF, $C_{J1} = C_{J2} = 52.2$ fF, $L_{J1} = L_{J2} = 5.7$ nH.

3.6 Electromagnetic Simulation of the Qubit Chip

We use a commercial software package for electromagnetic simulation (SONNET) to simulate individual parts of the chip an obtain the transmission coefficients between all relevant circuit components and an equivalent lumped-element model of the circuit. Using this equivalent model we calculate all relevant capacitances and inductances. We can then iteratively adapt the geometry of individual elements in order for them to match the designed parameter values. Figure 3.9a/b shows an example of a circuit geometry used in the simulation, fig. 3.9c shows the circuit model generated by this method and fig. 3.9d the mapping of this model to a simplified circuit consisting of two capacitively coupled Transmon qubits.

We can also simulate the Transmon qubits as harmonic oscillators by modeling their Josephson junction as an inductance that matches the Josephson inductance of the junction, as given by eq. (2.17). By simulating the resonance curve of this harmonic resonator and calculating the corresponding quality factor Q, we can estimate the relaxation rate of the qubit through the gate circuit. We can also obtain an estimate of

the coupling strength between the two qubits by simulating them as two coupled, linear resonators. We can obtain the impedance seen by the qubit through the gate circuit by this method as well, thereby being able to calculate the corresponding qubit relaxation rate.

3.7 Fabrication

We fabricate the processor on a high-resistivity silicon substrate with a 50 nm thermal oxide layer. First, we depose 150 nm of Niobium by magnetron sputtering. Afterwards, we spin a photo resist and define an etch mask through optical lithography. Then we dry-etch in a SF_6 plasma, defining the readout resonators, transmission lines and qubit flux lines on the chip. This optical patterning is performed for the wafer as a whole. Afterwards, we spin a bilayer of MAA/PMMA electron beam resist (with typically $1050\ \mathrm{nm}$ of MMA and $115\ \mathrm{nm}$ of PMMA thickness). Then the wafer gets diced and the qubits and JBA junctions are patterned per chip using electron beam lithography, using a double-angle shadow evaporation technique to define the Josephson junctions and capacitances on the chip. The e-beam resist is then lifted off chemically in an Acetone bath. We characterize the chip optically afterwards. In addition, we place "twin" structures of the Transmon qubits and the JBAs on each chip that we can use to measure their normal state resistance at room temperature in order to obtain an estimate of the corresponding resistance of the real structures. Giving the normal-state resistance of a Josephson junction we can calculate the Josephson energy by using the Ambegaokar-Baratoff relation

$$E_J = \frac{\phi_0 \pi \Delta}{2eR_n}, \tag{3.4}$$

where $E_J = \phi_0 I_c$. When measuring R_n at room temperature, a corrective factor of $\approx 17\%$ has to be applied to the resulting value of E_J to account for variations in R_n with temperature.

Following we discuss the detailed procedure followed for fabrication of the two-qubit processor chip.

1. **Niobium Sputtering**: Deposit 150 nm Niobium at an argon pressure of 1.25 mbar and a power of 0.66 W/cm^2 with a 5 minute pre-deposition and $\approx$ 2 min 20 sec deposition time.

2. **Spinning of Photo-Resist**: Spin S1813 + Shipley Primer at 6000 RPM for 60 sec, bake at 115 °C for 1 min 15 sec.

3. **Photo Lithography of Resonators**: Expose the wafer through a contact mask at 5 mW / cm^2 for 30 sec.

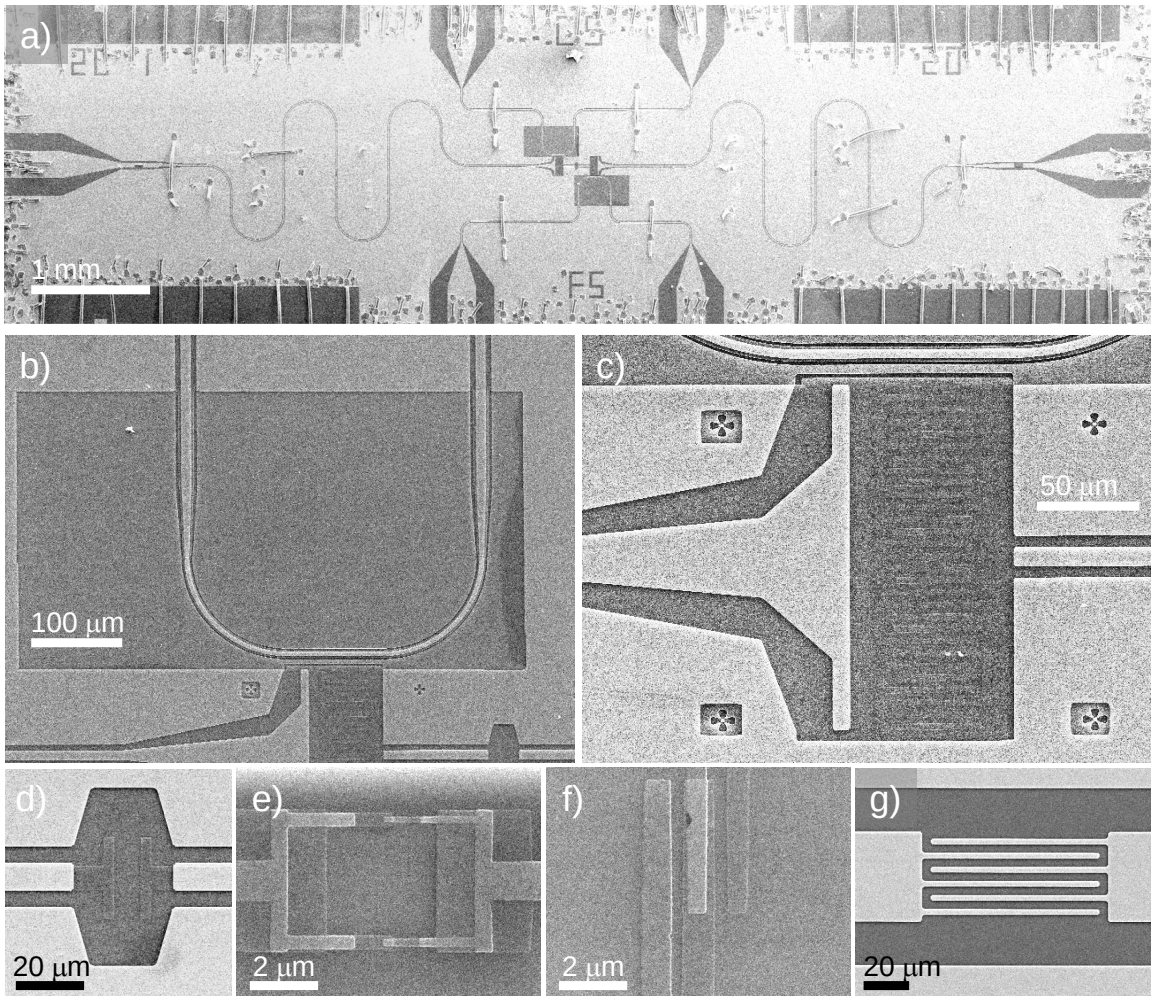

Figure 3.10: Scanning electron micrographs of the fabricated two-qubit processor chip. a) Stitched together micrograph of the whole chip, showing the two readout resonators coupled to their transmission lines, the two capacitively coupled Transmons, and the fast magnetic flux lines attached to each qubit. b-g) detailed views showing various parts of the chip: note that the aluminum electrodes are barely visible compared to the niobium ones that benefit from a much higher contrast. b) Flux line close to one of the qubits. The ground plane between the line and the qubit has been removed to suppress spurious shielding currents when sending fast flux pulses. c) Transmon qubit in its resonator housing. The left electrode is the center line of the resonator whereas the right one belongs to the coupling capacitor d) The two-qubit coupling capacitance. e) qubit SQUID loop with its two Josephson junctions. f) The CJBA Josephson junction. g) The readout resonator input capacitance.

4. **Development**: Develop in pure MF 319 for 50 s.

5. **Reactive Ion Etching**: Pump the RIE chamber to $P \leq 4 \times 10^{-5}$ mbar. Etch using 20 cc of SF_6, 10 cc Ar and 2 cc O_2 at a pressure of $\approx$ 0.013 mbar at a power of 50 W and a voltage of 150 V. The total etch time should be $\approx$ 60 sec + 10 sec for the finish. Remove the resists in warm acetone (40 ℃) for at least 10 min, possibly clean further in an ultrasonic bath.

6. **Niobium Surface Regeneration**: Pump the RIE chamber to $P \leq 4 \times 10^{-5}$ mbar, etch using 20 cc of SF_6, 10 cc Ar at $\approx$ 0.0133 mbar, 50 W and 150 V for 8 sec.

7. **Electron Resist Spinning**: Spin twice an MAA EL 10 layer at 2000 RPM for 60 sec, 6000 RPM for 2 sec. Bake after each step at 170 ℃ for 60 sec. Spin PMMA 950k A3 at 4000 RPM for 60 sec, 6000 RPM for 2 sec. Bake at 170 ℃ for 20 min. This should yield $\approx$ 1050 nm of MAA and 110 nm of PMMA (verify using interferometer).

8. **Dicing**: Dice the wafer using either a diamond cutter or wafer saw.

9. **Electron Beam Lithography of Transmons and CJBA junctions**: Clean the chip in iso-propanol (possibly in ultrasound) for less than 2 minutes. Perform electron beam lithography at a dose of $\approx$ 250-320 $\mu C/cm^2$. Develop the chip in a 1:3 acetone/iso-propanol solution for 50 sec.

10. **Aluminum Deposition**: Put the sample in the evaporation chamber and pump to $P < 10^{-6}$ mbar. Ion mill the sample at the two evaporation angles (typically $\pm 22\,\mathrm{deg}$) with 500 eV neutralized argon ions at the dose of $2 \cdot 10^{15}$/cm^2. Deposit first aluminum layer at a rate of 1 nm/sec. Oxidize at an adequate oxygen pressure (typically 15 - 25 mbar) for 10 min. Deposit the second aluminum layer at 1 nm/sec.

11. **Lift-Off**: Put the chip in a heated Acetone bath at 65 ℃ for at least 5 min. Rinse in Iso-Propanol. Thermally stabilize the chip at 100 ℃ for 1 min.

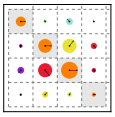

Chapter 4

Measurement Setup & Techniques

In this chapter we discuss the measurement setup and techniques used in our experiments. Our setup consists of the qubit chip presented in chapter 3, held at the 20 mK stage of a He_3/He_4 dilution refrigerator and connected to a signal generation and measurement chain including cryogenic microwave components and room temperature electronics. We describe how the processor chip is mounted, as well as the individual parts of the signal and measurement chain, putting emphasis on microwave pulse generation. Afterwards we discuss the calibration and compensation techniques that we use to correct signal imperfections when generating qubit drive and flux signals. Finally we introduce the different measurement protocols used for driving and reading the qubit, as well as for determining all relevant qubit parameters such as frequency, anharmonicity, and relaxation and dephasing times.

4.1 Chip Mounting

Chip mounting is illustrated in fig. 4.1. The chip is first attached to the lower part of the sample holder using wax (melting temperature 80 ℃). It is placed in a groove whose depth matches the height of the silicon chip, such that the top part of it is at the level of the surface of the sample holder after mounting. We use six small microwave PCBs, each equipped with a $50\ \Omega$ coplanar waveguide and a right-angle mini-SMP connector, which are also placed in matched grooves on the sample holder, as shown in fig. 4.1c. The PCBs are made of TMM10 with a dielectric constant of 10 close to that of the silicon chip. They are metalized on both sides with gold-coated copper and have vias to connect the metal layers on both sides. The three electrodes of each CPW line on the chip are wire-bonded to their counterparts on the PCBs using aluminum wires of 50 µm diameter. In addition, on-chip bond wires are used to reconnect separated parts of the ground plane that are initially isolated from each other because of the circuit topology, as shown in fig. 4.1d. This is important in order to avoid spurious on-chip resonances in

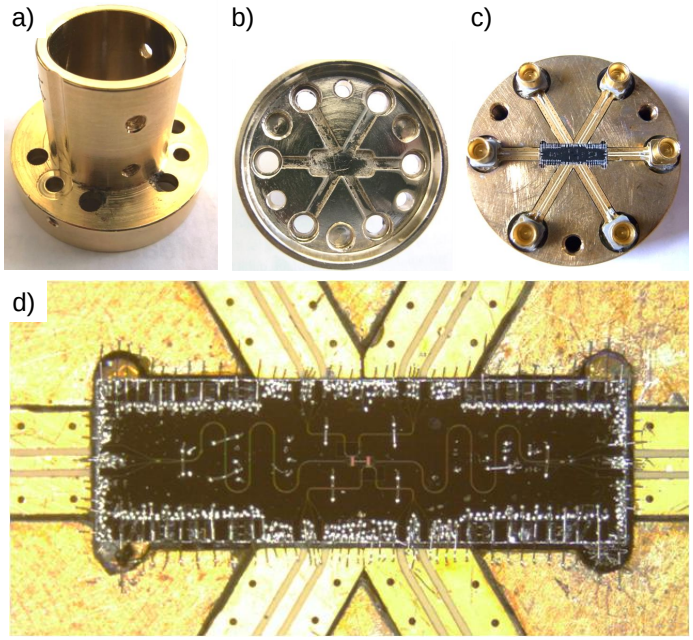

Figure 4.1: Chip mounting. Complete sample-holder (a), cover part as seen form below (b), and bottom part (c) with the mounted PCB carrying the qubit chip and the mini-SMP connectors. (d) chip wire-bonded to the PCB. Wire bonds to four CPW lines can be seen on the top and bottom of the picture, as well as on-chip bond wires reconnecting separated grounds inside the chip. The whole sample holder is screwed to the 20 mK stage of the dilution refrigerator.

the relevant frequency window, i.e. below 10 GHz [104].

The lower part of the sample holder with the chip and the small PCBs is then mounted to the gold-coated top part as shown in fig. 4.1a/b, which thermally anchors the chip to the mixing chamber of the refrigerator, shields it from electromagnetic noise and encloses it in a conducting cavity that is small enough to suppress box resonances in the relevant frequency window. Grooves in the top part of the sample holder, shown in fig. 4.1b, provide the necessary open space above the qubit chip and the six coplanar waveguides.

The whole sample-holder is mounted in the refrigerator by screwing it around a small coil that sits inside the cover and produces a DC magnetic field perpendicular to the chip. The distance between the chip and the lower end of the coil is less then 3 mm.

4.2 Signal Generation & Acquisition

Figure 4.2 shows the wiring of our experiment from room temperature down to the 20 mK stage. Except for the small coil that is shared by both qubits, the rest of the circuitry is duplicated for each of them and only one exemplary is shown on the figure. One can see the bifilar dc flux line and a fast coaxial 50 Ω flux line on the left, as well as a set of 50 Ω coaxial microwave drive and readout lines on the right. Lossy cables or wires made from special alloys such as CuNi, CuBe, stainless steel (SS) and manganin are used at intermediate temperatures, as needed for minimizing the heat transfer between the different stages. Between 20 mK and 4 K, superconducting NbTi cables are used for the measurement lines because they have both a low thermal conductivity and a

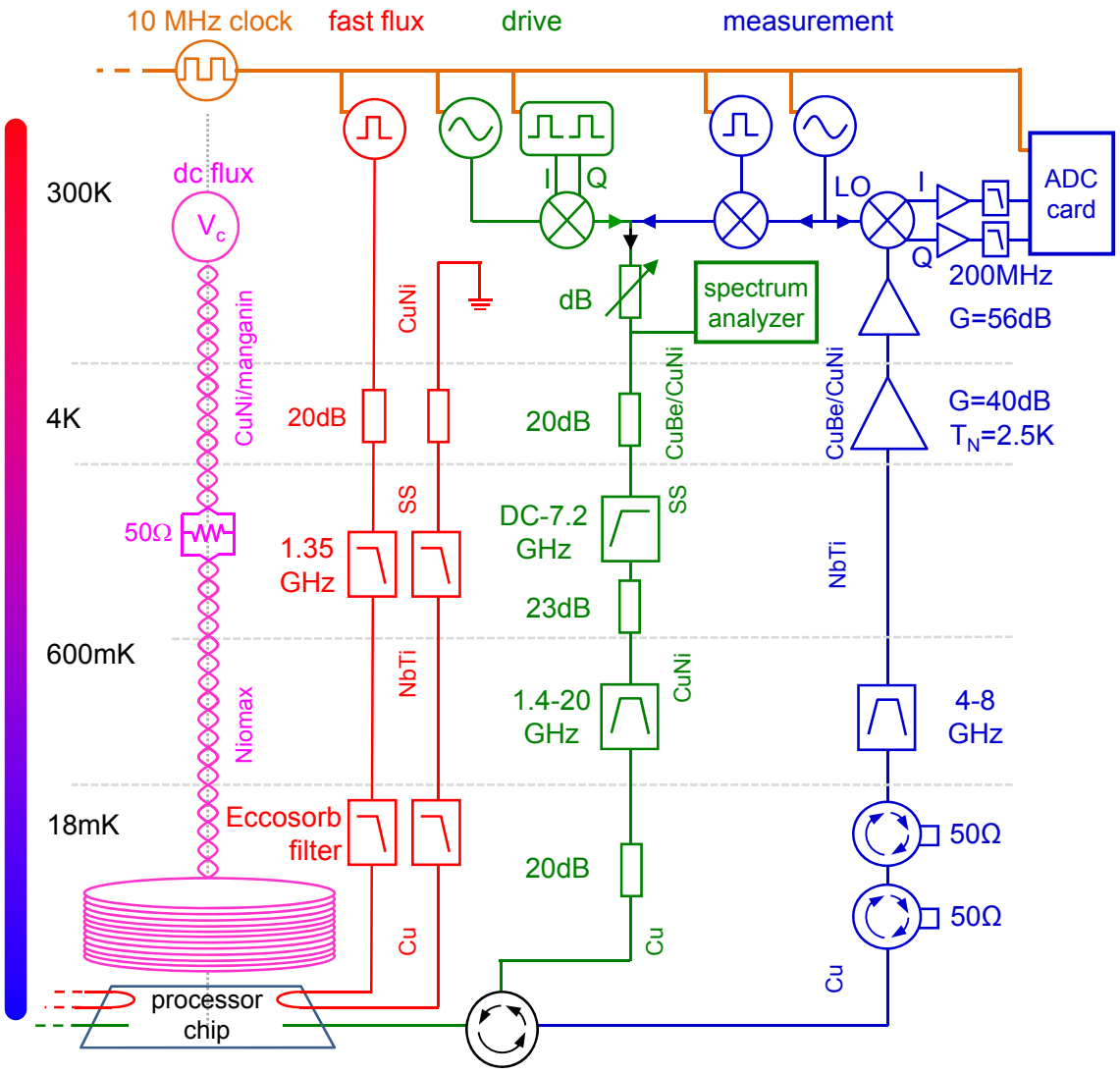

Figure 4.2: Measurement setup used for the two-qubit experiments. The very same drive and readout setup is used for both qubits, so that only one exemplary is shown. The role of each line is indicated on top, and the relevant parameters indicated beside each component, including the wire and cable materials. Elements shown are attenuators, low pass or bandpass filters, circulators and isolators, microwave amplifiers, IQ mixers, microwave and arbitrary waveform generators,and an acquisition board and a spectrum analyzer.

low microwave attenuation. Semi-flexible Copper microwave coaxial cables are used at 20 mK.

4.2.1 Driving and Measurement of the Qubits

Each of the qubits together with its corresponding readout resonator is fitted with an individual fast flux , drive, and measurement circuit. The microwave and arbitrary waveform generators used to control the experiment, as well as the acquisition systems,

are all phase-locked using 10MHz external clocking. At room temperature we generate qubit and readout resonator drive waveforms using phase-locked single-tone microwave sources whose continuous output is mixed with control pulses generated by two arbitrary waveform generators (more details in the next section). The qubit drive and readout drive signals are then combined on a single line and sent to the chip through a series of cryogenic attenuators and filters. A cryogenic circulator at 20 mK routes the incoming pulses to the qubit chip, where they are sent to the qubit readout resonator and finally reflected by it. The reflected signal passes again through the circulator and gets routed through a double isolator and a band-pass filter to a cryogenic high electron mobility amplifier (HEMT) with a gain of 40 dB. The amplified signal gets then transmitted to the room temperature electronics, where it is filtered and amplified further by more then 50 dB. Finally, the signal is demodulated using a two-quadrature mixer and a continuous microwave reference tone (local oscillator), the two resulting quadrature being further amplified, filtered below 200MHz and fed to two channels of a 4-channel ADC board. Flux pulses are generated using an arbitrary waveform generator at room temperature. The signal is then sent to the qubit chip through a 20 dB attenuator, through a Microtronics low-pass filter of the reflective type with a 1.35 GHz frequency cutoff, and through a custom-made high-frequency powder filter that uses an absorptive material (Eccosorb) to attenuate high-frequency noise. After passing through the transmission line on the qubit chip, the outgoing flux signal is routed to room temperature electronics using a transmission line identical to the input line. There, the signal can be measured, which is useful for characterizing possible signal imperfections caused by the non-ideal character of the line.

4.2.2 X-Y Pulse Generation by Microwave Single Sideband Mixing

As briefly mentioned above, a single-sideband mixing technique is used to generate the qubit X and Y driving pulses. More precisely, each qubit has its own IQ mixer driven with a continuous single-frequency microwave tone and two synchronized intermediate frequency control signals generated by an arbitrary waveform generator (Tektronix AWG5014b). In general, when feeding a signal $LO(t) = I_0 \cos(\omega_{LO} t)$ to the LO port of an IQ mixer and two signals $I(t)$, $Q(t)$ to its I and Q ports, one obtains a signal

$$RF(t) = I(t) \cos(\omega_{LO} t) + Q(t) \sin(\omega_{LO} t) \tag{4.1}$$

at the RF output port. (Since the IQ mixer that we use is a passive reciprocal device, one can as well feed two input signals to the LO and RF ports and obtain the demodulated signal quadratures at the I and Q ports after filtering, a technique that we make use of in our qubit readout scheme). Typically we use heterodyne single sideband mixing to

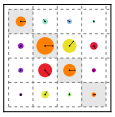

generate driving pulses that are tunable in frequency with respect to the local oscillator (carrier frequency), over the mixer bandwidth (several hundreds of MHz): Ideally, the I and Q signals should have the form $I(t) = s(t)\cos(\omega_{IF}t - \phi)$ and $Q(t) = s(t)\sin(\omega_{IF}t - \phi)$ in order to obtain an output pulse $RF(t) = s(t)\cos[(\omega_{LO} - \omega_{IF})t + \phi]$ that will induce a rotation of the qubit around axis X_ϕ laying in the equatorial plane of the Bloch sphere and making an angle ϕ with the X axis. The phase reference of the driving pulses is thus defined by both the carrier phase and the common starting time of the I and Q waveforms with respect to the carrier. Both quantities have to be kept constant over subsequent sequences. In addition, when performing experiments on multiple qubits, the phase differences between the reference phases of each qubit must also be conserved. We explain below in the section devoted to synchronization how these phase references are maintained. In the expression above $s(t)$ is the envelope of the pulse, the area of which defines the angle of rotation. For small rotation angle, we choose for s a Gaussian shape of the form

$$s(t) = s_0 \cdot \exp\left[-\frac{(t-t_0)^2}{2\sigma_t^2}\right] \tag{4.2}$$

with "rise time" $\sigma_t = 3$ ns and a cutoff at $-3\sigma_t \leq t - t_0 \leq 3\sigma_t$. The advantage of using such a Gaussian pulse [7] is that its Fourier transform is again a Gaussian, which, in contrast to a rectangular pulse, does not exhibit side lobes in the frequency domain and thus minimizes the leakage to higher Transmon levels discussed in section 3.2.2. To increase the Rabi angle of such a pulse, we just change its amplitude as far as it does not saturate the IQ mixer. For larger Rabi angles we simply add a flat plateau between the Gaussian rise and fall.

Commercially available IQ mixers are not perfect, and deviate from the ideal behavior given by eq. (4.1). Typical imperfections include large insertion losses –i.e. loss of power between the different ports of the mixer–, RF signal leakage at zero IQ-input, and frequency-dependent phase and amplitude errors of the mixed sideband signals. In order to achieve reliable single-qubit operations we need to correct these errors, as shown in Fig. 4.3. The signal leakage consists in a small part of the LO signal leaking through to the RF port even when the IQ inputs are zeroed. This leakage can be compensated by adding to the IQ ports DC offset voltages that depend on ω_{LO}. The appropriate offsets can be determined by applying a continuous signal at a frequency ω_{LO} to the LO port and minimizing the measured signal power at the RF port. Using this method, the leakage power can be reduced down to -80 dBm.

To correct the sideband amplitude and phase errors we apply another correction procedure. We first introduce the notation

$$A(t) = I(t) + iQ(t) = a(t)\exp\left[-i\phi(t)\right] \tag{4.3}$$

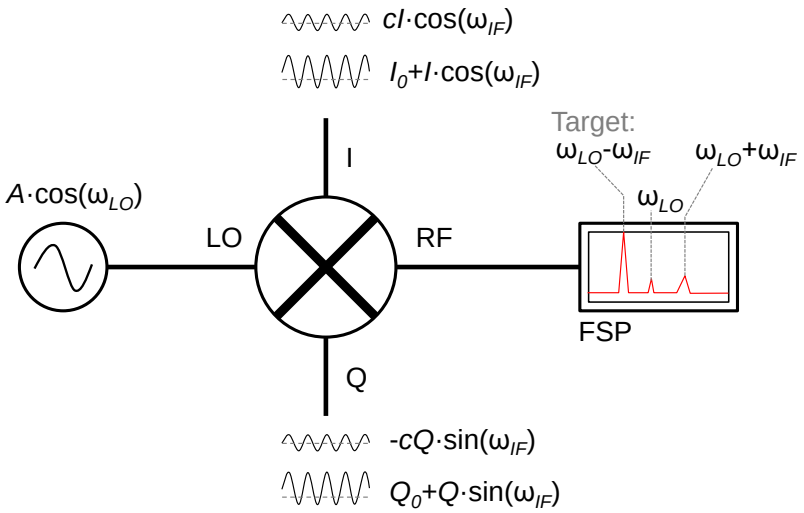

Figure 4.3: Illustration of the method used to measure and correct the imperfect behavior of the IQ mixers used for our heterodyne single-sideband generation of the qubit drives: the leakage of the LO signal to the RF port is measured continuously with a spectrum analyzer and is minimized by tuning the two offset voltages I_0 and Q_0 at the I and Q ports. To correct phase and amplitude errors during heterodyne mixing, we then add two sideband signals to the IF ports and minimize iteratively the measured RF power at $\omega_{LO} + \omega_{IF}$ by tuning the amplitude and phase of two correction waveforms added to the I and Q ports.

for any composite I and Q signal. We then consider such a signal at a single sideband frequency ω_{IF} and at a fixed complex amplitude $a(t) = a = a_0 \exp(i\phi_0)$ such that $A(t) = a \exp[-i\omega_{IF}t]$. The effect of the gain and phase imperfections are responsible for a spurious additional output signal at the mirrored sideband frequency $-\omega_{IF}$ with respect to the carrier. This unwanted signal would be obtained in a perfect mixer with an IQ signal $\varepsilon(\omega_{IF}, \omega_{LO})A^*(t)$. We can thus remove it by adding a small correction $c(\omega_{IF}, \omega_{LO})A^*(t)$ to our IQ input signal. The complex-valued correction coefficient $c(\omega_{IF}, \omega_{LO}) = |c| \exp(i \arg[c])$ usually depends both on the LO frequency ω_{LO} and the sideband frequency ω_{IF}. We thus determine it by generating a continuous single sideband at frequency $\omega_{LO} - \omega_{IF}$ and by finding iteratively the $c(\omega_{IF}, \omega_{LO})$ that minimizes the amplitude of the unwanted sideband at $\omega_{LO} + \omega_{IF}$, measured with a spectrum analyzer (see Figs. 4.2 and 4.3). Both the offset and the sideband-amplitude and -phase corrections have been automated using our data acquisition software. By using this optimization techniques we can lower the amplitudes of the ω_{LO} and $\omega_{LO} + \omega_{IF}$ peaks down to 80 dB and 70 dB below the targeted sideband at $\omega_{LO} - \omega_{IF}$, respectively.

Finally, it is important to tolerate the maximum and minimum absolute ratings for the signals applied to the I/Q as well as LO and RF ports of the mixer in order to avoid saturation and nonlinear response. For the mixer that we use in our setup (Hitite HMC 525), the maximum input powers are given as 20 dBm for the RF and I/Q ports and 27 dBm for the LO port. In addition, the maximum tolerable DC current of the mixer at the

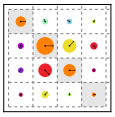

I/Q ports is limited to 3 mA, which restricts the DC offset voltage that we can supply to the mixer.

4.2.3 Fast Magnetic Flux Pulse Generation and Calibration

The fully symmetric coaxial line used for sending fast magnetic flux pulses to one of the qubits has been described above and is shown on Fig. 4.2. The low-pass filtering of the line is optimized to reduce high-frequency noise as much as possible while letting the line pass pulses with 2-3 ns rise time. Consequently, the pulse distortion by the line is not negligible. Another important imperfection in our pulse generation is the finite bandwidth of the arbitrary waveform generator we use (Tektronix AWG5014B). It is about 500 MHz and some ringing is observed at a few percent level for square pulses with rise times below 10 ns. For compensating all these imperfections, we measure the frequency response of each part of the whole circuit with our 1 GHz bandwidth acquisition system. A step function with 2 ns rise time and 1ns/sample is programmed on the AWG and measured at the output of the flux line. This allows us to obtain the response function of the generator (DAC) and of the input line. We then model the whole chain as shown on Fig. 4.4a, using the same response function for the identical input and output lines. The Fourier transform of the measured signal at the end of the output line is given as

$$\chi_{\mathrm{fl}}(\omega) = \chi_{signal} \cdot \chi_{DAC} \cdot \chi_{\mathrm{input}} \cdot \chi_{\mathrm{output}} \cdot \chi_{ADC}, \tag{4.4}$$

with χ_{signal} the Fourier transform of the ideal input signal, χ_{ADC} and χ_{DAC} the response functions of the DAC and ADC (which we measure independently), and $\chi_{\mathrm{input}} = \chi_{\mathrm{output}}$ the response function of the input and output transmission lines. By measuring χ_{fl}, subtracting the ADC and DAC responses from it, we obtain the input line response function χ_{input}. To correct the signal distortion seen by the qubit, we can then simply re-program the AWG with a corrected wave function with Fourier transform

$$\chi^{\mathrm{corr}}_{\mathrm{signal}} = \chi_{\mathrm{signal}} \cdot (\chi_{DAC} \cdot \chi_{\mathrm{input}})^{-1} \cdot \mathrm{G}(\omega, \omega_{co}). \tag{4.5}$$

Here, $G(\omega, \omega_{co})$ is a Gaussian filter function with a cutoff frequency ω_{co} that we apply to the inverse measured response function to eliminate the distortion at high frequencies caused by the fact that we are not able to accurately measure the response function of the flux line above the bandwidth of our digitizing board. Usually, we set this cutoff frequency to $\omega_{co}/2\pi = 400\ \mathrm{MHz}$, which allows us to correct most signal distortion in the frequency window relevant to this work, i.e. up to half a GHz. Figure 4.4b shows the measured response functions of the flux line and fig. 4.4c shows an exemplary measurement, where we first program an ideal waveform (in red) in the AWG, send it through the flux line, calculate the shape of the waveform at the sample (in magenta) by

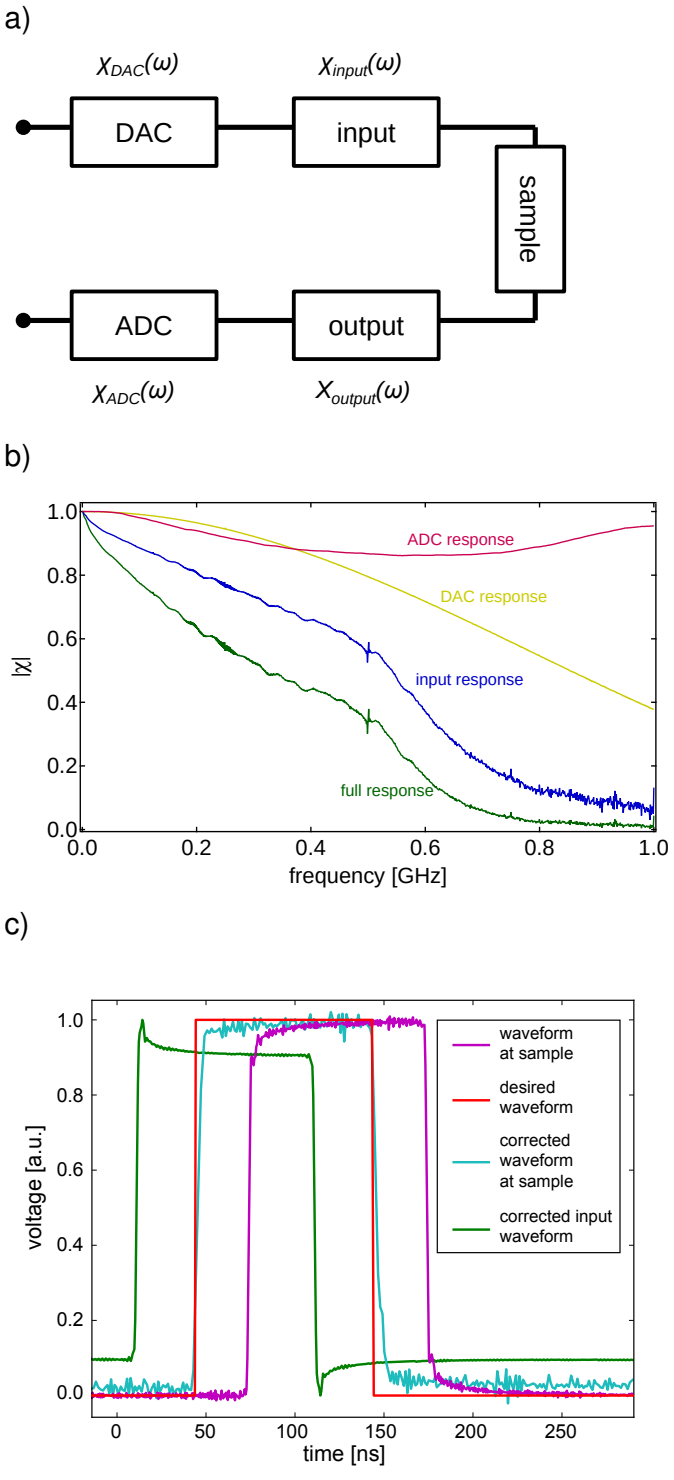

Figure 4.4: a) Schematic of the flux line chain used in our setup. The flux signal is generated by a DAC, fed through the input line to the sample, returned to room temperature through the output line and digitized by an ADC. b) Measured response functions of different parts of the flux line, showing the response of the DAC and ADC circuits and of the input part and the full flux line. c) Illustration of the signal correction method. We generate a desired waveform (in red) without applying any correction, measure the arriving signal at the sample (in magenta), calculate the response function of the line and generate a corrected signal (in green), which we measure again at the sample (in blue). The corrected signal corresponds to a good degree to the desired input signal.

measuring the waveform at the output of the line and subtracting the measured response functions of the ADC and the output line, then program a corrected waveform (in green) and finally measure the shape of this waveform at the sample again (in blue), which now corresponds closely to the ideal waveform.

After having corrected the response of the flux line by this technique, we can further

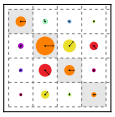

reduce signal distortion by directly probing the flux seen by the qubit at a given time. For this, we apply a small test flux signal $\phi_{ext}^{fl}(t)$ to the qubit, measure its frequency $\omega_{01}(t)$ and reconstruct the flux from the previously measured $\omega_{01}(\phi_{ext})$ curve. If the qubit frequency is chosen well away from its maximum and minimum frequencies, i.e. where $\gamma = \partial\omega_{01}/\partial\phi_{ext}^{fl} \neq 0$, and if the flux signal is comparably small, the time-dependent qubit frequency is $\omega_{01}(t) = \omega_{01}^{0} + \gamma.\delta\phi_{ext}^{fl}(t)$. The frequency displacement of the qubit is thus proportional to the applied flux signal. Now, if we drive the qubit with a calibrated X_π Rabi pulse at a given drive frequency ω_d at time t_0, the probability of finding it in state $|1\rangle$ afterwards is maximum if $\omega_d = \omega_{01}(t_0)$. Thus, by maximizing this probability as a function of ω_d, we can reconstruct the flux $\phi_{ext}^{fl}(t_0)$ seen by the qubit at any given moment. Of course, the time resolution achieved with this method is limited to the pulse duration of the X_π pulse, which is typical $3 - 5$ ns. After having reconstructed the flux signal $\phi_{ext}^{fl}(t)$ seen by the qubit, we can again calculate its Fourier transform and correct imperfections by further changing the input signal.

4.2.4 Microwave and DC Pulse Synchronization

In our experiment, each qubit possesses two microwave sources that generate the continuous tones for drive and readout. The two fast pulse signals mixed with the two driving tones of the two qubits are generated by a single 4-channel arbitrary waveform generator (Tektronix AWG5014B). A second AWG generates the flux pulses for the two qubits. The measurement of the reflected and demodulated readout signal of both qubits is done by a single ADC card. All these different signal generators and measurement devices need to be synchronized in order to keep the relative phases and time differences between them constant over successive individual runs of our experiment. For this, we use a 10 MHz frequency reference chain, whose master clock is generated by the AWG generating the qubit drive pulses. The reference signal is then passed on to all microwave sources and signal generators as well as oscilloscopes, spectrum analyzers and ADC cards in our setup. In addition, to avoid random phase-jitter between the signals of the two microwave sources that generate the drive pulses of the two qubits, their drive frequencies are chosen such that they correspond to a multiple of the repetition frequency of the master AWG, which is typically 50 kHz. When this condition is met, the relative phases between the two microwave signals is conserved between individual runs of an experiment, which is crucial when performing measurements sensitive to this phase such as quantum state tomography two entangled qubits. In addition, a 1 GHz phase synchronization chain is used to phase-lock the two microwave generators and reduce the phase drift between them.

4.3 Measurement Techniques

In this section, we discuss the techniques used to manipulate and characterize our two-qubit processor. We address qubit readout and describe how the relevant qubit parameters are determined.

4.3.1 Qubit Readout

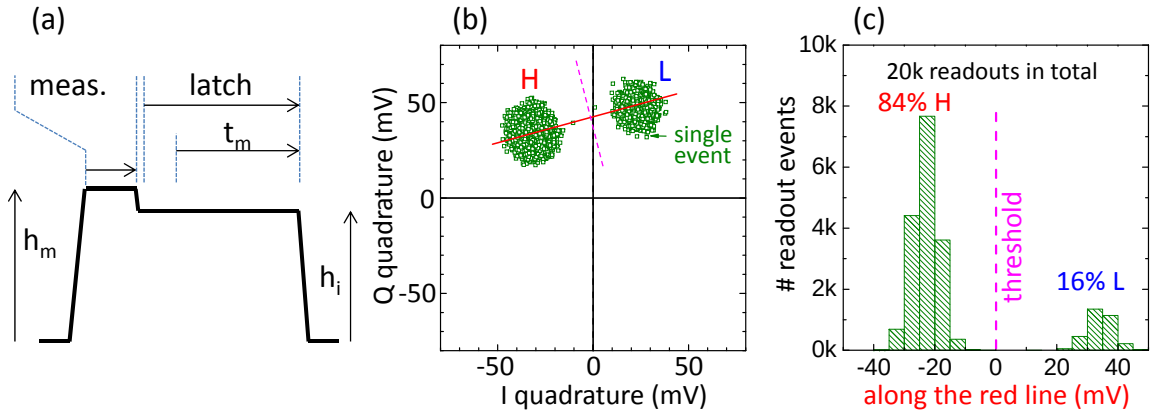

Figure 4.5: a) Microwave pulse envelope used for exciting the CJBA at readout.The pulse consists of a measurement part with amplitude h_m and a latching part with amplitude $h_l = 0.8 - 0.9h_m$. To determine the state of the resonator during the latching interval, the quadratures I and Q of the reflected signal are averaged over the time window t_m. b) Bimodal distribution of the time-averaged (I, Q) values obtained for a readout power close to the bifurcation threshold . The red dotted line perpendicular to the principal axis joining the two modes of the distribution and going through the mean quadratures (I_0, Q_0) provides an optimal separation between the two clusters corresponding to the L and H states. c) Histograms of the signal projected on the principal axis (red line), revealing a switching probability of 84% for the example shown.

The general principle of the CJBA readout used in this work is described in section 2.4.3. Here we explain how we choose its frequency f_d and drive amplitude a_d. To bring up the readout, we first determine by reflectometry the resonance frequency f_r of the CJBA in its linear regime, with the qubit in state $|0\rangle$ and largely detuned from the resonator. We then choose a relative drive detuning $\Omega = 2Q(f_d/f_r - 1) > \sqrt{3}$ (between 2 and 10 in practice, i.e. between 12 and 60 MHz) at which the bistable regime is accessible. The continuous drive tone at f_d is then split on two lines, one of them being mixed with the dc envelope coming from the AWG and sketched on fig. 4.5a. We then attenuate the resulting drive signal using a tunable attenuator at room temperature and send it to the CJBA. The reflected and amplified signal is then demodulated with the continuous drive present on the second line after the splitter, using an IQ demodulator. The resulting I/Q quadratures are further amplified, low-pass filtered at 200 MHz, and get digitized by

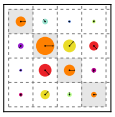

the ADC card at a sampling rate of 1 GSample/s during the time window $t_m = 1 - 2\mu$s sketched in fig. 4.5a. The digitized I/Q signals are then averaged over the whole measurement window to obtain a single measurement point in the IQ plane. This sequence is repeated a large number of times (typically 10^4) to obtain a statistical distribution of IQ points. We then repeat this procedure for various values of the input attenuation, each time calculating the estimated variance $\hat{\sigma}^2_{IQ} = \sum_i((I_i - \bar{I}_i)^2 + \sum_i (Q_i - \bar{Q}_i)^2)/n$ of the distribution. When starting with a high attenuation and reducing it, the input power sent to the CJBA will at some point be sufficient to make it switch from the L to the H state, thereby changing the phase and consequently the I and Q average values of the distribution. Since the switching is a stochastic process, we will observe two distinct sets of points close to the transition power. At an input power where approximately 50 % of switching occurs, the variance σ^2_{IQ} of the obtained IQ data points will be largest, as shown in fig. 4.5b. At this point, we subtract the averages $(I_0 = \sum_i I_i/n, Q_0 = \sum_i Q_i/n)$ from the data and perform a principal axis transformation, which diagonalizes their covariance matrix

$$\mathrm{var}_{IQ} = \begin{pmatrix} \mathrm{var}(I) & \mathrm{cov}(I,Q) \\ \mathrm{cov}(I,Q) & \mathrm{var}(Q) \end{pmatrix}. \tag{4.6}$$

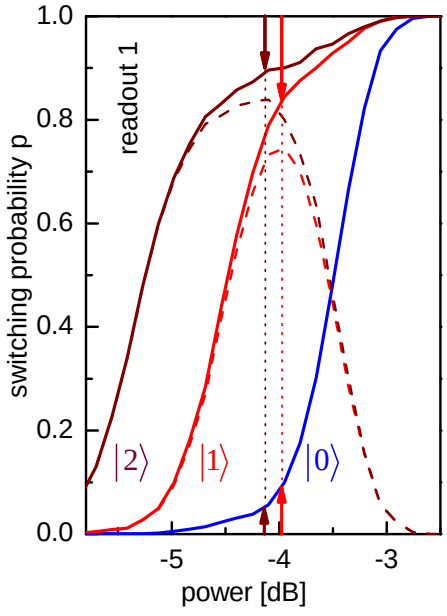

Figure 4.6: Exemplary S-curve measured for one of the qubit-readout. Shown is the switching probability p of the CJBA as a function of the readout signal power, plotted for the different qubit states $|0\rangle$,$|1\rangle$ and $|2\rangle$. The readout contrast between different states is given as difference between the associated switching probability curves. Light and dark red arrows indicate the optimal working points where the c_{01} and c_{02} readout contrasts are maximum, respectively.

Using this transformation, we project the measured (I,Q) points on the axis $\perp P$ joining the two sub-distribution, as shown in fig. 4.5, and obtain a bivalued one-dimensional probability distribution. Then, the obtained offsets I_0, Q_0 and principal axis rotation angle α_{IQ} gives us the discrimination criterion $Q_L < Q_0 + \tan\alpha_{IQ}(I - I_0)$ used to classify new data points as belonging to the L or H state at the chosen working point. Normally, if the measurement window t_m is large enough and no retrapping occurs during the mea-

surement, the distributions corresponding to the L and H states do not overlap, yielding perfect discrimination between them, as shown on the figure.

After having determined the I_0, Q_0 and α_{IQ}, we slightly tune the attenuation to obtain $\approx 20\%$ of switching. At this working point, the readout contrast of the CJBA is usually already sufficient to perform a simple qubit spectroscopy, as described in section 4.3.2 and calibrate a X_π Rabi pulse, as described in section 4.3.3. After having done this, we calibrate and optimize each qubit readout by measuring the switching probability as a function of the input power while either leaving the qubit in state $|0\rangle$ or exciting it to the state $|1\rangle$. Fig. 4.6 shows an example of such a measurement. Here, the difference c_{01} between the two curves corresponding to the $|1\rangle$ and $|0\rangle$ states defines the input-power dependent readout contrast. The optimal input power chosen for reading the qubit out is where the contrast is maximum. If desired, we use instead a $X_\pi^{12} \cdot X_\pi^{10}$ pulse sequence to bring the qubit into state $|2\rangle$ before readout. In this state, the dispersive shift of the resonator frequency is larger then in the state $|1\rangle$, therefore resulting in a larger readout contrast $\max(c_{02}) > \max(c_{01})$, as shown in fig. 4.6. This shelving of state $|1\rangle$ to state $|2\rangle$ is advantageous when performing e.g. single-run quantum algorithms on the processor, as described in chapter 6.

4.3.2 Qubit Spectroscopy

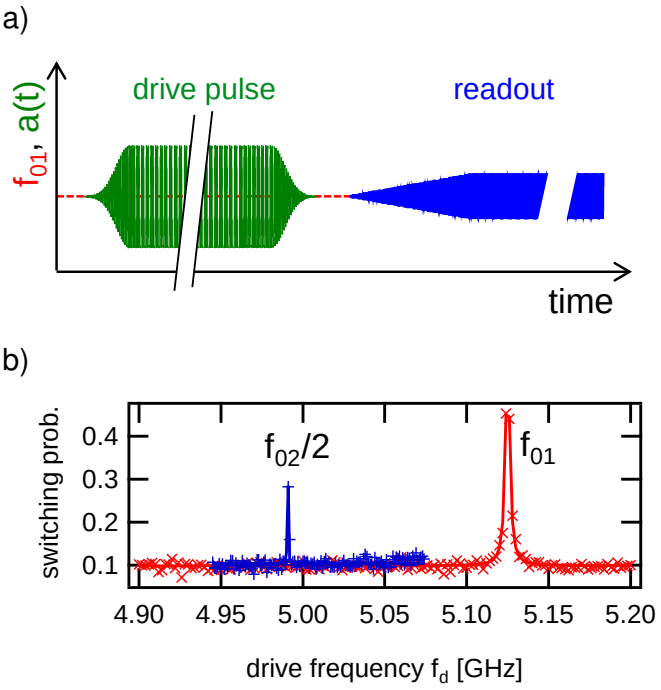

Figure 4.7: a) Qubit drive and readout pulse sequence used for qubit spectroscopy. b) Example of qubit spectrum showing the switching probability of the qubit readout when driving the qubit with 1 μs-long pulse as a function of the drive frequency. Low power spectroscopy (red points) shows only the $|0\rangle \rightarrow |1\rangle$ transition of the qubit at frequency f_{01}, whereas the 2-photon $|0\rangle \rightarrow |2\rangle$ transition at frequency $f_{02}/2$ is also observed at higher power (blue points). Lorentzian functions (lines) are fitted to these two spectroscopic lines.

In order to characterize the transition frequency and anharmonicity of the qubit we perform spectroscopic measurements. For this we drive the qubit with a long Rabi pulse

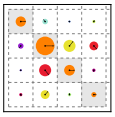

(usually > 1 μs) at a frequency ω_d. When the drive frequency ω_d is close to the ω_{01} frequency of the qubit, the drive pulse will induce a Rabi oscillation of the quantum state of the qubit. The induced rotation amplitude will be largest at $\omega_d = \omega_{01}$. Due to decoherence during the driven evolution, the maximum probability for measuring the qubit in the state $|1\rangle$ at the end of the pulse will be limited to 50 %. By repeating the pulse sequence shown in fig. 4.7a for a range of drive frequencies ω_d, a full spectroscopy of the qubit can be obtained. Fig. 4.7b shows an example of this, for different drive amplitudes. Here, the blue curve has been measured at 10 dB higher power then the red curve, which is sufficient to observe the two-photon $|0\rangle \rightarrow |2\rangle$ transition of the qubit at $f_{02}/2$. By fitting the two resonance curves with a Lorentzian model we obtain the qubit frequencies f_{01} and $f_{02}/2$, and from the equations of section 2.3.4, the charging and Josephson energies of the qubit at the given working point.

4.3.3 Rabi Oscillations

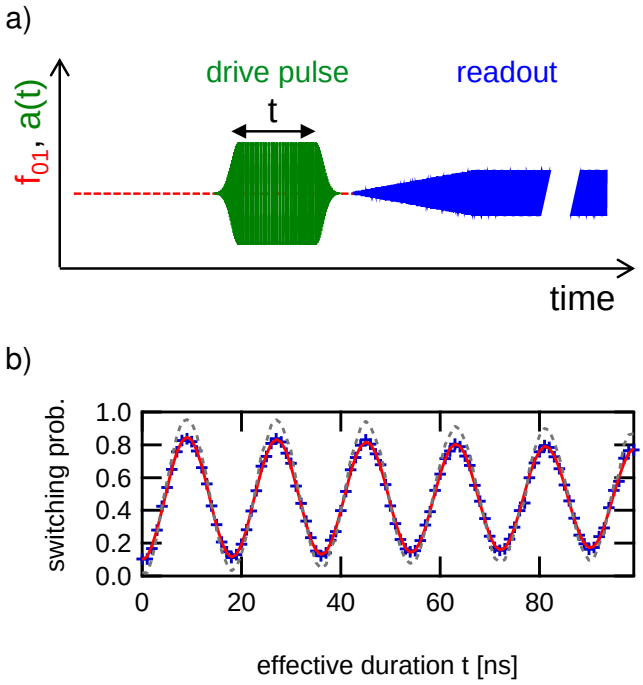

Figure 4.8: a) Qubit drive and readout pulse sequence used for measuring Rabi oscillations. b) Example of a measured Rabi oscillation showing the switching probability of the qubit readout when driving the qubit at f_{01} with a Gaussian drive pulse of increasing effective duration t (points). The measurement results are not corrected for readout errors. The line is a fit by an exponentially decaying sine function. The grey dashed line shows the measurement data corrected for readout errors.

After having obtained the proper qubit transition frequency f_{01}, we calibrate Rabi pulses. For this, we perform a Rabi oscillation experiment that consists in driving the qubit at $f_{01}$with pulses of increasing areas and in measuring its state immediately afterwards. Figure 4.8 shows the pulse sequence that we use and the resulting measurement data, the readout switching probability being expressed as a function of an equivalent pulse length at a nominal pulse height. As can be seen, the amplitude of the Rabi oscillations gets damped as $p(t) = p_0 + \Delta p \cos(\Omega t) \exp(-\Gamma_R t)$ due to relax-

ation and dephasing during the driven evolution. Also, the maximum readout contrast is limited due to readout errors characterized in details in the next chapter. From the fit of the Rabi data we obtain the Rabi frequency Ω, which we use to program precise single-qubit rotations in all our experimental sequences. Note that due to the finite anharmonicity of the qubit, there is always a finite leakage to the second excited state $|2\rangle$, which we discuss later.

4.3.4 Relaxation Time Measurement

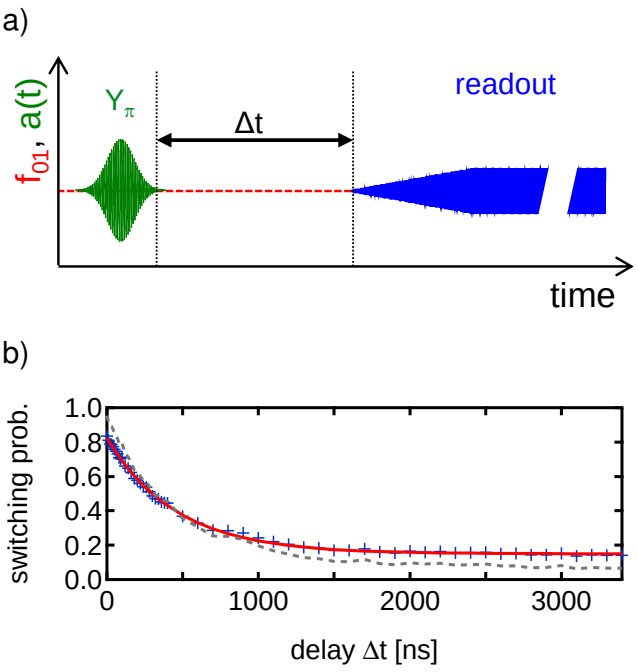

Figure 4.9: a) Qubit drive and readout pulse sequence used for relaxation time measurement. b) Example of relaxation time measurement showing the probability of measuring the qubit in state $|1\rangle$ as a function of the delay time between the preparation of the state $|1\rangle$ and the actual measurement of the qubit state (points). The line is a fit by a decaying exponential. The grey dashed line shows the measurement data corrected for readout errors.

Having obtained the transition frequency f_{01} and calibrated the Rabi frequency Ω, we measure the relaxation time of the qubit. For this, we put the qubit in state $|1\rangle$ by applying a X_π pulse and let it evolve freely afterwards for a given delay time before reading out its state, as shown in fig. 4.9a. As can be seen on fig. 4.9b, the probability decreases exponentially as a function of time. A fit of the function $p(|1\rangle) = p_0 + p_a \exp(-\Gamma_1 t)$ to the data yields the qubit relaxation rate Γ_1 at the given working point. In the following chapter we measure in more detail the relaxation time of both qubits as a function of their transition frequency and their detuning from the readout resonator.

4.3.5 Dephasing Time Measurement

We also characterize the dephasing of each qubit by performing a so-called *Ramsey fringe experiment*, consisting in two $Y_{-\pi/2}$ pulses separated by a delay time Δt and

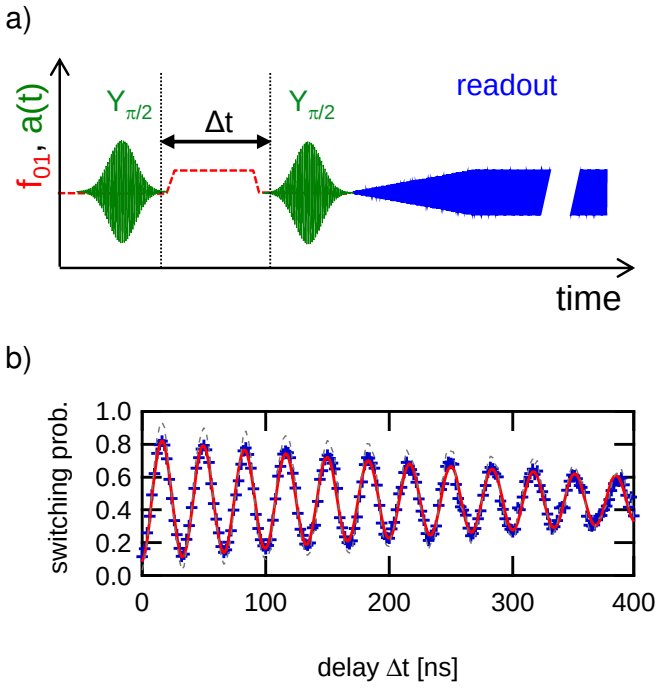

Figure 4.10: a) Qubit drive and readout pulse sequence used in a Ramsey experiment. (b) Example of a measured qubit Ramsey experiment showing the switching probability of the qubit readout (points) at the end of the sequence. Fitting the resulting curve with an attenuated sine-wave model (line) yields the dephasing rate Γ_ϕ and the qubit frequency f_{01} (see text). The grey dashed line shows the measurement data corrected for readout errors.

a readout immediately afterwards, as illustrated on Fig. 4.10a. We either choose microwave pulses detuned from f_{01} by an amount Δf, or use resonant microwave pulses together with a flux pulse that shifts the qubit frequency by Δf during the whole delay. After the first pulse the qubit is in state $1/\sqrt{2}(|0\rangle + |1\rangle)$ and acquires a phase $\Delta\phi = 2\pi\Delta f \Delta t$ during the delay. The final state of the qubit after applying the second $Y_{\pi/2}$ pulse therefore becomes

$$|\phi_f\rangle = 1/\sqrt{2}\begin{pmatrix} 1 & 1 \\ 1 & -1 \end{pmatrix} \cdot \begin{pmatrix} 1 \\ e^{i\Delta\phi} \end{pmatrix} = \begin{pmatrix} -\cos\Delta\phi/2 \\ i\sin\Delta\phi/2 \end{pmatrix}, \tag{4.7}$$

and the probability $p = \cos^2\Delta\phi/2$ to measure state $|1\rangle$ oscillates with frequency Δf as a function of the delay Δt . Due to dephasing and relaxation during the free evolution, the amplitude of these oscillations will decay. As explained in section 2.3.4, this decay takes the form $\exp(-\Gamma_2 t)$ with $\Gamma_2 = \Gamma_1/2 + \Gamma_\phi$ if the noise responsible for dephasing is white at low frequency, or the form $\exp(-\Gamma_1 t/2)\exp(-Bt^2)$ if the noise has a 1/f dependance. Even if the main dephasing source is 1/f flux noise of microscopic origin, the decay of the Ramsey oscillations is close to an exponential due to the relaxation contribution. So in practice, we fit the Ramsey data by $acos(\Delta f.t)\exp(-\Gamma_2 t)$ and deduce an effective dephasing rate Γ_ϕ. Furthermore, the fit provides an accurate measurement of Δf and consequently of the qubit frequency f_{01}, which is now known with a precision of 100 kHz.

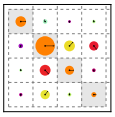

Chapter 5

Characterizing the Two-Qubit Processor

After having detailed the design of the processor and the measurement techniques employed in this work, we discuss in this chapter how we characterize the processor and demonstrate the basic functionality that we need to run meaningful quantum algorithms. In particular we show how we implement and characterize the universal $\sqrt{i\mathrm{SWAP}}$ two-qubit quantum gate with 90% fidelity, similar to the gate used in the following chapter to run the Grover search algorithm.

The chapter begins with the choice of the different working points during operation, based on the measurement of the basic qubit coherence properties and readout fidelities as a function of the qubit frequency. Then, single-qubit microwave gates are characterized. Afterwards, we discuss the generation and characterization of entanglement by quantum state tomography, and perform a test of the so-called CHSH Bell inequality. Finally, we discuss in detail how we characterize our $\sqrt{i\mathrm{SWAP}}$ gate by quantum process tomography: we explain how we estimate and/or fit the microwave pulse errors in order to remove the tomographic errors and obtain a fidelity that characterizes the gate alone.

5.1 Individual Qubit and Readout Characterization Choice of the Working Points

The first step in the characterization of the processor consists in obtaining all relevant qubit and readout parameters, as described in chapter 4. For this, we perform a set of measurements from which we obtain the qubit frequencies, anharmonicities, junction asymmetries, inter-qubit coupling, coupling to the microwave drive lines, coupling of each qubit to its readout, as well as qubit relaxation and dephasing times. Most of these parameters are measured for a range of qubit frequencies in order to pick up the best

working points for implementing the gate.

Qubit Frequency, Anharmonicity and Asymmetry

To obtain the Josephson and charging energies as well as the junction asymmetries of the qubits, we perform spectroscopic measurements of the single-photon $|0\rangle \rightarrow |1\rangle$ and two-photon $|0\rangle \rightarrow |2\rangle$ qubit transitions at different values of the external magnetic flux Φ_{ext}, as described in section 4.3.2. By fitting equations (2.67) and (2.61) to the resulting values $\omega_{01}(\Phi_{ext})$ and $\omega_{02}(\Phi_{ext})$ (see fig. 5.1a) we obtain all relevant qubit parameters. For our processor, these are $E_J^I/h = 36.2$ GHz, $E_c^I/h = 0.98$ GHz and $E_J^{II}/h = 43.1$ GHz, $E_C^{II}/h = 0.87$ GHz for the Josephson and charging energies of the two qubits, yielding anharmonicities $\alpha^I \approx 245$ MHz and $\alpha^{II} \approx 220$ MHz. For the qubit junction asymmetries, we obtain $d^I = 0.2$, $d^{II} = 0.35$.

Readout Parameters

To obtain the resonance frequencies and quality factors of the readout resonators we perform a simple measurement of the S_{11} reflection coefficient. The resulting frequencies are $f_R^I = 6.84$ GHz and $f_R^{II} = 6.70$ GHz with quality factors $Q^I \simeq Q^{II} = 730$. We measure the Kerr nonlinearity K of the resonators, as defined by eq. 2.102, by following the procedure given in [95, p. 166] and obtain $K^I \simeq K^{II} = -2.3 \pm 0.5 \times 10^{-5}$.

Qubit/Readout Coupling

The coupling of each qubit to its readout resonators is determined by spectroscopically measuring the avoided level crossing between them. For this, we perform a series of spectroscopic measurements of the resonator while tuning the qubit frequency from below the resonator frequency to above it. Performing such a measurement on a chip identical to the one used in the main experiment reported here yields a coupling coefficients $g_{01}^I \simeq g_{01}^{II} = 2\pi \cdot 50$ MHz.

Qubit Parameter Survey

In order to determine the optimal working points for our processor, we characterize the properties of the qubits in a large frequency window. For this, we perform an automated measurement of the transition frequencies ω_{01} and ω_{02}, of the readout contrasts c, and of the relaxation rate Γ_1 of each qubit at different values of the magnetic flux Φ_{ext}. The results are summarized in fig 5.1. The expected Purcell relaxation rates $\Gamma_{\text{Purcell}}^{I,II}$ as given by eq. (2.111) are shown in magenta and are much lower than the actual observed rates for the two qubits. We can also take into account qubit relaxation $\Gamma_{fl,c}^{I,II}$ due to a capacitive

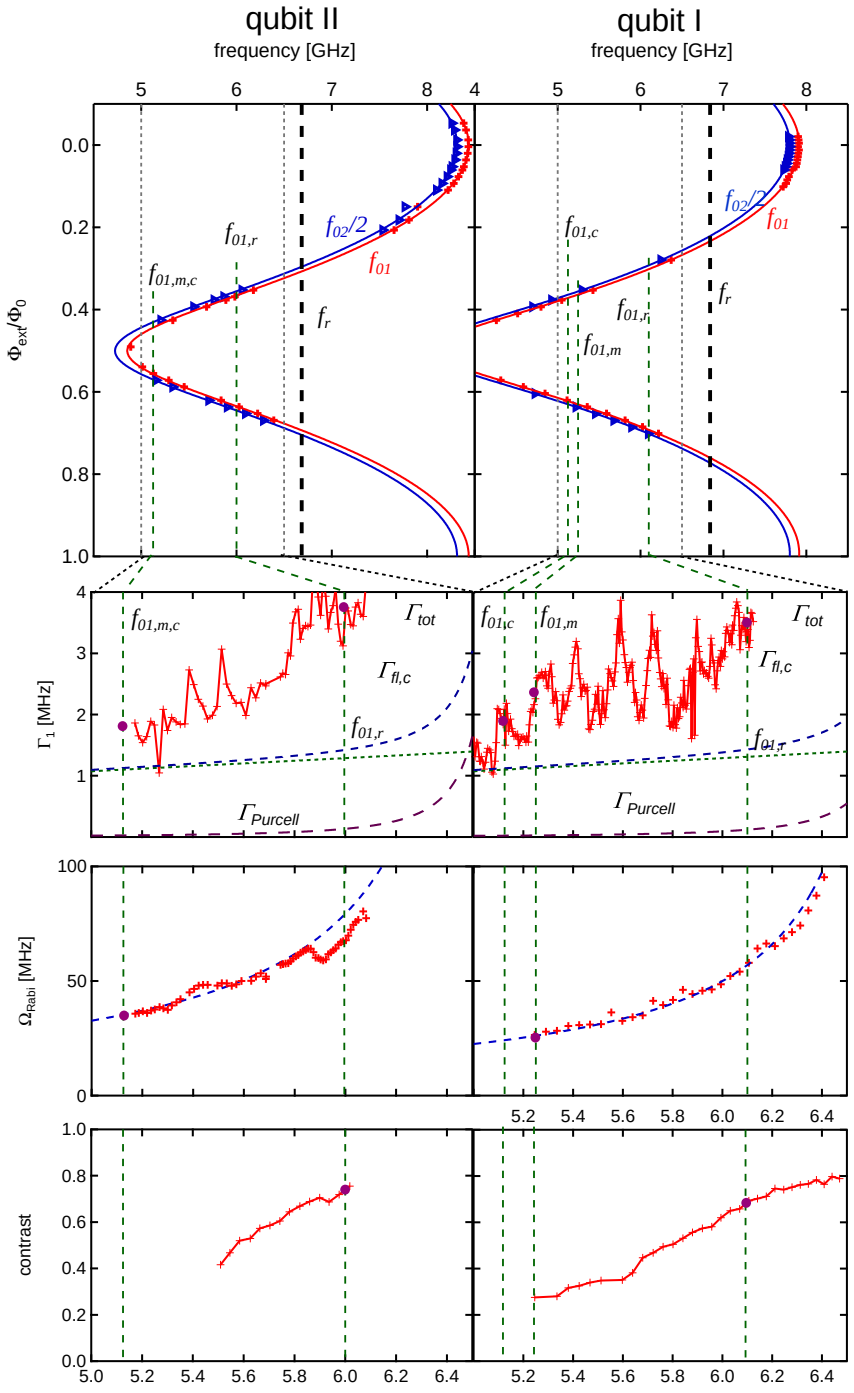

Figure 5.1: Parameter survey of the two qubits. a) Experimental (dots) and fitted (lines) qubit $f_{01}^{I,II}$ and $f_{12}^{I,II}$ frequencies. b) Experimental (red crosses) and expected (lines) relaxation rates Γ_1 of the qubits. The calculated contributions are those of the Purcell effect $\Gamma_{\mathrm{Purcell}}$ (magenta), the relaxation due to capacitive coupling to the flux line $\Gamma_{fl,c}$ (green) and their sum (blue). c) Rabi frequency $\Omega_{\mathrm{Rabi}}^{I,II}$ at a fixed drive amplitude, measured (red crosses) and modeled using eq. (2.95). d) Readout contrast c_{01} of the two qubits, for a range of qubit frequencies. The chosen processor working points $f_{01,r}^{I,II}$, $f_{01,m}^{I,II}$ and $f_{01,c}^{I,II}$ are also indicated with purple disks.

coupling of the qubit electrodes to the fluxline, which can be calculated using eq. (2.79). In order to reach the lowest measured relaxation rate, we fit a capacitive coupling $C_{g,fl} = 2\ \mathrm{fF}$ to the fluxline that we model as two parallel $50\ \Omega$ transmission lines equivalent to an effective impedance $Z_{fl} = 25\ \Omega$. However, this still cannot explain quantitatively the observed data: hence there must be at least one additional relaxation channel in our design that we have not captured. Since the observed Rabi frequencies of the qubits are in agreement with the expected Purcell filtering of the readout resonator, we can rule out additional relaxation through the readout gate circuit, leaving only microscopic channels or the coupling of the qubit to an unknown external impedance as possible causes of the observed relaxation.

The observed qubit Rabi frequencies $\Omega_{\mathrm{Rabi}}^{I,II}$ at a fixed drive input voltage V_{in} agree well with eq. (2.95). The best fit to this model, obtained with the measured resonator frequencies and quality factors and with only the input voltage V_{in} as a fitting parameter, is shown in blue and agrees well with the measurement data for both qubits, confirming that the filtering through the readout resonator works.

As expected, the readout contrast increases when decreasing the qubit-resonator detuning Δ, in accordance with an increase of the dispersive frequency shift given by eq. (2.97).

The qubit dephasing rates $\Gamma_\phi^{I,II}$ (which are not shown in the plot since they have not been measured systematically) vary between $2 - 4\ \mathrm{MHz}$ and do not show a clear dependence on the qubit frequencies.

Choice of Manipulation and Readout Working Points

Having characterized all parameters of the individual qubits as a function of ω_{01}^I and ω_{01}^{II}, we can choose the frequency working points for qubit manipulation and readout, and place them on fig. 5.1. For single-qubit manipulation and parking, we choose $\omega_{01,m}^I/2\pi = 5.247\ \mathrm{GHz}$ and $\omega_{01,m}^{II}/2\pi = 5.125\ \mathrm{GHz}$, where we have relaxation times $T_1^I(\omega_{01,m}^I) \approx 440\ \mathrm{ns}$ and $T_1^{II}(\omega_{01,m}^{II}) \approx 520\ \mathrm{ns}$. For qubit readout, we choose $\omega_{01,r}^I \approx 6.2\ \mathrm{GHz}$ and $\omega_{01,r}^{II} \approx 6.0\ \mathrm{GHz}$, where we have single-shot readout contrasts $c_{01}^I(\omega_{01,r}^I) \approx 75\%$ and $c_{01}^{II}(\omega_{01,r}^{II}) \approx 73\%$.

5.2 Two-Qubit Readout Characterization

The errors of an n-qubit readout are fully characterized by giving a complete set of switching probabilities $p_m(x_1x_2\ldots x_n|\,|y_1y_2\ldots y_n\rangle)$, which correspond to the probability of obtaining a readout outcome $x_1x_2\ldots x_n$ after preparing an input state $|y_1y_2\ldots y_n\rangle$, with $x_i, y_i \in \{0, 1\}$.

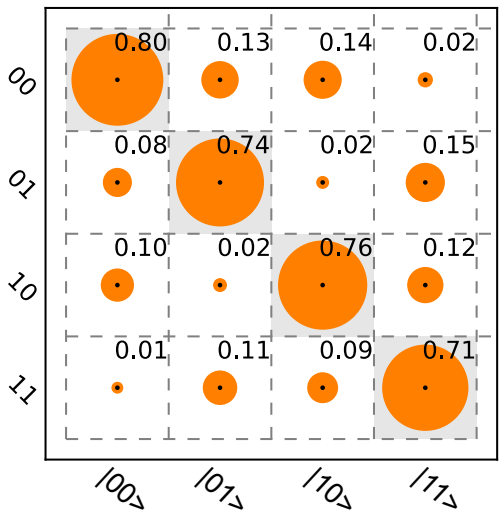

Figure 5.2: The measured readout matrix of our two-qubit processor. Shown are the conditional measurement probabilities $p_m(x_1x_2||y_1y_2\rangle)$, with $x_1, x_2, y_1, y_2 \in \{0, 1\}$. The diagonal elements correspond to the readout fidelities of the four basis states. The single qubit readout fidelities as obtained from the matrix are $p_m^I(0*||00\rangle) = 0.88$, $p_m^I(1*||10\rangle) = 0.85$, $p_m^{II}(*0||00\rangle) = 0.9$ and $p_m^{II}(*1||01\rangle) = 0.85$, the readout crosstalks are $p_m(0*||00\rangle) - p_m(0*||01\rangle) = -0.01$, $p_m(1*||10\rangle) - p_m(1*||11\rangle) = -0.02$, $p_m(*0||00\rangle) - p_m(*0||10\rangle) = 0$ and $p_m(*1||01\rangle) - p_m(*1||11\rangle) = -0.01$.

The single-qubit fidelities $p_m(0||0\rangle)$ and $p_m(1||1\rangle)$ can be simply obtained from an s-curve measurement, as explained in section 4.3.1. In order to calibrate the two-qubit readout errors, we perform an experiment at the readout working points indicated above, where we measure the full set of conditional probabilities $p(x||y\rangle)$ with $\{x, y\} \in \{00, 01, 10, 11\}$. For this purpose, the qubit register is initialized in each basis state before performing a simultaneous readout of the two qubits. By repeating and averaging the resulting outcomes we obtain the full set of conditional readout probabilities, which we plot as a 4×4 readout matrix $\mathbf{R}$, shown in fig. 5.2. Here, we assume that the state preparation errors of the input states, e.g. due to thermal excitation of the qubits out of the $|0\rangle$ state, erroneous single-qubit pulses or leakage to the qubit state $|2\rangle$, are sufficiently small so that they can be neglected. From the readout matrix, all conditional and unconditional readout fidelities as well as the readout crosstalk can be calculated. We can correct any measured set of probabilities $\mathbf{p}_R = (p_{00}, p_{01}, p_{10}, p_{11})$ for readout errors by simply multiplying it with the inverse of $\mathbf{R}$, such that $\mathbf{p}_R^{corr} = \mathbf{p}_R \cdot \mathbf{R}^{-1}$. For all experiments discussed in the remainder of this chapter, we will always correct readout errors by this method (unless indicated otherwise) and interpret $\mathbf{p}_R^{corr}$ as the occupation probabilities of the four computational basis states.

5.3 Single-Qubit Gate Characterization

To perform arbitrary single-qubit operations – as needed for implementing a quantum algorithm, for characterizing a two-qubit gate by quantum process tomography, or more simply for preparing a particular state and characterizing it by quantum state tomography– we need to implement a complete set of rotations like X, Y and Z. As already explained,

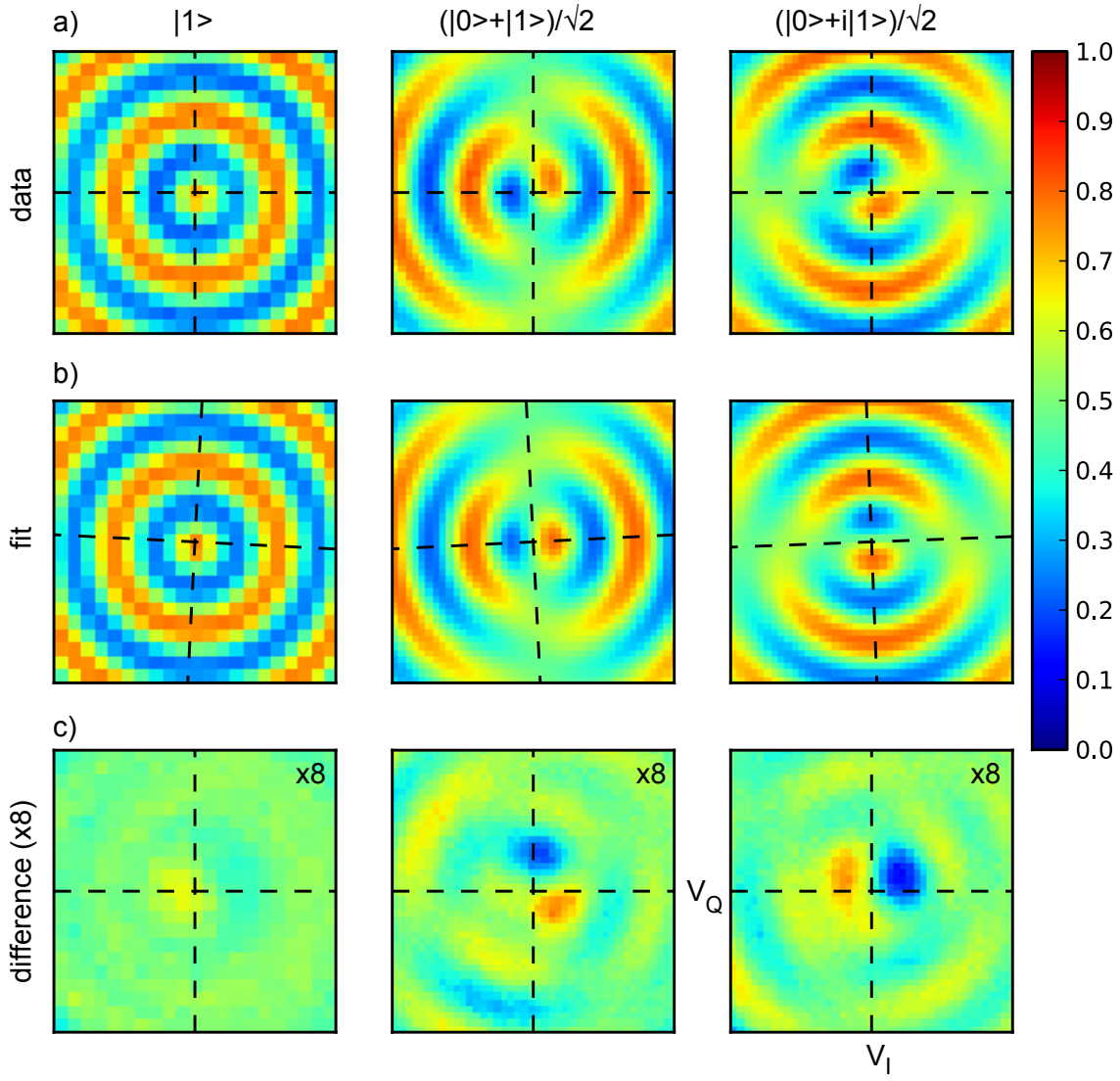

Figure 5.3: Characterization of single-qubit XY control. a) Measured state $|1\rangle$ occupation probability after preparing a qubit in one of the states $|1\rangle$, $1/\sqrt{2}(|0\rangle+|1\rangle)$ or $1/\sqrt{2}(|0\rangle+i\,|1\rangle)$ and subjecting it to a microwave drive pulse of constant duration and variable phase: $a(t) = V_I \cdot \cos\omega_{rf}t + V_Q \cdot \sin\omega_{rf}t$. b) Best fit to the data of the model given by eq. (5.1). c) Difference between measured data and fit (magnified x8)

rotations in the XY-plane are implemented through microwave drive pulses, where the phase of the drive pulse relative to an arbitrary reference determines the rotation axis and the amplitude the effective Rabi frequency. To characterize these drive pulses, we prepare a single qubit in the states $|1\rangle$, $1/\sqrt{2}(|0\rangle + |1\rangle)$ or $1/\sqrt{2}(|0\rangle + i\,|1\rangle)$, and subject it afterward to a single microwave pulse of varying amplitude and phase: this pulse of form $V(t) = V_I a(t) \cdot \cos\omega_{rf}t + V_Q a(t) \cdot \sin\omega_{rf}t$, is obtained by I-Q mixing the microwave carrier at ω_{rf} to DC $V_I a(t)$ and $V_Q a(t)$ pulse envelopes with the same constant duration, with Gaussian rise and fall, and with increasing amplitudes V_I and V_Q. We then measure and plot (see fig. 5.3) the occupation probability of state $|1\rangle$ as a function V_I, V_Q.

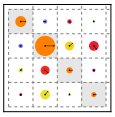

The qubit that was prepared in state $|1\rangle$ shows a rotational-invariant switching probability pattern, which is indeed what one expects for a qubit prepared in either $|0\rangle$ or $|1\rangle$. On the other hand, the switching probability distributions of the qubits prepared in the states $1/\sqrt{2}(|0\rangle + |1\rangle)$ and $1/\sqrt{2}(|0\rangle + i\,|1\rangle)$ are almost symmetric with respect to the axis along which the qubit has been prepared. Performing a fit of the model

$$|\psi_{out}\rangle = \exp\left(-i\frac{\varphi}{2}[\cos(\alpha+\alpha_0)\hat{\sigma}_x + \sin(\alpha+\alpha_0)\hat{\sigma}_y]\right)|\psi_{in}\rangle\,, \tag{5.1}$$

with $\alpha = \mathrm{atan}(c_Q Q/c_I I)$, to the measured occupation probability, we obtain the fitting parameters c_I, c_Q, φ , and the overall gate phase error $\alpha_0 \leq 2.8°$. This measurements demonstrate our ability to prepare and drive the qubit along arbitrary axes of the Bloch sphere. Nevertheless, the phase error α_0 depends on the rotation angle φ due to mixer imperfections, as can be seen on figure 5.3 where the error is larger for $\pi/2$ pulses. Consequently, we have also calibrated separately π and $\pi/2$ pulses for the experiments, as reported below.

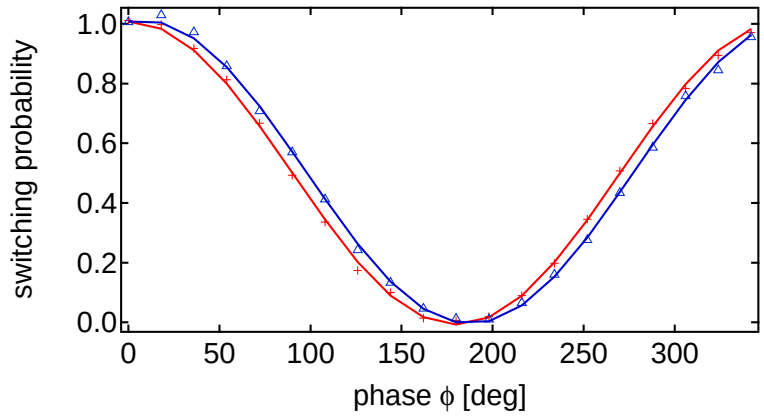

Figure 5.4: Measured (dots) and fitted (line) occupation probability of state $|1\rangle$ at the manipulation working point after subjecting the qubit to a $X_{\pi/2}\Phi_{\pi/2}$ pulse sequence, as a function of Φ. Red data corresponds to an uncorrected drive pulse, resulting in a phase error $\epsilon_\Phi \approx 7.66°$, whereas blue data corresponds to a corrected drive pulse, resulting in $\epsilon'_\Phi \approx 0.09°$.

We calibrate the length of our $\pi/2$ and π pulses by performing a Rabi experiment, as explained in section 4.3.3. We then correct errors in the direction Φ of the rotation axis by performing a so-called *amplified pulse error* sequence [75]. This sequence consists of a $X_{\pi/2}$ pulse followed by a $\Phi_{\pi/2}$ pulse, where Φ gives the rotation axis of the second pulse. Performing it for different values of Φ, measuring the state $|1\rangle$ occupation probability afterwards, and fitting the resulting curve to a model of the form $p(|1\rangle) = p_0 + p_a\cos(\Phi - \epsilon_\Phi)$ allows us then to extract both amplitude errors $\epsilon_a = |p_a - 0.5|$ and phase errors ϵ_Φ. These can be further amplified by interposing a number of identity operators $X_{\pi/2}X_{-\pi/2}$ between the two drive pulses, which we do not do in this work, however. The phase shift ϵ_Φ of the minimum of the curve with respect to π is due to both the leakage to the Transmon state $|2\rangle$ and the drive-induced frequency shift discussed

in section 3.2.2. The first source of error could be corrected by using special DRAG drive pulses [75], which we don't do in this work. We correct the second source of errors by detuning the drive frequency as explained in section 3.2.2. Figure 5.4 shows an exemplary APE measurement for qubit I, where the phase error for an uncorrected qubit pulse is $\epsilon_\Phi \approx 7.66°$, which gets reduced to $\epsilon'_\Phi \approx 0.09°$ by detuning the qubit drive frequency by $\Delta f_{dr} = -4$ MHz. We are thus able to perform single-qubit pulses with an angular precision $\leq 1°$, both in angle and in rotation direction, just after a calibration. Nevertheless, the experiment tends to drift and the errors thus tend to be larger when performing long measurements.

5.4 Demonstrating Two-Qubit Entanglement

We first choose the working point at which the two qubits will be resonantly coupled to perform a $\sqrt{i\mathrm{SWAP}}$ gate. Because the coupling strength g_{qq} defined by eq. 2.107 depends very weakly on this working point in the vicinity of the manipulation points defined above, we choose for a sake of simplicity to shift the frequency of only one qubit. So we will displace qubit I by -122 MHz $= 30 g_{qq}/2\pi$ (see below) from its manipulation point at $\omega^I_{01,m}/2\pi = 5.247$ MHz to the manipulation point of qubit II at $\omega^{II}_{01,m}/2\pi = 5.125$ MHz.

5.4.1 Coupling Strength Between Qubits

We then measure the qubit-qubit coupling strength g_{qq} at the coupling working point. For that purpose, the frequency ω^I_{01} of qubit I is tuned with the flux Φ^I_{ext} across the fixed frequency ω^{II}_{01} of qubit II; at each frequency a spectroscopic pulse is applied to qubit I, and qubit II is read out. Plotting the switching probability of readout II, one obtains the anticrossing shown on fig. 5.5: close to resonance, the eigenstates of the two-qubit system approach the two Bell states $|\Psi_\pm\rangle = 1/\sqrt{2}(|10\rangle \pm |01\rangle)$, which are both excited by the drive of qubit I and detected by measuring qubit II. Hence we observe two spectroscopic lines corresponding to the two transitions $|00\rangle \rightarrow 1/\sqrt{2}(|01\rangle + |10\rangle)$ and $|00\rangle \rightarrow 1/\sqrt{2}(|01\rangle - |10\rangle)$. Their maximum separation yields the coupling strength $2g_{qq}/2\pi = 8.3$ MHz.

5.4.2 Creation of Entanglement

Knowing the qubit-qubit coupling strength, we then perform a coherent swapping operation between the qubits by preparing the register either in $|01\rangle$ or $|10\rangle$ by shifting non adiabatically the frequency of qubit I down to that of qubit II during a well defined time,

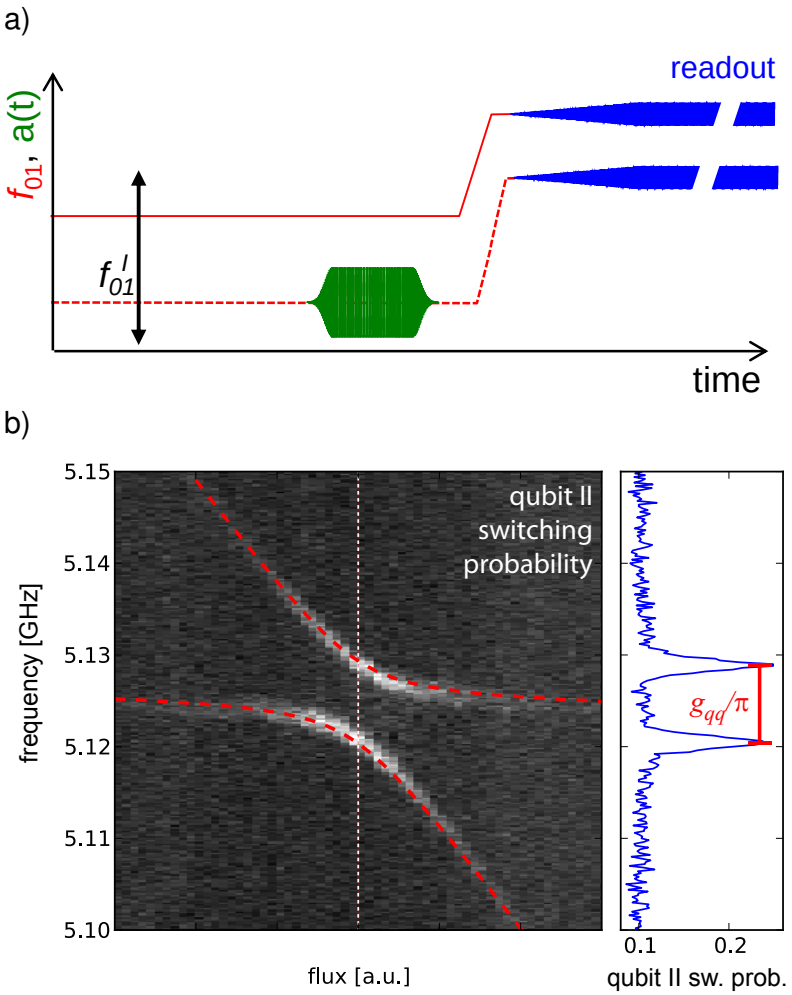

Figure 5.5: Measurement of the two-qubit anticrossing at the coupling working point. a) Pulse sequence used. b - left) Switching probability of readout II as a function of flux Φ_{ext}^{I} and frequency f_d of the spectroscopic pulse applied to qubit I . b - right) Cut at the middle of the anticrossing (dotted line in the 2D plot) yielding $2g_{qq}/2\pi = 8.3$ MHz.

and by measuring the two-qubit register directly afterward. The flux pulses used for this are optimized as explained in section 4.2.3. The expected evolution operator of the process is

$$U(t) = \exp\left(i\theta_I\hat{\sigma}_z^I + i\theta_{II}\hat{\sigma}_z^{II}\right)\begin{pmatrix} 1 & 0 & 0 & 0 \\ 0 & \cos(tg_{qq}) & -i\sin(tg_{qq}) & 0 \\ 0 & -i\sin(tg_{qq}) & \cos(tg_{qq}) & 0 \\ 0 & 0 & 0 & 1 \end{pmatrix}, \tag{5.2}$$

where $\theta_{I,II}$ are dynamical phases accumulated by each qubit due to their frequency shift with respect to their manipulation and parking point during the operation. For qubit I, this shift is directly applied on purpose and is large, whereas for qubit II, it is due to the

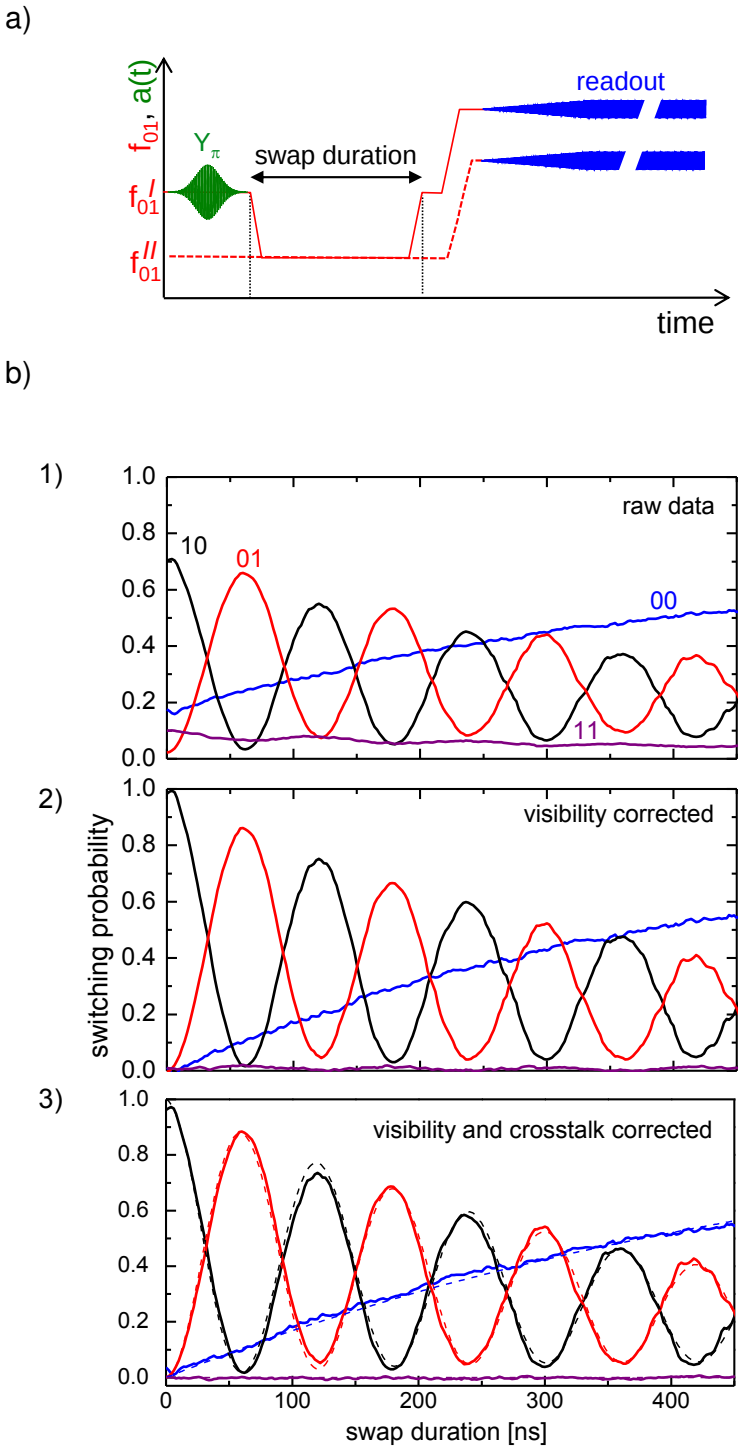

Figure 5.6: a) Pulse sequence used to create an entangled two-qubit state using a non-adiabatic pulse that brings the qubits in resonance for a well-defined time. b) State occupation probabilities for the two-qubit register during a coherent energy swap. b1) Shows the raw state probabilities corresponding to the states $|00\rangle$, $|01\rangle$, $|10\rangle$ and $|11\rangle$, b2) shows the same data corrected for the limited visibility of each qubit readout and b3) shows the fully corrected readout probabilities where we account for both visibility and inter-qubit readout crosstalk errors.

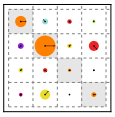

flux crosstalk and is small. As can be seen on eq. 5.2, the register state is expected to oscillate between the $|01\rangle$ and $|10\rangle$ states with frequency g_{qq}. The states $|00\rangle$ and $|11\rangle$ are not affected by the interaction except for a phase factor.

Figure 5.6 shows the experimental sequence used as well as the results obtained as a function of the coupling duration. Shown are the raw readout outcomes (i.e. without any corrections), the readout probabilities corrected for the individual readout visibilities, and the qubit state probabilities $p(|00\rangle)$, $p(|01\rangle)$, $p(|10\rangle)$ and $p(|11\rangle)$ obtained after correcting the outcomes for both readout visibilities and crosstalk using the readout matrix $\mathbf{R}$ of fig. 5.2. The data shows the expected swap between states $|01\rangle$ and $|10\rangle$, as well as the reduction of the swapping amplitude, caused by relaxation and dephasing. The swapping frequency $2g_{qq}/2\pi = 8.3\ \mathrm{MHz}$ agrees with the value obtained from the spectroscopic measurement. Figure 5.6c also shows a master equation simulation of the experiment using the Hamiltonian and the Lindblad super-operators discussed in section 2.5. This simulation involves the measured g_{qq} and the measured relaxation rates of the qubits at the coupling working point, whereas dephasing rates are left as free fitting parameters. The reason for this is that the effective dephasing rate of the two-qubit register in the $\{|01\rangle, |10\rangle\}$ sub-space is very different from the dephasing rates of individual qubits. Indeed, the transition frequency between the two eigenstates $|\psi_{\pm}\rangle = 1/\sqrt{2}(|01\rangle \pm |10\rangle)$ at resonance, i.e. $\omega_{01}^{\pm} = \omega_{01}^{I,II} \pm \sqrt{4g_{qq}^2 + \Delta^2}/2 \approx \omega_{01}^{I,II} \pm g_{qq} + \Delta^2/8g_{qq}$, is sensitive to variations of the frequency detuning Δ to second order only. Hence, the effective dephasing rate of the two-qubit system is much lower than the single-qubit dephasing rates. The computation of the transversal relaxation super-operator in the $\{|01\rangle, |10\rangle\}$ sub-space is made complicated by the 1/f nature of the Δ noise as well as by the non-Gaussian character of the noise in Δ^2. Consequently, we have chosen to reproduce the observed swapping using purely phenomenological and independent dephasing super-operators in the $\{|0\rangle, |1\rangle\}$ Hilbert spaces of each qubit. As can be seen, this purely phenomenological model agrees very well with the experimental data with $\Gamma_{\phi}^{I,II} = 2\mu$s, probably because dephasing has only a small effect.

5.4.3 Quantum State Tomography

The experiments that we describe in the following sections will require us to determine experimentally the density matrix of the two-qubit register. The method that we use for this is called *quantum state tomography* (QST) (see e.g. [91] for an overview), which we explain now. We also discuss the relevant sources of errors involved in QST as well as their effect on our results.

The $2^n \otimes 2^n$ density matrix ρ of an n-qubit system can be written as a weighted sum

of 2^n combinations of the tensor products of n single-qubit Pauli matrices:

$$\rho = \sum_{v_1,v_2\ldots v_n} \frac{c_{v_1,v_2\ldots v_n}\hat{\sigma}_{v_1}\otimes\hat{\sigma}_{v_2}\ldots\hat{\sigma}_{v_n}}{2^n} \tag{5.3}$$

$$c_{v_1,v_2\ldots v_n} = \mathrm{Tr}\left\{\hat{\sigma}_{v_1}\otimes\hat{\sigma}_{v_2}\ldots\otimes\hat{\sigma}_{v_n}\,\rho\right\}, \tag{5.4}$$

where $v_i \in \{I, X, Y, Z\}$ and the $c_{v_1,v_2\ldots v_n}$ are real-valued coefficients that describe the given density matrix. To reconstruct experimentally ρ, it is thus sufficient to measure the expectation values of $n^2 - 1$ coefficients on an ensemble of identically prepared states (the value of the $I^{\otimes n}$ operator is always 1). For our two-qubit system, this means measuring the average values of all 15 non-trivial combinations of the operators $\{I, \hat{\sigma}_x, \hat{\sigma}_y, \hat{\sigma}_z\} \otimes \{I, \hat{\sigma}_x, \hat{\sigma}_y, \hat{\sigma}_z\}$. However, in our experiments, we can only measure the $\hat{\sigma}_z$ operator of each qubit. Therefore, rather than measuring the $\hat{\sigma}_x$ and $\hat{\sigma}_y$ operators directly, we rotate the quantum state of each qubit such that the state vector along the desired measurement axis coincides with the z-axis of the Bloch sphere, and then measure $\hat{\sigma}_z$ instead. We can therefore replace the operators $\hat{\sigma}_x$ and $\hat{\sigma}_y$ with an effective measurement of $\hat{\sigma}_z$ preceded by a rotation $R_{X,Y}$ given as

$$R_X = \exp\left(-i\hat{\sigma}_y\pi/4\right), \tag{5.5}$$

$$R_Y = \exp\left(+i\hat{\sigma}_x\pi/4\right). \tag{5.6}$$

Note that if phase and amplitude errors are present in the tomography pulses, the operators actually measured are

$$R'_X = \exp\left(-i\left[+\hat{\sigma}_y\cos\alpha + \hat{\sigma}_x\sin\alpha\right]\left[\pi/4+\gamma\right]\right), \tag{5.7}$$

$$R'_Y = \exp\left(+i\left[-\hat{\sigma}_y\sin\beta + \hat{\sigma}_x\cos\beta\right]\left[\pi/4+\delta\right]\right), \tag{5.8}$$

where α and β represent phase errors, and γ and δ represent amplitude errors. A detailed discussion of how we fit these error parameters to experimental data will be given in section 5.5.2. For the simple tomography measurements presented in the next section, we will generally neglect these small errors (as common in the quantum optics and superconducting qubit communities), but we will take them into account when analyzing the tomography and preparation pulse errors of our implementation of the $\sqrt{i\mathrm{SWAP}}$ gate.

When using the direct reconstruction method for the density matrix, statistical and systematic measurement errors can produce a set of coefficients v_i that corresponds to a *non-physical* density matrix, i.e. a density matrix which violates either the positivity $\langle\psi|\,\rho\,|\psi\rangle > 0$ (for all valid states $|\psi\rangle$) or the unity-trace condition $\mathrm{Tr}(\rho) = 1$. To alleviate this problem, several techniques can be employed. We have used the so-called *maximum likelihood estimation* technique which we present in the next section.

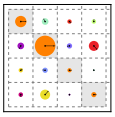

Maximum Likelihood Estimation of Quantum States

Maximum likelihood estimation is a method that numerically or analytically maximizes a likelihood function that depends on a number of measured outcomes and on a set of parameters that need to be estimated. The set of parameters that corresponds to the maximum of the probability function can then be interpreted as the one with the highest probability of generating the measured outcomes. When estimating the parameters of a density matrix with this method, the probability function to be maximized is the joint probability of obtaining the measured values $\{c_{XX\ldots X}, c_{YX\ldots X}, \ldots, c_{II\ldots I}\}$ for a given density matrix $\hat{\rho}$.

The joint measurement operators $\hat{\Sigma}_j = \hat{\sigma}_{v_1} \otimes \hat{\sigma}_{v_2} \ldots \otimes \hat{\sigma}_{v_n}$ have the eigenvalues ± 1 and can thus be written as

$$\hat{\sigma}_{v_1} \otimes \hat{\sigma}_{v_2} \ldots \otimes \hat{\sigma}_{v_n} = |+_j\rangle \langle +_j| - |-_j\rangle \langle -_j| , \tag{5.9}$$

where $|+_j\rangle$ and $|-_j\rangle$ are the eigenstates corresponding to the eigenvalues ± 1 of $\hat{\Sigma}_j$. When performing l consecutive measurements of the operator $\hat{\Sigma}_j$ on an ensemble of identically prepared states, the expectation value $\langle \hat{\Sigma}_j \rangle$ can be estimated as

$$\langle \hat{\Sigma}_j \rangle_\rho^{est} = \frac{1}{l} \sum_{i=1}^{l} m_i(\hat{\Sigma}_j, \rho), \tag{5.10}$$

where $m_i(\hat{\Sigma}, \rho)$ denotes the outcome of the i-th measurement of the operator $\hat{\Sigma}$ on the state described by the density matrix ρ. Since each outcome $m_i(\hat{\Sigma}_j, \rho)$ is Bernoulli distributed, the sum $\langle \hat{\Sigma}_j \rangle_\rho^{est}$ of them is binomially distributed with an expectation value $E(\langle \hat{\Sigma}_j \rangle_\rho^{est}) = \langle \hat{\Sigma}_j \rangle_\rho$ and a variance $\sigma^2(\langle \hat{\Sigma}_j \rangle_\rho^{est}) = 1/l \cdot (1 - \langle \hat{\Sigma}_j \rangle_\rho^2)$. For large sample sizes l, the binomial distribution can be well approximated by a normal distribution with the same expectation value and variance. The joint probability of obtaining a set of estimates $\{s_1, \ldots, s_{n^2-1}\}$ for the set of operators $\{\langle \hat{\Sigma}_1 \rangle_\rho, \ldots, \langle \hat{\Sigma}_{n^2-1} \rangle_\rho\}$ of a proposed density matrix ρ is thus given as

$$P\left(\langle \hat{\Sigma}_1 \rangle_\rho^{est} = s_1; \ldots; \langle \hat{\Sigma}_{n^2-1} \rangle_\rho^{est} = s_{n^2-1}\right) = \prod_{i=1}^{n^2-1} \exp\left(-\frac{l}{2} \frac{(s_i - \langle \hat{\Sigma}_i \rangle_\rho)^2}{1 - \langle \hat{\Sigma}_i \rangle_\rho^2}\right). \tag{5.11}$$

To be able to perform numerical optimization of the chosen density matrix parameters, we need to parametrize ρ using a set of unconstrained, real-valued parameters c_i. For this, we generate a matrix A from a list of $n^2 - 1$ parameters $\{c_1, \ldots, c_{n^2-1}\}$, where the diagonal elements of A are given as $\{|c_1|, \ldots, |c_{n-1}|, 1 - \min(1, \sum_i^{n-1} |c_i|)\}$ and the complex-valued off-diagonal elements by pairs $\{\ldots, c_i + ic_{i+1}, \ldots\}$ of the remaining parameters. From this matrix we generate a physical density matrix $\rho = AA^\dagger / \mathrm{Tr}(AA^\dagger)$.

In our experiment, we maximize this probability (or the logarithm of it) for a set of measured values s_i as a function of the parameters of a proposed density matrix ρ, obtaining the ρ which has the highest probability of having produced the observed measurement values.

5.4.4 Characterization of Two-Qubit States Using Quantum State Tomography

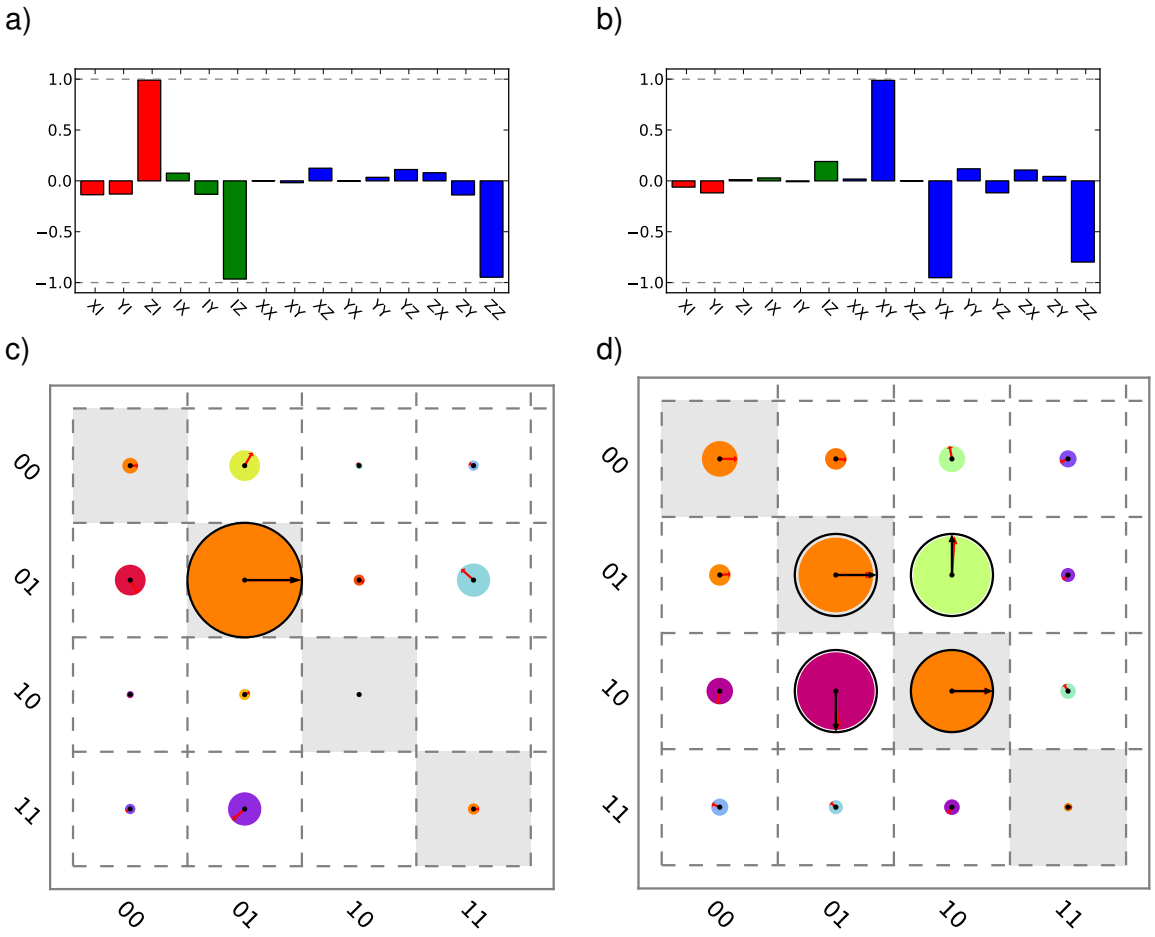

Figure 5.7: a/b) Measured Pauli sets of a prepared $|01\rangle$ input state and a corresponding output state (b) measured after a swapping time $t = 31$ ns and a phase-compensation z-pulse, showing the measured values of the single-qubit and multi-qubit Pauli operators. c/d) Corresponding density matrices of the input and output states, reconstructed using maximum likelihood estimation. The absolute value $|\rho_{ij}|$ of each element of the density matrix is represented by the size of each circle, whereas the phase $\angle\rho_{ij}$ is represented both by the color of the circle and the direction of the arrow. The state fidelities compared to the ideal states $|\psi^{in}\rangle = |01\rangle$ and $|\psi^{out}\rangle = 1/\sqrt{2}(|01\rangle + i\,|10\rangle)$ are $F_{tr}^{in} = 94\%$ and $F_{tr}^{out} = 84\%$, respectively. The density matrices of the ideal states are overlaid in black, for comparison.

Using the method described above, we reconstruct the density matrix of the two-

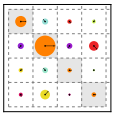

qubit register at different swapping times of the experiment described in fig. 5.6. We thus measure the full Pauli set on an ensemble of 10000 identical swap sequences by inserting tomography pulses just before readout. Figure 5.7 shows an example of two experimentally measured Pauli sets and their associated density matrices, measured at swapping times $t_a = 0$ ns and $t_b = 31$ ns. Note that for the measurement at t_b, a Z-pulse was applied to qubit II after the swap to compensate the phase given by the first operator in (5.2), as described in section 5.4.5. As can be seen, the obtained density matrix at t_a corresponds closely to a pure quantum state $|01\rangle$ with a fidelity $F_{tr} = 94\%$, whereas the density matrix at t_b corresponds to an entangled two-qubit state $1/\sqrt{2}(|01\rangle + |10\rangle)$ with fidelity $F_{tr} = 84\%$. These fidelities include the errors made when preparing the states, as well as the errors in the tomographic pulses, which are not easily separable. The raw density matrices obtained directly using eq. (5.3) (data not shown) possess negative eigenvalues $\lambda_a^1 = -0.0063$, $\lambda_a^2 = -0.0019$ and $\lambda_b^1 = -0.0485$, $\lambda_b^2 = -0.0002$, which are corrected using the ML estimation method. Nevertheless the difference between the raw and corrected ρ's are barely visible.

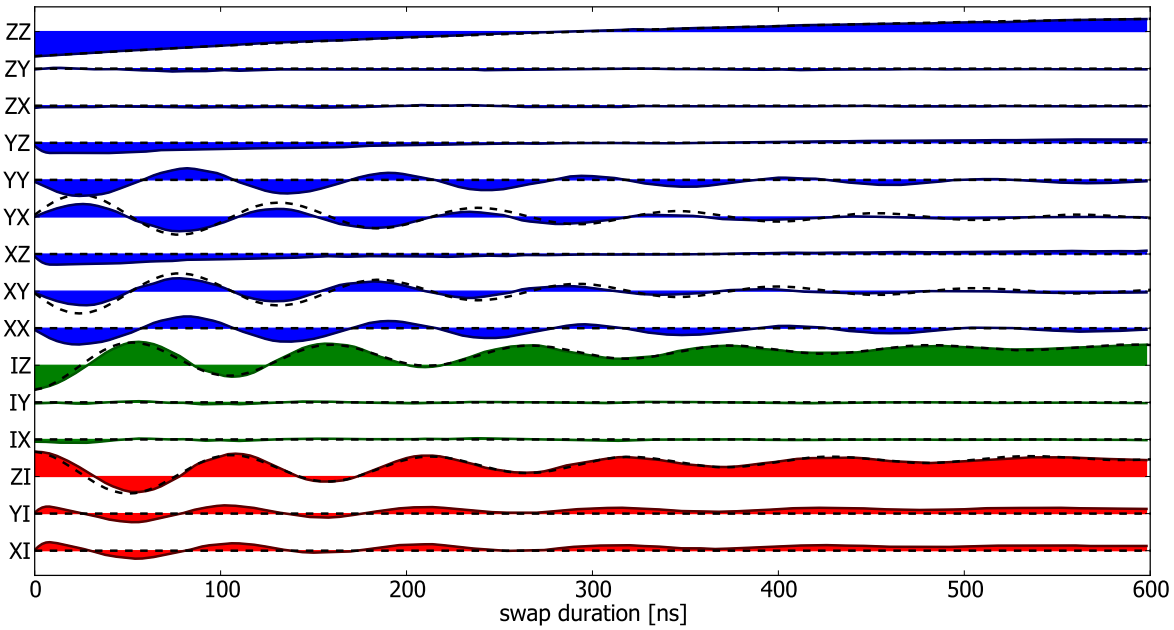

Figure 5.8: Measured Pauli operators $\hat{\sigma}_i \otimes \hat{\sigma}_j$ with $i, j \in \{I, X, Y, Z\}$ as a function of the interaction time. Shown are the 6 single-qubit operators as well as the 9 two-qubit correlation operators. The dashed line represents a master-equation simulation of the experiment, not modeling the dynamically acquired phase during the SWAP.

Measuring Pauli sets at different times, we then follow the evolution of the quantum state during the course of the swap. Figure 5.8 shows the result of such an experiment, where the measured averaged values of all Pauli operators are plotted as a function of the swapping time. Red and green curves correspond to the single-qubit Pauli operators $\hat{\sigma}^I_{X,Y,Z} \otimes \mathrm{I}$ and $\mathrm{I} \otimes \hat{\sigma}^{II}_{X,Y,Z}$, whereas the blue curves correspond to the two-qubit Pauli

operators $\hat{\sigma}^{I}_{X,Y,Z} \otimes \hat{\sigma}^{II}_{X,Y,Z}$. The dashed line corresponds to the integration of the master equation of system, in which the qubit coupling, the relaxation rate, and the dephasing rate are chosen as discussed above. As can be seen, the simulation agrees well with the experimental data, except for the oscillation of the XX and YY operators arising from the first operator in eq. (5.2), which are not included in the simulation.

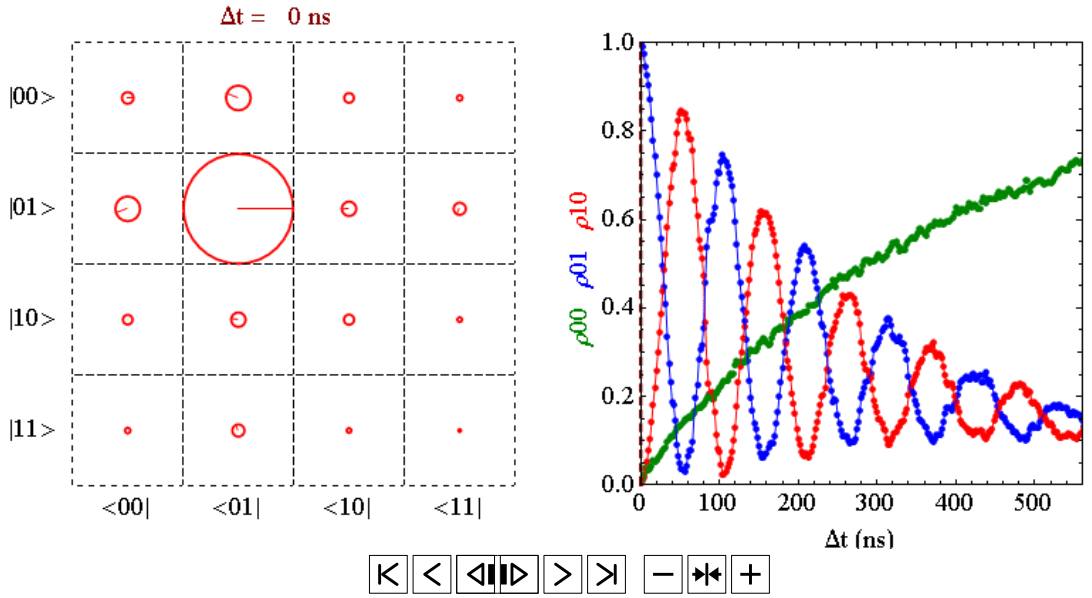

Figure 5.9: Movie of the reconstructed two-qubit register density matrices during the SWAP operation.

Figure 5.9 shows the same information as in fig. 5.8 but in the form of a time dependent reconstructed density matrices as in fig. 5.7. The readers of the electronic version of this thesis book can run a movie of this evolution by clicking on the control panel of the figure. For the readers of the paper book version, the frames of the movie (separated by 2 ns) are shown in the upper right corner of each page: when flipping the pages of the book, one can follow the coherent swapping between the qubits. The oscillation of the $|01\rangle$ and $|10\rangle$ populations at frequency g_{qq}, the oscillation of the corresponding coherences at frequency $2g_{qq}$, as well as the effect of decoherence are clearly visible.

5.4.5 Preparation and Characterization of Bell States

After having observed the swapping interaction, we check that we are able to prepare the four maximally entangled two-qubit states, known as the Bell states. The experimental protocol that we use is shown in fig. 5.10: it consists in preparing first the $|01\rangle$ or $|10\rangle$ register state and then subjecting it to a$\sqrt{i\mathrm{SWAP}}$ gate; according to eq. 5.2, such a gate is obtained by first bringing the qubit I in resonance with the qubit II during 1/4 of a swap period, i.e. 30 ns, and then canceling the first operator of eq. 5.2 using opposite

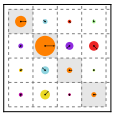

z rotations. The amplitude of this z pulse is determined by performing quantum state tomography on the final state, comparing the realized phase to the desired one and adjusting the height of the pulse accordingly. This protocol yields one of the two Bell states

$$|\Psi_+\rangle = \frac{1}{\sqrt{2}}\left(|01\rangle + |10\rangle\right), \tag{5.12}$$

$$|\Psi_-\rangle = \frac{1}{\sqrt{2}}\left(|01\rangle - |10\rangle\right). \tag{5.13}$$

To create the two other Bell states, we apply in addition a Y_π pulse to qubit I or II at the end of the sequence to transform states $|\Psi_+\rangle$ and $|\Psi_-\rangle$ into

$$|\Phi_+\rangle = \frac{1}{\sqrt{2}}\left(|00\rangle + |11\rangle\right), \tag{5.14}$$

$$|\Phi_-\rangle = \frac{1}{\sqrt{2}}\left(|00\rangle - |11\rangle\right), \tag{5.15}$$

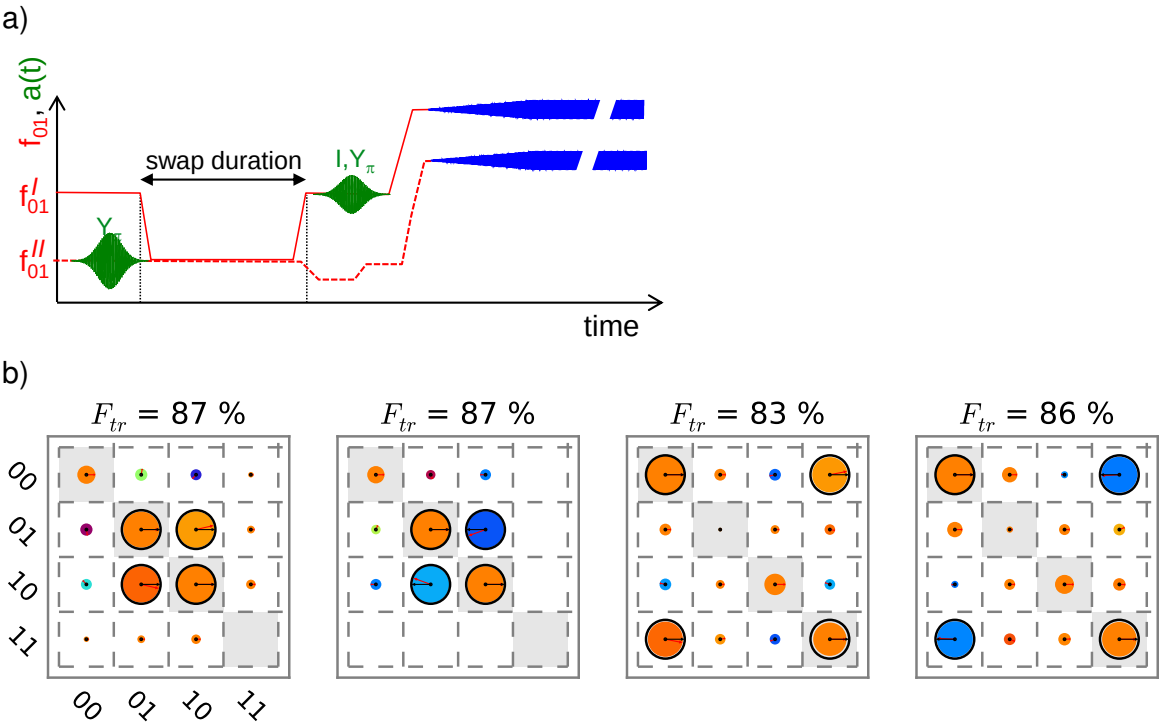

Figure 5.10: Generation and characterization of the four Bell states. a) Example of pulse sequence used to prepare $|\Psi_+\rangle$ or $|\Phi_+\rangle$ (see text). b) Measured density matrices of the targeted states $|\Psi_+\rangle$, $|\Psi_-\rangle$, $|\Phi_+\rangle$, and $|\Phi_-\rangle$ (left to right). Each measured matrix element a is represented by a colored disk with area proportional to$|a|$ and an arrow that represents the phase $arg(a)$. The ideal targeted states are represented by empty disks and black arrows. The fidelity F_{tr} with the ideal states is also indicated.

respectively. Finally, we also perform a quantum state tomography on the final states. Figure 5.10 shows the reconstructed density matrices ρ as well as the trace fidelity $F_{tr} = \langle\psi|\,\rho\,|\psi\rangle$ between them and the corresponding ideal states $|\psi\rangle$. This fidelity ranges between 83% and 87%.

5.4.6 Violation of the Bell Inequality

Another way to illustrate our ability to generate entangled states is to perform a so called *Bell test* [44, 9] on our two-qubit system.

We follow the experimental procedure proposed by Clauser *et. al.* [29, 49, 4] and prepare an entangled two-qubit state of the form

$$|\phi\rangle = \frac{1}{\sqrt{2}}\left(|01\rangle + e^{-i\phi}\,|10\rangle\right). \tag{5.16}$$

Then the expectation value of the operator

$$\mathrm{CHSH} = \mathrm{XX}_\varphi + \mathrm{XY}_\varphi + \mathrm{YY}_\varphi - \mathrm{YX}_\varphi \tag{5.17}$$

is measured, where the individual operators are given as

$$\begin{array}{rclcrcl} \mathrm{X} &=& \hat{\sigma}_x^I & & \mathrm{X}_\varphi &=& \hat{\sigma}_x^{II}\cdot\cos\varphi + \hat{\sigma}_y^{II}\cdot\sin\varphi, \\ \mathrm{Y} &=& \hat{\sigma}_y^I & & \mathrm{Y}_\varphi &=& \hat{\sigma}_y^{II}\cdot\cos\varphi - \hat{\sigma}_x^{II}\cdot\sin\varphi, \end{array} \tag{5.18}$$

with φ the angle of rotation of the measurement basis of qubit II with respect to that of qubit I. For a non-entangled state, $|\,\langle\mathrm{CHSH}\rangle\,|$ is bound by 2, whereas for an entangled state, its maximum value is $2\sqrt{2}$.

The pulse sequence used for this experiment is slightly different from the previous ones: qubit II is excited in state $|1\rangle$ with a π pulse and qubit I is brought to resonance with it for 1/4th of the swap period; then, single-qubit rotations are applied to align the qubit state with the measurement axis and $\hat{\sigma}_z^I\cdot\hat{\sigma}_z^{II}$ is measured. $\langle\mathrm{CHSH}\rangle$ is finally obtained by repeating this procedure on an ensemble of up to N=1000,000 identically prepared input states $|\phi\rangle$, for the four individual operators in the CHSH equation. Figure 5.11 shows the protocol used as well as the results obtained. As can be seen, the expectation value $\langle\mathrm{CHSH}\rangle$ varies sinusoidally as a function of the rotation angle φ. The maximum value of $\langle\mathrm{CHSH}\rangle$ reaches ≈ 1.40 and ≈ 2.52, for uncorrected and corrected readout outcomes, respectively. Thus, uncorrected data fail to violate the non-classical boundary whereas corrected data does exceed the boundary by about 22 standard deviations. In other words, a violation of the CHSH Bell inequality is observed in our two-qubit processor although the detector efficiency loophole cannot be closed, unlike at other experiments performed with phase qubits [3]. In addition, due to the measurement time required

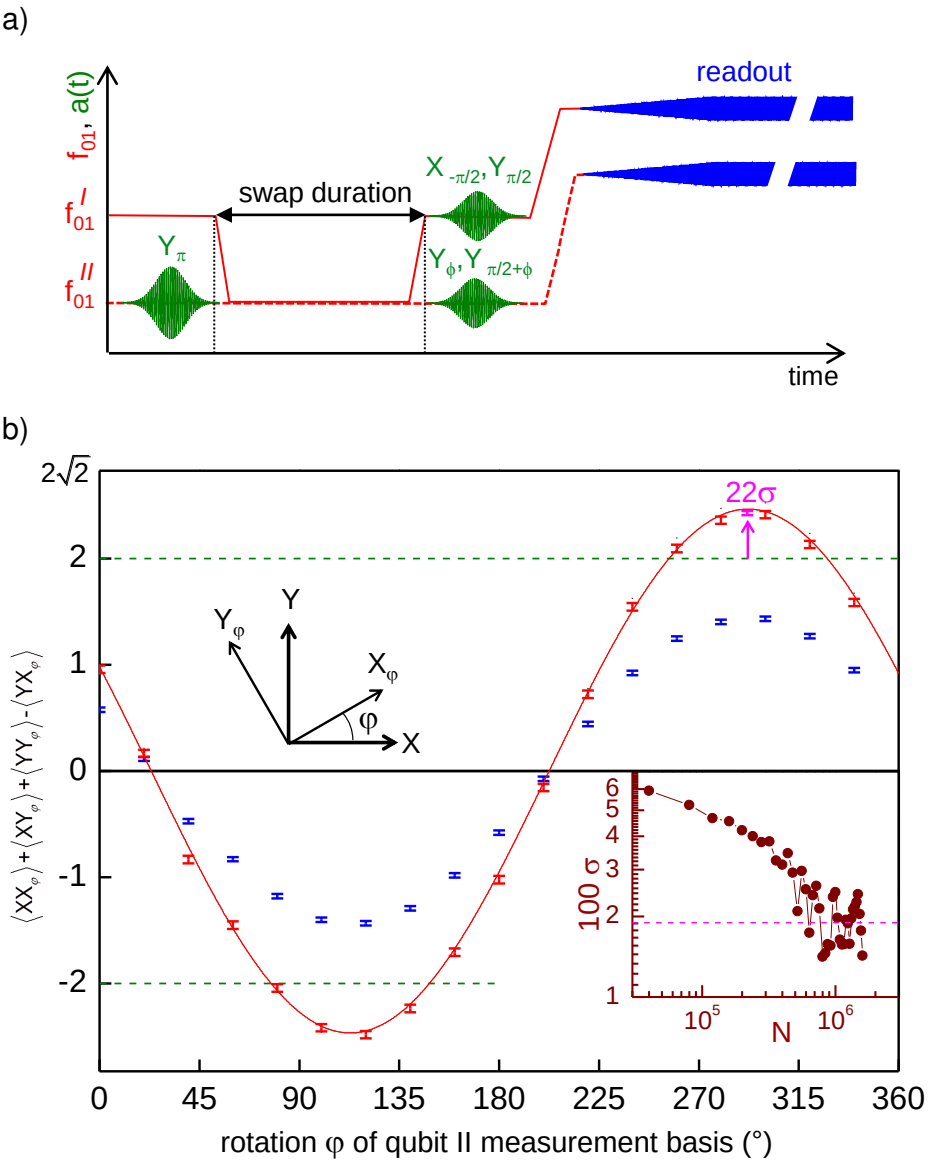

Figure 5.11: CHSH Bell test experiment. a) Experimental pulse sequence used (see text). b) Expectation value $\langle \mathrm{CHSH} \rangle$ of the CHSH operator measured for an ensemble of identically prepared Bell states $1/\sqrt{2}(|01\rangle + e^{-i\phi}|10\rangle)$, as a function of the rotation angle φ of the qubit II measurement basis. Blue and red markers correspond to measured data uncorrected and corrected for readout errors, respectively. The solid line is the best fit of the theory. The inset shows the standard deviation σ of the maximum value of the $\langle \mathrm{CHSH} \rangle$ as a function of the sample size N. For large N, σ is limited by a temperature induced experimental drift of the equipment (see text).

to determine the state of each qubit and the close proximity of the two qubits, we are obviously not able to close the communication or locality loophole either. However, when accepting the general validity of quantum mechanics, the violation of the Bell inequality in our processor can still serve as an entanglement witness and can be regarded as a benchmark for entanglement generation.

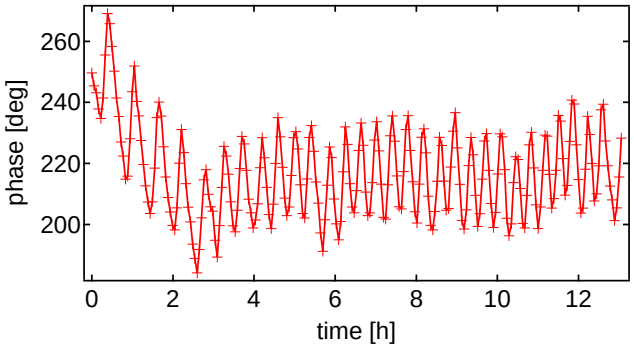

Figure 5.12: Measured phase ϕ of an experimentally prepared Bell state as a function of time, over a full night. The phase exhibits an "oscillatory" drift of the order of $40°$ being caused by temperature fluctuations.

Errors in the Bell test

Besides obvious readout errors that can be corrected, the main source of errors in our Bell experiment is a temperature induced drift of the measuring equipment. Most importantly, the phase of the arbitrary waveform generator (AWG) that generates the sideband pulses for driving the qubits, drifts with respect to the phase of the microwave sources, thereby changing the phase ϕ of the prepared Bell state $|\phi\rangle$ and the relative angle φ between the measurement bases of the two qubits. Figure 5.12 demonstrates this effect by showing the evolution of the phase ϕ extracted from subsequent CHSH data set as those of fig. 5.11, over a full night, and with the air conditioning system of the laboratory on: Oscillations of $\approx 40°$, correlated with the fan activity, are observed. They correspond to a time shift of the AWG of the order of 200 ps, which has indeed been observed independently using a fast oscilloscope. Note that data of fig. 5.11 had to be taken at a minimum of the temperature oscillation.

5.5 Realization and Characterization of the $\sqrt{i\mathrm{SWAP}}$ Gate

The implementation of the $\sqrt{i\mathrm{SWAP}}$ gate has already been explained in section 5.4.5 and is recalled on fig. 5.13: Qubit I is brought in resonance with qubit II during a time $t_{\sqrt{i\mathrm{SWAP}}} = 1/8g$, which, for our experimental value of $2g_{qq}/2\pi = 8.3$ MHz corresponds to $t_{\sqrt{i\mathrm{SWAP}}} \approx 30$ ns; then single-qubit Z rotations are applied to both qubits to compensate the dynamical phases θ_I and θ_{II} acquired during the swapping, as given by the first part of the operator (5.2). Again, the angles of these Z rotations are pre-calibrated by

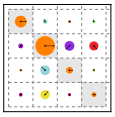

applying the gate to the input state $(|00\rangle + |01\rangle)/\sqrt{2}$, comparing the phases of the output state to the desired ones and changing the Z pulse amplitudes accordingly. The goal is now to quantify the fidelity of our gate and to analyze the error sources limiting this fidelity. This analysis is more demanding than simply demonstrating a violation of a Bell inequality, or than measuring by quantum state tomography particular entangled states with a high fidelity. The goal is now to demonstrate that the targeted evolution operator is implemented with a high fidelity whatever the chosen input state for the register. In this section, we explain the so-called quantum process tomography method used to reach that goal. In order to characterize the gate itself and not the protocol used to characterize it, we are led to model the drive errors and to measure them in a pre-calibration experiment. This allows us to remove the preparation and tomography errors from the gate characterization and to obtain an intrinsic $\sqrt{i\mathrm{SWAP}}$ gate fidelity (contrary to the state fidelities reported above that contained also tomographic errors).

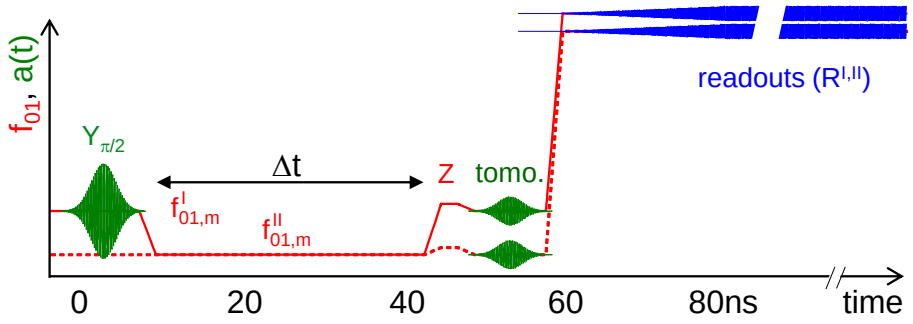

Figure 5.13: Experimental pulse sequence used for implementing the two-qubit $\sqrt{i\mathrm{SWAP}}$ gate. The sequence shown for an exemplary input state $|10\rangle$ consists in exciting the first qubit to the state $|1\rangle$, bringing the qubits in resonance for a time $t = 1/8g$, separating them and compensating the acquired dynamical phases by using two single-qubit Z-pulses. Finally, optional tomographic pulses are applied before reading out the qubit state at the optimal readout frequencies of the qubits.

5.5.1 Principle of Quantum Process Tomography

Quantum process tomography [97] is an ensemble of methods allowing one to fully characterize any experimental quantum process. The particular approach that we use and present below is called *standard quantum process tomography* (SQPT), but there exist other methods such as ancilla-assisted quantum process tomography [43, 33, 2] that we will not discuss.

Theoretical Description of a Quantum Process

As explained in section 2.5, any quantum process on an n-qubit system can be described by a set of at most $N = 4^n$ Kraus operators, as given by eq. (2.119):

$$\mathcal{E}(\rho) = \sum_i^N E_i \rho E_i^\dagger. \tag{5.19}$$

Now, if we express these operators E_i in a fixed operator basis $\tilde{E}_j$ such that $E_i = \sum_j^N a_{ij}\tilde{E}_j$, we can rewrite eq. (5.19) as

$$\begin{aligned}
\mathcal{E}(\rho) &= \sum_i^N \sum_j^N a_{ij}\tilde{E}_j\ \rho\ \sum_k^N a_{ik}^*\tilde{E}_k^\dagger && (5.20)\\
&= \sum_{j,k}^N \tilde{E}_j\ \rho\ \tilde{E}_k^\dagger \sum_i^N a_{ij}a_{ik}^* && (5.21)\\
&= \sum_{j,k}^N \tilde{E}_j\ \rho\ \tilde{E}_k^\dagger\ \chi_{jk}, && (5.22)
\end{aligned}$$

where we defined $\chi_{jk} = \sum_i a_{ij}a_{ik}^*$. Equation (5.22) is the χ-matrix representation of the quantum process in the basis $\{\tilde{E}_j\}$, which contains all the information about the process.

Implementation of Standard Quantum Process Tomography

The goal of SQPT is to obtain the N^2 independent real coefficients of the χ-matrix – or any other complete parametrization of the process – from a set of N experimentally measured output matrices $\{\mathcal{E}(\rho_i)\}$, given a set of N known and independent input matrices $\{\rho_i\}$. Note that measuring also the N input matrices might be required to know them with a sufficient accuracy, in particular when errors occur in their preparation. More precisely, one implements SQPT for a n-qubit system by using the following procedure:

1. Choose a set of N operators $\tilde{E}_j$ that forms a full basis for the operators acting on the n-qubit Hilbert space. One usually chooses $\tilde{E}_{j_1,j_2\ldots j_n} = \hat{\sigma}_{j_1} \otimes \hat{\sigma}_{j_2} \ldots \otimes \hat{\sigma}_{j_n}$, where $\hat{\sigma}_j$ are the single-qubit Pauli operators, i.e. $j \in \{I, X, Y, Z\}$.

2. Choose N pure quantum states $|\phi_i\rangle$ such that the basis $\{|\phi_1\rangle\langle\phi_1|, |\phi_1\rangle\langle\phi_2| \ldots, |\phi_N\rangle\langle\phi_{N-1}|, |\phi_N\rangle\langle\phi_N|\}$ spans the whole Hilbert space of input density matrices ρ. One usually chooses $|\phi\rangle \in \{|0\rangle, |1\rangle, (|0\rangle + |1\rangle)/\sqrt{2}, (|0\rangle + i|1\rangle)/\sqrt{2}\}^{\otimes n}$, where $^{\otimes n}$ denotes the n-dimensional Kronecker product of all possible permutations.

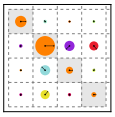

3. Prepare each of the chosen input states $\rho_i = |\phi_i\rangle \langle\phi_i|$, apply the gate operation, and determine the output states $\mathcal{E}(|\phi_i\rangle \langle\phi_i|)$ by quantum state tomography. Optionally, perform quantum state tomography of the prepared state ρ_i as well to determine experimental preparation and tomography errors.

4. After having determined the ρ_i and $\mathcal{E}(\rho_i)$, write $\mathcal{E}(\rho_i) = \sum_j \lambda_{ij}\tilde{\rho}_j$ in a complete basis $\{\tilde{\rho}_1, \ldots, \tilde{\rho}_{2^n}\}$ for the 2^nx2^n matrices. Usually one chooses $\tilde{\rho}_j$ matrices with only one element equal to one and all the others equal to zero. Calculate the $N^{\otimes 4}$ tensor β_{jk}^{mn} defined by $\tilde{E}_m\tilde{\rho}_j\tilde{E}_n^\dagger = \sum_k \beta_{jk}^{mn}\tilde{\rho}_k$, and insert this definition into eq. (5.22) to obtain

$$\sum_k \lambda_{ik}\tilde{\rho}_k \quad = \quad \sum_{m,n} \chi_{mn} \sum_k \beta_{ik}^{mn}\tilde{\rho}_k. \tag{5.23}$$

   Equating the two sides yields $\lambda_{ik} = \sum_{m,n} \beta_{ik}^{mn} \ \chi_{mn}$, which, by linear inversion, gives χ.

Similar to quantum state tomography, experimental errors occurring during quantum process tomography can produce a process matrix χ that is *non-physical* in the sense that the resulting quantum process does not obey the three axioms stated in section 2.5. Therefore, we render the obtained χ matrix physical by numerically searching the physical process matrix χ_{ph} that has the smallest distance $d = \|\chi - \chi_{ph}\|$ to the original one, using e.g. the Hilbert-Schmidt distance $\|A - B\| = \mathrm{Tr}(|A - B|)^2$.

Kraus Representation of the Process

To go back from the χ-matrix representation of the quantum process to the Kraus form given by eq. (2.119), one writes each process-independent operator $\tilde{E}_i$ as a sum of all the Kraus operators E_l, such that

$$\tilde{E}_i = \sum_l a_{il} \ E_l. \tag{5.24}$$

Inserting eq. (5.24) into eq. (5.22), we obtain

$$\mathcal{E}(\rho) \quad = \quad \sum_{j,k} \chi_{jk} \sum_{l,m} a_{jl}a_{km}^* E_l\rho E_m^\dagger \tag{5.25}$$

$$\quad = \quad \sum_i E_i\rho E_i^\dagger. \tag{5.26}$$

One finds hence the condition $\sum_{j,k} \chi_{jk}a_{jl}a_{km}^* = \delta_l^m$, or, written in matrix form $A\chi A^\dagger = \mathrm{I}$, which is fulfilled if A is the matrix of eigenvectors of χ, multiplied by the square root of

the corresponding diagonal matrix of eigenvalues. It is thus easy to obtain the Kraus representation of the quantum process by diagonalizing the Hermitian matrix χ.

The Kraus operator form of the quantum process can be useful since it shows in a simple way the different operators acting on the density matrix ρ. By ordering them as a function of their corresponding eigenvalues, one obtains the different unitary and non-unitary processes acting together on the density matrix ρ, ordered by importance.

5.5.2 Modeling and Determination of Tomography Errors

As already briefly mentioned, quantum process tomography (resp. quantum state tomography) used for characterizing a two-qubit gate (resp. state) requires additional manipulation steps that adds errors which should not be taken as gate errors (resp. state errors). In our experiment, the systematic single-qubit pulse errors impact both the prepared input states for process tomography, and the tomographic pulses themselves. In the first case, it is not a problem because the input states can also be measured and their discrepancy with respect to the targeted input states does not impact the process description. On the contrary, tomographic errors are a problem and should be removed from the gate description. Consequently, we pre-determine our pulse errors in the following way: We choose a model for the errors, which we discuss in the following two sections, and fit it to a large set of measured data, as presented afterwards.

Leakage Out of the Computational Hilbert-Space

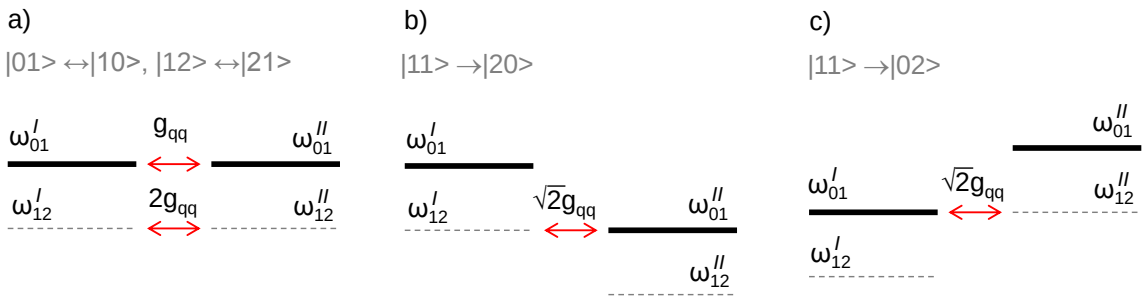

Figure 5.14: Energy level diagram illustrating the possible swapping interactions of two three-level Transmon qubits. Resonant transitions are a) the $|01\rangle \leftrightarrow |10\rangle$ and $|12\rangle \leftrightarrow |21\rangle$ transitions at $\omega_{01}^{I} = \omega_{01}^{II}$ (with swapping frequencies g_{qq} and $2g_{qq}$, respectively), b) the $|11\rangle \leftrightarrow |20\rangle$ transition at $\omega_{12}^{I} = \omega_{01}^{II}$ and c) the $|11\rangle \leftrightarrow |02\rangle$ transition at $\omega_{01}^{I} = \omega_{12}^{II}$ (both with a swapping frequency $\sqrt{2}g_{qq}$).

An error source that we estimate here is the leakage to the higher Transmon level $|2\rangle$, as discussed in section 3.2.2. This error can occur while driving the qubits or due to the swapping interaction between the $|11\rangle \leftrightarrow |20\rangle$ and $|11\rangle \leftrightarrow |02\rangle$ states of the three-level two-qubit Hamiltonian given by eq. (A.1), as illustrated in fig. 5.14. To quantify

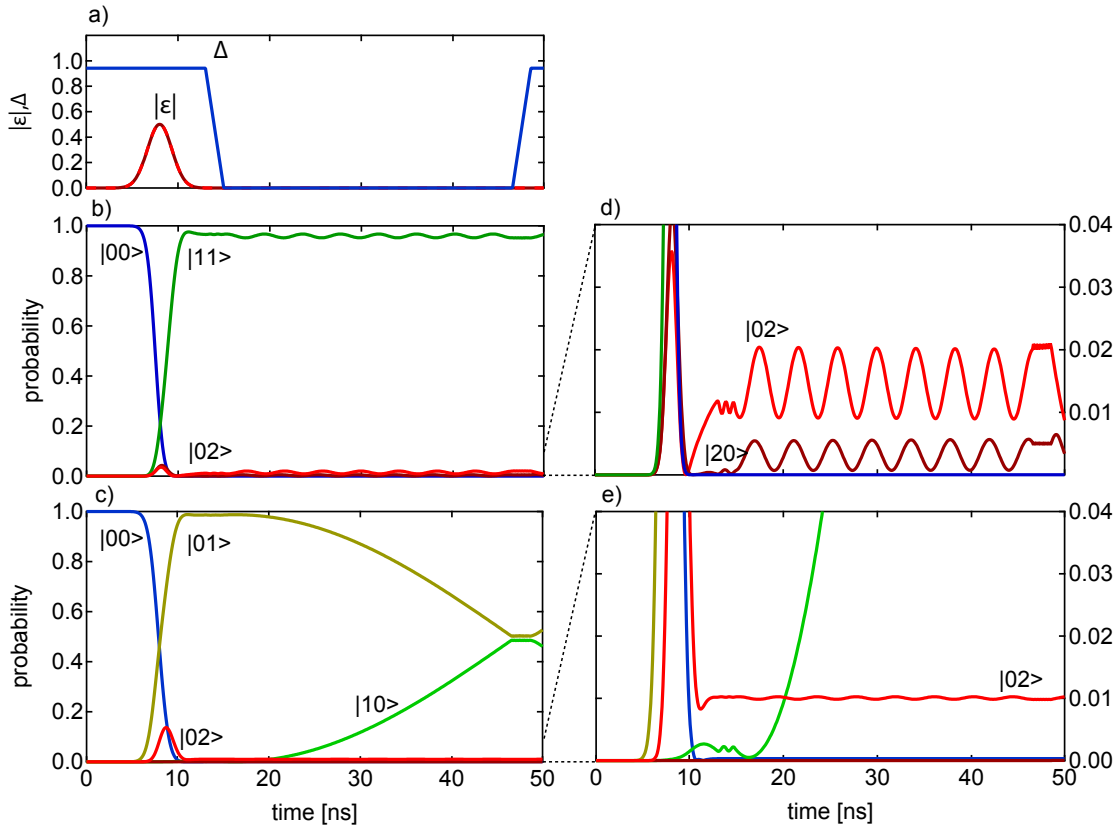

Figure 5.15: a1) Drive and flux waveforms for a simulated $\sqrt{i\mathrm{SWAP}}$ gate between two three-level Transmons. a2/a3) State occupation probabilities during the simulation for the input states $|01\rangle$ (a2) and $|11\rangle$ (a3). b1/b2) show a zoom-in on the two figures a2/a3). In both cases, a small excitation of the higher Transmon level $|2\rangle$ can be observed in the simulation. For the $|11\rangle$ input state, an oscillation between the states $|11\rangle$ and $|02\rangle/|20\rangle$ can be observed, which is an unwanted effect.

this leakage, we perform a simulation of our $\sqrt{i\mathrm{SWAP}}$ gate between two three-level Transmons, using the measured qubit parameters. We don't include decoherence that tends to lower the leakage and instead use the same Hamiltonian as in section A.1. Just as in our experiment, we generate the 16 different input states listed above using simulated Gaussian drive pulses with a rise time of $\delta t = 4$ ns while the qubits are detuned by $\Delta_{qq}/2\pi = 150$ MHz. We then reduce the detuning to $\Delta_{qq} = 0$ during $t_{\mathrm{SWAP}} \approx 31$ ns using a simulated flux pulse with a 2 ns rise time, as shown in fig. 5.15. We compute numerically the fidelity of the output state with an output state obtained from the ideal $\sqrt{i\mathrm{SWAP}}$ operation applied to the simulated input state. By examining the output density matrices we can then give an upper bound for the leakage error into the state $|2\rangle$, which in our case is $\approx 1.5\ \%$. Figure 5.15 exemplarily shows the simulated state occupation probabilities for the two input states $|01\rangle$ and $|11\rangle$. In both cases, a small excitation of the $|02\rangle$ and $|20\rangle$ Transmon states can be observed at the end of the sequence. The $|11\rangle$ input state, which should not be affected by the SWAP operation,

shows a small oscillation due to the coupling to the $|02\rangle$ state.

Since the obtained overall error is small, we neglect the leakage to state $|2\rangle$ in the error model that we present now. Please note that the results of this simulation should be regarded as a rough estimate since the inclusion of higher Transmon levels would certainly alter the obtained error boundaries.

Modeling and Determining Pulse Errors

The error model we use includes errors both in the preparation of the states (index prep) and in the tomographic pulses (index tomo). The errors included are angular errors $\varepsilon_{\mathrm{I,II}}^{\mathrm{prep}}$ on the nominal π rotations around $X_{\mathrm{I,II}}$, $\eta_{\mathrm{I,II}}^{\mathrm{prep,tomo}}$and $\delta_{\mathrm{I,II}}^{\mathrm{prep,tomo}}$ on the nominal $\pi/2$ rotations around $X_{\mathrm{I,II}}$ and $Y_{\mathrm{I,II}}$, a possible departure $\xi_{\mathrm{I,II}}$ from orthogonality of $\left(\overrightarrow{X_{\mathrm{I}}}, \overrightarrow{Y_{\mathrm{I}}}\right)$ and $\left(\overrightarrow{X_{\mathrm{II}}}, \overrightarrow{Y_{\mathrm{II}}}\right)$, and a possible rotation $\mu_{\mathrm{I,II}}$ of the tomographic XY frame with respect to the preparation one. The rotation operators used for preparing the states and doing their tomography are thus given by

$$
\begin{aligned}
X_{\mathrm{I,II}}^{\mathrm{prep}}(\pi) &= e^{-\mathrm{i}\left(\pi+\varepsilon_{\mathrm{I,II}}^{\mathrm{prep}}\right)\hat{\sigma}_{\mathrm{x}}^{\mathrm{I,II}}/2},\\
X_{\mathrm{I,II}}^{\mathrm{prep}}(-\pi/2) &= e^{+\mathrm{i}\left(\pi/2+\eta_{\mathrm{I,II}}^{\mathrm{prep}}\right)\hat{\sigma}_{\mathrm{x}}^{\mathrm{I,II}}/2},\\
Y_{\mathrm{I,II}}^{\mathrm{prep}}(\pi/2) &= e^{-\mathrm{i}\left(\pi/2+\delta_{\mathrm{I,II}}^{\mathrm{prep}}\right)\left[\cos\left(\xi_{\mathrm{I,II}}\right)\hat{\sigma}_{\mathrm{y}}^{\mathrm{I,II}}-\sin\left(\xi_{\mathrm{I,II}}\right)\hat{\sigma}_{\mathrm{x}}^{\mathrm{I,II}}\right]/2},\\
X_{\mathrm{I,II}}^{\mathrm{tomo}}(\pi/2) &= e^{-\mathrm{i}\left(\pi/2+\eta_{\mathrm{I,II}}^{\mathrm{tomo}}\right)\left[\sin\left(\mu_{\mathrm{I,II}}\right)\hat{\sigma}_{\mathrm{x}}^{\mathrm{I,II}}+\cos\left(\mu_{\mathrm{I,II}}\right)\hat{\sigma}_{\mathrm{y}}^{\mathrm{I,II}}\right]/2},\\
Y_{\mathrm{I,II}}^{\mathrm{tomo}}(-\pi/2) &= e^{+\mathrm{i}\left(\pi/2+\delta_{\mathrm{I,II}}^{\mathrm{tomo}}\right)\left[\cos\left(\mu_{\mathrm{I,II}}+\xi_{\mathrm{I,II}}\right)\hat{\sigma}_{\mathrm{y}}^{\mathrm{I,II}}-\sin\left(\mu_{\mathrm{I,II}}+\xi_{\mathrm{I,II}}\right)\hat{\sigma}_{x}^{\mathrm{I,II}}\right]/2}.
\end{aligned}
$$

We determine these error parameters by fitting the model to a large set of measured data. A natural choice is to use the sixteen input states that we use for the quantum process tomography. These input states are given as $\{\rho_{\mathrm{in}}^{\mathrm{e}} = U\,|0\rangle\,\langle 0|\,U^{\dagger}\}$ with

$$
\{U\} = \{I_{\mathrm{I}}, X_{\mathrm{I}}^{\mathrm{prep}}(\pi), Y_{\mathrm{I}}^{\mathrm{prep}}(\pi/2), X_{\mathrm{I}}^{\mathrm{prep}}(-\pi/2)\}\otimes\{I_{\mathrm{II}}, X_{\mathrm{II}}^{\mathrm{prep}}(\pi), Y_{\mathrm{II}}^{\mathrm{prep}}(\pi/2), X_{\mathrm{II}}^{\mathrm{prep}}(-\pi/2)\}, \tag{5.27}
$$

and each input state yields a Pauli set $\{\langle P_{\mathrm{k}}^{\mathrm{e}}\rangle = Tr\left(\rho_{\mathrm{in}}^{\mathrm{e}}P_{\mathrm{k}}^{\mathrm{e}}\right)\}$ with $\{P_{\mathrm{k}}^{\mathrm{e}}\} = \{I_{\mathrm{I}}, X_{\mathrm{I}}^{\mathrm{e}}, Y_{\mathrm{I}}^{\mathrm{e}}, Z_{\mathrm{I}}\}\otimes$ $\{I_{\mathrm{II}}, X_{\mathrm{II}}^{\mathrm{e}}, Y_{\mathrm{II}}^{\mathrm{e}}, Z_{\mathrm{II}}\}$, $X^{\mathrm{e}} = Y^{\mathrm{tomo}}(-\pi/2)^{\dagger}\hat{\sigma}_{z}Y^{\mathrm{tomo}}(-\pi/2)$, and $Y^{\mathrm{e}} = X^{\mathrm{tomo}}(\pi/2)^{\dagger}\hat{\sigma}_{\mathrm{z}}X^{\mathrm{tomo}}(\pi/2)$.

Figure 5.16 shows the 16 measured Pauli sets as well as the best fit to the data, which yields $\varepsilon_{\mathrm{I}}^{\mathrm{prep}} = -1°$, $\varepsilon_{\mathrm{II}}^{\mathrm{prep}} = -3°$, $\eta_{\mathrm{I}}^{\mathrm{prep}} = 3°$, $\eta_{\mathrm{II}}^{\mathrm{prep}} = 4°$, $\delta_{\mathrm{I}}^{\mathrm{prep}} = -6°$, $\delta_{\mathrm{II}}^{\mathrm{prep}} = -3°$, $\eta_{\mathrm{I}}^{\mathrm{tomo}} = -6°$, $\eta_{\mathrm{II}}^{\mathrm{tomo}} = -4°$, $\lambda_{\mathrm{I}}^{\mathrm{tomo}} = 12°$, $\lambda_{\mathrm{II}}^{\mathrm{tomo}} = 5°$, $\xi_{\mathrm{I}} = 1°$, $\xi_{\mathrm{II}} = -2°$, and $\mu_{\mathrm{I}} = \mu_{\mathrm{II}} = -11°$.

5.5.3 Experimental Chi matrix and Gate Fidelity

We can now perform the standard process tomography of our two-qubit gate by following the procedure outlined in the previous sections: the 16 input and 16 output Pauli sets are measured by standard quantum state tomography. Knowing the tomographic errors

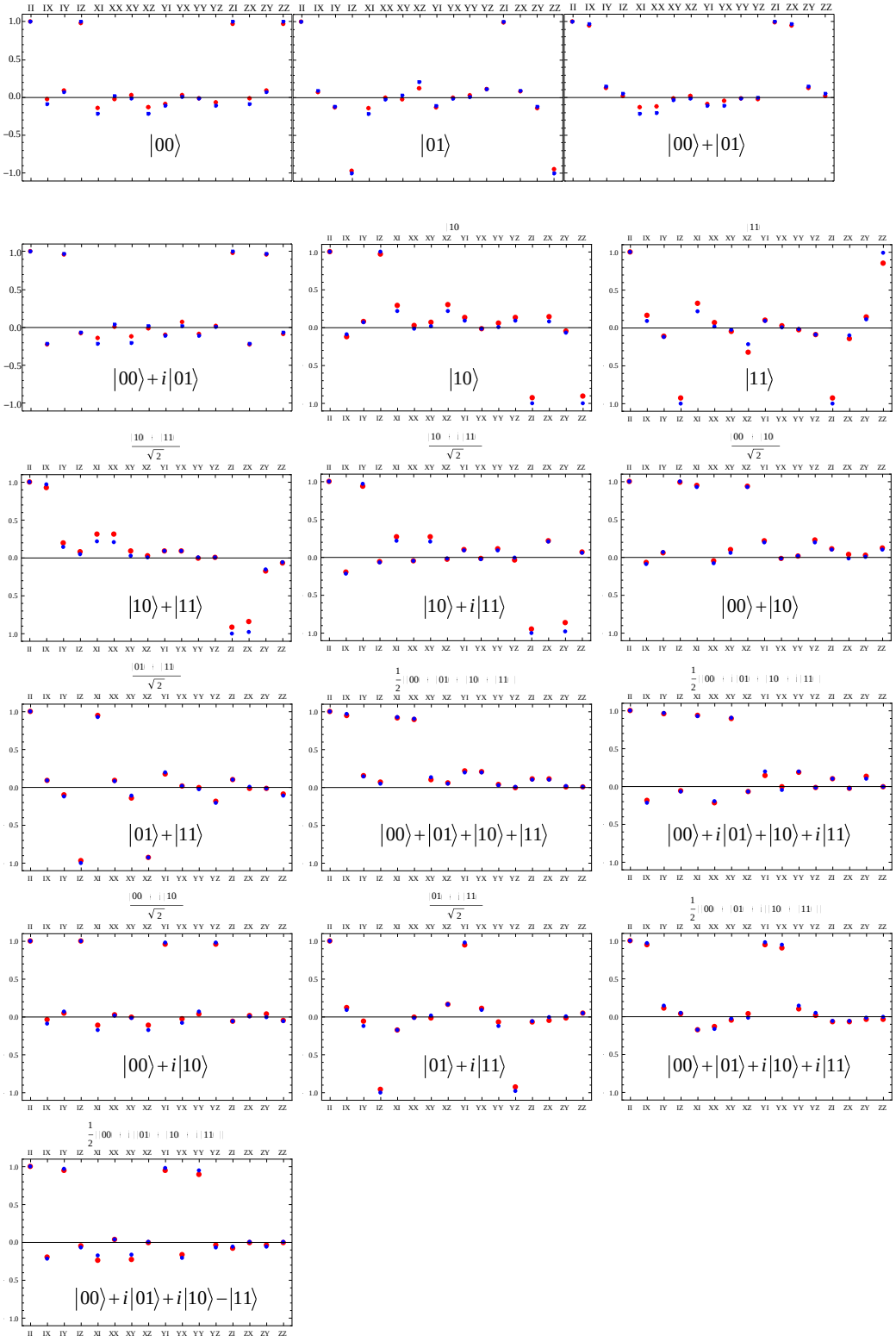

Figure 5.16: Fitting of the pulse errors at state preparation and tomography. Measured (red) and fitted (blue - see text) Pauli sets $\langle P_{\mathrm{k}}^{\mathrm{e}} \rangle$ for the sixteen targeted input states $\{|0\rangle, |1\rangle, |0\rangle + |1\rangle, |0\rangle + i\,|1\rangle\}^{\otimes 2}$. The $\{II, IX, IY, IZ, XI, ...\}$ operators indicated on the abscissa are the targeted operators and not those actually measured (due to tomographic errors).

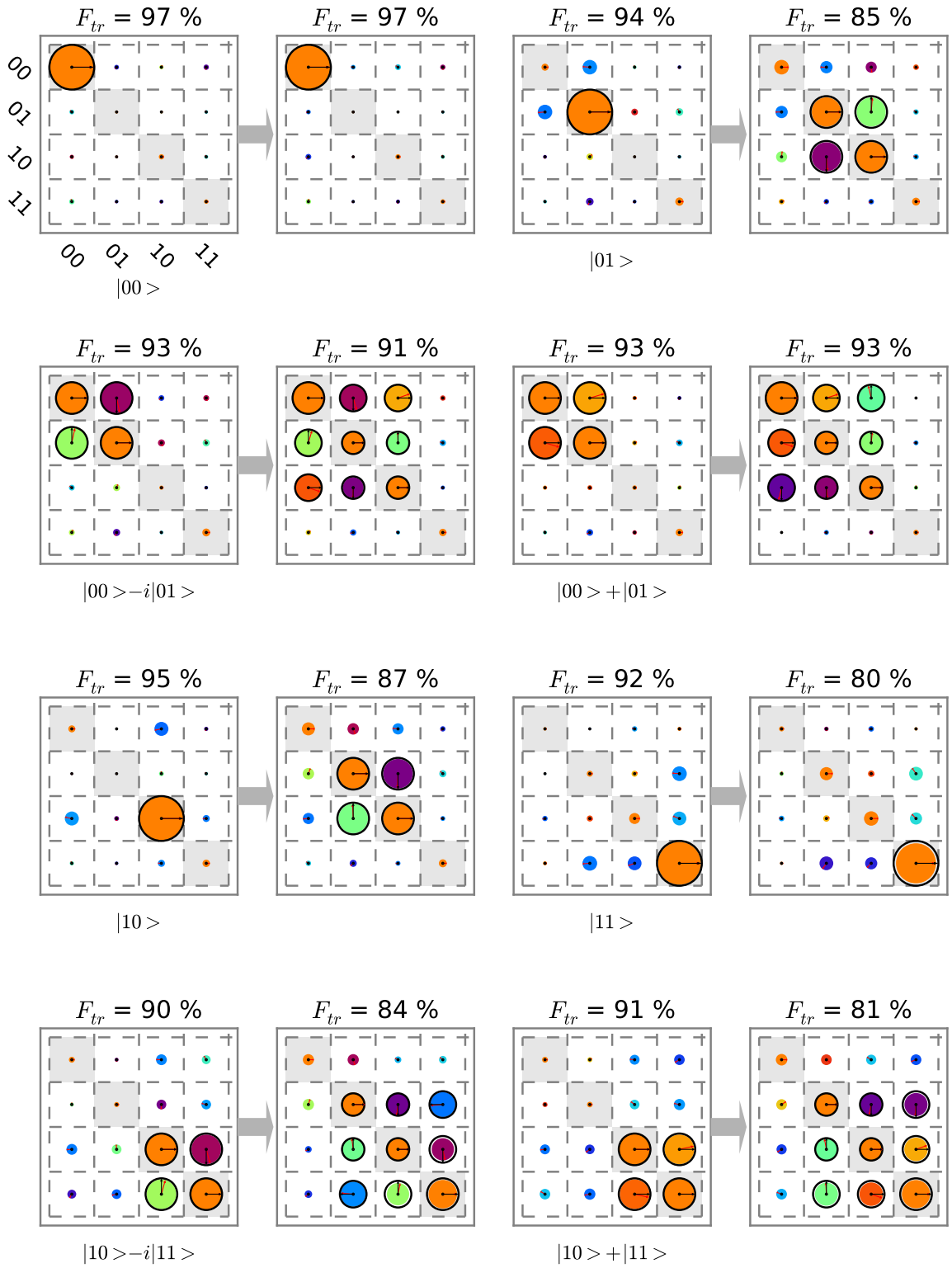

Figure 5.17: Experimental input and output density matrices used for quantum process tomography of our $\sqrt{i\mathrm{SWAP}}$ gate. Shown are the input/output pairs for the 16 different input states indicated below each matrix and the corresponding output matrices with their state fidelities. The corresponding ideal matrices are overlaid in black. (part I/II)

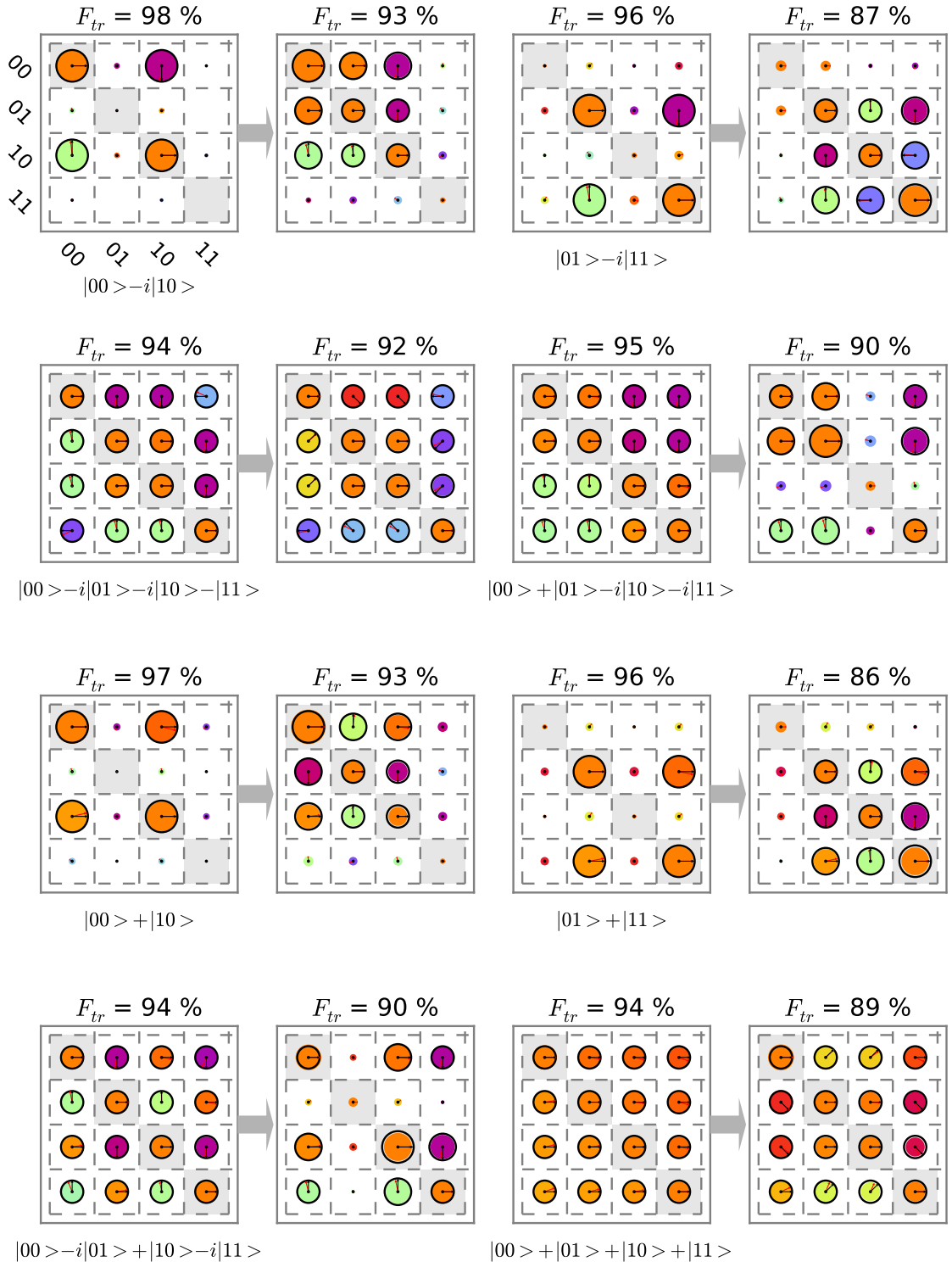
F_{tr} = 98 %
F_{tr} = 93 %
F_{tr} = 96 %
F_{tr} = 87 %
00
01
10
11
00 01 10 11
$|00>-i|10>$
$|01>-i|11>$
F_{tr} = 94 %
F_{tr} = 92 %
F_{tr} = 95 %
F_{tr} = 90 %
$|00>-i|01>-i|10>-|11>$
$|00>+|01>-i|10>-i|11>$
F_{tr} = 97 %
F_{tr} = 93 %
F_{tr} = 96 %
F_{tr} = 86 %
$|00>+|10>$
$|01>+|11>$
F_{tr} = 94 %
F_{tr} = 90 %
F_{tr} = 94 %
F_{tr} = 89 %
$|00>-i|01>+|10>-i|11>$
$|00>+|01>+|10>+|11>$

Figure 5.18

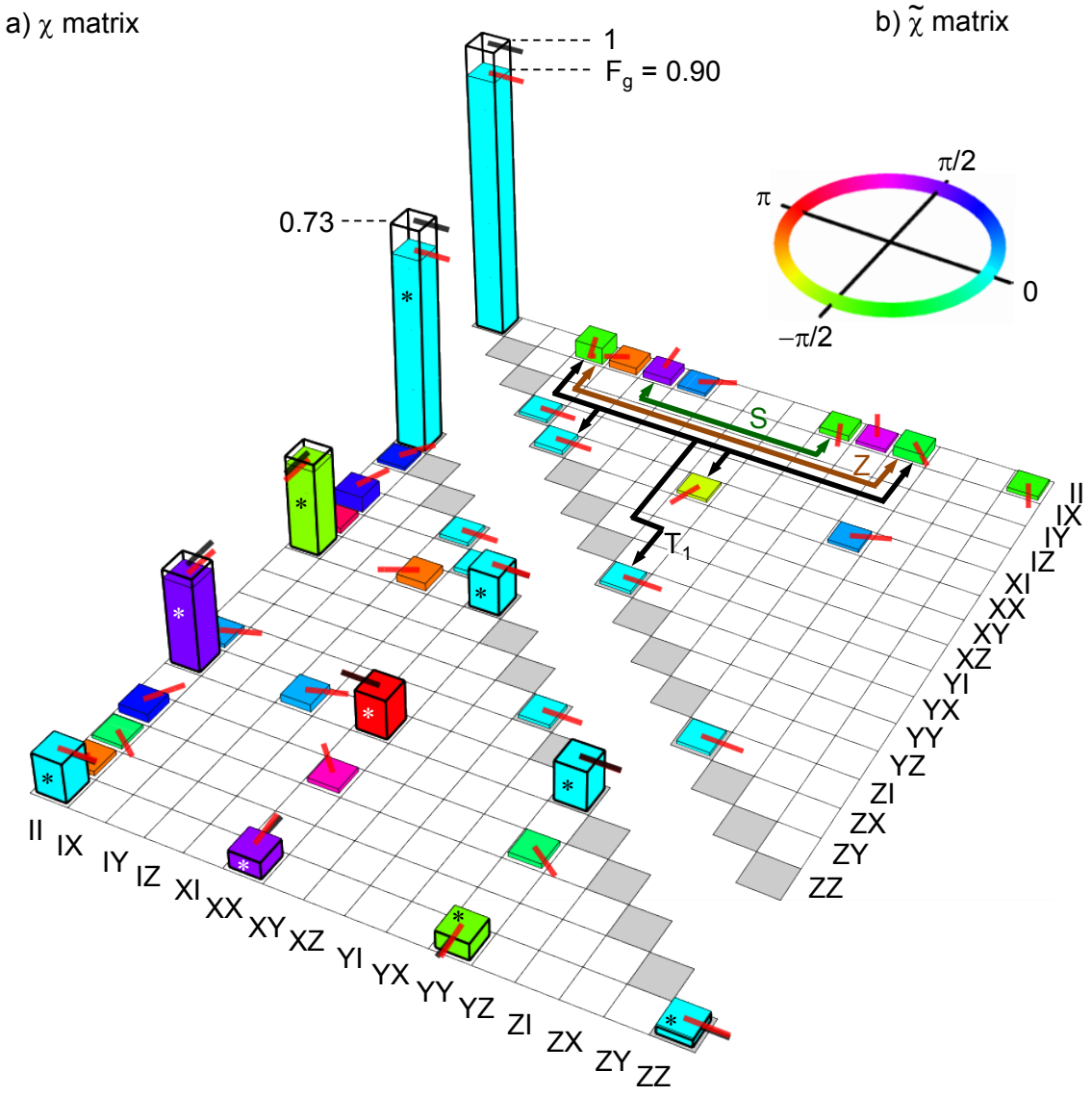

Figure 5.19: Reconstructed χ process matrix of our implementation of the $\sqrt{iSWAP}$ quantum gate. a) Superposition of the ideal (empty thick bars) and experimental (color filled bars) lower part of the Hermitian matrix χ (elements below 1% not shown). Each complex matrix element is represented by a bar with height proportional to its modulus and a red phase pointer at the top of the bar (as well as a filling color for experiment) giving its argument (top left inset). Expected peaks are marked by a star. b) Error process matrix $\tilde{\chi} = \chi \cdot \chi_{id}^{-1}$. The colored arrows grouping different elements of $\tilde{\chi}$ indicate unitary and non-unitary error processes to which the corresponding matrix elements can be associated.

and thus $\{\langle P_k^e \rangle\}$, we then invert the linear relation $\{\langle P_k^e \rangle = Tr\,(\rho P_k^e)\}$ to find the 16×16 matrix B that links the vector $\overrightarrow{\langle P_k^e \rangle}$ to the columnized density matrix $\overrightarrow{\rho}$, i.e. $\overrightarrow{\rho} = B.\overrightarrow{\langle P_k^e \rangle}$. The matrix B is finally applied to the measured 16 input and 16 output Pauli sets to find the 16 $(\rho_{in,}, \rho_{out})_k$ couples to be used for calculating the gate map. Figures 5.17 and 5.18 show the experimentally determined $(\rho_{in,}, \rho_{out})_k$ pairs, with a comparison to the ideal ones. The targeted input states are annotated below the corresponding ρ_{in}. The

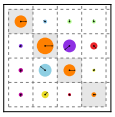

trace fidelity (2.8) between the experimental and ideal matrices is indicated above.

From these input/output matrices, we calculate the χ matrix of the quantum process by the method described above. This χ matrix is shown in fig. 5.19, together with matrix χ_{id} of an ideal $\sqrt{i\mathrm{SWAP}}$ process. The fidelity of the gate process is $F_g = \mathrm{Tr}(\chi\chi_{id}) = 0.90$.

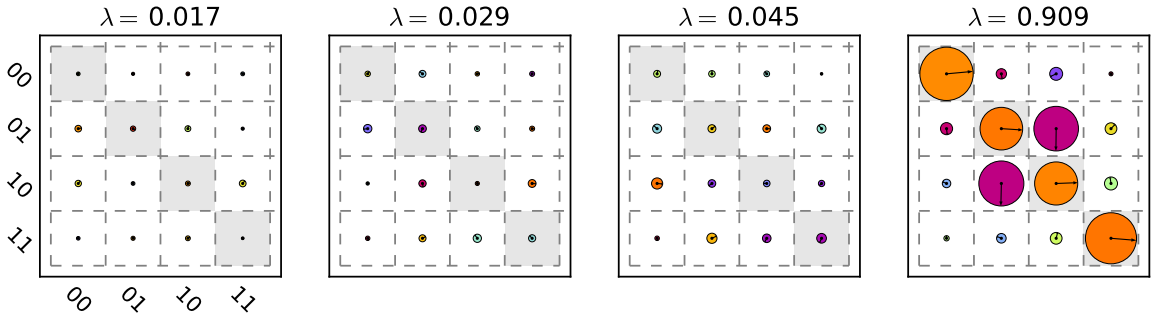

Figure 5.20: Experimental Kraus operators of the implemented $\sqrt{i\mathrm{SWAP}}$ gate, as obtained from the diagonalization of the χ_{exp} matrix in fig. 5.19. Shown are only the four operators with the largest eigenvalues, which together account for $> 99.9\%$ of the operator weights and therefore describe the process with very good accuracy.

From the experimental χ matrix, we then calculate the Kraus operators. In our case, the 4 largest eigenvalues λ_i of χ (for which $\sum_i \lambda_i = 1$) sum up to a value > 0.999 and therefore suffice to describe the process with high accuracy. The corresponding 4 Kraus operators with their eigenvalues are shown in fig. 5.20. As can be seen, the operator associated to the largest eigenvalue $\lambda = 0.909$ corresponds closely to the unitary $\sqrt{i\mathrm{SWAP}}$ operator. The other operators are largely non-unitary and describe the decoherence in the quantum process. Since the Kraus operators contain the same information on the quantum process as the χ-matrix, we can fit the observed operators to a decoherence model of the quantum process to obtain an estimate of the relaxation and dephasing rates. However, since we already performed the same operation above using the χ-matrix, we will not repeat it here.

5.5.4 Gate Error Analysis

To better visualize the discrepancy between the experimental and ideal χ matrices, the error process matrix $\tilde{\chi} = \chi \cdot \chi_{id}^{-1}$ is also shown in fig. 5.19. This matrix that would simply be the identity matrix if the gate was perfect, displays the errors in a rather cryptic way. To understand the origin of the errors, we finally fit to $\tilde{\chi}$ a master equation model of the quantum process, which involves a frequency offset when performing the swapping interaction, errors in the amplitude of the compensating Z pulses applied after the swap, as well as individual relaxation and dephasing super-operators. The relaxation and

dephasing rates employed in the simulation are the same as those discussed in section 5.4.2, whereas the unitary error parameters are fitted to maximize the fidelity between the simulated and measured $\tilde{\chi}$ matrices. Using this technique, we infer an error budget of the quantum process that quantifies the contributions of individual error sources.

We find a total gate error of 10%, where we can attribute 8% of the errors to relaxation and decoherence during the process and 2% to unitary gate errors. By plotting the different $\tilde{\chi}$ matrices that would correspond to each error source if it was alone, we see which matrix element is produced in the matrix. This allows us to localize the different error sources in the measured $\tilde{\chi}$, as shown by the arrows in fig. 5.19.

5.6 Conclusion

In this chapter we demonstrated that we can implement a universal set of quantum gates on our two-qubit processor. We created and characterized entangled two-qubit states, performed quantum state tomography, implemented the $\sqrt{i\mathrm{SWAP}}$ quantum gate with a fidelity of 90% and analyzed the most important error sources of the gate operation.

In the next chapter, we use the set of universal gates to run a simple quantum search algorithm on our two-qubit processor, showing that we are able to demonstrate quantum speed-up for a real-world problem, albeit at a scale which is not yet practically useful.

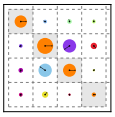

Chapter 6

Running the Grover Search Algorithm

This chapter describes an experimental implementation of the so-called *Grover search algorithm* with our two-qubit quantum processor. The first section provides a short introduction of the algorithm and motivates the interest in realizing it. The following sections then discuss the details of its experimental realization. We show the results that we obtained and compare the algorithm fidelity and efficiency to that of an equivalent, classical algorithm. Finally, we analyze all relevant unitary and non-unitary error sources relevant to our experiment and provide a quantitative error model of our implementation of the algorithm.

6.1 Introduction & Motivation

Search algorithms are of great importance in many domains of mathematics and computer science. One such search problem that often arises and which will be discussed in the following sections can be formulated in simple terms as follows:

Assume that we have a search space $\mathcal{S}$ that consists of a finite number N of states $s \in \mathcal{S}$. The solution to our search problem corresponds to a subset of M states of the search space $\mathcal{T} \subset \mathcal{S}$. We can then define a search function $\mathcal{C}(s) : \mathcal{S} \rightarrow \{0, 1\}$ that discriminates between states that solve the search problem and states that don't, such that $\mathcal{C}(s) = 1$ for $s \in \mathcal{T}$ and $\mathcal{C}(s) = 0$ otherwise. In accordance with the general convention in the literature on the Grover search algorithm, we will often refer to this search function as the *Oracle function* or (in a quantum-mechanical context) as the *Oracle operator*.

Using this definition of the search problem, the goal of a search algorithm is to find all states $t \in \mathcal{S}$ for which $\mathcal{C}(t) = 1$. In the following, for the sake of simplicity we assume that the solution set $\mathcal{T}$ contains only one single state t. This special case can be generalized to cases where more than one solution to the search problem exists (see e.g. [91, 84]

for a detailed review)

The first step in order to solve a search problem of the kind described above using classical or quantum computation is to map the problem to a form suitable for solution by a digital (quantum) computer. For this, we first number and encode the N input states $i \in \mathcal{S}$ in binary form as $i = (b_l^i, \ldots, b_0^i)_B$, where l is the length of the binary register able to hold all N input states. With this definition, it is then trivial to find a mathematical representation of $\mathcal{C}$ that operates on a binary input register.

Using these assumptions and definitions, it can be shown that the most efficient classical search algorithm for solving the search problem above will use $\mathcal{O}(N)$ calls of the function $\mathcal{C}$ to find the solution of the search problem. If assuming that calling $\mathcal{C}$ is much more "expensive" in time or resources than any other operation, $\mathcal{O}(N)$ will then also correspond to the overall computational efficiency of the algorithm.

Amazingly, in 1997, Lov Grover found a quantum algorithm that could solve this search problem with only $\mathcal{O}(\sqrt{N})$ calls to the function $\mathcal{C}$ [54]. His algorithm achieves this by repeatedly calling a quantum-mechanical implementation of the function $\mathcal{C}$, starting from a highly superposed qubit register $\sum_i^N |i\rangle$ and applying a special operator to the resulting output state afterwards. The individual steps of his algorithm are given as follows:

1. Initialize a qubit register to the state $|\psi\rangle = |0\rangle$ (corresponding to a binary input state $|0000\ldots0_B\rangle$)

2. Apply the generalized Hadamard operation to the qubit register, producing a fully superposed quantum state
$$|\psi\rangle = \frac{1}{\sqrt{N}} \sum_{i=0}^{N-1} |i\rangle$$

3. Repeat the following sequence $\mathcal{O}(\sqrt{N})$ times:

   a) Apply the *Oracle operator* $|i\rangle \rightarrow (-1)^{\mathcal{C}(i)} |i\rangle$.

   b) Apply the so-called *diffusion operator* $|i\rangle \rightarrow -|i\rangle + \frac{2}{N} \sum_{j=0}^{N-1} |j\rangle$.

4. Measure the state of the quantum register in the computational basis $|i\rangle$.

Note that for the description above we have enumerated the states of the qubit register from $|0\rangle$ to $|N-1\rangle$. The Grover algorithm makes use of quantum parallelism to solve the search problem $\mathcal{O}(\sqrt{N})$ times faster than the most efficient classical algorithm. To understand better the strategy it uses, the different steps of the algorithm can be rephrased in the following, more general way:

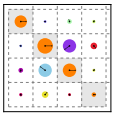

- First, the algorithm creates a fully superposed quantum state which contains all possible solutions to the search problem at once. The amplitudes and phases of each individual state are all equal in the beginning.

- Then, it applies the Oracle operator to this superposed state. The effect of the Oracle is to turn the phase of the state t for which $\mathcal{C}(t) = 1$ by an angle π. As will be shown later, such an Oracle operator can be implemented in a straightforward way for any classical search function.

- In the next step, it applies a diffusion operator to the quantum state which transfers a fraction of the amplitude from states with zero phase to the states with π phase, increasing thus the amplitude of the latter. In this process, the phases of all states get also turned back to zero, allowing the algorithm to repeat the sequence above.

- Repeating these two operations increases each time the amplitude of the states that correspond to a solution of the search problem until the amplitudes of all the other states vanish. After that point, the process reverses and the amplitude is transferred back to the original states. It is therefore crucial to stop the repetition sequence given above after the right number of iterations.

By implementing the search function as a quantum operator acting on a superposition, the Grover algorithm is able to somehow evaluate it in one single call for all possible input states. This so-called *quantum parallelism* provides the basis for the speed-up of the search in comparison to a classical algorithm. However, being able to encode the result of the search function in the phase of a multi-qubit state does not directly translate to a speed advantage since it is usually very hard to extract this phase information from the quantum state. Indeed, to extract the values of all phases from an N-qubit state, it would be necessary to perform $\mathcal{O}(2^N)$ measurements on an ensemble of such identically prepared quantum states. However, extracting the amplitudes from such a state takes only $\mathcal{O}(N)$ measurements, that in addition can usually be carried out in parallel. It is for this reason that the Grover algorithm uses an operator that transforms the information encoded in the phases of the qubits to an information encoded in their amplitude. However, since the conversion between phase to amplitude information through the application of an unitary operator is limited by certain physical constraints, the algorithm needs to repeat the encode-and-transfer sequence described above $\mathcal{O}(\sqrt{N})$ times. [73, 85, 68, 1, 40, 71, 19]

To analyze further the constraints and principles of the algorithm, we will discuss a more detailed derivation of it starting from the Schrödinger equation and we will also explain what limits the efficiency of the phase-to-amplitude conversion in the algorithm.

6.1.1 Deriving the Grover Algorithm from Schrödinger's Equation

An interesting derivation of the Grover algorithm starting from Schrödinger's equation has been detailed by Grover himself in a seminal paper [55] and shall be briefly rediscussed here since it sheds light on the basic principles on which the algorithm is based. The derivation begins by considering a quantum system governed by Schrödinger's equation, which can be written as (setting $\hbar = 1$ for better readability)

$$-i\frac{\partial}{\partial t}\psi(x,t) = \frac{\partial^2}{\partial x^2}\psi(x,t) - V(x)\psi(x,t) \tag{6.1}$$

Here $\psi(x,t)$ describes the wave-function and V is a time-independent potential. Let us assume that the potential $V(x)$ is shaped as in fig. 6.1, i.e. possessing a global minimum of energy. When one initializes the system to a state $\psi_0(x,t_0)$ and lets it evolve for a given time, $\psi(x,t)$ will be attracted by the minimum of potential energy and "fall into it" much like a classical particle in such a potential would[1]. We might thus ask if we can encode the solution to a search problem as a point of minimum energy x_0 of a potential $V(x)$, take an initial state $\psi_0(x,t_0)$ and let it evolve into a state that has a high probability around x_0, thereby solving the search problem. To answer this question, it is first necessary to discretize the wave function $\psi(x,t)$ such that it can represent the search problem stated in the last section, and which is defined over a finite number of states. In the most simple case, we can use a regular grid of points x_i with a spacing Δx for this, as shown in fig. 6.1b. Discretizing the time evolution of eq. 6.1 in steps Δt as well and defining $\epsilon = \Delta t/\Delta x^2$, we obtain a new equation of the form

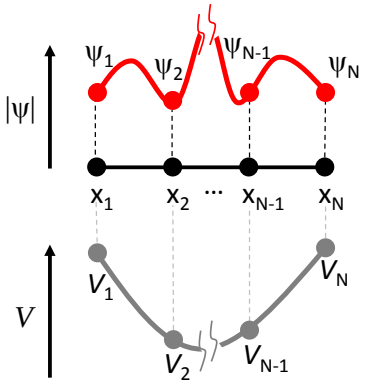

Figure 6.1: Wave function $\psi(x)$ and potential $V(x)$ defined on a grid of points $x_1, \ldots, x_N$. A minimum of the potential can encode a search value x_i.

$$-\frac{\psi_i^{t+\Delta t} - \psi_x^t}{\Delta t} = \frac{\psi_{i+1}^t + \psi_{i-1}^t - 2\psi_x^t}{\Delta x^2} - V(x_i)\psi_i^t \tag{6.2}$$

where we have written $\psi(x_i,t) = \psi_i^t$. For a circular grid with N points we can write this equation in matrix form as

$$\vec{\psi}^{t+\Delta t} = S^{\Delta t} \cdot \vec{\psi}^t \tag{6.3}$$

[1] Of course, since there is no dissipation, the state will not come to rest at the minimum point of energy but rather oscillate around it conserving its total potential and kinetic energy.

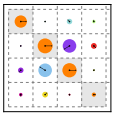

with S being a state transition matrix of the form

$$S^{\Delta t} = \begin{pmatrix} 1-2i\epsilon - iV(x_1)\Delta t & i\epsilon & 0 & \dots & i\epsilon \\ i\epsilon & 1-2i\epsilon - iV(x_2)\Delta t & i\epsilon & \dots & 0 \\ 0 & i\epsilon & \ddots & & \vdots \\ \vdots & & & \ddots & \vdots \\ i\epsilon & 0 & \dots & i\epsilon & 1-2i\epsilon - iV(x_N)\Delta t \end{pmatrix} \tag{6.4}$$

For infinitesimal times Δt we can separate the effect of the potential $V(x)$ on the wave function from the spatial dispersion $\propto i\epsilon$ by writing $S^{\Delta t} \approx D \cdot R$ with

$$D = \begin{pmatrix} 1-2i\epsilon & i\epsilon & 0 & 0 & \dots & i\epsilon \\ i\epsilon & 1-2i\epsilon & i\epsilon & 0 & \dots & 0 \\ \dots & \ddots & & & & \vdots \\ i\epsilon & 0 & 0 & \dots & i\epsilon & 1-2i\epsilon \end{pmatrix} \tag{6.5}$$

and

$$R = \begin{pmatrix} e^{-iV(x_1)\Delta t} & 0 & \dots & 0 & \\ 0 & e^{-iV(x_2)\Delta t} & \dots & 0 & \\ 0 & \dots & & 0 & e^{-iV(x_N)\Delta t} \end{pmatrix} \tag{6.6}$$

This approximation is correct to order $\mathcal{O}(\epsilon)$ up to an irrelevant renormalization factor. Now, we can repeatedly apply the matrix product $D \cdot R$ to the wave function to obtain its state after a given finite time t by writing

$$\vec{\psi}^{t_0+t} = \left(\prod_{i=1}^{t/\Delta t} D \cdot R \right) \cdot \vec{\psi}^{t} \tag{6.7}$$

This technique of splitting up the full evolution operator into a product of two or more non-commuting operators that are applied repeatedly to the wave function to obtain its state after a finite time is sometimes referred to as *Trotterization* – in reference to the so-called *Lie-Trotter formula* on which it is based – and on which digital quantum simulation relies[72, 69].

As can be seen in eq. (6.7), the evolution of the wave function at infinitesimal times is governed by two processes: The interaction with the potential V and a diffusion process that mixes different spatial parts of the wave function with each other. The operator D resembles a Markov diffusion process since each row and column of the matrix sums up to unity, whereas R changes the phase of each element of the wave function as a function of the local potential seen by it. If we apply R to a fully superposed initial state of

the form $\psi_i = 1$ (omitting the normalization factor for simplicity) and assume that $V_i = 0$ for $i \neq j$ and $V_j \Delta t = \pi/2$ (the potential thus encoding a search function with $\mathcal{C}(j) = 1$ and $\mathcal{C}(i) = 0$ for $i \neq j$), the element ψ_j will get turned according to $\psi_j \rightarrow i\psi_j$, whereas all other elements ψ_i will remain unchanged. Applying the operator D to the resulting state will transform ψ_j according to $\psi_j \rightarrow \psi_j(i + 2\epsilon(1 + i))$ with a corresponding amplitude $\sqrt{1 + 4\epsilon + \mathcal{O}(\epsilon^2)}$ and the adjacent states $\psi_{j\pm1}$ according to $\psi_{j\pm1} \rightarrow \psi_{j\pm1}(1 - \epsilon(1 + i))$ with an amplitude $\sqrt{1 - 2\epsilon + \mathcal{O}(\epsilon^2)}$. Hence there is a transfer of amplitude between the state whose phase has been turned and its neighboring states. If we reset the phases of all the ψ_i to zero afterwards, we can iterate the application of $D \cdot R$ until all of the amplitude has been transferred to the element ψ_j which corresponds to a solution to the search problem. This is, in essence, exactly what the Grover algorithm does, the only difference being that it replaces the matrix D with an unitary matrix that maximizes the amplitude transfer to the states solving the search problem, thereby speeding up the algorithm. As stated before, the efficiency with which the algorithm can transfer amplitude between different states is limited by physical constraints. In the next section, we will therefore discuss exactly what limits this efficiency and which unitary diffusion matrix one should choose to maximize it.

Efficiency of Quantum Searching

As discussed by L. Grover [55], it is interesting to ask what is the maximum amount of amplitude that can be transferred in a single step of the Grover search algorithm and which matrix D should be chosen to maximize this transfer. To answer this question and derive the ideal diffusion matrix, we will assume first that, without loss of generality, the matrix R which encodes the value of the search function $\mathcal{C}$ in the quantum state of the qubit register can be written as

$$R \;=\; \mathrm{I} - 2 \sum_{j=0}^{N-1} \mathcal{C}(j) \left|j\right\rangle \left\langle j\right| . \tag{6.8}$$

This operator will flip the sign of all states for which $\mathcal{C}(j) = 1$. Now, the next step consists in finding a diffusion or state transfer matrix which will maximize the amplitude transfer to states tagged by the Oracle operator above and which will also reset the phases of the quantum register to zero afterwards, such that we might apply the Oracle operator to the resulting state again. In the most general case, such a state transfer matrix will have the form

$$D_c = \begin{pmatrix} b & a & a & \dots & a \\ a & b & a & \dots & a \\ \vdots & & \ddots & & \vdots \\ a & & \dots & a & b \end{pmatrix} . \tag{6.9}$$

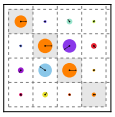

Here, we assume that all non-diagonal elements of the matrix are equal, which is well justified since we have no knowledge of the structure of the search space of the problem and therefore want to treat all basis states equally during the phase-to-amplitude conversion. Furthermore, since both the initial quantum state and the Oracle operator as given by eq. (6.8) contain only real numbers and we demand that the quantum state after applying D_c may contain only positive real numbers as well it is easy to show that a, b must be real numbers. Finally, the unitarity of quantum operators demands that $D_c^\dagger D_c = \mathrm{I}$, which for the matrix above is equivalent to the two conditions

$$1 = b^2 + (N-1)a^2, \tag{6.10}$$

$$0 = 2ab + (N-2)a^2. \tag{6.11}$$

Solving these two equations for a, b yields the trivial solution $b = \pm 1$, $a = 0$ and the more interesting one $b = \pm(1 - 2/N)$, $a = \mp 2/N$. As can be checked easily, the solution $b = 1 - 2/N$, $a = 2/N$ results in a maximum amplitude transfer from states $|i\rangle$ for which $\mathcal{C}(i) = 0$ to states $|j\rangle$ for which $\mathcal{C}(j) = 1$. Thus the ideal diffusion matrix to be used in the Grover algorithm is given as

$$D = \begin{pmatrix} -1+2/N & 2/N & 2/N & \dots & 2/N \\ 2/N & -1+2/N & 2/N & \dots & 2/N \\ \vdots & & \ddots & & \vdots \\ 2/N & 2/N & 2/N & \dots & -1+2/N \end{pmatrix}. \tag{6.12}$$

This matrix, together with an Oracle operator R as given by eq. (6.8) will yield the maximum amplitude transfer from states not solving the search problem to states that solve it. Repeating the application of $D \cdot R$ on an initially fully superposed quantum state for $\mathcal{O}(\sqrt{N})$ times will transform the input state to a state containing only the solutions of the search problem.

For the two-qubit case, the Oracle and diffusion operators R and D of the previous sections are

$$R = \begin{pmatrix} (-1)^{\mathcal{C}(00)} & 0 & 0 & 0 \\ 0 & (-1)^{\mathcal{C}(01)} & 0 & 0 \\ 0 & 0 & (-1)^{\mathcal{C}(10)} & 0 \\ 0 & 0 & 0 & (-1)^{\mathcal{C}(11)} \end{pmatrix}, \tag{6.13}$$

$$D = \frac{1}{2}\begin{pmatrix} -1 & 1 & 1 & 1 \\ 1 & -1 & 1 & 1 \\ 1 & 1 & -1 & 1 \\ 1 & 1 & 1 & -1 \end{pmatrix}. \tag{6.14}$$

Before discussing the experimental implementation of this algorithm, we will show how we can compare its computational efficiency to that of an equivalent classical algorithm in order to assess the achieved quantum speed-up.

6.1.2 Comparison to Classical Algorithms

To be able to compare the Grover algorithm as outlined here to a classical version solving the same search problem, we will now discuss another variant of the algorithm that uses an ancilla qubit to encode the result of the search function. This implementation will make it possible to devise a classical algorithm that can be directly compared to the quantum algorithm.

6.1.3 Ancilla-based Implementation of the Algorithm

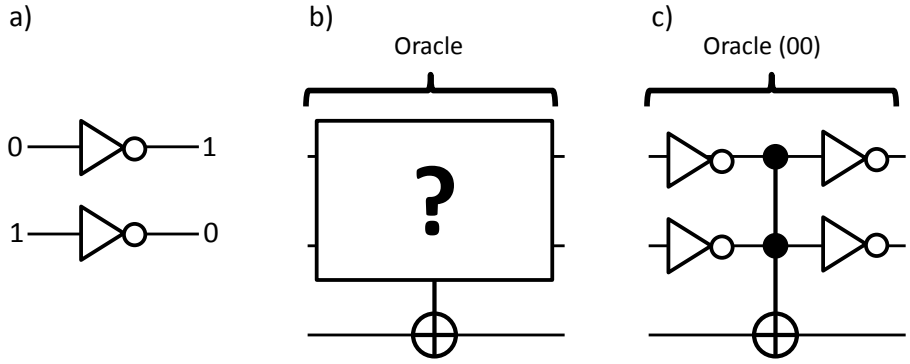

Figure 6.2: a) Definition of the NOT logic gate used in the following diagrams. b) Ancilla-based implementations of the Oracle functions $\mathcal{C}$ for two qubits. The state of the third bit get flipped if the search function $\mathcal{C}(i) = 1$ for the given input state i. c) Example of an ancilla-based search function returning a true value for the input state 00.

The implementation of the Grover search algorithm as outlined above encodes the value of the search function $\mathcal{C}$ directly in the phase of the input state supplied to this function. This makes it hard to compare the algorithm to a classical search algorithm which operates on a binary input state and, in general, cannot encode the result of the search function directly in this state. It is therefore useful to formulate a version of the Grover algorithm where the Oracle function does not directly encode the tagged state in the input qubit register but rather uses an ancilla qubit to store the result of calling $\mathcal{C}$. Such a representation of the algorithm, although of little practical relevance, is useful since it allows us to directly compare the quantum algorithm to a classical counterpart implemented using reversible logic gates, thus making it possible to benchmark the quantum algorithm and provide an estimation of the quantum speed-up that can be achieved.

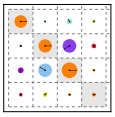

Exemplary implementations of ancilla-based search functions $\mathcal{C}$ implemented using reversible (quantum) gates are shown in fig. 6.2 for the two-qubit case. There, a three-qubit Tofolli gate in combination with several single-qubit NOT gates (that can be easily implemented as single-qubit X_π rotations) are used to flip the state of an ancilla-qubit conditionally on the input state of the gate. Using a similar approach, any arbitrary classical search function $\mathcal{C}$ that can be implemented with a set of universal reversible logic gates (e.g. the Toffoli gate and the NOT gate) can be directly mapped to a corresponding quantum operator that works on quantum-mechanical input states and implements the classical search function.

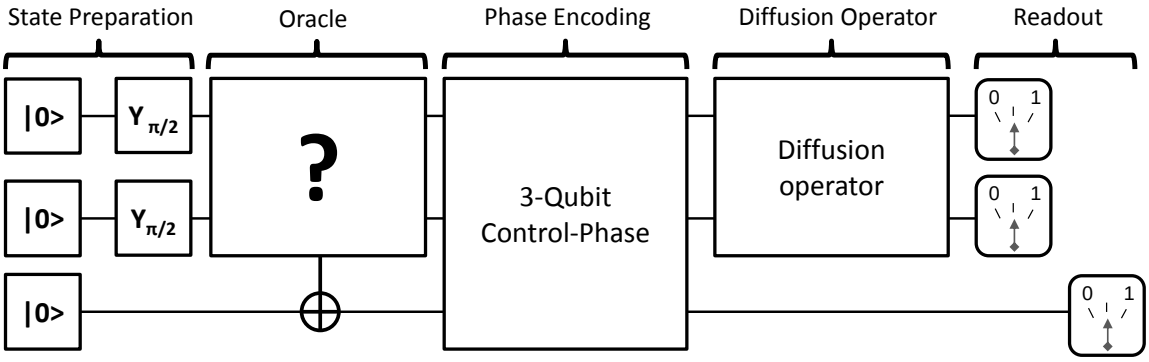

Figure 6.3: Full version of an ancilla-based implementation of the two-qubit Grover search algorithm. The algorithm flips the state of a (third) control qubit for one of the four possible input states in accordance to an unknown Oracle function. It then applies a three-qubit control-phase operation of that maps $|xy1\rangle \rightarrow -|xy1\rangle$, $|xy0\rangle \rightarrow |xy0\rangle$ to encode the state of the control qubit directly in the two input qubits. Then, a diffusion operator is used to determine the state which has been tagged by the Oracle function.

Now, to use the Grover algorithm with such an ancilla-based quantum Oracle, it is necessary to re-encode the result of the Oracle in the qubit input state. Figure 6.3 shows a version of the two-qubit Grover algorithm that achieves exactly this by using a three-qubit control-control-not (CCNOT) gate C of the form

$$C = \mathrm{I}^{8\otimes 8} - 2\sum_{ij} |ij1\rangle \langle ij1| \,. \tag{6.15}$$

After the re-encoding of the result, the ancilla qubit is not needed during the remainder of the algorithm but must not be read out before the algorithm terminates. A discussion of possible realizations of the ancilla-based Oracle operator can also be found in [84].

6.1.4 Comparison to a Classical Algorithm

In order to quantify the speed-up achieved by a quantum algorithm, it is necessary to define an equivalent classical algorithm to which we can compare it. Using the re-

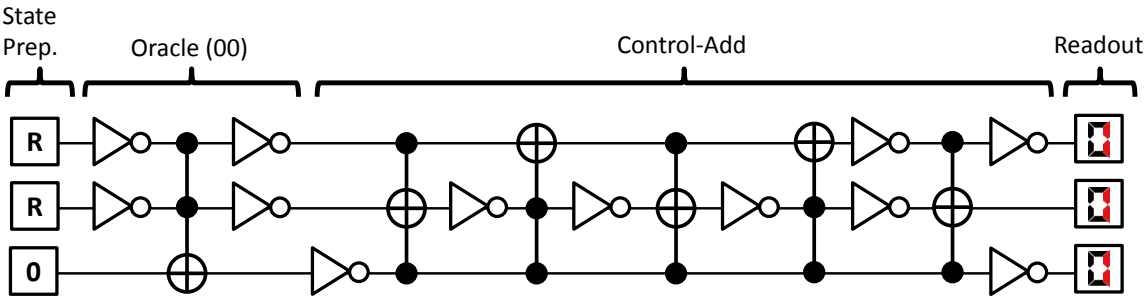

Figure 6.4: Classical reversible implementation of a query-and-guess search algorithm on a two-bit input register. An exemplary Oracle function can be implemented using two single-bit NOT operations and a Toffoli gate. R designates the generation of a random binary value at the beginning of the algorithm. If the Oracle does not yield the correct answer, the test state is incremented. The average success probability of the algorithm is 50 %.

versible, ancilla-based implementation of the search function that was introduced in the last section, it is straightforward to formulate a classical algorithm that solves the same problem as the Grover algorithm and then compare the number of evaluations of the search function $\mathcal{C}$ of the two. In this work, we compare our quantum algorithm to two particular classical algorithms that we refer to as "query" and "query-and-guess". The query algorithm evaluates $\mathcal{C}$ for n states, returning the searched state if it finds it among them and returning no value at all otherwise. The query-and-guess algorithm also evaluates $\mathcal{C}$ for n states, but even if the searched state is not found, it returns a guess of it by e.g. picking one of the remaining states at random. A possible two-bit implementation of a classical reversible query-and-guess algorithm that evaluates $\mathcal{C}$ only once is shown in fig. 6.4, achieving a success probability of 50 % by evaluating $\mathcal{C}$ for a randomly generated two-bit input value r and returning r if $\mathcal{C}(r) = 1$ or $r + 1 (\mathrm{mod}\ 4)$ otherwise. Allowing two or three evaluations of $\mathcal{C}$ will increase the success probability to 75 % or 100 %, respectively. The success probability of an equivalent two-qubit query algorithm would be 25 % for one evaluation of $\mathcal{C}$, 50 % for two, 75 % for three and 100 % for four. In general, for a search space with N states, the success probabilities of the query and query-and-guess algorithms as a function of n are $p_s^q(n) = n/N$ (for $n \leq N$) and $p_s^{qg}(n) = (n+1)/N$ (for $n \leq N-1$), which become equivalent for $N \to \infty$ but deviate significantly for small N.

6.2 Experimental Implementation

The Grover algorithm has been implemented for two and three qubits using nuclear magnetic resonance (NMR) [25, 115] as well as for two qubits using trapped ions [20] and recently NV centers in diamond [103]. In 2009, L. DiCarlo *et. al.* implemented it using a superconducting two-qubit processor [38] achieving $> 80\%$ output state fidelity,

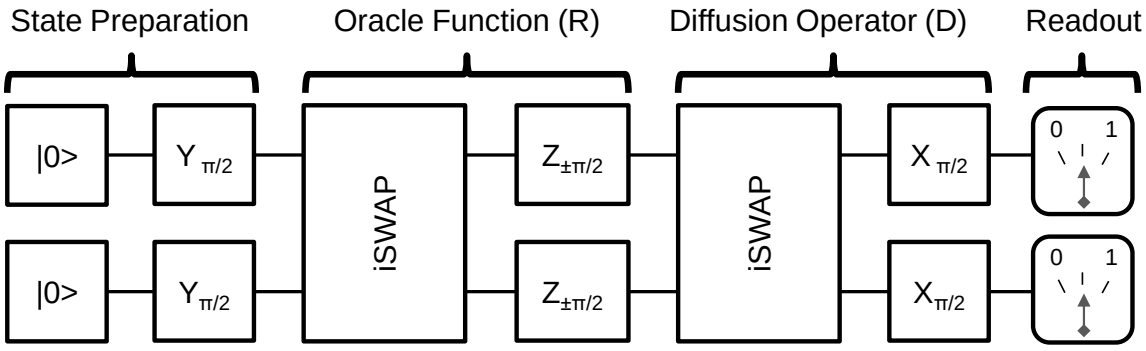

Figure 6.5: Schematic of our implementation of the Grover search algorithm. The algorithm consists in generating a fully superposed input state, applying the Oracle function to it and analyzing the resulting state by applying the Diffusion transform and reading out the value of the qubit register afterwards.

albeit without using a sufficiently efficient readout scheme of the qubit register and therefore not being able to demonstrate quantum speed-up. The demonstration of quantum speed-up for the Grover search algorithm using a superconducting two-qubit processor with individual-qubit readouts is one of the main goals of this thesis work.

We implement the compiled version of the two-qubit Grover algorithm, which encodes the result of calling the Oracle function $\mathcal{C}(x)$ with an input state x directly in the phase of x, as described above. The gate sequence of the algorithm is shown in fig. 6.5 and consists of two $i\mathrm{SWAP}$ gates and six single-qubit gates applied to an initial state $|00\rangle$. Here, the first $i\mathrm{SWAP}$ gate (which includes a $Z^I_{\theta_I} \otimes Z^{II}_{\theta_{II}}$ gate sequence to compensate the acquired phases of the qubits) together with the two single-qubit $Z_{\pm\pi/2}$ rotations implements the Oracle function $\mathcal{C}(x)$ as given by eq. (6.13), where the signs of the rotation operations determines the state which is tagged by the Oracle ($--$, $-+$, $+-$ and $++$ for $\mathcal{C}_{00}$, $\mathcal{C}_{01}$, $\mathcal{C}_{10}$ and $\mathcal{C}_{11}$, respectively). This state can be either $|00\rangle$ (corresponding to a $Z^I_{-\pi/2} \cdot Z^{II}_{-\pi/2}$ rotation), $|01\rangle$ ($Z^I_{-\pi/2} \cdot Z^{II}_{\pi/2}$), $|10\rangle$ ($Z^I_{\pi/2} \cdot Z^{II}_{-\pi/2}$) or $|11\rangle$ ($Z^I_{\pi/2} \cdot Z^{II}_{\pi/2}$). After the encoding, the second $i\mathrm{SWAP}$ operation (which also includes Z compensation pulses) together with the following $X^I_{\pi/2} \cdot X^{II}_{\pi/2}$ single-qubit operations implements the diffusion operator as given by eq. (6.14). The final step of the algorithm consists in reading out the two-qubit register.

6.2.1 Pulse Sequence

We implement the gate sequence described above using microwave and fast flux pulses. To minimize gate errors, we perform a series of calibration measurements before to tune-up the individual single- and two-qubit gates needed for the algorithm, as explained in chapter 5. In addition, we run individual parts of the algorithm successively and perform quantum state tomography to characterize the state of the quantum register after each

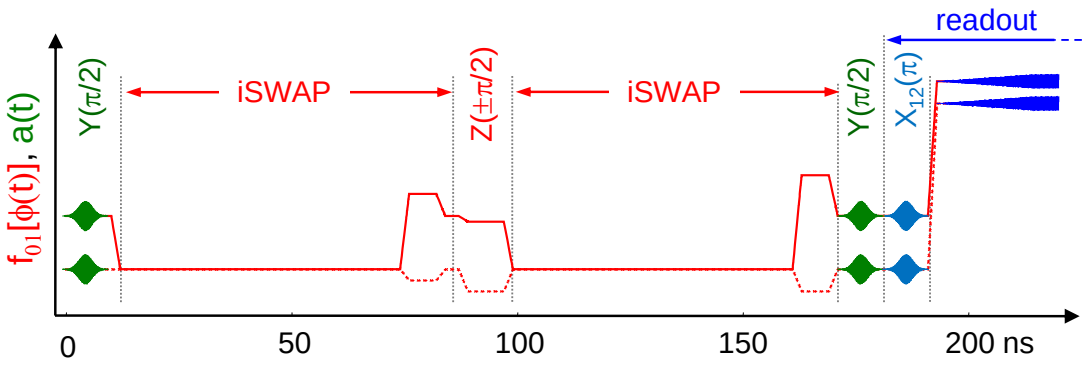

Figure 6.6: Pulse sequence used to realize the two-qubit Grover quantum search algorithm. First, a $Y_{\pi/2}$ pulse is applied to each qubit to produce the fully superposed state $1/2(|00\rangle + |01\rangle + |10\rangle + |11\rangle)$. Then, an $i\mathrm{SWAP}$ gate is applied, followed by a $Z_{\pm\pi/2}$ gate on each qubit, which combined correspond to the application of the Oracle function. The resulting state is then analyzed using another $i\mathrm{SWAP}$ gate and two $X_{\pi/2}$ gates to extract the state tagged by the Oracle. Optionally, a Y_{π}^{12} pulse is applied to each qubit to increase the readout fidelity.

step of the algorithm, optimizing the gate operations applied to the qubit in order to maximize the fidelity of the measured states in respect to the ideal ones. However, we optimize only the state preparation and Oracle operator itself on a per-state basis, whereas the diffusion operator D is optimized only once for all possible Oracles, as required for benchmarking a real quantum algorithm. cases do not optimize the Figure 6.6 shows an experimental pulse sequence for the Grover algorithm with an Oracle operator $\mathcal{C}_{00}$. Shown are the frequencies of the two qubits during the run time of the algorithm and the microwave drive and readout pulses applied to them.

6.3 Results

We now present the experimental results obtained with our implementation of the Grover algorithm: Quantum state tomography is first used to determine the register density matrices during the algorithm, and single-run results are then presented and discussed.

6.3.1 State Tomography of the Quantum Register

Figure 6.7b shows the experimentally measured density matrices of the two-qubit register when running the Grover search algorithm for the four possible Oracle functions. For each of those four cases, quantum state tomography was performed after each step of the algorithm, as indicated in fig. 6.7a. The fidelity diminishes during the algorithm due to dephasing and relaxation. The state fidelities for the final output states of the algorithm are 68% for the $\mathcal{C}_{00}$, 64% for the $\mathcal{C}_{01}$, 61% for the $\mathcal{C}_{10}$ and 65% for the $\mathcal{C}_{11}$ Oracle functions.

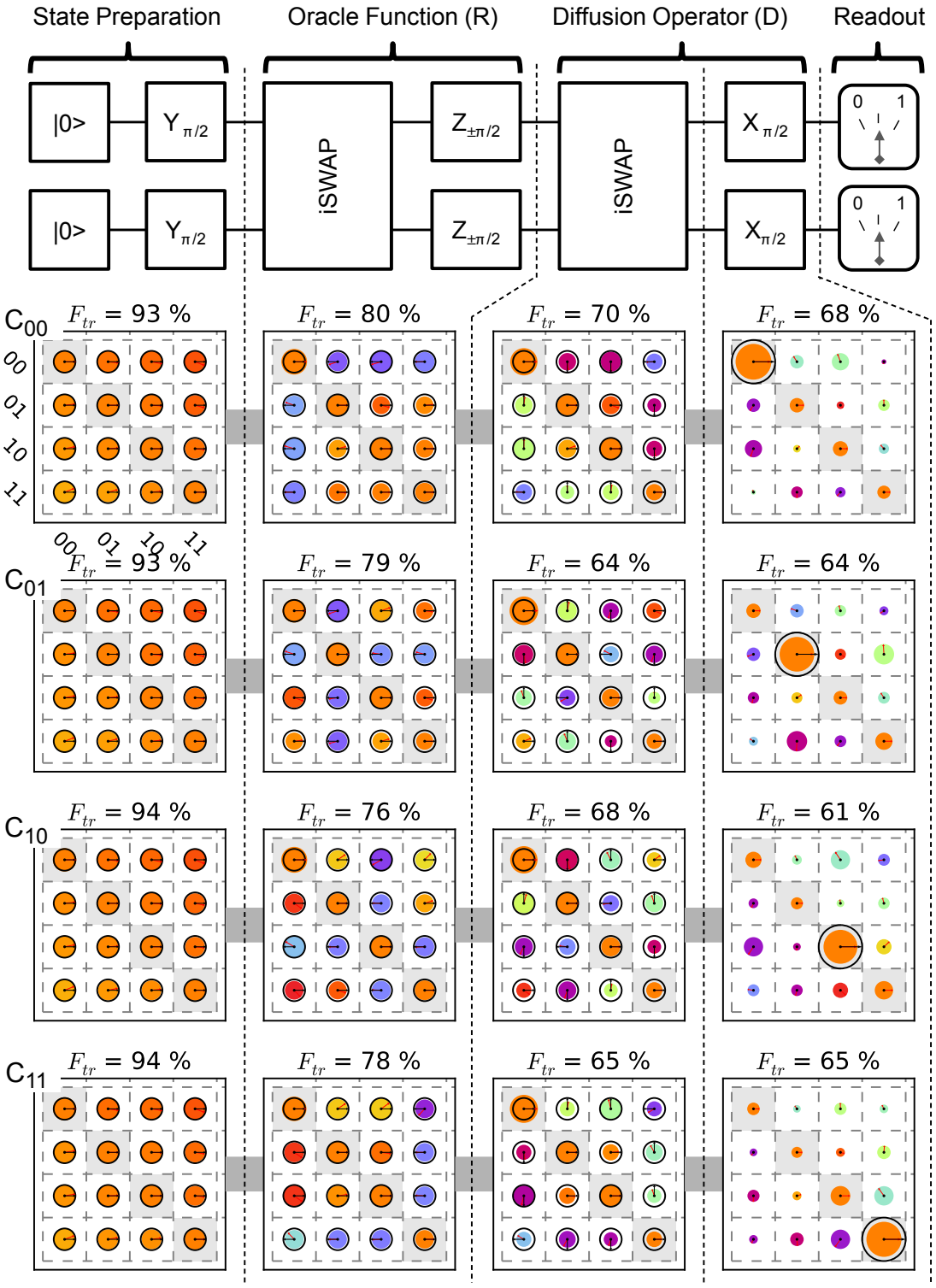

Figure 6.7: a) Schematic of the implemented algorithm, indicating the steps at which quantum state tomography has been performed. b) Experimental (filled circles) and theoretical (black outline) density matrices at different steps of the Grover search algorithm as indicated by the dotted lines, shown for four individual runs of the algorithm corresponding to different Oracle functions tagging the state $|00\rangle$, $|01\rangle$, $|10\rangle$ or $|11\rangle$. The trace fidelity (2.8) between experimental and theoretical density matrices is indicated above each matrix.

6.3.2 Single Run Results

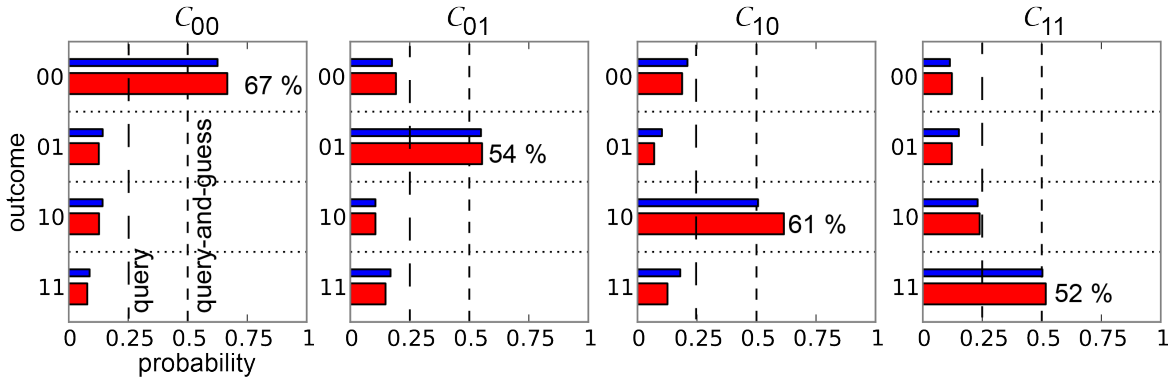

Figure 6.8: Single-run success probabilities of our implementation of the Grover search algorithm, for the four possible Oracle functions. Red bars correspond to measured values, whereas blue ones are calculated using the measured density matrices after the final step of the algorithm and the measured two-qubit readout matrix as shown in fig. 6.12. Dashed lines indicate the average success probabilities of classical query and query-and-guess algorithms, for comparison.

The experimental state tomographies presented above show that we can implement the Grover search algorithm with average output state fidelity of 64 % using our two-qubit processor. However, the analysis of the two-qubit register by quantum state tomography at the end of the algorithm does not prove that we can achieve real quantum speed-up with our processor. For this, it is necessary to directly read out the state of the qubit register at the end of the algorithm *without* performing any kind of error correction afterwards. By looking at this "raw" outcome data and generating statistics over many single runs of the processor, we quantify the success rate and the fidelity of the implemented algorithm. The results of such measurements, performed for the four possible Oracle functions, are shown in fig. 6.8. Besides the single-run probabilities for all four Oracle functions, the diagram shows for comparison the expected outcome probabilities calculated based on the quantum state tomographies discussed above and the readout matrix of the two-qubit processor shown in fig. 6.12. As can be seen, the agreement between the measured and calculated probabilities is fairly good. Deviations between expected and measured outcome probabilities (such as for the $|10\rangle$ state when using the C_{10} Oracle) might be explained by a drift of the experimental parameters between the measurement of the state tomographies and the single-run data. The dashed lines in the diagrams correspond to the success probabilities of classical single-evaluation query and query-and-guess algorithms, which are 25 % and 50 %, respectively, and which provide a benchmark against which we measure the quantum speed-up of our algorithm. Our implementation of the Grover search algorithm outperforms such classical algorithms for all Oracle functions, if only by 2-17 % for the "query-and-guess" algorithm.

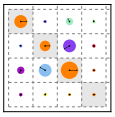

6.4 Algorithm Fidelity

$ab/\|uv\rangle$	$\|00\rangle$	$\|01\rangle$	$\|10\rangle$	$\|11\rangle$	$\sum$	f_{ab}
00	0.666	0.192	0.188	0.122	1.168	57.0 %
01	0.127	0.554	0.071	0.122	0.874	63.4 %
10	0.128	0.106	0.615	0.239	1.088	56.5 %
11	0.079	0.148	0.126	0.517	0.870	59.4 %

Table 6.1: Conditional probabilities $p_{ab/|uv\rangle}$ and user fidelities f_{ab} for all possible outcomes ab for our implementation of Grover's algorithm.

We define the average fidelity f_i of the algorithm in a single run as the conditional probability of finding the correct state $|i\rangle$ given a certain Oracle function $\mathcal{C}_i$. We also define *user fidelities*

$$f_{ab} = p(|ab\rangle\,|ab) = \frac{p(ab|\,|ab\rangle)}{\sum\limits_{uv} p(uv|\,|uv\rangle)}, \tag{6.16}$$

where $p(ab|\,|ab\rangle)$ is the conditional probability of obtaining the search result ab given the Oracle operator $|ab\rangle$. These user fidelities are complementary to the average fidelity and correspond to the conditional probabilities of having found the correct state given a certain measured state, averaged over all possible Oracle functions. For all four Oracles, both the single-run and user fidelities as shown in tab. 6.1 are $> 50\%$, hence demonstrating quantum speed-up in comparison with a classical query-and-guess algorithm.

6.5 Comparison to a Classical Search Algorithm

As discussed above, we compare our implementation of the Grover algorithm to the classical query and query-and-guess algorithms in order to quantify the quantum speed-up achieved. More precisely, we calculate the success probability of our algorithm to find the solution of the search problem after n runs as

$$p_s(n) = \sum_{i=1}^{n} (1 - p_s^0)^{i-1} p_s^0, \tag{6.17}$$

where p_s^0 is the single-run success probability of the algorithm. Figure 6.9 shows $p_s(n)$ for our implementation of the Grover algorithm as obtained for all four Oracle operators, together with the success probabilities of the query and query-and-guess classical algorithms. As can be seen, our implementation of the Grover algorithm beats the query algorithm for $n \leq 3$ evaluations of $\mathcal{C}$ and the classical query-and-guess algorithm for

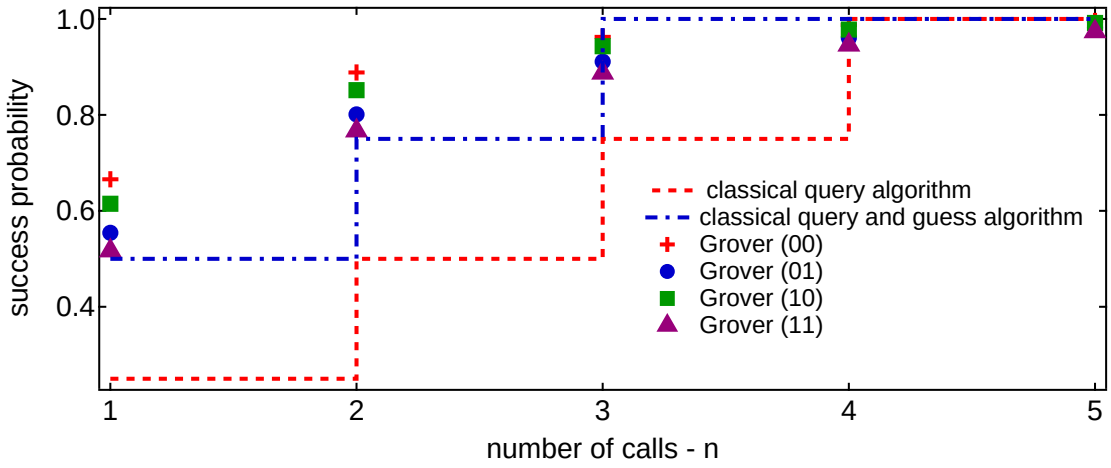

Figure 6.9: Comparison between our measured success probability of our implementation of the Grover algorithm and the calculated success probabilities of the query and query-and-guess classical algorithms as a function of the number n of runs.

$n \leq 2$. However, unlike the classical algorithms, it never converges to 100 % success probability due to always-present unitary and non-unitary errors in our system.

6.6 Error Analysis

Three kind of errors arise in our implementation of the Grover algorithm:

1. Deterministic, unitary gate errors.
2. Stochastic errors introduced due to qubit decoherence.
3. Readout errors (due to qubit relaxation during readout, insufficient readout sensitivity or retrapping of the readout resonator state).

6.6.1 Gate Errors & Decoherence

As far as gate errors and unitary errors are concerned, we quantify them by fitting an error model described below to the experimental data. In contrast to chapter 5, where we used a full master-equation model to simulate the implemented $\sqrt{i\mathrm{SWAP}}$ gate, we use now an operator-based formalism to model the Grover algorithm with all relevant unitary and non-unitary errors in a simple and intuitive way. Hence, rather than performing a time-integration of an effective Hamiltonian, we start with an initial density matrix ρ and apply a sequence of unitary gate operators O_i to it in order to simulate the individual steps of the algorithm, including possible unitary gate errors. In addition, we approximate decoherence by inserting after each operation O_i non-unitary relaxation

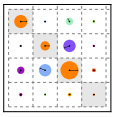

and dephasing operators with rates Γ_1 or Γ_ϕ and duration Δt_i equal to the duration of O_i (note that dephasing is treated here in a phenomenological way, as discussed in section 2.5).

The non-unitary single-qubit operators describing amplitude-damping of the qubit state are [91]

$$E_1^{\Gamma_1}(\Delta t) = \begin{pmatrix} 1 & 0 \\ 0 & \sqrt{1-\gamma_{\Gamma_1}(\Delta t)} \end{pmatrix} \qquad E_2^{\Gamma_1}(\Delta t) = \begin{pmatrix} 0 & \sqrt{\gamma_{\Gamma_1}(\Delta t)} \\ 0 & 0 \end{pmatrix}, \tag{6.18}$$

whereas phase-damping operators describing qubit dephasing are written as

$$E_1^{\Gamma_\phi}(\Delta t) = \begin{pmatrix} 1 & 0 \\ 0 & \sqrt{1-\gamma_{\Gamma_\phi}(\Delta t)} \end{pmatrix} \qquad E_2^{\Gamma_\phi}(\Delta t) = \begin{pmatrix} 0 & 0 \\ 0 & \sqrt{\gamma_{\Gamma_\phi}(\Delta t)} \end{pmatrix}. \tag{6.19}$$

Both operators are applied to a quantum state ρ according to

$$\rho \to \mathcal{E}_{\Delta t}(\rho, E) = E_1(\Delta t)\rho E_1^\dagger(\Delta t) + E_2(\Delta t)\rho E_2^\dagger(\Delta t) \tag{6.20}$$

and yield a trace-preserving, non-unitary evolution of the density matrix ρ. The decoherence fractions γ used in the operators are given by

$$\gamma_{\Gamma_1}(\Delta t) = 1 - \exp\left(-\Delta t \Gamma_1\right), \tag{6.21}$$

$$\gamma_{\Gamma_\phi}(\Delta t) = 1 - \exp\left(-\Delta t \Gamma_\phi/2\right), \tag{6.22}$$

where Δt is the time during which the state is exposed to the given decoherence process. Normally, decoherence processes occur continuously during the run time of the algorithm. However, in our simulation we apply the operators (6.19) and (6.18) to the quantum state at discrete times $\{t_1, \ldots, t_i, \ldots, t_n\}$, using effective decoherence rates $\gamma_{\Gamma_1}(\Delta t_i)$ and $\gamma_{\Gamma_\phi}(\Delta t_i)$ with $\Delta t_i = t_{i+1} - t_i$ to model the decoherence between times t_i and t_{i+1}. In order for this approximation to be valid, the integration time Δt_i needs to be small compared to the relaxation and dephasing times of the qubits, i.e. $\Delta t_i \ll 1/\Gamma_1, 1/\Gamma_\phi$. We assure this by splitting up long unitary operators O_i with duration Δt_i into an equivalent sequence of n operators $O_i^{1/n}$ with durations $\Delta_i t/n$, after each of which we apply the decoherence process using an adapted integration time $\Delta t_i/n$, as shown in fig. 6.10. If n is chosen sufficiently large, the condition formulated above will always be fulfilled.

Using these definitions, we formulate a full error model taking into account the following error sources:

- **Energy relaxation and dephasing**: Energy relaxation and dephasing of the qubits is modeled by applying the operators given by eqs. (6.18) and (6.19) with rates

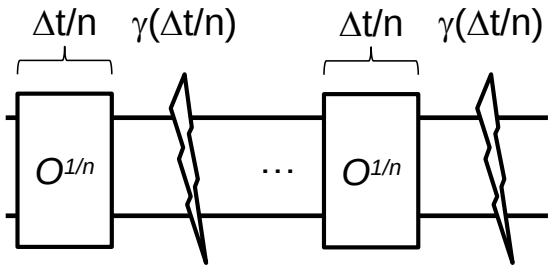

Figure 6.10: Finite difference model of a unitary gate sequence O with a duration Δt that is subjected to a decoherence process with rate $\gamma(\Delta t)$: The evolution operator O is split into a sequence of n operators $O^{1/n}$, each of which is subjected to a decoherence process with an effective rate $\gamma(\Delta t/n)$.

(6.21) and (6.22) to the quantum state after each unitary operator during the algorithm. Operators with an experimental duration larger than $\Delta t_{\max} = 5$ ns are split up into a sequence of sub-operators with durations $\Delta t \leq \Delta t_{\max}$, where we apply the decoherence process after each of these sub-operators.

- **Single-qubit gate errors**: Rotation angle and axis errors of the single-qubit X_α and Y_α gates are modeled by replacing them with operators of the form $X_\alpha \rightarrow \phi_{\alpha'} = \cos\phi X_{\alpha'} + \sin\phi Y_{\alpha'}$ and $Y_\alpha \rightarrow \varphi_{\alpha'} = \sin\varphi X_{\alpha'} + \cos\varphi Y_{\alpha'}$. For Z-type single-qubit operators, we have only rotation angle errors by replacing $Z_\beta \rightarrow Z_{\beta'}$
- **Two-qubit gate errors:** Errors in the $i\mathrm{SWAP}$ operator are modeled using the representation of the iSWAP gate given by eq. (2.108), replacing t and Δ with $\epsilon = tg_e$ and $\delta = \Delta/g$. In addition, we model the errors in the Z compensation pulses by including single-qubit rotations of the form $Z^I_{\theta_I} \otimes Z^{II}_{\theta_{II}}$.

The full algorithm with unitary and non-unitary errors and taking into account all gate times can be written as

$$
\begin{aligned}
O_{\mathrm{Grover}}(\rho) &= O_7(O_6(O_5(O_4(O_3(O_2(O_1(\rho))))))) \\
O_1(\rho) &= \mathcal{D}^{\times 2}_{5\text{ ns}}\left(\left[\varphi^I_{\alpha_I} \otimes \varphi^{II}_{\alpha_{II}}\right]^{1/2}, \rho\right) \\
O_2(\rho) &= \mathcal{D}^{\times 16}_{3.875\text{ ns}}\left(i\mathrm{SWAP}(\epsilon_1, \delta_1)^{1/16}, \rho\right) \\
O_3(\rho) &= \mathcal{D}_{5\text{ ns}}\left(Z^I_{\theta_I} \otimes Z^{II}_{\theta_{II}}, \rho\right) \\
O_4(\rho) &= \mathcal{D}_{5\text{ ns}}\left(Z_{\beta_I} \otimes Z_{\beta_{II}}, \rho\right) \\
O_5(\rho) &= \mathcal{D}^{\times 16}_{3.875\text{ ns}}\left(i\mathrm{SWAP}(\epsilon_2, \delta_2)^{1/16}, \rho\right) \\
O_6(\rho) &= \mathcal{D}_{5\text{ ns}}\left(Z^I_{\lambda_I} \otimes Z^{II}_{\lambda_{II}}, \rho\right) \\
O_7(\rho) &= \mathcal{D}^{\times 2}_{5\text{ ns}}\left(\left[\phi^I_{\gamma_I} \otimes \phi^{II}_{\gamma_{II}}\right]^{1/2}, \rho\right),
\end{aligned}
\tag{6.23}
$$

where $\mathcal{D}_{\Delta t}(M,\rho) = \mathcal{E}_{\Delta t}(\mathcal{E}_{\Delta t}(\mathcal{E}_{\Delta t}(\mathcal{E}_{\Delta t}(M\rho M^\dagger, E^{\Gamma^I_1}\otimes \mathrm{I}), E^{\Gamma^I_\phi}\otimes \mathrm{I}), \mathrm{I}\otimes E^{\Gamma^{II}_1}), \mathrm{I}\otimes E^{\Gamma^{II}_\phi})$ and $\mathcal{D}^{\times n}_{\Delta t}(M,\rho)$ is the n-fold recursive application of $\mathcal{D}_{\Delta t}(M,\cdot)$ to ρ. Figure 6.11a shows a schematic of this sequence, indicating above each operator its duration. Numerical optimization is used to fit this error model to the experimentally obtained density matrices

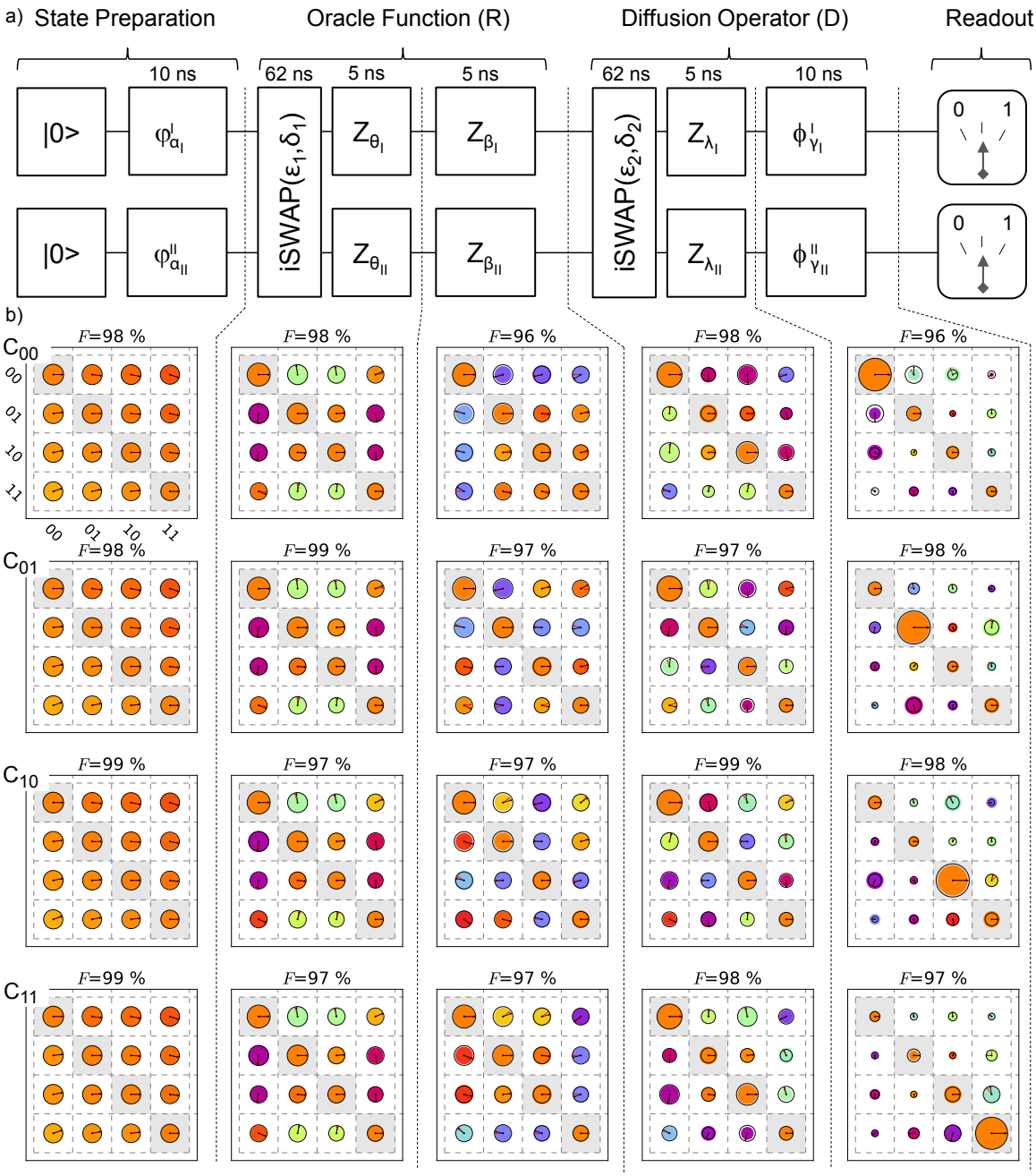

Figure 6.11: a) Schematic of the unitary error model given by eq. (6.23), which we use to analyze our experimental implementation of the Grover search algorithm. Dotted lines indicate the times at which the quantum state has been measured by state tomography. The execution time of the experimental sequence implementing each operator is indicated above it. b) Experimentally measured density matrices at different times during the algorithm (black outlines) together with matrices corresponding to the best fit of the error model (filled circles) to the data, plotted for four individual runs of the algorithm corresponding to different Oracle operators. The state fidelity between the measured and simulated density matrices is indicated above each panel.

measured after each step of the algorithm, as obtained in four individual runs using different Oracle operators tagging the states $|00\rangle$, $|01\rangle$, $|10\rangle$ and $|11\rangle$. We fit the parameters of the operators O_i that model each individual step i of the algorithm by maximizing the fidelity between the experimentally obtained output density matrix ρ_i^{exp} of the step and the modeled one ρ_i^{mod}, which is calculated based on the experimental input density matrix $\rho_{i-1}^{\mathrm{exp}}$ as $\rho_i^{\mathrm{mod}} = O_i(\rho_{i-1}^{\mathrm{exp}})$. For the first step, we set the input state to $\rho_0^{\mathrm{exp}} = |00\rangle\langle 00|$. The parameters of the operators O_i are not allowed to vary between the four different runs, except for $\beta_{I,II}$, which were adjusted independently for each Oracle operator. This yields in total 24 parameters that are fitted to a data set containing 20 density matrices, each corresponding to 15 measured real values. The density matrices corresponding to the best fit together with the experimentally measured matrices are shown in fig. 6.11b. The obtained error parameters are summarized in tab. 6.2. As before, the qubit relaxation and dephasing rates of $\Gamma_1^I = (436\ \mathrm{ns})^{-1}$, $\Gamma_1^{II} = (520\ \mathrm{ns})^{-1}$, $\Gamma_\phi^I = \Gamma_\phi^{II} = (600\ \mathrm{ns})^{-1}$ were determined independently and are not part of the fit.

value	$\alpha_I(^\circ)$	$\alpha_{II}(^\circ)$	$\varphi_I(^\circ)$	$\varphi_{II}(^\circ)$	$\epsilon_I(^\circ)$	$\epsilon_{II}(^\circ)$	$\theta_I(^\circ)$	$\theta_{II}(^\circ)$
absolute	93.4	88.2	101.5	96.8	88.7	96.6	-19.8	-20.8
deviation	(3.4)	(-1.8)	(11.5)	(6.8)	(-1.3)	(6.6)	(-19.8)	(-20.8)

	δ_I (MHz)	δ_{II} (MHz)	$\gamma_I(^\circ)$	$\gamma_{II}(^\circ)$	$\phi_I(^\circ)$	$\phi_{II}(^\circ)$	$\lambda_I(^\circ)$	$\lambda_{II}(^\circ)$
absolute	-0.128	0.181	87.2	91.2	-1.0	-5.0	8.7	4.6
deviation	(-0.128)	(0.181)	(-2.8)	(1.2)	(-1.0)	(-5.0)	(8.7)	(4.6)

run	$\mathcal{C}_{00}$	$\mathcal{C}_{01}$	$\mathcal{C}_{10}$	$\mathcal{C}_{11}$
$\beta_I(^\circ)$	-92.4 (-2.4)	90.2 (0.2)	-92.9 (-2.9)	87.3 (-2.7)
$\beta_{II}(^\circ)$	-98.1 (-8.1)	-94.0 (-4.0)	81.4 (-8.6)	77.5 (-12.5)

Table 6.2: Shown are the absolute values and deviations (in parenthesis) of the parameters of the error model given by eq. (6.23) for the measured density matrices.

Our error model is able to capture most of the observed experimental errors and can reproduce to a large extent the observed density matrices. The state fidelities according to eq. 2.6 between the measured density matrices and those of the fitted error model are all $\geq 97\%$. The rotation angle and axis errors of the X/Y pulses vary between $\pm 3^\circ$ and $\pm 12^\circ$, respectively, which is comparable with the single-qubit gate errors estimated in chapter 5. The errors in the Z rotations are considerably larger and vary between $\pm 20^\circ$, which can be explained by the reduced accuracy with which we calibrate these gates and by a drift of our measurement equipment during the experiment, as described in section 5.4.6.

Given the large number of fitting parameters and the phenomenological treatment of dephasing, these results can suffer from large uncertainties and only show the order of magnitude of different errors and their impact on the register density matrices along the

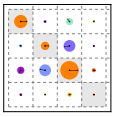

algorithm.

Fidelity of the Oracle and Diffusion Operators

It is interesting to analyze the individual output state fidelities of the Oracle and diffusion operators. For this, we compare the action of the ideal operators D and R given by eqs. (6.14) and (6.13) on a given input state with that of the experimentally implemented ones. We do this by applying the ideal operators D and R to their experimentally measured two-qubit input density matrices $\rho^{\mathrm{exp}}_{\mathrm{in},D,R}$ and calculating the fidelity of the resulting matrices with the experimentally obtained output matrices $\rho^{\mathrm{exp}}_{\mathrm{out},D,R}$:

$$F(D) = F(D\rho^{\mathrm{exp}}_{\mathrm{in},D}D^{\dagger}, \rho^{\mathrm{exp}}_{\mathrm{out},D}), \tag{6.24}$$

$$F(R) = F(R\rho^{\mathrm{exp}}_{\mathrm{in},R}R^{\dagger}, \rho^{\mathrm{exp}}_{\mathrm{out},R}), \tag{6.25}$$

where we make use of the state fidelity F given by eq. 2.6. By this method, we obtain the following experimental fidelities for the Oracle and diffusion operations:

Operator / State	$\|00\rangle$	$\|01\rangle$	$\|10\rangle$	$\|11\rangle$	Average
D	92.3	93.4	94.3	91.7	92.9
R	94.5	93.6	88.5	87.7	91.1

Table 6.3: Measured fidelities (in %) of the quantum Oracle and diffusion operators used in the Grover search algorithm according to eqs. (6.24) and (6.25).

As can be seen, we are able to implement both the diffusion operator and the quantum Oracle with an average fidelity $> 90\%$.

6.6.2 Readout Errors

Another direct source of errors affecting the single-run fidelities of the algorithm are readout errors. As explained in chapter 4 qubit relaxation during the readout process reduces the visibility of individual qubit states and introduces errors when reading out the qubit register in the final step of the algorithm. We can easily quantify those readout errors by using the readout matrix that was introduced in chapter 5. When running the Grover algorithm, we use the $|1\rangle \rightarrow |2\rangle$ shelving method described in chapter 4 to increase the readout contrast and thereby the algorithm fidelity. This technique reduces single-qubit readout errors but increases inter-qubit readout crosstalk. The measured readout matrix for the Grover experiment is shown in fig. 6.12. As can be seen, the single-qubit readout fidelities range between 87 - 96 % and the combined two-qubit readout fidelities between 75 - 88 %. Depending on the qubit state we also observe between 3-5 % inter-qubit readout crosstalk.

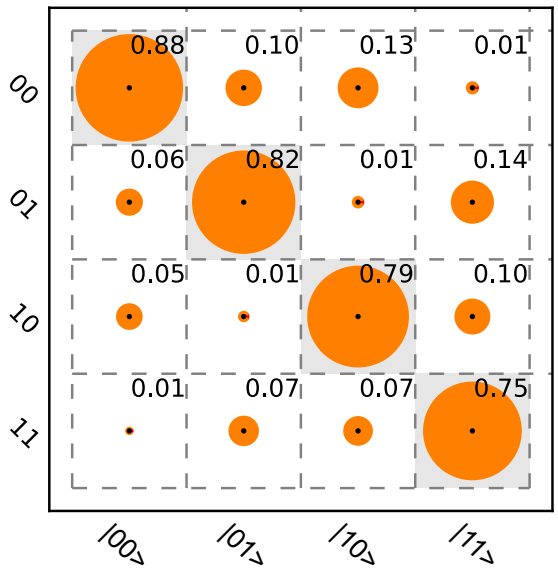

Figure 6.12: The measured readout matrix for the Grover experiment. Shown are the conditional probabilities $p_m(x|y)$ of obtaining a readout value x after having prepared a qubit state $|y\rangle$, where $x, y \in \{00, 01, 10, 11\}$. The readout fidelities for the different qubit states range between 75 - 88 %, the inter-qubit readout crosstalk ranges between 3-5 %.

6.7 Conclusions

We have shown that we can implement the Grover search algorithm with our quantum processor and achieve a single-run fidelity that is sufficient to demonstrate simple probabilistic quantum speed-up, as compared to a classical, reversible search algorithm. The error model formulated in this chapter is able to account for most of the observed imperfections and can explain the data we observed. Unfortunately, the coherence times of our qubits do not permit the realization of more complex algorithms with our processor, but nevertheless it provides a proof-of-principle of our approach to build a superconducting quantum computer with individual-qubit single shot readout.

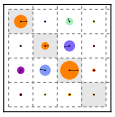

Chapter 7

Designing a Scalable Qubit Architecture

In chapters 5 and 6 we discussed the characterization and use of an elementary two-qubit quantum processor. With this processor, we demonstrated individual-qubit single-shot readout with up to 89 % readout contrast. We also implemented and characterized a universal $\sqrt{i\mathrm{SWAP}}$ two-qubit gate with 90 % gate fidelity and used it to run the Grover search algorithm, for which we obtained a single-run fidelity between 52% and 67%, therefore demonstrating probabilistic quantum speed-up.

However, as we explain in this chapter, the approach to quantum computing that we presented cannot be scaled beyond a few qubits. Hence, in order to realize a larger-scale quantum computer it will be necessary to devise a new kind of scalable qubit architecture, where “scalable” means that the overhead for adding a qubit to a quantum processor does not require an exponential amount of physical or computational resources. In the literature, several proposals for scalable superconducting qubit architectures have been formulated, using e.g. a parametric coupling between qubits [13] or relying on the storage of quantum information in a separate entity, such as a superconducting resonator [50, 78]. In the following sections, we propose a different architecture, based on the recently introduced double-Transmon qubit [51, 112] and using a tunable qubit-qubit coupling scheme as well as a single-shot readout method for individual qubits. After giving a short overview of our proposed architecture, we show how we can implement a four-qubit processor with it. Furthermore, we discuss the possible limitations and shortcomings of the architecture. Finally, we put our work in context with other recent developments in the field of superconducting qubits and point out possible future research directions.

7.1 Requirements

A scalable architecture for quantum computing should fulfill all of DiVincenzo's criteria as discussed in section 1.1 and in addition not require an exponential experimental overhead in computational or physical resources for each qubit that is added to the quantum computer [17]. Today, the two issues that are not addressed well by current qubit architectures (such as the quantum bus architecture used by many groups today [38, 119]) concern the qubit-qubit coupling and the readout of individual qubits. The quantum bus architecture, for instance, has an "always-ON"-type coupling scheme between the qubits, given by the Hamiltonian (2.109). This scheme makes it hard to precisely control the coupling between individual qubits if a large number of them is present, since the effective coupling amplitude between any two qubits decreases $\propto 1/\Delta$ as a function of their detuning Δ. Therefore, it becomes increasingly difficult and eventually impossible to deterministically switch on and off the coupling between individual qubits due to the limited available frequency space that can be allocated to each qubit (the so-called *frequency crowding*). Also, keeping track of all the involved phases and frequencies of the full coupled qubit register incurs a computational overhead that increases exponentially with the qubit number [50]. Using a direct capacitive coupling between individual qubits suffers from the same problem. Therefore, to be really scalable, a qubit architecture needs to have at least the following properties:

1. Well-defined qubits with long coherence times.
2. A single-shot, high-fidelity readout method for individual qubits.
3. High-fidelity single-qubit control.
4. Tunable and robust coupling between any two qubits.
5. Sub-exponential (ideally even sub-linear) scaling of resources when adding more qubits to the computer.

As already said, the current CQED architectures fulfill most of these properties (to varying degrees) but fail to provide a tunable qubit-qubit coupling and a single-shot individual-qubit readout. In the following sections we discuss a proposal for an architecture that can potentially possess all of the above properties.

7.2 Architecture Proposal

Our proposed architecture follows the general CQED principles in that it uses Transmon qubits coupled to each other via a resonator acting as a quantum bus. However, instead

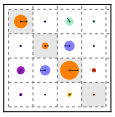

of using a single Transmon to represent each logical qubit, we could use two of them that are capacitively coupled to each other and act therefore as a qubit "molecule". As shown by J. Gambetta *et. al.*, if we couple the two Transmons of such a molecule to the quantum bus with the same coupling constant, symmetry properties of the Hamiltonian of the molecule make it possible to fully decouple one of its eigenstates from the quantum bus [51]. This allows thus to remedy the problem of frequency crowding, since while the qubit is in this state (or in the ground state $|0\rangle$) no spurious coupling to other qubits will be present, regardless of the chosen qubit-qubit detuning. In the following section, we discuss the properties of this approach and the proposed qubit-qubit coupling scheme.

7.2.1 The Double Transmon

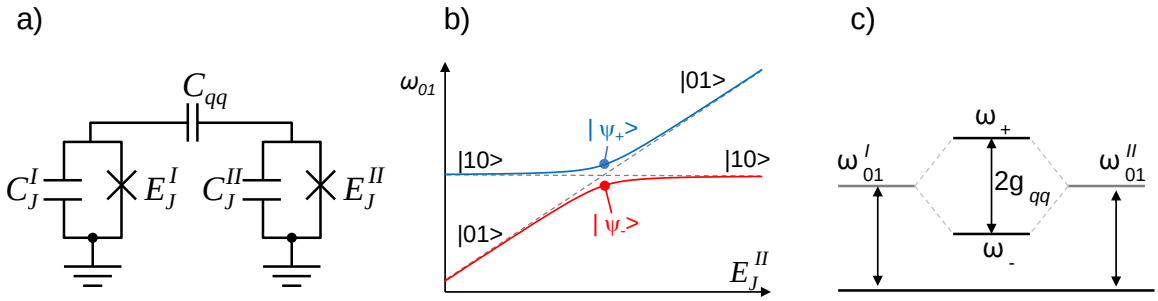

Figure 7.1: a) Schematic of the double Transmon qubit. b) Corresponding energy level diagram as a function of E_J^{II}. For $|\Delta| \gg g_{qq}$, the eigenstates are given as $|00\rangle$, $|01\rangle$, $|10\rangle$ and $|11\rangle$, whereas for $\Delta = 0$, they are $|00\rangle$, $|\psi_\pm\rangle = (|01\rangle \pm |10\rangle)/\sqrt{2}$ and $|11\rangle$, with eigenenergies $E_{00} = 0$, $E_\pm = \hbar\omega_\pm = \hbar(\omega_{01}^{I,II} \pm g_{qq})$ and $E_{11} = \hbar(\omega_{01}^I + \omega_{01}^{II})$, as shown in c).

The Hamiltonian of the double Transmon (see fig. 7.1) can be written as [112, 51]

$$\hat{H}_{dt} = \hat{H}_q + \hat{H}_{qq} \tag{7.1}$$

$$\hat{H}_q/\hbar = \omega_{01}^I \hat{\sigma}_z^I + \omega_{01}^{II} \hat{\sigma}_z^{II} \tag{7.2}$$

$$\hat{H}_{qq}/\hbar = g_{qq}\left(\hat{\sigma}_+^I \hat{\sigma}_-^{II} + \hat{\sigma}_-^I \hat{\sigma}_+^{II}\right). \tag{7.3}$$

$\hat{H}_{dt}$ consists of the individual qubit Hamiltonians and the coupling Hamiltonian as given by eq. (2.106). As before, we can rewrite $\hat{H}_{qq}$ in the two-qubit eigen basis $|00\rangle$, $|01\rangle$, $|10\rangle$, $|11\rangle$ of $\hat{H}_q$ as

$$\hat{H}_{qq}/\hbar = g_{qq}\left(|10\rangle\langle 01| + |01\rangle\langle 10|\right) \tag{7.4}$$

When the qubit frequencies are on resonance such that $\Delta = \omega_{01}^I - \omega_{01}^{II} = 0$, the eigenstates of $\hat{H}_{dt}$ are given as $|00\rangle$,$|11\rangle$, $|\psi_+\rangle = 1/\sqrt{2}(|01\rangle + |10\rangle)$ and $|\psi_-\rangle = 1/\sqrt{2}(|01\rangle - |10\rangle)$. Far off resonance, where $\Delta \gg g_{qq}$, the eigenstates will correspond to those of the uncoupled Hamiltonian $\hat{H}_q$. When coupling both Transmons to the cavity with the same

coupling constant g_{01} as given by eq. (2.91) through the capacitance C_{qb}, we obtain a coupling Hamiltonian similar to eq. (2.109):

$$\hat{H}_{qr}/\hbar = g_{01}\left(\hat{\sigma}_+^I\hat{a} + \hat{\sigma}_-^I\hat{a}^\dagger\right) + g_{01}\left(\hat{\sigma}_+^{II}\hat{a} + \hat{\sigma}_-^{II}\hat{a}^\dagger\right). \tag{7.5}$$

Here, the Hamiltonian of the resonator is given by eq. (2.45). The coupling operator between the two qubits and the resonator contains the sums $\hat{\sigma}_+^{I+II} = \hat{\sigma}_+^I + \hat{\sigma}_+^{II}$ and $\hat{\sigma}_-^{I+II} = \hat{\sigma}_-^I + \hat{\sigma}_-^{II}$. Rewriting it in the eigen basis of $\hat{H}_{qq}$ at $\Delta = 0$ yields the representation

$$\hat{H}_{qr} = \sqrt{2}g_{01}\left[\left(|11\rangle\langle\psi_+| + |\psi_+\rangle\langle 00|\right)\hat{a} + \left(|\psi_+\rangle\langle 11| + |00\rangle\langle\psi_+|\right)\hat{a}^\dagger\right]. \tag{7.6}$$

As can be seen, the qubit state $|\psi_-\rangle$ does not couple at all to the resonator, whereas the state $|\psi_+\rangle$ couples to it with an enhanced rate $\sqrt{2}g_{01}$. The states $|01\rangle = (|\psi_+\rangle + |\psi_-\rangle)/\sqrt{2}$ and $|10\rangle = (|\psi_+\rangle - |\psi_-\rangle)/\sqrt{2}$ couple to the resonator with the bare rate g_{01}. Thus, if we operate the double Transmon at $\Delta = 0$ and "park" the qubit in the state $|\psi_-\rangle$, we can effectively switch off the coupling to the resonator. To switch the coupling on again, we can perform an adiabatic transfer from the state $|\psi_-\rangle$ to the state $|10\rangle$ or $|01\rangle$ [112]. Alternatively, we can induce the transition $|\psi_-\rangle \rightarrow |\psi_+\rangle$ by using two single qubit pulses $X_\pi^I Y_\pi^{II}$, which however requires the possibility to drive each of the Transmons separately.

This coupling approach eliminates hence the frequency crowding problem and implements a fully controllable, on-demand qubit-qubit coupling scheme. In addition, parking the qubit in the state $|\psi_-\rangle$ reduces dephasing of the qubit state due to first-order flux noise, as explained in chapter 5.

7.3 Designing and Realizing A Four-Qubit Architecture

The schematic of the proposed architecture is given in fig. 7.2, showing a double Transmon capacitively coupled to a quantum bus (realized as a $\lambda/2$ transmission line resonator) and to a CJBA readout resonator, which is in turn capacitively coupled to an input transmission line. Each of the Transmons I, II is realized as a split-CPB, thereby making it frequency-tunable through an external flux $\Phi_{ext}^{I,II}$. Since the coupling scheme as discussed in section 7.2.1 requires only one of the two Transmons to be fast-frequency tunable, the design requires only one fast flux line per double Transmon. The flux of the other Transmon can be tuned to any desired bias point by using superconducting coils mounted above the chip, a technique which can be extended to a few qubits [8]. The capacitive coupling of each of the two Transmons to the quantum bus and the readout resonator is identical, which is necessary in order to be able to cancel the interaction of the logical qubit with the resonator in the state $|\psi_-\rangle$, as discussed in section 7.2.1.

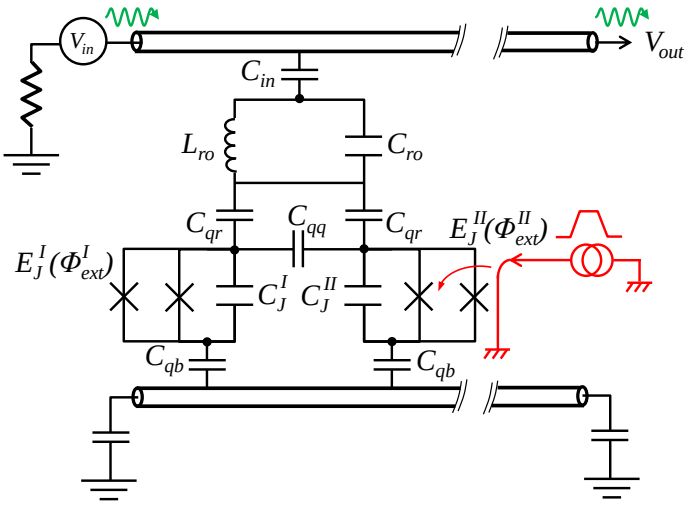

Figure 7.2: Schematic of a qubit/readout unit cell of the proposed scalable architecture. Shown is a harmonic resonator capacitively coupled to an input transmission line and to two frequency-tunable Transmon qubits, which are in turn coupled to a coplanar waveguide $\lambda/2$ resonator that acts as a quantum bus to the other qubits. One of the two Transmons is equipped with a fast magnetic flux line. For sake of clarity we have omitted the capacitances of the LC resonator and the Transmon qubits to the ground node in the circuit schematic.

As before, we can position the qubits at different, optimized frequencies for different processor operations. For qubit readout and driving, we can use a multiplexed input transmission line. In order to avoid crosstalk between individual readout resonators when driving them, we separate their resonance frequencies from each other by a small amount, typically 50 MHz. The frequency of the quantum bus is chosen in function of the minimum qubit working frequencies such that the coupling of each qubit to the bus can be made sufficiently large to realize a two-qubit gate on a time scale that is small compared to the decoherence time of the qubits.

7.3.1 Processor Operation

Here we discuss the operation principles of the proposed quantum processor. In the following paragraphs, we refer to the individual qubit frequencies of the i-th double Transmon as $\omega_{01}^{I,i}$ and $\omega_{01}^{II,i}$ and define $\Delta_i = \omega_{01}^{I,i} - \omega_{01}^{II,i}$ as the detuning between them. In addition, we denote the logical qubit states of the i-th double Transmon as $|x^i\rangle$.

As before, four basic processor operations need to be realized:

- Qubit parking (i.e. no operation)
- Single-qubit gates
- Two-qubit gates
- Qubit readout

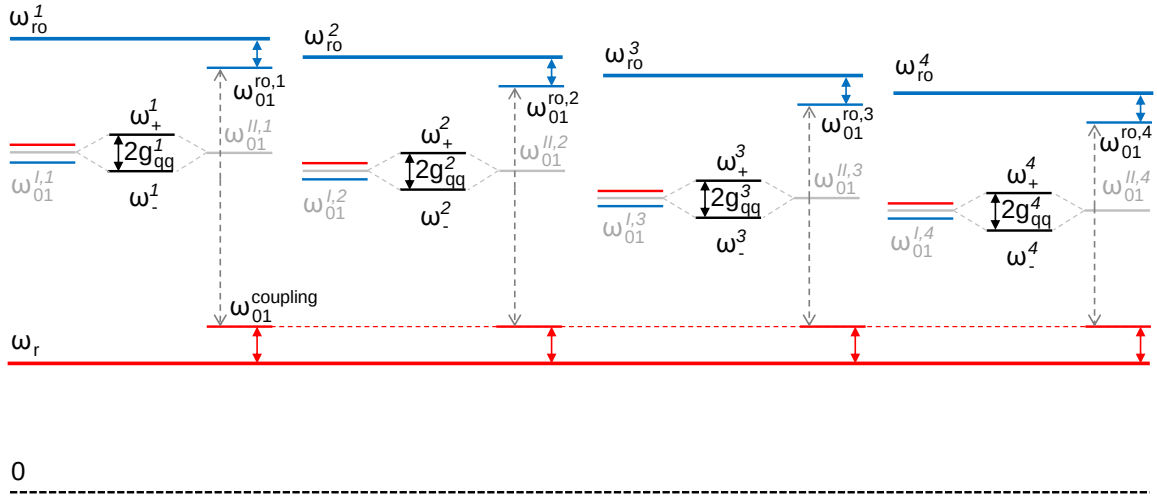

Figure 7.3: Operating frequencies of the proposed four-qubit processor, showing the frequencies of the quantum bus (ω_r, red), the readout resonators (ω_{ro}, blue) and the four double-Transmons qubits during parking (black), manipulation (red) or readout (blue). Grey bars indicate the frequencies of the uncoupled Transmon states.

As for our two-qubit processor, for each of these operations we move the involved qubits to different frequencies, defining hence frequency bands for parking, qubit manipulation and qubit readout, as shown in fig. 7.3. In the following paragraphs, we explain how we realize each of the operations mentioned above.

Qubit Parking

When not performing single-qubit or two-qubit operations, all qubits are "parked" by default. For this, each logical qubit i is positioned at a common frequency $\omega_{01}^{I,i} = \omega_{01}^{II,i} = \omega_{01}^{\text{park}}$, where its computational states are given as $|00^i\rangle$ and $\left|\psi_-^i\right\rangle$. The qubit is hence fully decoupled from the quantum bus and its readout resonator, eliminating the relaxation through the Purcell effect and the spurious coupling to other parked qubits of the processor. Qubit readout is also performed at the parking frequency (as explained below), hence this frequency should be chosen to provide an optimal readout contrast.

Single-Qubit Gates

To realize single-qubit gates, we perform an adiabatic passage from $\Delta_i = 0$ to $\Delta_i \gg g_{qq}^i$ by changing $\omega_{01}^{II,i}$, thereby performing a transfer $\left|\psi_-^i\right\rangle \rightarrow |01^i\rangle$. We can then drive the $|00^i\rangle \rightarrow |01^i\rangle$ transition of the qubit through the readout resonator or coupling bus and afterwards perform an adiabatic passage back to the parking position. Note that there will be a spurious coupling of the driven qubit to the $|00\rangle$ states of all parked qubits, which can be made small by choosing a sufficiently large detuning between the driving and

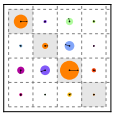

parking frequencies, but which can nevertheless limit the scalability of this architecture for large numbers of qubits.

Two-Qubit Gates

To realize a two-qubit gate between the qubits i and j, we adiabatically decrease the frequencies $\omega_{01}^{II,i}$ and $\omega_{01}^{II,j}$ to the point $\omega_{01}^{II,i} = \omega_{01}^{II,j} = \omega_{01}^{\text{coupling}}$, performing an adiabatic transfer $\left|\psi_{-}^{i}\right\rangle \rightarrow |01^i\rangle$ and $\left|\psi_{-}^{j}\right\rangle \rightarrow |01^j\rangle$. At this frequency, there will be a resonant interaction between the logical qubits of the form $\hbar g_{qq}^{ij}(|01^i, 00^j\rangle \langle 00^i, 01^j| + |00^i, 01^j\rangle \langle 01^i, 00^j|)$ with a coupling rate $g_{qq}^{ij}(\omega_{01}^{\text{coupling}}) = g_{01}^{i} g_{01}^{j}(\Delta_i^{\text{bus}} + \Delta_j^{\text{bus}})/2\Delta_i^{\text{bus}}\Delta_j^{\text{bus}}$, where $\Delta_i^{\text{bus}} = |\omega_{\text{bus}} - \omega_{01}^{II,i}|$ and $g_{01}^{i,j}$ are the qubit-resonator coupling constants of qubits i and j. Please note that there will also be a spurious coupling of the same form to the $|00\rangle$ state of all other qubits k. This residual coupling can be made small by choosing a sufficiently large detuning $\omega_{\text{park}} - \omega_{\text{coupling}} \gg g_{qq}^{ik}, g_{qq}^{jk}$, as explained in section 3.2.3.

Qubit Readout

To read out the state of qubit i, we perform an adiabatic passage to the state $|10^i\rangle$ by displacing $\omega_{01}^{II,i}$. This state can be read out using the dispersive interaction with the readout resonator. The parking frequency $\omega_{01}^{\text{park}}$ at which the readout is performed should therefore be chosen such that the readout contrast is optimal.

7.3.2 Design Parameters

As before, we need to choose the maximum transition frequency f_{01}^{max} and anharmonicity as well as the junction asymmetry for each qubit of the processor. The choice of these parameters has already been discussed in detail in chapter 3 and will therefore not be repeated here. In addition, we need to choose the qubit-qubit coupling g_{qq} and the qubit-resonator couplings g_{01}^{i}, for which we take into account the following criteria:

g_{qq} should be large enough to be able to perform an adiabatic transition $|\psi_{-}\rangle \rightarrow |01\rangle$ in a time which is small compared to the relaxation and dephasing times of the qubit. We choose therefore a coupling $2g_{qq}/2\pi = 50\ \text{MHz}$, which is large enough to be able to perform fast adiabatic transitions.

The qubit-resonator coupling g_{01}^{i} should be sufficiently large to perform a two-qubit gate in a time small compared to the qubit decoherence time, yet not too large in order to avoid spurious coupling between the $|01^i\rangle$ state of the active qubits and the $|00\rangle$ state of the idling qubits during a gate operation. Taking the design of the two-qubit processor for reference, we choose $2g_{qq}^{ij}/2\pi = 10\ \text{MHz}$ as the desired two-qubit coupling. For a qubit-resonator detuning $\Delta_i^{\text{bus}}/2\pi = 500\ \text{MHz}$, the effective qubit-qubit coupling rate as

given by eq. (2.110) then yields a required qubit-resonator coupling $g_{01}^{i}/2\pi \geq 71$ MHz. Assuming that we park the idling qubits at a detuning $\Delta_i^{\mathrm{bus}}/2\pi = 1$ GHz to the bus while performing two-qubit gates, the chosen coupling corresponds to an acceptably low residual coupling amplitude of 1.5 % between the active and idling qubits.

Finally, taking the design of the two-qubit processor as a reference, we choose a qubit-readout coupling (as generated by C_{qr}) of $g_{01}^{ro}/2\pi = 50$ MHz and a qubit-readout resonator detuning $\Delta_i^{\mathrm{ro}} = 1$ GHz at the readout frequency. Using the same reference frequency band from 4-8 GHz as for the two-qubit processor, we choose the frequency of the quantum bus as $\omega_{\mathrm{bus}}/2\pi = 4$ GHz and the frequencies of the CJBA readouts as $\omega_{ro}^{i}/2\pi = 7$ GHz $+ i \cdot 60$ MHz, displacing the frequency between adjacent CJBAs by 60 MHz, which is sufficient to avoid crosstalk when driving the readout resonators. This yields a working frequency $\omega_{01}^{\mathrm{coupling}} = 4.5$ GHz for qubit-qubit coupling, a parking frequency $\omega_{01}^{\mathrm{parking}} = 5.0$ GHz and readout frequencies starting at $\omega_{01}^{\mathrm{ro,I}} = 6.0$ GHz.

7.3.3 Implementation

Here we present the implementation of a "predecessor" of a full double-Transmon four-qubit architecture, where we use single Transmons instead to implement logical qubits, thereby simplifying fabrication and making it possible to test the readout and coupling elements of the proposed architecture without having to deal with the complexity of the double Transmons.

For the fabrication of the four qubit architecture, we use the same techniques as described in chapter 3. However, we change the design of the Transmon capacitance from an interdigitated to a parallel plate geometry, aiming to decrease the electric field strength inside the sample substrate, which was shown to be, to a large extent, responsible for intrinsic qubit dephasing and relaxation [94]. Furthermore, instead of using coplanar $\lambda/2$ resonators for the CJBA resonators, we implement them using lumped LC circuit elements, thereby significantly reducing their size. Again, all circuit components have been extensively modeled using microwave simulation software (SONNET) before fabrication. Fig. 7.4 shows a series of SEM images of the realized single-Transmon four-qubit chip. First measurements carried out with this chip have been performed to test the qubit manipulation and readout, and will be discussed in the thesis of V. Schmitt. As an example, fig. 7.5 shows a microwave transmission measurement of the four multiplexed JBA readouts on the chip.

7.3.4 Scalability of the Proposed Architecture

The proposed qubit architecture solves the problem of individual-qubit single shot readout and tunable qubit-qubit coupling for a single register of logical qubits coupled to a

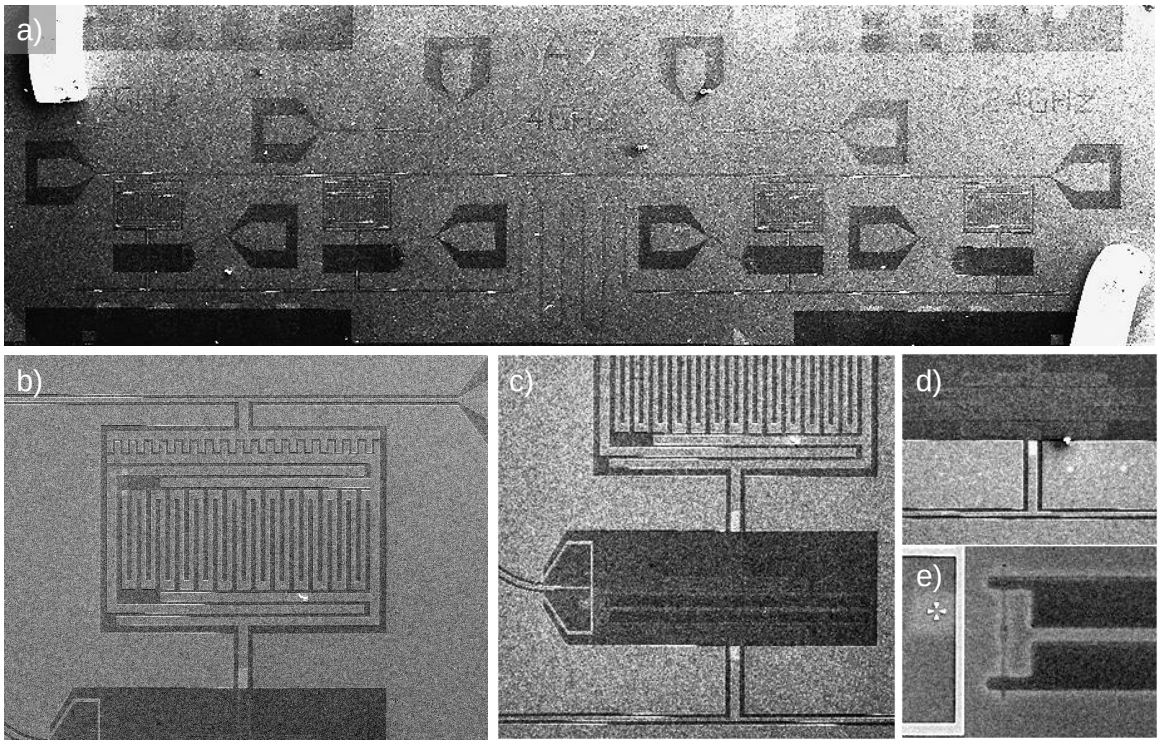

Figure 7.4: Photos of the realized four-qubit chip. a) A stitched together image of the whole chip, showing the input transmission line, the readout resonators, qubit cells, fast flux lines and quantum bus. b) A detailed view of a single readout resonator, showing the CJBA realized in lumped elements and capacitively coupled to the input transmission line (above) as well as the qubit cell (below). c) A detailed view of a single Transmon qubit, which is capacitively coupled to its readout resonator and the quantum bus and inductively coupled to a fast flux line. d) The bus coupling capacitance of a single qubit. e) A detailed view of the qubit capacitance and SQUID as well as the adjacent fast flux line.

quantum bus. The architecture requires $n+1$ fast signal lines and n DC bias lines for n qubits, hence being scalable with a linear increase in resources. However, the size of the qubit-resonator coupling capacitances limits the number of qubits that can be coupled to a single quantum bus, since placing the capacitances too close to each other will induce spurious qubit-qubit coupling. Furthermore, the spurious couplings of the form $|00^i, 01^j\rangle\langle 01^i, 00^j| + |01^i, 00^j\rangle\langle 00^i, 01^j|$, which are always present during single- and two-qubit gates, can induce further unitary errors. Our proposed architecture is thus not intrinsically scalable beyond a few tens of qubits. In order to scale further, it would therefore be necessary to use several independent registers of qubits, each connected to a separate quantum bus and coupled together by using “shuttle” qubits. These shuttle qubits would be coupled to two or more quantum buses and act solely as tunable couplers between different registers, as proposed e.g. by [41, 95].

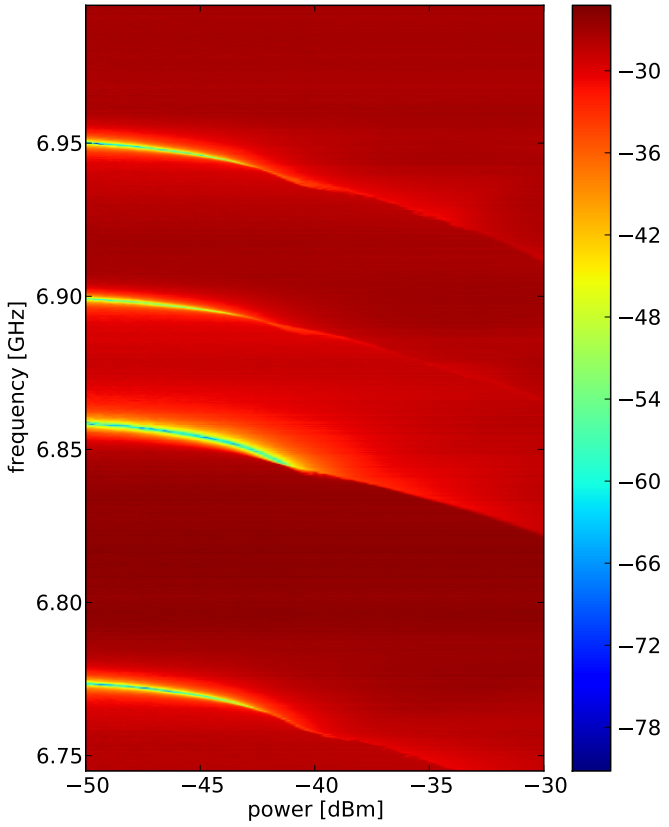

Figure 7.5: Measured $|S_{12}|$ transmission coefficient of drive and readout line of our four-qubit chip, with the four qubits far detuned from the resonators. Clearly visible are the resonances of the four CJBA resonators and their bifurcation at nominal input powers between -42dB and -40 dB.

7.4 Conclusions

I propose a four-qubit architecture based on double-Transmon qubits can potentially alleviate current problems of superconducting qubit architectures such as frequency crowding and could allow the scaling up of superconducting quantum processors to a few tens of qubits. Viewing the recent experimental advances in Transmon relaxation and dephasing times [94] that allow for a large number of quantum gates during the qubit's coherence time, the dominant roadblock on the way to scalable superconducting quantum computing seems today to be the realization of a tunable coupling scheme for a large number of qubits. Besides the possible approach presented here, different proposals have been made for solving this issue by relying e.g. on isolating logical qubits by storing their quantum information in resonators [50, 78] or quantum memories based e.g. on electronic or nuclear spins [127, 66, 67].

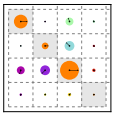

Chapter 8

Conclusions

In this thesis work, we implemented a two-qubit processor using superconducting Transmon qubits that are capacitively coupled to each other. Each of the qubit possesses its own single-shot QND readout realized using a Josephson bifurcation amplifier. Using a direct capacitive coupling between the qubits, we implemented the universal $\sqrt{i\mathrm{SWAP}}$ quantum gate and used it to create entangled two-qubit states. In addition, we implemented the Grover quantum search algorithm, demonstrating probabilistic quantum speed-up beyond the classical boundary for a four-element search problem.

Despite our successful implementation of a simple two-qubit quantum processor, the approach that we have chosen to realize it is not scalable beyond a few qubits: The fixed, always-ON type of qubit-qubit coupling employed in our processor makes it impossible to reliably switch on and off the coupling between individual qubits when increasing their number. Furthermore, the qubit coherence times that we achieved in our experiments would not be sufficient to run large-scale algorithms.

To overcome these problems, it would be necessary to increase the coherence times of superconducting qubits by a large factor and to devise a quantum computing architecture that solves the coupling problem. In chapter 7 of this work, we propose a qubit architecture that might provide a tunable coupling scheme and would therefore be scalable beyond a small number of qubits. This architecture is compatible with different kinds of Transmon qubits and could thus be implemented using the recently developed 3D Transmons [94], which exhibit very large coherence times. Together, long coherence times and a tunable qubit-qubit coupling could then possibly allow the realization of a superconducting qubit processor with a few tens of qubits.

Overall, considering the recent progress that has been made on various issues related to superconducting qubits, the realization of a superconducting quantum computer seems no longer an impossible task, although a daunting one.

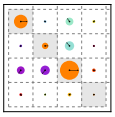

Appendix A

Modeling of Multi-Qubit Systems

Here we discuss the modeling and simulation of two coupled three-level Transmon qubits, using analytical calculations to obtain the relevant qubit energies and explaining the master equation simulation of the two-qubit system, which we use to quantify the leakage errors associated to the qubit level $|2\rangle$ when realizing the $\sqrt{i\mathrm{SWAP}}$ gate, as described in chapter 5.

A.1 Two-Qubit Three-Level Hamiltonian

The Hamiltonian of two uncoupled three-level Transmon qubits can be written in the basis $\{00, 01, 02, 10, 11, 12, 20, 21, 22\}$ as

$$\hat{H} = \begin{pmatrix} e_0^I + e_0^{II} & & & & & & & & \\ & e_0^I + e_1^{II} & & & & & & & \\ & & e_0^I + e_2^{II} & & & & & & \\ & & & e_1^I + e_0^{II} & & & & & \\ & & & & \ddots & & & & \\ & & & & & e_2^I + e_1^{II} & & & \\ & & & & & & e_2^I + e_2^{II} & & \end{pmatrix}. \quad \text{(A.1)}$$

Without loss of generality, we assume $e_0^I = 0$, $e_0^{II} = 0$. We then define $\omega_{01}^I = e_1^I$, $\omega_{01}^{II} = e_1^{II}$, $\Delta_{01} = \omega_{01}^{II} - \omega_{01}^I$ and $\alpha^I = e_2^I - 2e_1^I$ and $\alpha^{II} = e_2^{II} - 2e_1^{II}$. In this basis, the

interaction Hamiltonian for a capacitive coupling of the form (2.106) is given as

$$\hat{H}_i = \begin{pmatrix} 0 & 0 & 0 & g & 0 & 0 & 0 & 0 & 0 \\ 0 & 0 & 0 & 0 & 0 & 0 & 0 & 0 & 0 \\ 0 & 0 & 0 & 0 & \sqrt{2}g & 0 & 0 & 0 & 0 \\ 0 & g & 0 & 0 & 0 & 0 & 0 & 0 & 0 \\ 0 & 0 & \sqrt{2}g & 0 & 0 & 0 & \sqrt{2}g & 0 & 0 \\ 0 & 0 & 0 & 0 & 0 & 0 & 0 & 2g & 0 \\ 0 & 0 & 0 & 0 & \sqrt{2}g & 0 & 0 & 0 & 0 \\ 0 & 0 & 0 & 0 & 0 & 2g & 0 & 0 & 0 \\ 0 & 0 & 0 & 0 & 0 & 0 & 0 & 0 & 0 \end{pmatrix}. \tag{A.2}$$

We then go to the interaction picture with $\hat{H}_0 = \hat{H}$. There, the interaction Hamiltonian $\hat{H}_i$ acquires some time-dependent terms and is given as

$$\hat{H}_i = \begin{pmatrix} 0 & \dots & & & & & & & \\ 0 & 0 & \dots & & & & & & \\ 0 & 0 & 0 & \dots & & & & & \\ 0 & ge^{-i\Delta t} & 0 & 0 & \dots & & & & \\ 0 & 0 & \sqrt{2}ge^{-i(\Delta-\alpha^{II})t} & 0 & 0 & \dots & & & \\ 0 & 0 & 0 & 0 & 0 & 0 & \dots & & \\ 0 & 0 & 0 & 0 & \sqrt{2}ge^{-i(\Delta+\alpha^{I})t} & 0 & 0 & \dots & \\ 0 & 0 & 0 & 0 & 0 & 2ge^{-i(\Delta+\alpha^{I}-\alpha^{II})t} & 0 & 0 & \dots \\ 0 & 0 & 0 & 0 & 0 & 0 & 0 & 0 & 0 \end{pmatrix}. \tag{A.3}$$

A.1.1 Qubit Driving

The qubit driving can be modeled by the Hamiltonian (3.1), which acquires some time-dependent terms due to the chosen reference frame and is now given as

$$\hat{H}_d = \alpha \begin{pmatrix} 0 & \epsilon^*(t) & 0 \\ \epsilon(t) & 0 & \sqrt{2}\epsilon^*(t)\exp(i\alpha t) \\ 0 & \sqrt{2}\epsilon(t)\exp(-i\alpha t) & 0 \end{pmatrix}. \tag{A.4}$$

The two-qubit drive Hamiltonians are given as $\hat{H}_d^I = \hat{H}_d \otimes \mathbf{I}$ and $\hat{H}_d^{II} = \mathbf{I} \otimes \hat{H}_d$.

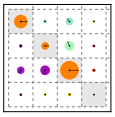

A.1.2 Relaxation and Dephasing

We model relaxation and dephasing of the three-level system using a set of six Lindblad operators. The relaxation operators are based on the three matrices

$$\sigma_{01}^{-} = \begin{pmatrix} 0 & 1 & 0 \\ 0 & 0 & 0 \\ 0 & 0 & 0 \end{pmatrix}, \qquad \sigma_{12}^{-} = \begin{pmatrix} 0 & 0 & 0 \\ 0 & 0 & 1 \\ 0 & 0 & 0 \end{pmatrix}, \qquad \sigma_{02}^{-} = \begin{pmatrix} 0 & 0 & 1 \\ 0 & 0 & 0 \\ 0 & 0 & 0 \end{pmatrix} \tag{A.5}$$

and the dephasing operators on

$$\sigma_{01}^{z} = \begin{pmatrix} 1 & 0 & 0 \\ 0 & -1 & 0 \\ 0 & 0 & 0 \end{pmatrix}, \qquad \sigma_{12}^{z} = \begin{pmatrix} 0 & 0 & 0 \\ 0 & 1 & 0 \\ 0 & 0 & -1 \end{pmatrix}, \qquad \sigma_{02}^{z} = \begin{pmatrix} 1 & 0 & 0 \\ 0 & 0 & 0 \\ 0 & 0 & -1 \end{pmatrix}. \tag{A.6}$$

Using these matrices, we define a set of three relaxation operators $L_{01}^{r} = \sqrt{\Gamma_{10}^{r}}\sigma_{01}^{-}$, $L_{12}^{r} = \sqrt{\Gamma_{12}^{r}}\sigma_{12}^{-}$ and $L_{02}^{r} = \sqrt{\Gamma_{02}^{r}}\sigma_{02}^{-}$ as well as a set of dephasing operators $L_{01}^{\phi} = \sqrt{\Gamma_{01}^{\phi}/2}\sigma_{01}^{z}$, $L_{12}^{\phi} = \sqrt{\Gamma_{12}^{\phi}/2}\sigma_{12}^{z}$, $L_{02}^{\phi} = \sqrt{\Gamma_{02}^{\phi}/2}\sigma_{02}^{z}$. From the single-qubit operators the corresponding two-qubit operators can be obtained as $L_i^I = L_i \otimes \mathbf{I}$ and $L_i^{II} = L_i \otimes \mathbf{I}$.

A.2 Master Equation Simulation

For numerical analysis, it is convenient to rewrite the Lindblad equation (2.122) in vector form as

$$\frac{d\vec{\rho}}{dt} = \mathcal{L}(t)\vec{\rho}(t), \tag{A.7}$$

where $\vec{\rho}$ is a column vector containing all elements of ρ and $\mathcal{L}$ is a "superoperator" that contains all Lindblad operators and acts on the vectorized density matrix. For a density matrix with dimension $N \times N$, the superoperator has a dimension $N^2 \times N^2$, which makes the numerical solution of eq. (A.7) computationally expensive for large N. However, for two coupled three-level Transmons the resulting matrix has the dimension 81×81, which still allows a reasonably fast simulation of the system.

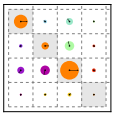

Bibliography

[1] J. Ahn, T. C. Weinacht, and P. H. Bucksbaum. Information storage and retrieval through quantum phase. *Science*, 287(5452):463–465, Jan. 2000.

[2] J. B. Altepeter, D. Branning, E. Jeffrey, T. C. Wei, P. G. Kwiat, R. T. Thew, J. L. O'Brien, M. A. Nielsen, and A. G. White. Ancilla-assisted quantum process tomography. *Physical Review Letters*, 90(19):193601, May 2003.

[3] M. Ansmann, H. Wang, R. C. Bialczak, M. Hofheinz, E. Lucero, M. Neeley, A. D. O'Connell, D. Sank, M. Weides, J. Wenner, A. N. Cleland, and J. M. Martinis. Violation of Bell's inequality in Josephson phase qubits. *Nature*, 461(7263):504–506, 2009.

[4] A. Aspect, P. Grangier, and G. Roger. Experimental realization of Einstein-Podolsky-Rosen-Bohm gedankenexperiment: A new violation of Bell's inequalities. *Physical Review Letters*, 49(2):91–94, July 1982.

[5] R. Barends, N. Vercruyssen, A. Endo, P. J. de Visser, T. Zijlstra, T. M. Klapwijk, P. Diener, S. J. C. Yates, and J. J. A. Baselmans. Minimal resonator loss for circuit quantum electrodynamics. *Applied Physics Letters*, 97(2):023508 –023508–3, July 2010.

[6] J. T. Barreiro, M. Müller, P. Schindler, D. Nigg, T. Monz, M. Chwalla, M. Hennrich, C. F. Roos, P. Zoller, and R. Blatt. An open-system quantum simulator with trapped ions. *Nature*, 470(7335):486–491, Feb. 2011.

[7] C. Bauer, R. Freeman, T. Frenkiel, J. Keeler, and A. Shaka. Gaussian pulses. *Journal of Magnetic Resonance (1969)*, 58(3):442–457, July 1984.

[8] M. Baur. *Realizing Quantum Gates and Algorithms with Three Superconducting Qubits*. PhD thesis, ETH Zürich, Zürich, 2012.

[9] J. Bell. On the Einstein Podolsky Rosen paradox. *Physics*, pages 195–200, 1964.

[10] P. Benioff. Quantum mechanical Hamiltonian models of Turing machines. *Journal of Statistical Physics*, 29(3):515–546, 1982.

[11] P. Bertet, I. Chiorescu, G. Burkard, K. Semba, C. J. P. M. Harmans, D. P. DiVincenzo, and J. E. Mooij. Dephasing of a superconducting qubit induced by photon noise. *Physical Review Letters*, 95(25):257002, Dec. 2005.

[12] P. Bertet, I. Chiorescu, C. J. P. M. Harmans, and J. E. Mooij. Dephasing of a flux-qubit coupled to a harmonic oscillator. *arXiv:cond-mat/0507290*, July 2005.

[13] P. Bertet, C. Harmans, and J. Mooij. Parametric coupling for superconducting qubits. *Physical Review B*, 73(6), Feb. 2006.

[14] R. C. Bialczak, M. Ansmann, M. Hofheinz, E. Lucero, M. Neeley, A. D. O'Connell, D. Sank, H. Wang, J. Wenner, M. Steffen, A. N. Cleland, and J. M. Martinis. Quantum process tomography of a universal entangling gate implemented with Josephson phase qubits. *Nature Physics*, 6(6):409, 2010.

[15] A. Blais, J. Gambetta, A. Wallraff, D. I. Schuster, S. M. Girvin, M. H. Devoret, and R. J. Schoelkopf. Quantum-information processing with circuit quantum electrodynamics. *Physical Review A*, 75(3):032329, Mar. 2007.

[16] A. Blais, R.-S. Huang, A. Wallraff, S. M. Girvin, and R. J. Schoelkopf. Cavity quantum electrodynamics for superconducting electrical circuits: An architecture for quantum computation. *Physical Review A*, 69(6):062320, June 2004.

[17] R. Blume-Kohout, C. Caves, and I. Deutsch. Climbing mount scalable: Physical resource requirements for a scalable quantum computer. *Foundations of Physics*, 32(11):1641–1670, 2002.

[18] V. Bouchiat, D. Vion, P. Joyez, D. Esteve, and M. H. Devoret. Quantum coherence with a single Cooper pair. *Physica Scripta*, T76(1):165, 1998.

[19] S. L. Braunstein and A. K. Pati. Speed-up and entanglement in quantum searching. *Quantum Info. Comput.*, 2(5):399–409, Aug. 2002.

[20] K.-A. Brickman, P. Haljan, P. Lee, M. Acton, L. Deslauriers, and C. Monroe. Implementation of Grover's quantum search algorithm in a scalable system. *Physical Review A*, 72(5), Nov. 2005.

[21] H.-J. Briegel, T. Calarco, D. Jaksch, J. I. Cirac, and P. Zoller. Quantum computing with neutral atoms. *Journal of Modern Optics*, 47(2-3):415–451, 2000.

[22] G. Burkard, R. H. Koch, and D. P. DiVincenzo. Multilevel quantum description of decoherence in superconducting qubits. *Physical Review B*, 69(6):064503, Feb. 2004.

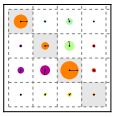

[23] I. Chiorescu, Y. Nakamura, C. J. P. M. Harmans, and J. E. Mooij. Coherent quantum dynamics of a superconducting flux qubit. *Science*, 299(5614):1869 –1871, Mar. 2003.

[24] J. M. Chow, L. DiCarlo, J. M. Gambetta, F. Motzoi, L. Frunzio, S. M. Girvin, and R. J. Schoelkopf. Optimized driving of superconducting artificial atoms for improved single-qubit gates. *Physical Review A*, 82(4):040305, Oct. 2010.

[25] I. Chuang, N. Gershenfeld, and M. Kubinec. Experimental implementation of fast quantum searching. *Physical review letters*, 80(15):3408–3411, 1998.

[26] J. I. Cirac and P. Zoller. Quantum computations with cold trapped ions. *Physical Review Letters*, 74(20):4091–4094, May 1995.

[27] J. Clarke. *The SQUID Handbook: Fundamentals and Technology of SQUIDs and SQUID Systems*, volume 1. Wiley-VCH, 2005.

[28] J. Clarke, A. N. Cleland, M. H. Devoret, D. Esteve, and J. M. Martinis. Quantum mechanics of a macroscopic variable: The phase difference of a Josephson junction. *Science*, 239(4843):992–997, Feb. 1988.

[29] J. F. Clauser, M. A. Horne, A. Shimony, and R. A. Holt. Proposed experiment to test local hidden-variable theories. *Physical Review Letters*, 23(15):880–884, Oct. 1969.

[30] E. Collin, G. Ithier, A. Aassime, P. Joyez, D. Vion, and D. Esteve. NMR-like control of a quantum bit superconducting circuit. *Physical Review Letters*, 93(15):157005, Oct. 2004.

[31] A. Cottet. *Implementation of a quantum bit in a superconducting circuit*. PhD thesis, Université Paris VI, Paris, 2002.

[32] D. L. Creedon, Y. Reshitnyk, W. Farr, J. M. Martinis, T. L. Duty, and M. E. Tobar. High Q-factor sapphire whispering gallery mode microwave resonator at single photon energies and millikelvin temperatures. *Applied Physics Letters*, 98(22):222903–222903–3, June 2011.

[33] G. M. D'Ariano and P. Lo Presti. Quantum tomography for measuring experimentally the matrix elements of an arbitrary quantum operation. *Physical Review Letters*, 86(19):4195–4198, May 2001.

[34] C. M. Dawson and M. A. Nielsen. The Solovay-Kitaev algorithm. *arXiv:quant-ph/0505030*, May 2005.

[35] D. Deutsch. Quantum theory, the Church-Turing principle and the universal quantum computer. *Proceedings of the Royal Society of London. A. Mathematical and Physical Sciences*, 400(1818):97 –117, July 1985.

[36] M. Devoret. Quantum fluctuations in electrical circuits. In *Les Houches Session on Quantum Fluctuations*, volume LXIII, pages 351–386. Elsevier, 1995.

[37] M. H. Devoret, J. M. Martinis, and J. Clarke. Measurements of macroscopic quantum tunneling out of the zero-voltage state of a current-biased Josephson junction. *Physical Review Letters*, 55(18):1908–1911, Oct. 1985.

[38] L. DiCarlo, J. M. Chow, J. M. Gambetta, L. S. Bishop, B. R. Johnson, D. I. Schuster, J. Majer, A. Blais, L. Frunzio, S. M. Girvin, and R. J. Schoelkopf. Demonstration of two-qubit algorithms with a superconducting quantum processor. *Nature*, 460(7252):240–244, July 2009.

[39] L. DiCarlo, M. D. Reed, L. Sun, B. R. Johnson, J. M. Chow, J. M. Gambetta, L. Frunzio, S. M. Girvin, M. H. Devoret, and R. J. Schoelkopf. Preparation and measurement of three-qubit entanglement in a superconducting circuit. *Nature*, 467(7315):574–578, 2010.

[40] S. Ding and Z. Jin. Review on the study of entanglement in quantum computation speedup. *Chinese Science Bulletin*, 52(16):2161–2166, 2007.

[41] D. P. DiVincenzo. The physical implementation of quantum computation. *Fortschritte der Physik*, 48(9-11):771–783, Sept. 2000.

[42] D. P. DiVincenzo. Fault-tolerant architectures for superconducting qubits. *Physica Scripta*, T137:014020, Dec. 2009.

[43] W. Dür and J. I. Cirac. Nonlocal operations: Purification, storage, compression, tomography, and probabilistic implementation. *Physical Review A*, 64(1):012317, June 2001.

[44] A. Einstein, B. Podolsky, and N. Rosen. Can quantum-mechanical description of physical reality be considered complete? *Physical Review*, 47(10):777–780, May 1935.

[45] E. Farhi, J. Goldstone, S. Gutmann, and M. Sipser. Quantum computation by adiabatic evolution. *arXiv:quant-ph/0001106*, Jan. 2000.

[46] A. Fedorov, L. Steffen, M. Baur, and A. Wallraff. Implementation of a Toffoli gate with superconducting circuits. *arXiv:1108.3966*, Aug. 2011.

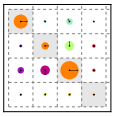

[47] R. Feynman. Simulating physics with computers. *International Journal of Theoretical Physics*, 21(6):467–488, 1982.

[48] M. H. Freedman, A. Kitaev, and Z. Wang. Simulation of topological field theories by quantum computers. *Communications in Mathematical Physics*, 227(3):587–603, 2002.

[49] S. J. Freedman and J. F. Clauser. Experimental test of local hidden-variable theories. *Physical Review Letters*, 28(14):938–941, Apr. 1972.

[50] A. Galiautdinov, A. N. Korotkov, and J. M. Martinis. Resonator–zero-qubit architecture for superconducting qubits. *Physical Review A*, 85(4):042321, Apr. 2012.

[51] J. M. Gambetta, A. A. Houck, and A. Blais. Superconducting qubit with Purcell protection and tunable coupling. *Physical Review Letters*, 106(3):030502, Jan. 2011.

[52] R. Gerritsma, G. Kirchmair, F. Zähringer, E. Solano, R. Blatt, and C. F. Roos. Quantum simulation of the Dirac equation. *Nature*, 463(7277):68–71, Jan. 2010.

[53] L. K. Grover. A fast quantum mechanical algorithm for database search. In *Proceedings of the twenty-eighth annual ACM symposium on Theory of computing*, STOC '96, page 212–219, New York, NY, USA, 1996. ACM.

[54] L. K. Grover. Quantum mechanics helps in searching for a needle in a haystack. *Physical Review Letters*, 79(2):325–328, July 1997.

[55] L. K. Grover. From Schrödinger's equation to the quantum search algorithm. *American Journal of Physics*, 69(7):769–777, 2001.

[56] S. Haroche and J.-M. Raimond. *Exploring the Quantum: Atoms, Cavities and Photons*. Oxford University Press, 2006.

[57] M. Hofheinz, H. Wang, M. Ansmann, R. C. Bialczak, E. Lucero, M. Neeley, A. D. O'Connell, D. Sank, J. Wenner, J. M. Martinis, and A. N. Cleland. Synthesizing arbitrary quantum states in a superconducting resonator. *Nature*, 459(7246):546–549, May 2009.

[58] B. Johnson. *Controlling Photons in Superconducting Electrical Circuits*. PhD thesis, Yale University, New Haven, 2010.

[59] J. Jones. NMR quantum computation. *Progress in Nuclear Magnetic Resonance Spectroscopy*, 38(4):325–360, June 2001.

[60] B. Josephson. Possible new effects in superconductive tunneling. *Physics Letters*, 1(7):251–253, July 1962.

[61] M. Khalil, F. Wellstood, and K. Osborn. Loss dependence on geometry and applied power in superconducting coplanar resonators. *IEEE Transactions on Applied Superconductivity*, 21(3):879 –882, June 2011.

[62] A. Kitaev. Fault-tolerant quantum computation by anyons. *Annals of Physics*, 303(1):2–30, Jan. 2003.

[63] E. Knill, R. Laflamme, and G. J. Milburn. A scheme for efficient quantum computation with linear optics. *Nature*, 409(6816):46–52, Jan. 2001.

[64] J. Koch, T. M. Yu, J. Gambetta, A. A. Houck, D. I. Schuster, J. Majer, A. Blais, M. H. Devoret, S. M. Girvin, and R. J. Schoelkopf. Charge-insensitive qubit design derived from the Cooper pair box. *Physical Review A*, 76(4):042319, Oct. 2007.

[65] K. Kraus, A. Böhm, J. D. Dollard, and W. H. Wootters, editors. *States, Effects, and Operations Fundamental Notions of Quantum Theory Lectures in Mathematical Physics at the University of Texas at Austin*. Lecture Notes in Physics. Springer, 1983. DOI: 10.1007/3-540-12732-1.

[66] Y. Kubo, I. Diniz, A. Dewes, V. Jacques, A. Dréau, J.-F. Roch, A. Auffeves, D. Vion, D. Esteve, and P. Bertet. Storage and retrieval of a microwave field in a spin ensemble. *Physical Review A*, 85(1):012333, Jan. 2012.

[67] Y. Kubo, C. Grezes, A. Dewes, T. Umeda, J. Isoya, H. Sumiya, N. Morishita, H. Abe, S. Onoda, T. Ohshima, V. Jacques, A. Dréau, J.-F. Roch, I. Diniz, A. Auffeves, D. Vion, D. Esteve, and P. Bertet. Hybrid quantum circuit with a superconducting qubit coupled to a spin ensemble. *Physical Review Letters*, 107(22):220501, Nov. 2011.

[68] B. P. Lanyon, M. Barbieri, M. P. Almeida, and A. G. White. Experimental quantum computing without entanglement. *Physical Review Letters*, 101(20):200501, Nov. 2008.

[69] B. P. Lanyon, C. Hempel, D. Nigg, M. Müller, R. Gerritsma, F. Zähringer, P. Schindler, J. T. Barreiro, M. Rambach, G. Kirchmair, M. Hennrich, P. Zoller, R. Blatt, and C. F. Roos. Universal digital quantum simulation with trapped ions. *Science*, 334(6052):57–61, July 2011.

[70] M. T. Levinsen, R. Y. Chiao, M. J. Feldman, and B. A. Tucker. An inverse AC Josephson effect voltage standard. *Applied Physics Letters*, 31(11):776 –778, Dec. 1977.

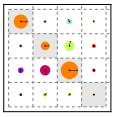

[71] N. Linden and S. Popescu. Good dynamics versus bad kinematics: Is entanglement needed for quantum computation? *Physical Review Letters*, 87(4):047901, July 2001.

[72] S. Lloyd. Universal quantum simulators. *Science*, 273(5278):1073–1078, Aug. 1996.

[73] S. Lloyd. Quantum search without entanglement. *Physical Review A*, 61(1):010301, Dec. 1999.

[74] D. Loss and D. P. DiVincenzo. Quantum computation with quantum dots. *Physical Review A*, 57(1):120–126, Jan. 1998.

[75] E. Lucero, J. Kelly, R. C. Bialczak, M. Lenander, M. Mariantoni, M. Neeley, A. D. O'Connell, D. Sank, H. Wang, M. Weides, J. Wenner, T. Yamamoto, A. N. Cleland, and J. M. Martinis. Reduced phase error through optimized control of a superconducting qubit. *Physical Review A*, 82(4):042339, Oct. 2010.

[76] H. Mabuchi and A. C. Doherty. Cavity quantum electrodynamics: Coherence in context. *Science*, 298(5597):1372–1377, Nov. 2002.

[77] F. Mallet, F. R. Ong, A. Palacios-Laloy, F. Nguyen, P. Bertet, D. Vion, and D. Esteve. Single-shot qubit readout in circuit quantum electrodynamics. *Nat Phys*, 5(11):791–795, Nov. 2009.

[78] M. Mariantoni, H. Wang, T. Yamamoto, M. Neeley, R. C. Bialczak, Y. Chen, M. Lenander, E. Lucero, A. D. O'Connell, D. Sank, M. Weides, J. Wenner, Y. Yin, J. Zhao, A. N. Korotkov, A. N. Cleland, and J. M. Martinis. Implementing the quantum von Neumann architecture with superconducting circuits. *Science*, 334(6052):61 –65, Oct. 2011.

[79] J. M. Martinis, K. B. Cooper, R. McDermott, M. Steffen, M. Ansmann, K. D. Osborn, K. Cicak, S. Oh, D. P. Pappas, R. W. Simmonds, and C. C. Yu. Decoherence in Josephson qubits from dielectric loss. *Physical Review Letters*, 95(21):210503, Nov. 2005.

[80] J. M. Martinis, M. H. Devoret, and J. Clarke. Energy-level quantization in the zero-voltage state of a current-biased Josephson junction. *Physical Review Letters*, 55(15):1543–1546, Oct. 1985.

[81] J. M. Martinis, M. H. Devoret, and J. Clarke. Experimental tests for the quantum behavior of a macroscopic degree of freedom: The phase difference across a Josephson junction. *Physical Review B*, 35(10):4682–4698, Apr. 1987.

[82] J. M. Martinis, S. Nam, J. Aumentado, and C. Urbina. Rabi oscillations in a large Josephson-junction qubit. *Physical Review Letters*, 89(11):117901, 2002.

[83] A. Megrant, C. Neill, R. Barends, B. Chiaro, Y. Chen, L. Feigl, J. Kelly, E. Lucero, M. Mariantoni, P. J. J. O'Malley, D. Sank, A. Vainsencher, J. Wenner, T. C. White, Y. Yin, J. Zhao, C. J. Palmstrøm, J. M. Martinis, and A. N. Cleland. Planar superconducting resonators with internal quality factors above one million. *Applied Physics Letters*, 100(11):113510–113510–4, Mar. 2012.

[84] D. Mermin. *Quantum Computer Science*. Cambridge University Press, 1st edition, 2007.

[85] D. A. Meyer. Sophisticated quantum search without entanglement. *Physical Review Letters*, 85(9):2014–2017, Aug. 2000.

[86] C. Monroe, D. M. Meekhof, B. E. King, W. M. Itano, and D. J. Wineland. Demonstration of a fundamental quantum logic gate. *Physical Review Letters*, 75(25):4714–4717, Dec. 1995.

[87] J. E. Mooij, T. P. Orlando, L. Levitov, L. Tian, C. H. van der Wal, and S. Lloyd. Josephson persistent-current qubit. *Science*, 285(5430):1036 –1039, 1999.

[88] F. Motzoi, J. M. Gambetta, P. Rebentrost, and F. K. Wilhelm. Simple pulses for elimination of leakage in weakly nonlinear qubits. *Physical Review Letters*, 103(11):110501, 2009.

[89] Y. Nakamura, Y. A. Pashkin, and J. S. Tsai. Coherent control of macroscopic quantum states in a single-Cooper-pair box. *Nature*, 398(6730):786–788, Apr. 1999.

[90] F. Nguyen. *Cooper Pair Box Circuits: Two-Qubit Gate, Single-Shot Readout, and Current to Frequency Conversion*. PhD thesis, Université Paris VI, Saclay, 2008.

[91] M. A. Nielsen and I. L. Chuang. *Quantum Compuation and Quantum Information*. Cambridge University Press, 2000.

[92] S. Osnaghi, P. Bertet, A. Auffeves, P. Maioli, M. Brune, J. M. Raimond, and S. Haroche. Coherent control of an atomic collision in a cavity. *Physical Review Letters*, 87(3):037902, June 2001.

[93] L. Ozyuzer, A. E. Koshelev, C. Kurter, N. Gopalsami, Q. Li, M. Tachiki, K. Kadowaki, T. Yamamoto, H. Minami, H. Yamaguchi, T. Tachiki, K. E. Gray, W.-K. Kwok, and U. Welp. Emission of coherent THz radiation from superconductors. *Science*, 318(5854):1291–1293, Nov. 2007.

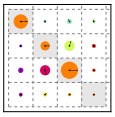

[94] H. Paik, D. I. Schuster, L. S. Bishop, G. Kirchmair, G. Catelani, A. P. Sears, B. R. Johnson, M. J. Reagor, L. Frunzio, L. I. Glazman, S. M. Girvin, M. H. Devoret, and R. J. Schoelkopf. Observation of high coherence in Josephson junction qubits measured in a three-dimensional circuit QED architecture. *Physical Review Letters*, 107(24):240501, Dec. 2011.

[95] A. Palacios-Laloy. *Superconducting Qubit in a Resonator: Test of the Leggett-Garg Inequality and Single-Shot Readout*. PhD thesis, Commissariat à l'Energie Atomique, Saclay, 2010.

[96] J. H. Plantenberg, P. C. d. Groot, C. J. P. M. Harmans, and J. E. Mooij. Demonstration of controlled-NOT quantum gates on a pair of superconducting quantum bits. *Nature*, 447(7146):836, June 2007.

[97] J. F. Poyatos, J. I. Cirac, and P. Zoller. Complete characterization of a quantum process: The two-bit quantum gate. *Physical Review Letters*, 78(2):390–393, Jan. 1997.

[98] D. M. Pozar. *Microwave Engineering*. Wiley, 4 edition, Nov. 2011.

[99] E. Purcell. Spontaneous emission probabilities at radio frequencies. In *Physical Review*, volume 69, page 681, 1946.

[100] R. Raussendorf and H. J. Briegel. A one-way quantum computer. *Physical Review Letters*, 86(22):5188–5191, May 2001.

[101] M. D. Reed, L. DiCarlo, S. E. Nigg, L. Sun, L. Frunzio, S. M. Girvin, and R. J. Schoelkopf. Realization of three-qubit quantum error correction with superconducting circuits. *arXiv:1109.4948*, Sept. 2011.

[102] C. Rigetti, S. Poletto, J. M. Gambetta, B. L. T. Plourde, J. M. Chow, A. D. Corcoles, J. A. Smolin, S. T. Merkel, J. R. Rozen, G. A. Keefe, M. B. Rothwell, M. B. Ketchen, and M. Steffen. Superconducting qubit in waveguide cavity with coherence time approaching 0.1ms. *arXiv:1202.5533*, Feb. 2012.

[103] T. v. d. Sar, Z. H. Wang, M. S. Blok, H. Bernien, T. H. Taminiau, D. M. Toyli, D. A. Lidar, D. D. Awschalom, R. Hanson, and V. V. Dobrovitski. Decoherence-protected quantum gates for a hybrid solid-state spin register. *Nature*, 484(7392):82–86, Apr. 2012.

[104] D. I. Schuster. *Circuit Quantum Electrodynamics*. PhD thesis, Yale University, New Haven, 2007.

[105] N. Shenvi, J. Kempe, and K. B. Whaley. Quantum random-walk search algorithm. *Physical Review A*, 67(5):052307, May 2003.

[106] P. Shor. Algorithms for quantum computation: discrete logarithms and factoring. In *Foundations of Computer Science, 1994 Proceedings., 35th Annual Symposium on*, pages 124 –134, Nov. 1994.

[107] P. W. Shor. Polynomial-time algorithms for prime factorization and discrete logarithms on a quantum computer. *arXiv:quant-ph/9508027*, Aug. 1995. SIAM J.Sci.Statist.Comput. 26 (1997) 1484.

[108] I. Siddiqi, R. Vijay, M. Metcalfe, E. Boaknin, L. Frunzio, R. J. Schoelkopf, and M. H. Devoret. Dispersive measurements of superconducting qubit coherence with a fast latching readout. *Physical Review B*, 73(5):054510, Feb. 2006.

[109] I. Siddiqi, R. Vijay, F. Pierre, C. M. Wilson, M. Metcalfe, C. Rigetti, L. Frunzio, and M. H. Devoret. RF-Driven Josephson bifurcation amplifier for quantum measurement. *Physical Review Letters*, 93(20):207002, Nov. 2004.

[110] R. W. Simmonds, K. M. Lang, D. A. Hite, S. Nam, D. P. Pappas, and J. M. Martinis. Decoherence in Josephson phase qubits from junction resonators. *Physical Review Letters*, 93(7):077003, Aug. 2004.

[111] J. Simon, W. S. Bakr, R. Ma, M. E. Tai, P. M. Preiss, and M. Greiner. Quantum simulation of antiferromagnetic spin chains in an optical lattice. *Nature*, 472(7343):307–312, Apr. 2011.

[112] S. J. Srinivasan, A. J. Hoffman, J. M. Gambetta, and A. A. Houck. Tunable coupling in circuit quantum electrodynamics using a superconducting charge qubit with a V-shaped energy level diagram. *Physical Review Letters*, 106(8):083601, Feb. 2011.

[113] D. J. Van Harlingen, T. L. Robertson, B. L. T. Plourde, P. A. Reichardt, T. A. Crane, and J. Clarke. Decoherence in Josephson-junction qubits due to critical-current fluctuations. *Physical Review B*, 70(6):064517, Aug. 2004.

[114] L. M. K. Vandersypen, M. Steffen, G. Breyta, C. S. Yannoni, M. H. Sherwood, and I. L. Chuang. Experimental realization of Shor's quantum factoring algorithm using nuclear magnetic resonance. *Nature*, 414(6866):883–887, Dec. 2001.

[115] L. M. K. Vandersypen, M. Steffen, M. H. Sherwood, C. S. Yannoni, G. Breyta, and I. L. Chuang. Implementation of a three-quantum-bit search algorithm. *Applied Physics Letters*, 76(5):646, 2000.

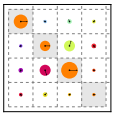

[116] R. Vijay, M. H. Devoret, and I. Siddiqi. Invited review article: The Josephson bifurcation amplifier. *Review of Scientific Instruments*, 80(11):111101–111101–17, Nov. 2009.

[117] R. Vijay, C. Macklin, D. H. Slichter, S. J. Weber, K. W. Murch, R. Naik, A. N. Korotkov, and I. Siddiqi. Quantum feedback control of a superconducting qubit: Persistent Rabi oscillations. *arXiv:1205.5591*, May 2012.

[118] D. Vion, A. Aassime, A. Cottet, P. Joyez, H. Pothier, C. Urbina, D. Esteve, and M. H. Devoret. Manipulating the quantum state of an electrical circuit. *Science*, 296(5569):886 –889, May 2002.

[119] A. Wallraff, D. I. Schuster, A. Blais, L. Frunzio, R.-S. Huang, J. Majer, S. Kumar, S. M. Girvin, and R. J. Schoelkopf. Strong coupling of a single photon to a superconducting qubit using circuit quantum electrodynamics. *Nature*, 431(7005):162–167, 2004.

[120] H. Walther, B. T. H. Varcoe, B.-G. Englert, and T. Becker. Cavity quantum electrodynamics. *Reports on Progress in Physics*, 69(5):1325–1382, May 2006.

[121] H. Wang, M. Hofheinz, J. Wenner, M. Ansmann, R. C. Bialczak, M. Lenander, E. Lucero, M. Neeley, A. D. OConnell, D. Sank, M. Weides, A. N. Cleland, and J. M. Martinis. Improving the coherence time of superconducting coplanar resonators. *Applied Physics Letters*, 95(23):233508 –233508–3, Dec. 2009.

[122] T. Yamamoto, M. Neeley, E. Lucero, R. C. Bialczak, J. Kelly, M. Lenander, M. Mariantoni, A. D. O'Connell, D. Sank, H. Wang, M. Weides, J. Wenner, Y. Yin, A. N. Cleland, and J. M. Martinis. Quantum process tomography of two-qubit controlled-Z and controlled-NOT gates using superconducting phase qubits. *Physical Review B*, 82(18):184515, Nov. 2010.

[123] T. Yamamoto, Y. A. Pashkin, O. Astafiev, Y. Nakamura, and J. S. Tsai. Demonstration of conditional gate operation using superconducting charge qubits. *Nature*, 425(6961):941, Oct. 2003.

[124] B. Yurke and J. S. Denker. Quantum network theory. *Physical Review A*, 29(3):1419–1437, Mar. 1984.

[125] S.-B. Zheng. One-step synthesis of multiatom Greenberger-Horne-Zeilinger states. *Physical Review Letters*, 87(23):230404, Nov. 2001.

[126] S.-B. Zheng and G.-C. Guo. Efficient scheme for two-atom entanglement and quantum information processing in cavity QED. *Physical Review Letters*, 85(11):2392–2395, Sept. 2000.

[127] X. Zhu, S. Saito, A. Kemp, K. Kakuyanagi, S.-i. Karimoto, H. Nakano, W. J. Munro, Y. Tokura, M. S. Everitt, K. Nemoto, M. Kasu, N. Mizuochi, and K. Semba. Coherent coupling of a superconducting flux qubit to an electron spin ensemble in diamond. *Nature*, 478(7368):221–224, Oct. 2011.

Characterization of a Two-Transmon Processor with Individual Single-Shot Qubit Readout

A. Dewes,[1] F. R. Ong,[1] V. Schmitt,[1] R. Lauro,[1] N. Boulant,[2] P. Bertet,[1] D. Vion,[1] and D. Esteve[1]
[1]*Quantronics group, Service de Physique de l'État Condensé (CNRS URA 2464), IRAMIS, DSM, CEA-Saclay, 91191 Gif-sur-Yvette, France*
[2]*LRMN, Neurospin, I2BM, DSV, 91191CEA-Saclay, 91191 Gif-sur-Yvette, France*
(Received 26 September 2011; published 2 February 2012)

We report the characterization of a two-qubit processor implemented with two capacitively coupled tunable superconducting qubits of the transmon type, each qubit having its own nondestructive single-shot readout. The fixed capacitive coupling yields the $\sqrt{i\mathrm{SWAP}}$ two-qubit gate for a suitable interaction time. We reconstruct by state tomography the coherent dynamics of the two-bit register as a function of the interaction time, observe a violation of the Bell inequality by 22 standard deviations after correcting readout errors, and measure by quantum process tomography a gate fidelity of 90%.

DOI: 10.1103/PhysRevLett.108.057002 PACS numbers: 85.25.Cp, 03.67.Lx, 74.78.Na

Quantum-information processing is one of the most appealing ideas for exploiting the resources of quantum physics and performing tasks beyond the reach of classical machines [1]. Ideally, a quantum processor consists of an ensemble of highly coherent two-level systems, the qubits, that can be efficiently reset, that can follow any unitary evolution needed by an algorithm using a universal set of single- and two-qubit gates, and that can be readout projectively. In the domain of electrical quantum circuits [2], important progress [3–7] has been achieved recently with the operation of elementary quantum processors based on different superconducting qubits. Those based on transmon qubits [3,4,8,9] are well protected against decoherence but embed all the qubits in a single resonator used both for coupling them and for joint readout. Consequently, individual readout of the qubits is not possible and the results of a calculation, as the Grover search algorithm demonstrated on two qubits [3], cannot be obtained by running the algorithm only once. Furthermore, the overhead for getting a result from such a processor without single-shot readout but with a larger number of qubits overcomes the speed-up gain expected for any useful algorithm. The situation is different for processors based on phase qubits [5,6,10], where the qubits are more sensitive to decoherence but can be read individually with high fidelity, although destructively. This significant departure from the wished scheme can be circumvented, when needed, since a destructive readout can be transformed into a nondestructive one at the cost of adding one ancilla qubit and one extra two-qubit gate for each qubit to be read projectively. Moreover, energy release during a destructive readout can result in a sizable cross talk between the readout outcomes, which can also be solved at the expense of a more complex architecture [10,11].

In this work, we operate a new architecture that comes closer to the ideal quantum processor design than the above-mentioned ones. Our circuit is based on frequency tunable transmons that are capacitively coupled. Although the coupling is fixed, the interaction is effective only when the qubits are on resonance, which yields the $\sqrt{i\mathrm{SWAP}}$ universal gate for an adequate coupling duration. Each qubit is equipped with its own nondestructive single-shot readout [12,13] and the two qubits can be read with low cross talk. In order to characterize the circuit operation, we reconstruct the time evolution of the two-qubit register density matrix during the resonant and coherent exchange of a single quantum of excitation between the qubits by quantum state tomography. Then, we prepare a Bell state with concurrence 0.85, measure the Clauser-Horne-Shimony-Holt (CHSH) entanglement witness, and find a violation of the corresponding Bell inequality by 22 standard deviations. We then characterize the $\sqrt{i\mathrm{SWAP}}$ universal gate operation by determining its process map with quantum process tomography [1]. We find a gate fidelity of 90% due to qubit decoherence and systematic unitary errors.

The circuit implemented is schematized in Fig. 1(a): the coupled qubits with their respective control and readout subcircuits are fabricated on a Si chip [see Supplemental Material (SM), Sec. I [14]]. The chip is cooled down to 20 mK in a dilution refrigerator and connected to room-temperature sources and measurement devices by attenuated and filtered control lines and by two measurement lines equipped with cryogenic amplifiers. Each transmon $j = \mathrm{I}, \mathrm{II}$ is a capacitively shunted SQUID characterized by its Coulomb energy E_C^j for a Cooper pair, the asymmetry d_j between its two Josephson junctions, and its total effective Josephson energy $E_J^j(\phi_j) = E_J^j|\cos(x_j)|\sqrt{1 + d_j^2 \tan^2(x_j)}$, with $x_j = \pi\phi_j/\phi_0$, ϕ_0 the flux quantum, and ϕ_j the magnetic flux through the SQUIDs induced by two local current lines with a 0.5 GHz bandwidth. The transition frequencies $\nu_j \simeq \sqrt{2E_C^j E_J^j}/h$ between the two lowest energy states $|0\rangle_j$ and $|1\rangle_j$ can thus be tuned by ϕ_j. The qubits are coupled by a capacitor with nominal value $C_c \simeq 0.13$ fF and form a register with the Hamiltonian (see Sec. II of the SM [14])

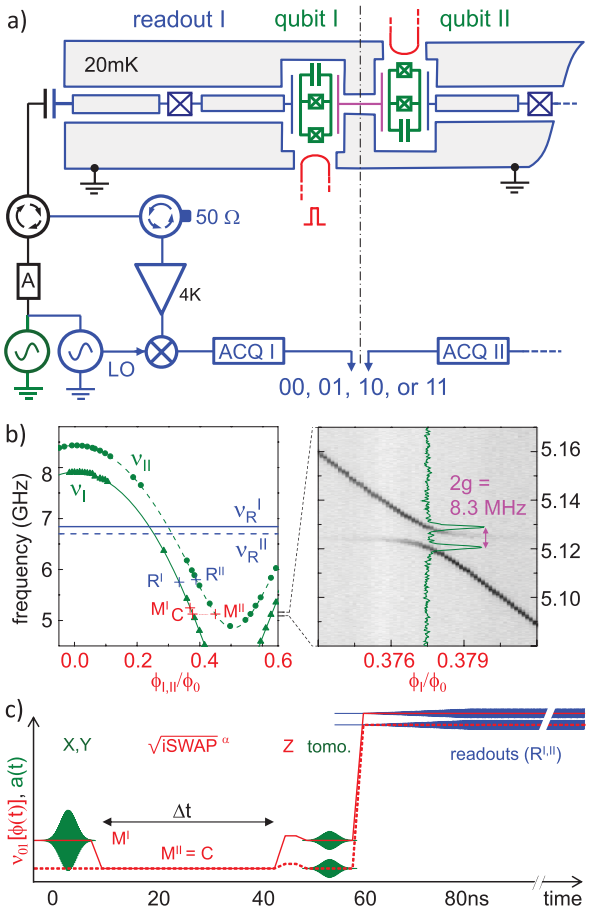

FIG. 1 (color). (a) Circuit schematics of the experiment showing the qubits I and II in green, their readout devices in grayed blue, and the homodyne detection circuits with their digitizer (ACQ) in blue. (b) Left-hand panel: Spectroscopy of the sample showing the resonator frequencies $\nu_R^{\mathrm{I}} = 6.84$ GHz and $\nu_R^{\mathrm{II}} = 6.70$ GHz (horizontal lines), and the measured (disks, triangles) and fitted (lines) qubit frequencies $\nu_{\mathrm{I,II}}$ as a function of their flux bias $\phi_{\mathrm{I,II}}$ when the other qubit is far detuned. Right-hand panel: Spectroscopic anticrossing of the two qubits revealed by the 2D plot of $p_{01} + p_{10}$ as a function of the probe frequency and of ϕ_{I}, at $\nu_{\mathrm{II}} = 5.124$ GHz. (c) Typical pulse sequence including X or Y rotations, a $\sqrt{i\mathrm{SWAP}}^{\alpha}$ gate, Z rotations, and tomographic and readout pulses. Microwave pulses $a(t)$ for qubit (green) and for readout (blue) are drawn on top of the $\nu_{\mathrm{I,II}}(\phi)$ dc pulses (red lines).

$H = h(-\nu_{\mathrm{I}}\sigma_z^{\mathrm{I}} - \nu_{\mathrm{II}}\sigma_z^{\mathrm{II}} + 2g\sigma_y^{\mathrm{I}}\sigma_y^{\mathrm{II}})/2$. Here h is the Planck constant, $\sigma_{x,y,z}$ are the Pauli operators, $2g = \sqrt{E_C^{\mathrm{I}}E_C^{\mathrm{II}}\nu_{\mathrm{I}}\nu_{\mathrm{II}}}/E_{Cc} \ll \nu_{\mathrm{I,II}}$ is the coupling frequency, and E_{Cc} the Coulomb energy of a Cooper pair on the coupling capacitor. The two-qubit gate is defined in the uncoupled basis $\{|uv\rangle\} \equiv \{|0\rangle_{\mathrm{I}}, |1\rangle_{\mathrm{I}}\} \otimes \{|0\rangle_{\mathrm{II}}, |1\rangle_{\mathrm{II}}\}$, at a working point $M_{\mathrm{I,II}}$ where the qubits are sufficiently detuned ($\nu_{\mathrm{II}} - \nu_{\mathrm{I}} \gg 2g$) to be negligibly coupled. Bringing them on resonance at a frequency ν in a time much shorter than $1/2g$ but much longer than $1/\nu$, and keeping them on resonance during a time Δt, one implements an operation $\Theta_{\mathrm{I}}\Theta_{\mathrm{II}}\sqrt{i\mathrm{SWAP}}^{(8g\Delta t)}$, which is the product of the

$$\sqrt{i\mathrm{SWAP}} = \begin{pmatrix} 1 & 0 & 0 & 0 \\ 0 & 1/\sqrt{2} & -i/\sqrt{2} & 0 \\ 0 & -i/\sqrt{2} & 1/\sqrt{2} & 0 \\ 0 & 0 & 0 & 1 \end{pmatrix}$$

gate to an adjustable power and of two single qubit phase gates $\Theta_j = \exp(i\theta_j\sigma_z^j/2)$ accounting for the dynamical phases $\theta_j = \int 2\pi(\nu - \nu_J)dt$ accumulated during the coupling. The exact $\sqrt{i\mathrm{SWAP}}$ gate can thus be obtained by choosing $\Delta t = 1/8g$ and by applying a compensation rotation Θ_j^{-1} to each qubit afterward.

For readout, each qubit is capacitively coupled to its own $\lambda/2$ coplanar waveguide resonator with frequency ν_R^j and quality factor $Q_j \simeq 700$. The frequency ν_R^j is shifted by $\pm\chi$ depending on the measured qubit state, with $\chi \simeq g_0^2/(\nu_R^j - \nu_j)$ and g_0 the qubit-resonator coupling frequency. Each resonator is made nonlinear with a Josephson junction and is operated as a Josephson bifurcation amplifier, as explained in detail in [13]: ideally, it switches from a low to a high amplitude oscillating state when qubit state $|1\rangle$ is measured. Consequently, the homodyne measurement [see Fig. 1(a)] of two microwave pulses simultaneously applied to and reflected from the two resonators yields a two-bit outcome uv that maps with a high fidelity the state $|uv\rangle$ on which the register is projected; the probabilities p_{uv} of the four possible outcomes are determined by repeating the same experimental sequence a few 10^4 times. Single qubit rotations $u(\theta)$ by an angle θ around an axis $\vec{u}$ of the XY plane of the Bloch sphere are obtained by applying Gaussian microwave pulses directly through the readout resonators, with frequencies ν_j, phases $\varphi_j = (\vec{X}, \vec{u})$, and calibrated areas $A_j \propto \theta$; a sufficiently high power is used to compensate for the filtering effect of each resonator, which depends on the detuning $\nu_j - \nu_R^j$. Rotations around Z are obtained by changing temporarily $\nu_{\mathrm{I,II}}$ with dc pulses on the current lines.

The sample is first characterized by spectroscopy [see Fig. 1(b)], and a fit of the transmon model to the data yields the sample parameters (see Sec. III of the SM [14]). The working points where the qubits are manipulated ($M^{\mathrm{I,II}}$), resonantly coupled (C), and readout ($R^{\mathrm{I,II}}$) are chosen to yield sufficiently long relaxation times ~ 0.5 μs [15] during gates, negligible residual coupling during single qubit rotations and readout, and best possible fidelities at readout. Figure 1(b) shows these points as well as the spectroscopic anticrossing of the two qubits at point C, where $2g = 8.3$ MHz in agreement with the design value of C_c. Then, readout errors are characterized at $R^{\mathrm{I,II}}$ (see Sec. IV of the SM [14]): In a first approximation, the errors are independent for the two readouts and are of about 10% and 20% when reading $|0\rangle$ and $|1\rangle$, respectively. This limited

fidelity results for a large part from energy relaxation of the qubits at readout. In addition, we observe a small readout cross talk, i.e., a variation of up to 2% in the probability of an outcome of readout j depending on the state of the other qubit. All these effects are calibrated by measuring the four p_{uv} probabilities for each of the four $|uv\rangle$ states, which allows us to calculate a 4×4 readout matrix $\mathcal{R}$ linking the p_{uv}'s to the $|uv\rangle$ populations.

Repeating the pulse sequence shown in Fig. 1(c) at $M^{\mathrm{I}} = 5.247$ GHz, $M^{\mathrm{II}} = C = 5.125$ GHz, $R^{\mathrm{I}} = 5.80$ GHz, $R^{\mathrm{II}} = 5.75$ GHz, and applying the readout corrections $\mathcal{R}$, we observe the coherent exchange of a single excitation initially stored in qubit I. We show in Fig. 2 the time evolution of the measured $|uv\rangle$ populations, in fair agreement with a prediction obtained by integration of a simple time independent Liouville master equation of the system, involving the independently measured relaxation times $T_1^{\mathrm{I}} = 0.44$ μs and $T_1^{\mathrm{II}} = 0.52$ μs, and two independent effective pure dephasing times $T_\varphi^{\mathrm{I}} = T_\varphi^{\mathrm{II}} = 2.0$ μs as fitting parameters. Tomographic reconstruction of the register density matrix ρ is obtained by measuring the expectation values of the 15 two-qubit Pauli operators $\{P_k\} = \{I, X, Y, Z\}_{\mathrm{I}} \otimes \{I, X, Y, Z\}_{\mathrm{II}} - \{II\}$, the X_j and Y_j measurements being obtained using tomographic pulses $\vec{Y}_j$ ($-90°$) or $\vec{X}_j$ ($90°$) just before readout. The ρ matrix is calculated from the Pauli set by global minimization of the Hilbert-Schmidt distance between the possibly nonphysical ρ and all physical (i.e., positive-semidefinite) ρ's. This can be done at regular intervals of the coupling time to produce a movie of $\rho(\Delta t)$ (see the Supplemental Material [14]) showing the swapping of the $|10\rangle$ and $|01\rangle$ populations at frequency $2g$, the corresponding oscillation of the coherences, as well as the relaxation towards $|00\rangle$. Figure 2 shows $\{\langle P_k\rangle\}$ and ρ only at $\Delta t = 0$ ns and after a $\sqrt{i\mathrm{SWAP}}$ obtained at $\Delta t = 31$ ns with Θ_j^{-1} rotations of $\theta_{\mathrm{I}} \simeq -65°$ and $\theta_{\mathrm{II}} \simeq +60°$. The fidelity $F = \langle\psi_{\mathrm{id}}|\rho|\psi_{\mathrm{id}}\rangle$ of ρ with the ideal density matrices $|\psi_{\mathrm{id}}\rangle\langle\psi_{\mathrm{id}}|$ is 95% and 91%, respectively, and is limited by errors on the preparation pulse, statistical noise, and relaxation.

To quantify in a different way our ability to entangle the two qubits, we prepare a Bell state $|10\rangle + e^{i\psi}|01\rangle$ (with $\psi = \theta_{\mathrm{II}} - \theta_{\mathrm{I}}$) using the pulse sequence of Fig. 1(c) with $\Delta t = 31$ ns and no Θ_j^{-1} rotations, and measure the CHSH

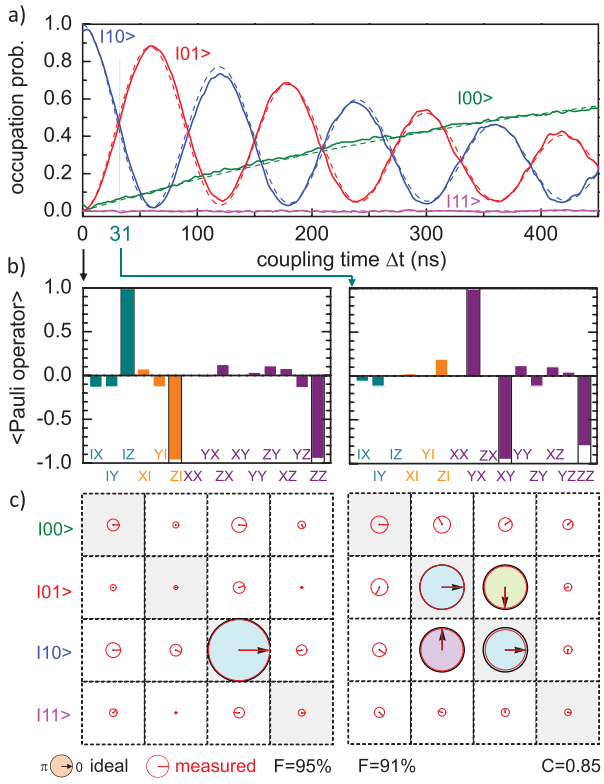

FIG. 2 (color). Coherent swapping of a single excitation between the qubits. (a) Experimental (solid lines) and fitted (dashed lines) occupation probabilities of the four computational states $|00\rangle \ldots |11\rangle$ as a function of the coupling duration. No Z or tomographic pulses are applied here. (b),(c) State tomography of the initial state (left) and of the state produced by the $\sqrt{i\mathrm{SWAP}}$ gate (right). (b) Ideal (empty bars) and experimental (color filling) expected values of the 15 Pauli operators $IX, \ldots, ZZ$. (c) Corresponding ideal (color-filled black circles with black arrow) and experimental (red circle and arrow) density matrices, as well as fidelity F and concurrence C. Each complex matrix element is represented by a circle with an area proportional to its modulus (diameter equals cell size for unit modulus) and by an arrow giving its argument. See Sec. VI of the SM [14] for a real and imaginary part representation of the matrices.

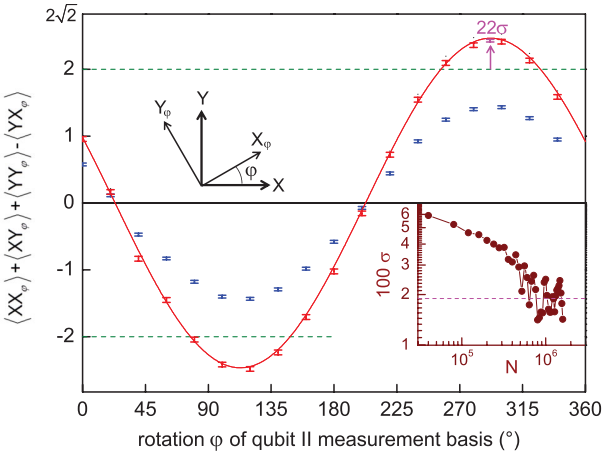

FIG. 3 (color). Test of the CHSH-Bell inequality on a $|10\rangle + e^{i\psi}|01\rangle$ state by measuring the qubits along X^{I} or Y^{I} and X_φ^{II} or Y_φ^{II} (see top-left inset), respectively. Blue (red) error bars are the experimental CHSH entanglement witness determined from the raw (readout-error corrected) measurements as a function of the angle φ between the measuring basis, whereas solid line is a fit using ψ as the only fitting parameter. Height of error bars is ± 1 standard deviation $\sigma(N)$ (see bottom-right inset), with N the number of sequences per point. Note that averaging beyond $N = 10^6$ does not improve the violation because of a slow drift of φ.

entanglement witness $\langle XX_\varphi\rangle + \langle XY_\varphi\rangle + \langle YY_\varphi\rangle - \langle YX_\varphi\rangle$ as a function of the angle φ between the orthogonal measurement bases of qubits I and II. Figure 3 compares the results obtained with and without correcting the readout errors with what is theoretically expected from the decoherence parameters indicated previously: unlike in [11] and because of a readout contrast limited to 70%–75%, the witness does not exceed the classical bound of 2 without correcting the readout errors. After correction, it reaches 2.43, in good agreement with the theoretical prediction (see also [16]), and exceeds the classical bound by up to 22 standard deviations when averaged over 10^6 sequences.

In a last experiment, we characterize the imperfections of our $\sqrt{i\mathrm{SWAP}}$ gate by quantum process tomography [1]. We build a completely positive map $\rho_{\mathrm{out}} = \mathcal{E}(\rho_{\mathrm{in}}) = \sum_{m,n}\chi_{mn}P'_m\rho_{\mathrm{in}}P'^{\dagger}_n$ characterized by a 16×16 matrix χ expressed here in the modified Pauli operator basis $\{P'_k\} = \{I, X, Y' = iY, Z\}^{\otimes 2}$, for which all matrices are real. For that purpose, we apply the gate (using pulse sequences similar to that of Fig. 1(c), with $\Delta t = 31$ ns and Θ_j^{-1} rotations) to the 16 input states $\{|0\rangle, |1\rangle, |0\rangle + |1\rangle, |0\rangle + i|1\rangle\}^{\otimes 2}$ and characterize both the input and output states by quantum state tomography. By operating as described previously, we would obtain apparent input and output density matrices including errors made in the state tomography itself, which we do not want to include in the gate map. Instead, we fit the 16 experimental input Pauli sets by a model (see Sec. V of the SM [14]) including amplitude and phase errors for the X and Y preparation and tomographic pulses, in order to determine which operator set $\{P^e_k\}$ is actually measured. The input and output matrices $\rho_{\mathrm{in,out}}$ corrected from the tomographic errors only are calculated by inverting the linear relation $\{\langle P^e_k\rangle = \mathrm{Tr}(\rho P^e_k)\}$ and by applying it to the experimental Pauli sets. We then calculate from the $\{\rho_{\mathrm{in,out}}\}$ set an Hermitian χ matrix that is not necessarily physical due to statistical errors, and which we render physical by taking the nearest Hermitian positive matrix. This final χ matrix is shown and compared to the ideal matrix χ_{id} in Fig. 4, which yields a gate fidelity $F_g = \mathrm{Tr}(\chi\chi_{\mathrm{id}}) = 0.9$ [17] for a single run of the gate. To better understand the imperfections, we also show the map $\tilde{\chi}$ of the actual process preceded by the inverse ideal process [18]. The first diagonal element of $\tilde{\chi}$ is equal to F_g by construction. Then, main visible errors arise from unitary operations and reduce fidelity by 1%–2% (a fit yields a too long coupling time inducing a 95° swap instead of 90° and $\theta_{\mathrm{I,II}}$ rotations too small by 3.5° and 7°, respectively). On the other hand the known relaxation and dephasing times reduce fidelity by 8% but is barely visible in $\tilde{\chi}$ due to a spread over many matrix elements with modulus of the order of or below the 1%–2% noise level.

In conclusion, we have demonstrated a high fidelity $\sqrt{i\mathrm{SWAP}}$ gate in a two Josephson qubit circuit with individual nondestructive single-shot readouts, observed a violation of the CHSH-Bell inequality, and followed the register's dynamics by tomography. Although quantum coherence and readout fidelity are still limited in this circuit, they are sufficient to test in the near future simple quantum algorithms and get their result in a single run, which would demonstrate the concept of quantum speed-up.

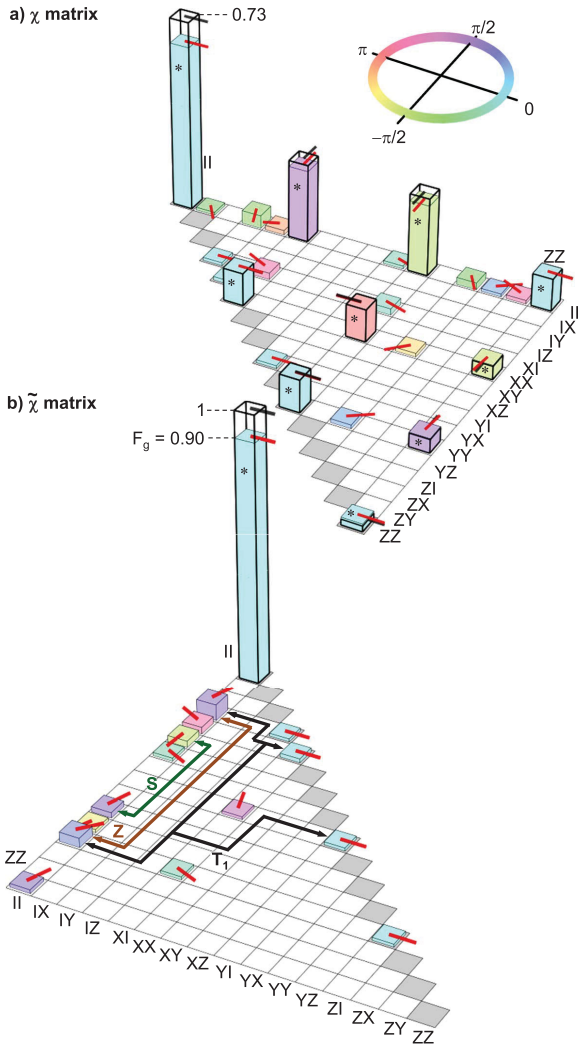

FIG. 4 (color). Map of the implemented $\sqrt{i\mathrm{SWAP}}$ gate yielding a fidelity $F_g = 90\%$. Superposition of the ideal (empty thick bars) and experimental (color-filled bars) upper part of the Hermitian process matrix χ (a) and lower part of the Hermitian error matrix $\tilde{\chi}$ (b), in the two-qubit Pauli operators basis $\{II, \ldots, ZZ\}$. Expected elements are marked with a star, and elements below 1% are not shown. Each complex matrix element is represented by a bar with height proportional to its modulus and by an arrow at the top of the bar (as well as a filling color for the experiment—see top inset) giving its argument. See also Sec. VI of the SM [14] for a real and imaginary part representation of these matrices and for additional information. Labeled arrows indicate the main visible contributions to errors, i.e., a too long swapping time (S), too small rotations $\theta_{\mathrm{I,II}}$ (Z), and relaxation (T_1)—see text.

We gratefully acknowledge discussions with J. Martinis and his co-workers, with M. Devoret, D. DiVicenzo, A. Korotkov, P. Milman, and within the Quantronics group, technical support from P. Orfila, P. Senat, and J. C. Tack, as well as financial support from the European research contracts MIDAS and SOLID, from ANR Masquelspec and C'Nano, and from the German Ministry of Education and Research.

[1] M. A. Nielsen and I. L. Chuang, *Quantum Computation and Quantum Information* (Cambridge University Press, Cambridge, England, 2000).
[2] J. Clarke and F. Wilhelm, Nature (London) **453**, 1031 (2008).
[3] L. DiCarlo *et al.*, Nature (London) **460**, 240 (2009).
[4] L. DiCarlo *et al.*, Nature (London) **467**, 574 (2010).
[5] T. Yamamoto *et al.*, Phys. Rev. B **82**, 184515 (2010).
[6] R. C. Bialczak *et al.*, Nature Phys. **6**, 409 (2010).
[7] J. M. Chow *et al.*, Phys. Rev. Lett. **107**, 080502 (2011).
[8] J. Koch *et al.*, Phys. Rev. A **76**, 042319 (2007).
[9] J. A. Schreier *et al.*, Phys. Rev. B **77**, 180502(R) (2008).
[10] M. Mariantoni *et al.*, Science **334**, 61 (2011).
[11] M. Ansmann *et al.*, Nature (London) **461**, 504 (2009).
[12] I. Siddiqi *et al.*, Phys. Rev. Lett. **93**, 207002 (2004).
[13] F. Mallet *et al.*, Nature Phys. **5**, 791 (2009).
[14] See Supplemental Material at http://link.aps.org/supplemental/10.1103/PhysRevLett.108.057002 for additional information about the sample preparation and experimental setup, the two-qubit Hamiltonian, the sample parameters, the readout characterization, the removal of errors on tomographic pulses, as well as for different representations of the matrices shown in Figs. 2 and 4.
[15] The relaxation times $T_1 \sim 0.5$ μs are twice as low as in Ref. [13], which is likely due to a lack of control of the electromagnetic impedance as seen from the qubit in the present and more complicated circuit and/or to the large asymmetry d of the transmons that opens a new relaxation channel.
[16] J. M. Chow *et al.*, Phys. Rev. A **81**, 062325 (2010).
[17] Note that F_g is also equal to Shumacher's fidelity $\mathrm{Tr}[S_{\mathrm{id}}^{\dagger}S]/\mathrm{Tr}[S_{\mathrm{id}}^{\dagger}S_{\mathrm{id}}]$ with S (S_{id}) the super operator of the actual (ideal unitary) process and that fidelities F for the 16 output states range between 80% and 99.5%.
[18] A. G. Kofman and A. N. Korotkov, Phys. Rev. A **80**, 042103 (2009); private communication.

Supplementary Information for Characterization of a two-transmon processor with individual single-shot qubit readout

A. Dewes[1], F. R. Ong[1], V. Schmitt[1], R. Lauro[1], N. Boulant[2], P. Bertet[1], D. Vion[1], and D. Esteve[1]
[1] *Quantronics group, Service de Physique de l'État Condensé (CNRS URA 2464), IRAMIS, DSM, CEA-Saclay, 91191 Gif-sur-Yvette, France and*
[2] *I2BM, Neurospin, LRMN, 91191CEA-Saclay, 91191 Gif-sur-Yvette, France*
(Dated: December 8, 2011)

I. SAMPLE PREPARATION AND EXPERIMENTAL SETUP

- Sample fabrication: the sample is fabricated on a silicon chip oxidized over 50 nm. A 150 nm thick niobium layer is first deposited by magnetron sputtering and then dry-etched in a SF_6 plasma to pattern the readout resonators, the current lines for frequency tuning, and their ports. Finally, the transmon qubit, the coupling capacitance and the Josephson junctions of the resonators are fabricated by double-angle evaporation of aluminum through a shadow mask patterned by e-beam lithography. The first layer of aluminum is oxidized in a $Ar - O_2$ mixture to form the oxide barrier of the junctions. The chip is glued with wax on a printed circuit board (PCB) and wire bonded to it. The PCB is then screwed in a copper box anchored to the cold plate of a dilution refrigerator.

- Qubit microwave pulses: The qubit drive pulses are generated by two phase-locked microwave generators whose continuous wave outputs are fed to a pair of I/Q-mixers. The two IF inputs of each of these mixers are provided by a 4-Channel 1 GS/s arbitrary waveform generator (AWG Tektronix AWG5014). Single-sideband mixing in the frequency range of $50 - 300$ MHz is used to generate multi-tone drive pulses and to obtain a high ON/OFF ratio (> 50 dB) of the signal at the output of the mixers. Phase and amplitude errors of the mixers are corrected by measuring the signals at the output and applying sideband and carrier frequency dependent corrections in amplitude and offset to the IF input channels.

- Flux Pulses: The flux control pulses are generated by a second AWG and sent to the chip through a transmission line, equipped with 40 dB of attenuation distributed over different temperature stages and a pair of 1 GHz absorptive low-pass filters at 4 K. The input signal of each flux line is fed back to room temperature through an identical transmission line and is then measured to compensate the non-ideal frequency response of the line.

- Readout Pulses: The pulses for the Josephson bifurcation amplifier (JBA) readouts are generated by mixing the continuous signals of a pair of microwave generators with IF pulses provided by a 1 GS/s arbitrary function generator. Each readout pulse consists of a measurement part with a rise time of 30 ns and a hold time of 100 ns, followed by a $2\,\mu s$ long latching part at 90 % of the pulse height.

- Drive and Measurement Lines: The drive and readout microwave signals of each qubit are combined and sent to the sample through a pair of transmission lines that are attenuated by 70 dB over different temperature stages and filtered at 4 K and 300 mK. A microwave circulator at 20 mK separates the input signals going to the chip from the reflected signals coming from the chip. The latter are amplified by 36 dB at 4 K by two cryogenic HEMT amplifiers (CIT Cryo 1) with noise temperature 5 K. The reflected readout pulses get further amplified at room temperature and are then demodulated with the continuous signals of the readout microwave sources. The IQ quadratures of the demodulated signals are sampled at 1 GS/s by a 4-channel Data Acquisition system (Acqiris DC282).

II. TWO-QUBIT HAMILTONIAN

The Hamiltonian of a Cooper pair box j [s2, s1] with total Coulomb energy $E_{\mathrm{C}}^{\mathrm{j}}$ (for a Cooper pair), with total Josephson energy $E_{\mathrm{J}}^{\mathrm{j}}(\phi_{\mathrm{j}})$, with island charge N_{j} (in Cooper pair units) and conjugated phase variable δ_{j}, biased by a gate charge $N_{\mathrm{g,j}}$, is $H_{\mathrm{j}} = E_{\mathrm{C}}^{\mathrm{j}} \left(\widehat{N_{\mathrm{j}}} - N_{\mathrm{g,j}}\right)^2 - E_{\mathrm{J}}^{\mathrm{j}}(\phi_{\mathrm{j}})\cos\left[\widehat{\delta_{\mathrm{j}}} - \delta_{\mathrm{j,0}}(\phi_{\mathrm{j}})\right]$ with $\tan\left(\delta_{\mathrm{j,0}}\right) = d_{\mathrm{j}}\tan\left(\pi\phi_{\mathrm{j}}/\phi_0\right)$. In the limit $E_{\mathrm{J}}^{\mathrm{j}} \gg E_{\mathrm{C}}^{\mathrm{j}}$ [8] that corresponds to the transmon qubit and when restricting the Hilbert space to the two lowest eigenstates $\{|0\rangle_{\mathrm{j}}, |1\rangle_{\mathrm{j}}\}$, the $N_{\mathrm{g,j}}$ parameters become irrelevant, and one has $\langle 0|\,\widehat{N_{\mathrm{j}}}\,|0\rangle \simeq \langle 1|\,\widehat{N_{\mathrm{j}}}\,|1\rangle \simeq 0$, $\langle 1|\,\widehat{N_{\mathrm{j}}}\,|0\rangle = 2^{-3/4} i \left(E_{\mathrm{J}}^{\mathrm{j}}/E_{\mathrm{C}}^{\mathrm{j}}\right)^{1/4}$, and $H_{\mathrm{j}} = -h\nu_{\mathrm{j}}\sigma_{\mathrm{z}}^{\mathrm{j}}/2$ with $\nu_{\mathrm{j}} \simeq \sqrt{2E_{\mathrm{C}}^{\mathrm{j}}E_{\mathrm{J}}^{\mathrm{j}}(\phi_{\mathrm{j}})}/h$. When coupling two such transmon qubits by

a capacitance C_c much smaller than each total island capacitance, the total Hamiltonian is $H = H_1 + H_2 + H_{int}$ with $H_{int} = 2E_C^I E_C^{II}/E_{Cc}\widehat{N_1}\widehat{N_2}$ and E_{Cc} the Coulomb energy of a Cooper pair on the coupling capacitor. Using the matrix elements above leads to $H_{int} = hg\sigma_y^I\sigma_y^{II}$ with $g = \sqrt{E_C^I E_C^{II}\nu_I\nu_{II}}/(2E_{Cc})$. This symmetric and purely transverse coupling term $\sigma_y^I\sigma_y^{II}$ (exchange term) is not surprising since each charge on a transmon island varying at the frequency of the other qubit plays the role of a resonant gate drive for this second qubit, and makes it rotate around an equatorial axis of its Bloch sphere. The precise YY nature (rather than XX for instance) is on the other hand meaningless and is a matter of initial convention for the global phases of the $|0\rangle$ and $|1\rangle$ states.

III. SAMPLE PARAMETERS

The sample is first characterized by spectroscopy (see Fig. 1.b of main text). The incident power used is high enough to observe the resonator frequency ν_R, the qubit line ν_{01}, and the two-photon transition at frequency $\nu_{02}/2$ between the ground and second excited states of each transmon (data not shown). A fit of the transmon model to the data yields the sample parameters $E_J^I/h = 36.2\,\text{GHz}$, $E_C^I/h = 0.98\,\text{GHz}$, $d_I = 0.2$, $E_J^{II}/h = 43.1\,\text{GHz}$, $E_C^{II}/h = 0.87\,\text{GHz}$, $d_{II} = 0.35$, $\nu_R^I = 6.84\,\text{GHz}$, and $\nu_R^{II} = 6.70\,\text{GHz}$. The qubit-readout anti crossing at $\nu = \nu_R$ yields the qubit-readout couplings $g_0^I \simeq g_0^{II} \simeq 50\,\text{MHz}$. Independent measurements of the resonator dynamics (data not shown) yield quality factors $Q_I = Q_{II} = 730$ and Kerr non linearities [s3],[13] $K_I/\nu_R^I \simeq K_{II}/\nu_R^{II} \simeq -2.3 \pm 0.5 \times 10^{-5}$.

IV. READOUT CHARACTERIZATION

Errors in our readout scheme are discussed in detail in [13] for a single qubit. First, incorrect mapping $|0\rangle \to 1$ or $|1\rangle \to 0$ of the projected state of the qubit to the dynamical state of the resonator can occur, due to the stochastic nature of the switching between the two dynamical states. As shown in Fig. IV.1, the probability p to obtain the outcome 1 varies continuously from 0 to 1 over a certain range of drive power P_d applied to the readout. When the shift in power between the two $p_{|0\rangle,|1\rangle}(P_d)$ curves is not much larger than this range, the two curves overlap and errors are significant even at the optimal drive power where the difference in p is maximum. Second, even in the case of non overlapping $p_{|0\rangle,|1\rangle}(P_d)$ curves, the qubit initially projected in state$|1\rangle$ can relax down to $|0\rangle$ before the end of the measurement, yielding an outcome 0 instead of 1. The probability of these two types of errors vary in opposite directions as a function of the frequency detuning $\Delta = \nu_R - \nu > 0$ between the resonator and the qubit, so that a compromise has to be found for Δ. Besides, the contrast $c = Max\left(p_{|1\rangle} - p_{|0\rangle}\right)$ can be increased [13] by shelving state $|1\rangle$ into state $|2\rangle$ with a microwave π pulse at frequency ν_{12} just before the readout resonator pulse. The smallest errors $e_0^{I,II}$ and $e_1^{I,II}$ when reading $|0\rangle$ and $|1\rangle$ are found for $\Delta_I = 440\,\text{MHz}$ and $\Delta_{II} = 575\,\text{MHz}$ and are shown by arrows in the top panels of Fig. IV.1: $e_0^I = 5\%$ and $e_1^I = 13\%$ (contrast $c_I = 1 - e_0^I - e_1^I = 82\%$), and $e_0^{II} = 5.5\%$ and $e_1^{II} = 12\%$ ($c_{II} = 82\%$). When using the $|1\rangle \to |2\rangle$ shelving before readout, $e_0^I = 2.5\%$ and $e_2^I = 9.5\%$ (contrast $c_I = 1 - e_0^I - e_2^I = 88\%$), and $e_0^{II} = 3\%$ and $e_2^{II} = 8\%$ ($c_{II} = 89\%$). These best results are very close to those obtained in [12], but are unfortunately not relevant to this work.

Indeed, when the two qubits are measured simultaneously, one has also to take into account a possible readout crosstalk, i.e. an influence of the projected state of each qubit on the outcome of the readout of the other qubit. We do observe such an effect and have to minimize it by increasing $\Delta_{I,II}$ up to $\sim 1\,\text{GHz}$ (where the dispersive shift $\chi \simeq 2.5\,\text{MHz}$ is still large enough), and by not using the shelving technique. An immediate consequence shown in Fig. IV.1(b) is a reduction of the $c_{I,II}$ contrasts. The errors when reading $|0\rangle$ and $|1\rangle$ are now $e_0^I = 19\,\%$ and $e_1^I = 7\,\%$ (contrast $c_I = 74\%$) and $e_0^{II} = 19\,\%$ and $e_1^{II} = 12\,\%$ (contrast $c_{II} = 69\%$). Then to characterize the errors due to crosstalk, we measure the 4×4 readout matrix $\mathcal{R}$ linking the probabilities p_{uv} of the four possible uv outcomes to the population of the four $|uv\rangle$ states. As shown in Fig. IV.1(c-d), we then rewrite $\mathcal{R} = \mathcal{C}_{CT}.(\mathcal{C}_I \otimes \mathcal{C}_{II})$ as the product of a 4×4 pure crosstalk matrix $\mathcal{C}_{CT}$ with the tensorial product of the two 2×2 single qubit readout matrices

$$\mathcal{C}_{I,II} = \begin{pmatrix} 1 - e_0^{I,II} & e_1^{I,II} \\ e_0^{I,II} & 1 - e_1^{I,II} \end{pmatrix}.$$

In the worst case, the readout crosstalk is 2.1%. We also illustrate on the figure the impact of the readout errors on our swapping experiment by comparing the bare readout outcomes uv, the outcomes corrected from the independent readout errors only, and the$|uv\rangle$ population calculated with the full correction including crosstalk.

We now explain briefly the cause of the readout crosstalk in our processor. Unlike what was observed for other qubit readout schemes using switching detectors [5], the crosstalk we observe is not directly due to an electromagnetic perturbation induced by the switching of one detector that would help or prevent the switching of the other one.

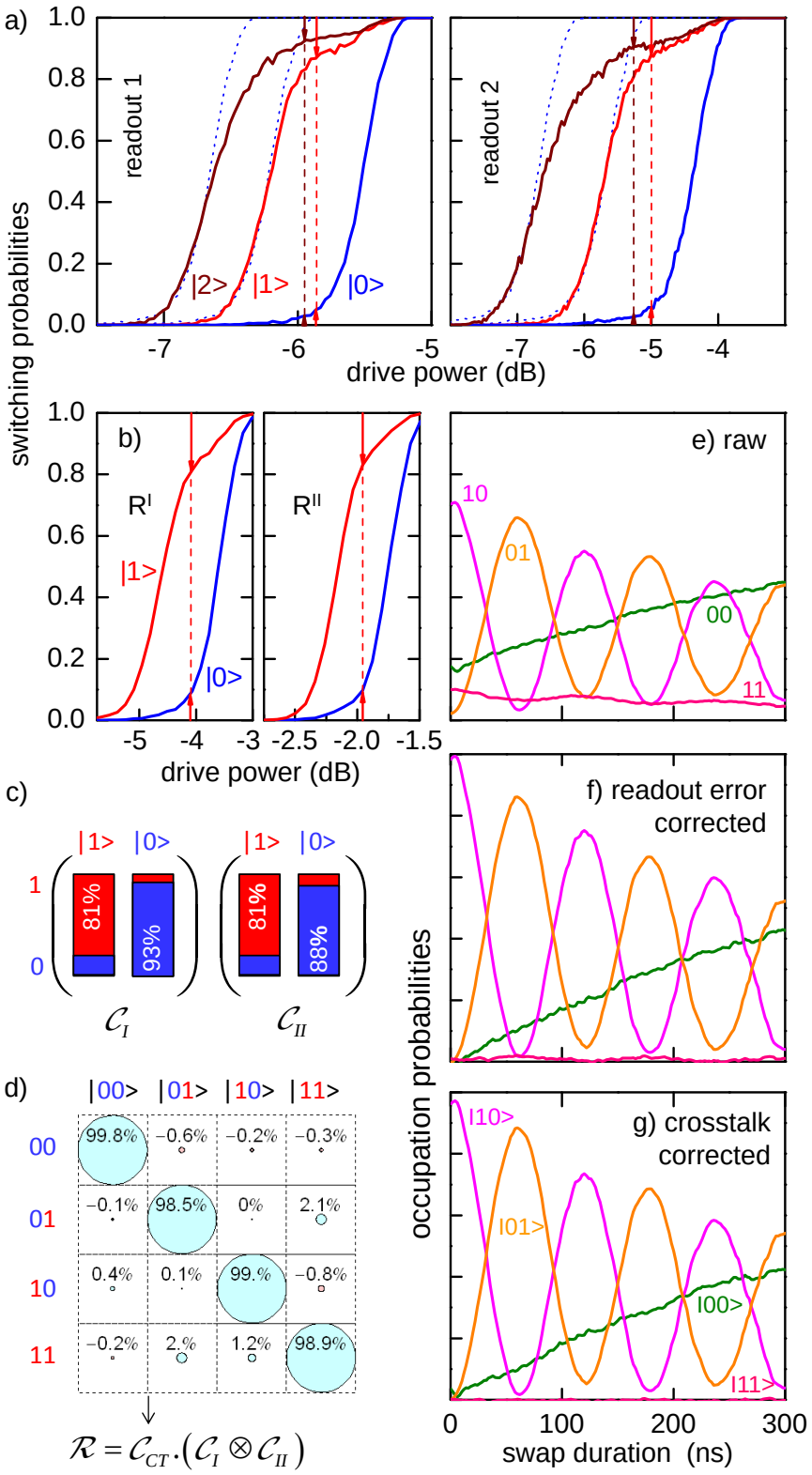

Figure IV.1: Readout imperfections and their correction. (a) Switching probabilities of the readouts as a function of their driving power, with the qubit prepared in state$|0\rangle$ (blue), $|1\rangle$ (red), or $|2\rangle$ (brown), at the optimal readout points. The arrows and dashed segments indicate the readout errors and contrast, at the power where the later is maximum. (b) Same as (a) but at readout points $R^{\mathrm{I,II}}$ used in this work. (c-d) Single readout matrices $\mathcal{C}_{\mathrm{I,II}}$ and pure readout crosstalk matrix $\mathcal{C}_{\mathrm{CT}}$ characterizing the simultaneous readout of the two qubits. (e-g) bare readout outcomes uv, outcomes corrected from the independent readout errors only, and$|uv\rangle$ population calculated with the full correction including crosstalk for the swapping experiment of Fig. 2.

Indeed, when both qubits frequencies $\nu_{\rm I,II}$ are moved far below $\nu_{\rm R}^{\rm I,II}$, the readout crosstalk disappears: the switching of a detector has no measurable effect on the switching of the other one. The crosstalk is actually due to the rather strong ac-Stark shift $\sim 2\,(n_{\rm H}-n_{\rm L})\,g_0^2/(R-\nu_{\rm R}) \sim 500\,{\rm MHz}$ of the qubit frequency when a readout resonator switches from its low to high amplitude dynamical state with $n_{\rm L}\sim 10$ and $n_{\rm H}\sim 10^2$ photons, respectively. The small residual effective coupling between the qubits at readout can then slightly shift the frequency of the other resonator, yielding a change of its switching probability by a few percent. Note that coupling the two qubits by a resonator rather than by a fixed capacitor would solve this problem.

V. REMOVING ERRORS ON TOMOGRAPHIC PULSES BEFORE CALCULATING THE GATE PROCESS MAP

Tomographic errors are removed from the process map of our $\sqrt{iSWAP}$ gate using the following method. The measured Pauli sets corresponding to the sixteen input states are first fitted by a model including errors both in the preparation of the state (index *prep*) and in the tomographic pulses (index *tomo*). The errors included are angular errors $\varepsilon_{\rm I,II}^{\rm prep}$ on the nominal π rotations around $X_{\rm I,II}$, $\eta_{\rm I,II}^{\rm prep,tomo}$and $\delta_{\rm I,II}^{\rm prep,tomo}$ on the nominal $\pi/2$ rotations around $X_{\rm I,II}$ and $Y_{\rm I,II}$, a possible departure $\xi_{\rm I,II}$ from orthogonality of $\left(\overrightarrow{X_{\rm I}},\overrightarrow{Y_{\rm I}}\right)$ and $\left(\overrightarrow{X_{\rm II}},\overrightarrow{Y_{\rm II}}\right)$, and a possible rotation $\mu_{\rm I,II}$ of the tomographic XY frame with respect to the preparation one. The rotation operators used for preparing the states and for doing their tomography are thus given by

$$
\begin{aligned}
X_{\rm I,II}^{\rm prep}(\pi) &= e^{-{\rm i}\left(\pi+\varepsilon_{\rm I,II}^{\rm prep}\right)\sigma_{\rm x}^{\rm I,II}/2},\\
X_{\rm I,II}^{\rm prep}(-\pi/2) &= e^{+{\rm i}\left(\pi/2+\eta_{\rm I,II}^{\rm prep}\right)\sigma_{\rm x}^{\rm I,II}/2},\\
Y_{\rm I,II}^{\rm prep}(\pi/2) &= e^{-{\rm i}\left(\pi/2+\delta_{\rm I,II}^{\rm prep}\right)\left[\cos(\xi_{\rm I,II})\sigma_{\rm y}^{\rm I,II}-\sin(\xi_{\rm I,II})\sigma_{\rm x}^{\rm I,II}\right]/2},\\
X_{\rm I,II}^{\rm tomo}(\pi/2) &= e^{-{\rm i}\left(\pi/2+\eta_{\rm I,II}^{\rm tomo}\right)\left[\sin(\mu_{\rm I,II})\sigma_{\rm x}^{\rm I,II}+\cos(\mu_{\rm I,II})\sigma_{\rm y}^{\rm I,II}\right]/2},\\
Y_{\rm I,II}^{\rm tomo}(-\pi/2) &= e^{+{\rm i}\left(\pi/2+\delta_{\rm I,II}^{\rm tomo}\right)\left[\cos(\mu_{\rm I,II}+\xi_{\rm I,II})\sigma_{\rm y}^{\rm I,II}-\sin(\mu_{\rm I,II}+\xi_{\rm I,II})\sigma_{x}^{\rm I,II}\right]/2}.
\end{aligned}
$$

The sixteen input states are then $\left\{\rho_{\rm in}^{\rm e}=U\left|0\right\rangle\left\langle 0\right|U^{\dagger}\right\}$ with $\{U\} = \{I_{\rm I}, X_{\rm I}^{\rm prep}(\pi), Y_{\rm I}^{\rm prep}(\pi/2), X_{\rm I}^{\rm prep}(-\pi/2)\}\otimes\{I_{\rm II}, X_{\rm II}^{\rm prep}(\pi), Y_{\rm II}^{\rm prep}(\pi/2), X_{\rm II}^{\rm prep}(-\pi/2)\}$, and each input state yields a Pauli set $\{\langle P_{\rm k}^{\rm e}\rangle = Tr\left(\rho_{\rm in}^{\rm e}P_{\rm k}^{\rm e}\right)\}$ with $\{P_{\rm k}^{\rm e}\} = \{I_{\rm I}, X_{\rm I}^{\rm e}, Y_{\rm I}^{\rm e}, Z_{\rm I}\}\otimes\{I_{\rm II}, X_{\rm II}^{\rm e}, Y_{\rm II}^{\rm e}, Z_{\rm II}\}$, $X^{\rm e} = Y^{\rm tomo}(-\pi/2)^{\dagger}\sigma_z Y^{\rm tomo}(-\pi/2)$, and $Y^{\rm e} = X^{\rm tomo}(\pi/2)^{\dagger}\sigma_{\rm z}X^{\rm tomo}(\pi/2)$. Figure V.1 shows the best fit of the modeled $\{\langle P_k^{\rm e}\rangle\}$ set to the measured input Pauli sets, yielding $\varepsilon_{\rm I}^{\rm prep}=-1^{\circ}$, $\varepsilon_{\rm II}^{\rm prep}=-3^{\circ}$, $\eta_{\rm I}^{\rm prep}=3^{\circ}$, $\eta_{\rm II}^{\rm prep}=4^{\circ}$, $\delta_{\rm I}^{\rm prep}=-6^{\circ}$, $\delta_{\rm II}^{\rm prep}=-3^{\circ}$, $\eta_{\rm I}^{\rm tomo}=-6^{\circ}$, $\eta_{\rm II}^{\rm tomo}=-4^{\circ}$, $\lambda_{\rm I}^{\rm tomo}=12^{\circ}$, $\lambda_{\rm II}^{\rm tomo}=5^{\circ}$, $\xi_{\rm I}=1^{\circ}$, $\xi_{\rm II}=-2^{\circ}$, and $\mu_{\rm I}=\mu_{\rm II}=-11^{\circ}$.

Knowing the tomographic errors and thus $\{\langle P_{\rm k}^{\rm e}\rangle\}$, we then invert the linear relation $\{\langle P_{\rm k}^{\rm e}\rangle = Tr\left(\rho P_{\rm k}^{\rm e}\right)\}$ to find the 16×16 matrix B that links the vector $\overrightarrow{\langle P_{\rm k}^{\rm e}\rangle}$ to the columnized density matrix $\overrightarrow{\rho}$, i.e. $\overrightarrow{\rho} = B.\overrightarrow{\langle P_{\rm k}^{\rm e}\rangle}$. The matrix B is finally applied to the measured sixteen input and sixteen output Pauli sets to find the sixteen $(\rho_{\rm in,},\rho_{\rm out})_{\rm k}$ couples to be used for calculating the gate map.

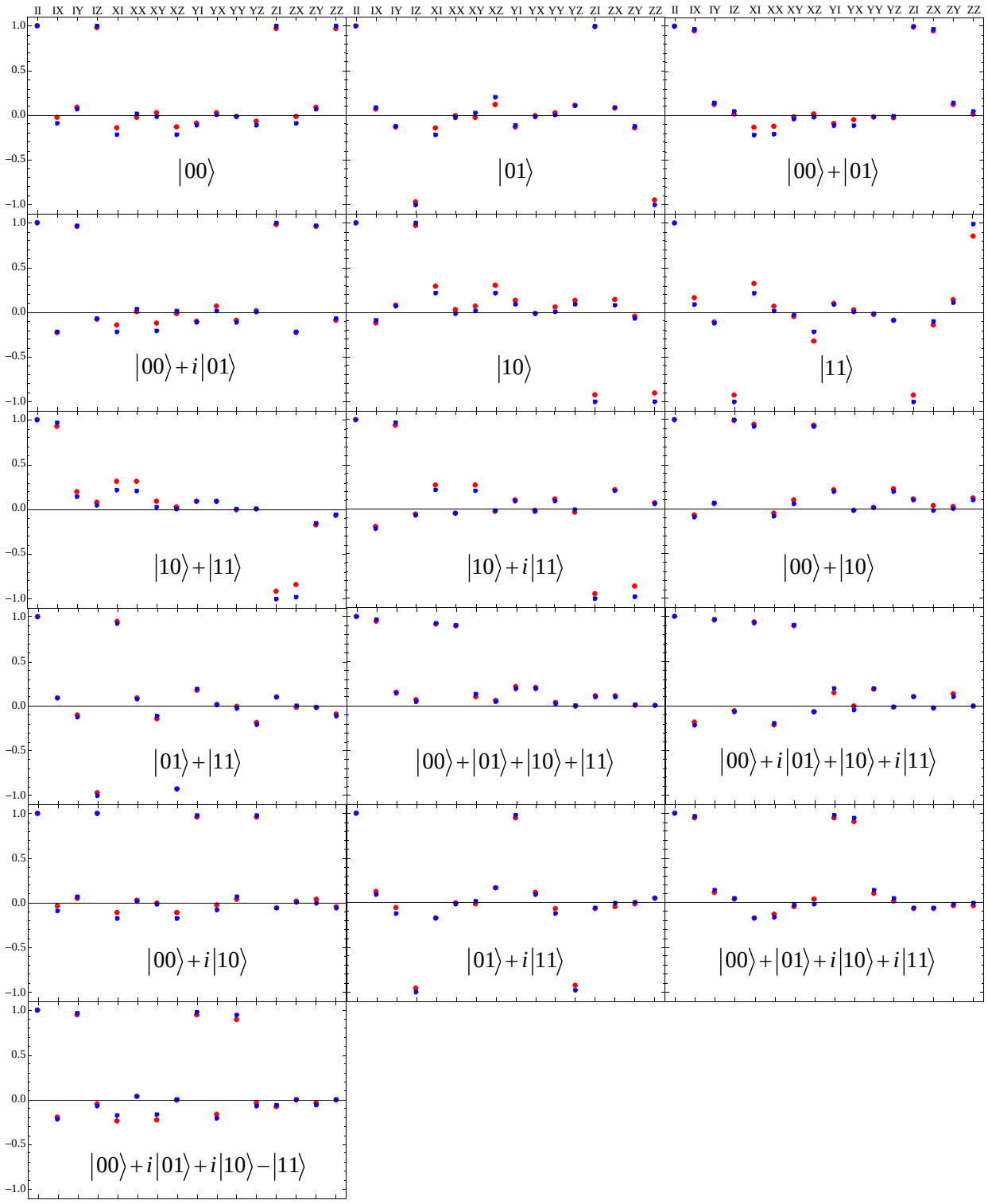

Figure V.1: Fitting of the pulse errors at state preparation and tomography. Measured (red) and fitted (blue - see text) Pauli sets $\langle P_{\mathrm{k}}^{\mathrm{e}} \rangle$ for the sixteen targeted input states $\{|0\rangle, |1\rangle, |0\rangle + |1\rangle, |0\rangle + i\,|1\rangle\}^{\otimes 2}$. The $\{II, IX, IY, IZ, XI, ...\}$ operators indicated in abscissa are the targeted operators and not those actually measured (due to tomographic errors).

VI. REAL AND IMAGINARY PART REPRESENTATION OF THE MATRICES OF MAIN FIGURES 2 AND 4.

The ρ , χ and $\widetilde{\chi}$ matrices of figures 2 and 4 of the main text are represented in an unconventional way that allows to encode both the modulus and the argument of each matrix element in the same matrix cell. Figures VI.1 to VI.3 show the same matrices using the more conventional real and imaginary part representation.

In addition, we show in Fig. VI.4 the contributions of relaxation, of inaccurate swapping time and of inaccurate rotations $\theta_{\mathrm{I,II}}$ to the error matrix $\widetilde{\chi}$. Contribution of relaxation is directly calculated from the independently measured values of the relaxation time T_1, whereas the two other contributions result from a fit to the whole experimental $\widetilde{\chi}$ matrix.

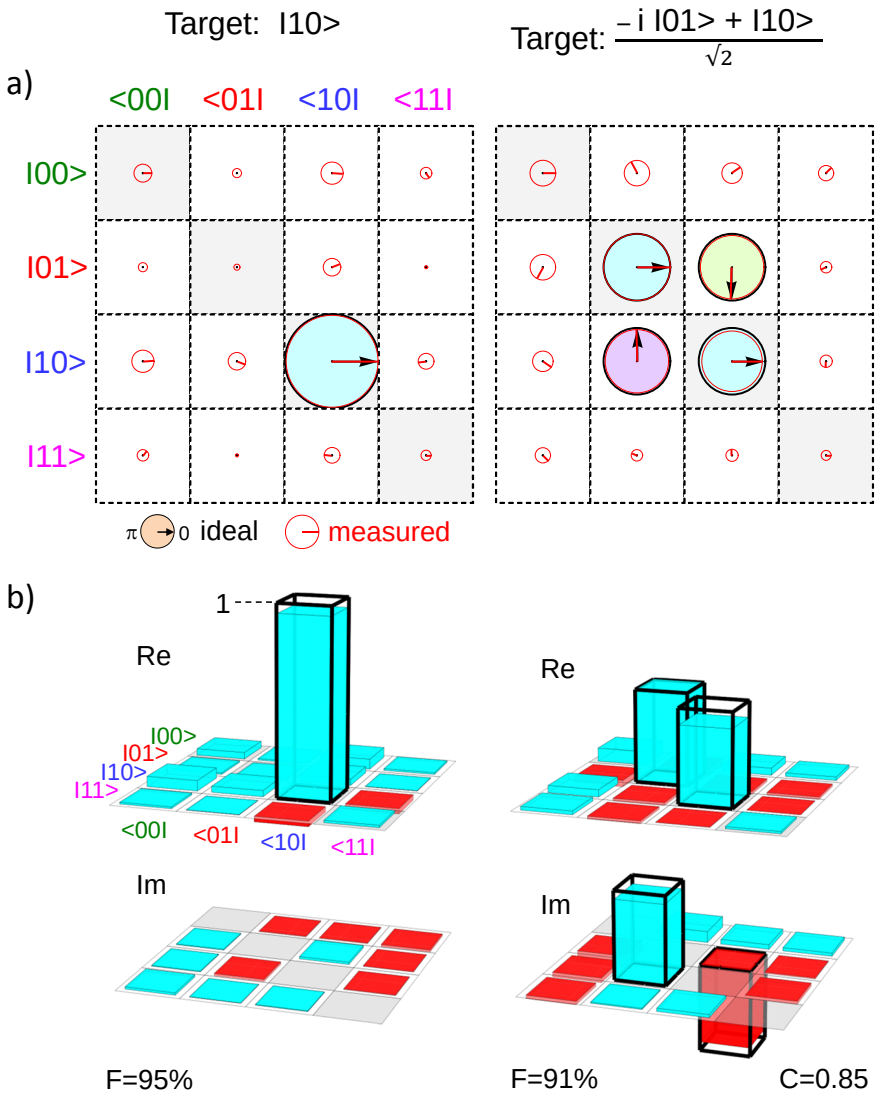

Figure VI.1: Same ideal and experimental density matrices as in Fig. 2, before and after one operation of the $\sqrt{iSWAP}$ gate. (a) Color-filled black circles with black arrow is the ideal matrix whereas red circles and arrows is the experimental one. Each complex matrix element is represented by a circle with an area proportional to its modulus (diameter = cell size for unit modulus) and by an arrow giving its argument (usual trigonometric convention). (b) Real (top) and imaginary (bottom) parts of the same matrices, with positive and negative numbers being encoded along the vertical direction. The ideal matrix is represented by thick black empty bars, whereas experimental data are shown as blue-filled (positive) or red-filled (negative) thin bars.

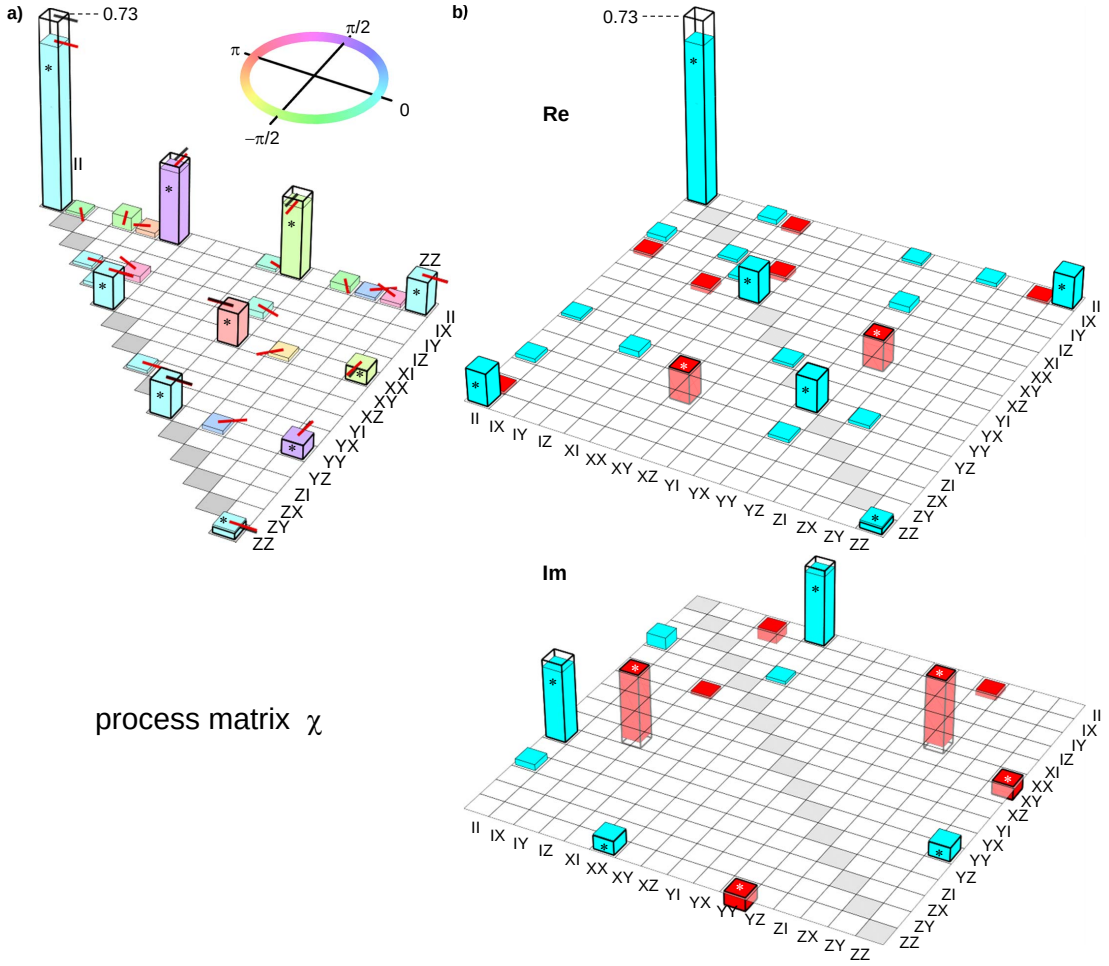

Figure VI.2: Same ideal and experimental process matrix χ as in Fig. 4(a). Expected elements are marked with a star and elements below 1% are not shown. (a) Each complex matrix element is represented by a bar with height proportional to its modulus and by an arrow at the top of the bar (as well as a filling color for the experiment - see top inset) giving its argument. (b) Real (top) and imaginary (bottom) parts of the same matrix, with positive and negative numbers being encoded along the vertical direction. The ideal matrix is represented by thick black empty bars, whereas experimental data are shown as blue-filled (positive) or red-filled (negative) thin bars.

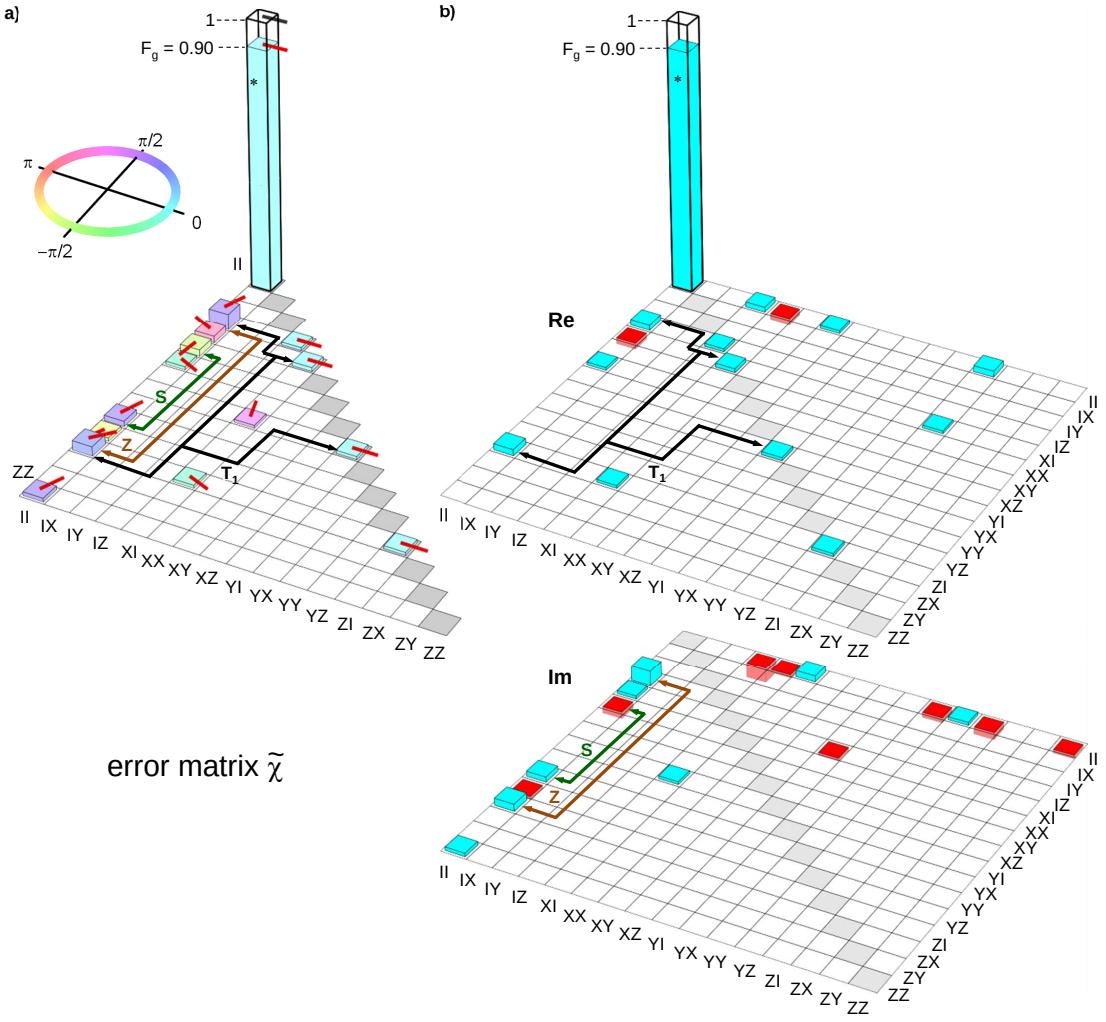

Figure VI.3: Same ideal and experimental error matrix $\widetilde{\chi}$ as in Fig. 4(b). The $IIII$ matrix element is the only expected one; elements with modulus below 1% are not shown. (a) Each complex matrix element is represented by a bar with height proportional to its modulus and by an arrow at the top of the bar (as well as a filling color for the experiment - see left inset) giving its argument. (b) Real (top) and imaginary (bottom) parts of the same matrix, with positive and negative numbers being encoded along the vertical direction. The ideal matrix is represented by thick black empty bars, whereas experimental data are shown as blue-filled (positive) or red-filled (negative) thin bars. Labeled arrows indicate the main visible contributions to errors, i.e. a too long swapping time (S), too small rotations $\theta_{\mathrm{I,II}}$ (Z), and relaxation (T_1).

[s1] D. Vion *et al.*, Science 296, 886 (2002).
[s2] A. Cottet, Ph.D. thesis, Universite Paris VI, 2002.
[s3] F. R. Ong *et al.*, Phys. Rev. Lett. 106, 167002 (2011).

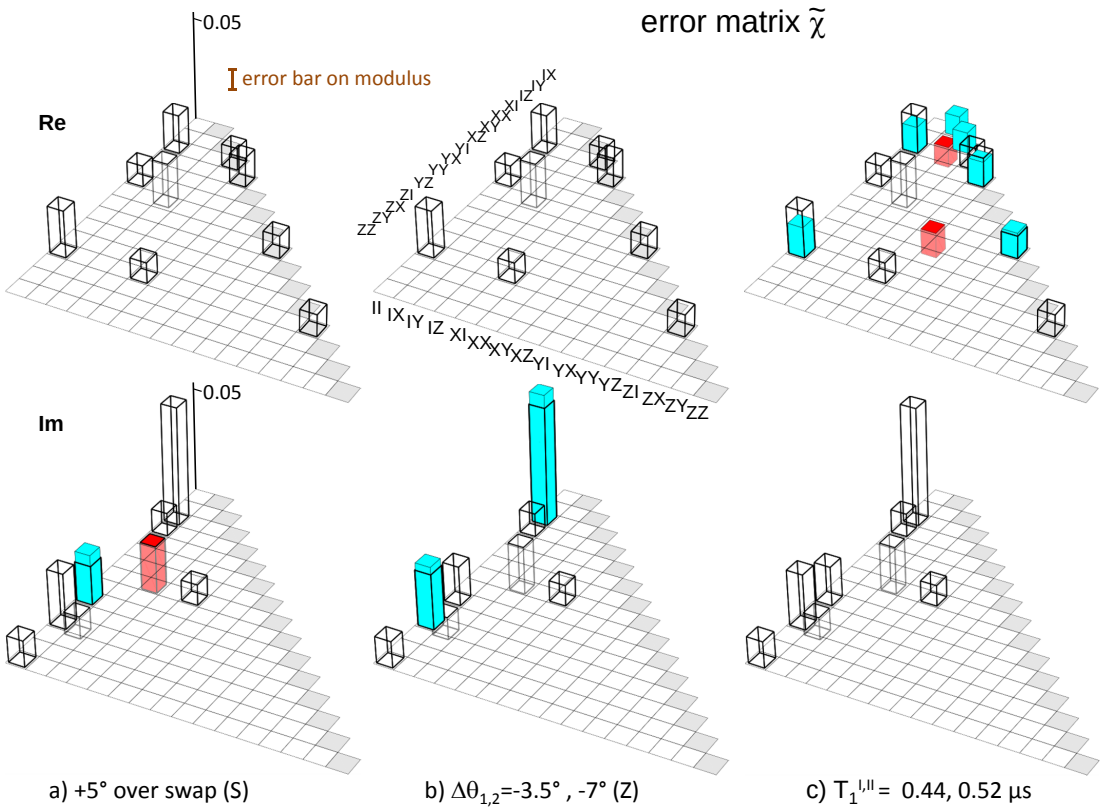

Figure VI.4: Experimental (empty bars) and calculated (color-filled thin bars) $\tilde{\chi}$ matrix for the three error contributions S, Z, and T_1 mentionned in the text and indicated in Figs. 4(b) and VI.3. Note that the vertical scale is expanded by a factor 10 with respect to other figures, and that matrix element $IIII$ as well as elements with modulus below the statistical error of 1% (see error bar) are not shown. Contribution T_1 is directly calculated from the independently measured values of the relaxation time T_1, whereas contributions S and Z result from a fit to the whole experimental $\tilde{\chi}$ matrix (including the many small elements below 1%).

PHYSICAL REVIEW B **85**, 140503(R) (2012)

Quantum speeding-up of computation demonstrated in a superconducting two-qubit processor

Andreas Dewes,[1] Romain Lauro,[1] Florian R. Ong,[1] Vivient Schmitt,[1] Perola Milman,[2,3] Patrice Bertet,[1] Denis Vion,[1] and Daniel Esteve[1]

[1]*Service de Physique de l'Etat Condensé/IRAMIS/DSM (CNRS URA 2464), CEA Saclay, 91191 Gif-sur-Yvette, France*

[2]*Laboratoire Matériaux et Phénomènes Quantiques, Université Paris Diderot, 10 rue Alice Domon et Léonie Duquet, 75205 Paris, France*

[3]*Université Paris-Sud 11, Institut de Sciences Moléculaires d'Orsay (CNRS), 91405 Orsay, France*

(Received 20 October 2011; revised manuscript received 31 January 2012; published 5 April 2012)

We operate a superconducting quantum processor consisting of two tunable transmon qubits coupled by a swapping interaction, and equipped with nondestructive single-shot readout of the two qubits. With this processor, we run the Grover search algorithm among four objects and find that the correct answer is retrieved after a single run with a success probability between 0.52 and 0.67, which is significantly larger than the 0.25 achieved with a classical algorithm. This constitutes a proof of concept for the quantum speed-up of electrical quantum processors.

DOI: 10.1103/PhysRevB.85.140503 PACS number(s): 85.25.Cp, 03.67.Lx, 74.78.Na

The proposition of quantum algorithms[1–3] that perform useful computational tasks more efficiently than classical algorithms has motivated the realization of physical systems[4] able to implement them and to demonstrate quantum speed-up. The versatility and the potential scalability of electrical circuits make them very appealing for implementing a quantum processor built as sketched in Fig. 1. Ideally, a quantum processor consists of a scalable set of quantum bits that can be efficiently reset, that can follow any unitary evolution needed by an algorithm using a universal set of single- and two-qubit gates, and that can be read projectively.[5] The nonunitary projective readout operations can be performed at various stages of an algorithm, and in any case at the end in order to get the final outcome. Quantum processors based on superconducting qubits have already been operated, but they fail to meet the above criteria in different aspects. With the transmon qubit[6,7] derived from the Cooper pair box,[8] simple quantum algorithms, namely, the Deutsch-Jozsa algorithm,[9] the Grover search algorithm,[1] and a three-qubit quantum error correction code, were demonstrated in two- and three-qubit processors with the coupling between the qubits mediated by a cavity also used for readout.[10,11] In this circuit, the qubits are not read independently, but the value of a single collective variable is determined from the cavity transmission measured over a large number of repeated sequences. By applying suitable qubit rotations prior to this measurement, the density matrix of the two-qubit register was inferred at different steps of the algorithm, and it was found to be in good agreement with the predicted one. Demonstrating quantum speed-up is, however, more demanding than measuring a collective qubit variable since it requests to obtain an outcome after a single run, i.e., to perform the single-shot readout of the qubit register. Up to now, single-shot readout in superconducting processors has been achieved only for phase qubits.[12,13] In a multiphase-qubit processor equipped with single-shot but destructive readout of each qubit, the Deutsch-Jozsa algorithm[9] was demonstrated in Ref. 12 with a success probability of order 0.7 in a single run, to be compared to 0.5 for a classical algorithm. Very recently a similar processor ran a compiled version of Shor's algorithm,[2] yielding prime factors of 15 with a 48% success rate.[14]

Since the Deutsch-Jozsa classification algorithm is not directly related to any practical situation, demonstrating quantum speed-up for more useful algorithms in an electrical processor designed along the blueprint of Fig. 1 is an important goal.[14] In this Rapid Communication, we report the operation of a two-transmon-qubit processor[15] that comes closer to the ideal scheme than those previously mentioned, and the single-shot run of the Grover search algorithm among four objects. Since, in this case, the algorithm ideally yields the answer after one algorithm step, its success probability after a single run provides a simple benchmark. We find that our processor yields the correct answer at each run, with a success probability that ranges between 0.52 and 0.67, whereas a single-step classical algorithm using a random query would yield the correct answer with probability 0.25.

The sample and the setup used for this experiment are the very same as those described and characterized in detail in Ref. 15. The sample fabrication and parameters are summarized in Secs. I and II of the Supplemental Material,[16] whereas the scheme of our processor and its mode of operation are recalled in Fig. 2: Two tunable transmon qubits coupled by a fixed capacitor are embedded in two identical control and readout subcircuits. The Hamiltonian of the two qubits {I,II} is $H/h = (-\nu_{\mathrm{I}}\sigma_z^{\mathrm{I}} - \nu_{\mathrm{II}}\sigma_z^{\mathrm{II}} + 2g\sigma_y^{\mathrm{I}}\sigma_y^{\mathrm{II}})/2$, where $\sigma_{x,y,z}$ are the Pauli operators, $\nu_{\mathrm{I,II}}$ are the qubit frequencies controlled by the flux applied to each transmon superconducting quantum intereference device (SQUID) loop with fast (0.5-GHz bandwidth) local current lines, and $g = 4.6\ \mathrm{MHz} \ll \nu_{\mathrm{I,II}}$ is the coupling frequency controlled by the coupling capacitance (see Sec. II of the Supplemental Material and Ref. 17). The achieved frequency control allows us to place the two transmons on resonance during times precise enough for performing the universal two-qubit gate $\sqrt{\mathrm{iSWAP}}$ (Ref. 15) and the exchange gate iSWAP used in this work. The qubit frequencies are tuned to different values for single-qubit manipulation, two-qubit gate operation, and readout (see Sec. III of the Supplemental Material[16]). The readout is independently and simultaneously performed for each qubit using the single-shot method of Ref. 18. It is based on the dynamical transition of a nonlinear resonator[19,20] that maps the quantum state of each transmon to the bifurcated or nonbifurcated state of its resonator, which

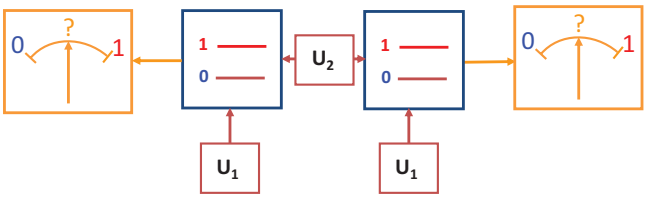

FIG. 1. (Color online) Schematic blueprint of a quantum processor based on quantum gates, represented here in the two-qubit case relevant for our experiment. A quantum processor consists of a qubit register that can perform any unitary evolution needed by an algorithm under the effect of a universal set of quantum gates (single-qubit gate U_1, two-qubit gate U_2). Ideally, all the qubits may be read projectively, and may be reset.

yields a binary outcome for each qubit. This readout method is potentially nondestructive, but its nondestructive character is presently limited by relaxation during the readout pulse. In order to further improve the readout fidelity, we resort to a shelving method that exploits the second excited state of the transmon. For this purpose, a microwave pulse that induces a transition from state $|1\rangle$ toward the second excited state $|2\rangle$ of the transmon is applied just before the readout pulse, as demonstrated in Ref. 18 (this variant does not alter the nondestructive aspect of the readout method since an extra pulse bringing state $|2\rangle$ back to state $|1\rangle$ could be applied after readout). Although the readout contrast achieved with this shelving method and with optimized microwave pulses reaches 0.88 and 0.89 for the two qubits, respectively, the values achieved at working points suitable for processor operation are lower and equal to 0.84 and 0.83. The sources of readout errors are discussed in Sec. IV of the Supplemental Material[16] and include a small readout crosstalk contribution. The overall readout fidelity is thus characterized by a 4×4 matrix $\mathcal{R}$, giving the readout outcome probabilities for each of the input states of the two-qubit register.

In order to characterize the evolution of this register during the algorithm, we determine its density matrix by state tomography. For this purpose, we measure the expectation values of the extended Pauli set of operators $\{\sigma_x I, \ldots, \sigma_z \sigma_z\}$ by applying the suitable rotations just before readout and by averaging typically 10^4 times. Note that the readout errors are corrected by inverting the readout matrix $\mathcal{R}$ when determining the expectation value of the Pauli set, and thus do not contribute to tomography errors, as explained in Ref. 15. The density matrix ρ is then taken as the acceptable positive-semidefinite matrix that, according to the Hilbert-Schmidt distance, is the closest to the possibly nonphysical one derived from the measurement set. In order to characterize the fidelity of the algorithm at all steps, we use the state fidelity $F = \langle\psi|\rho|\psi\rangle$, with $|\psi\rangle$ the ideal quantum state at the step considered; F is in this case the probability for the qubit register to be in state $|\psi\rangle$.

The Grover search algorithm[1] consists of retrieving a particular basis state in a Hilbert space of size N using a function able to discriminate it from the other ones. This function is used to build an oracle operator that tags the searched state. Starting from the superposition $|\phi\rangle$ of all register states, a unitary sequence that incorporates the oracle operator is repeated about $\sqrt{N}$ times, and eventually yields the

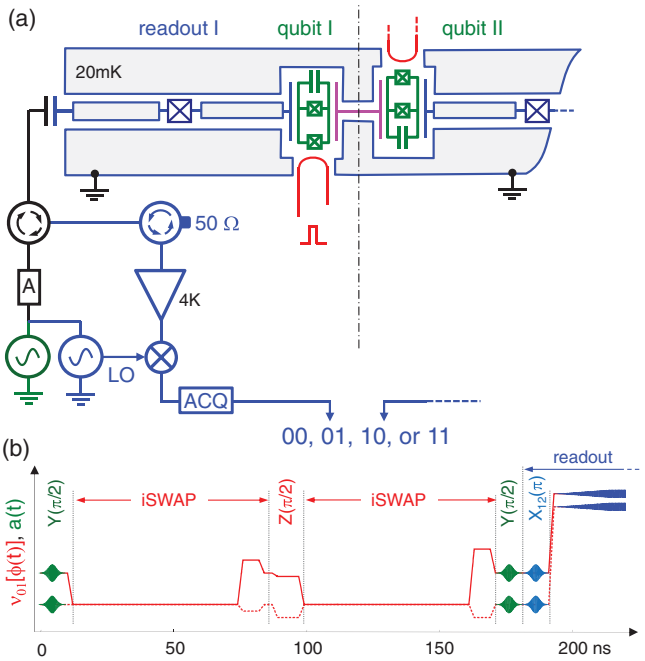

FIG. 2. (Color online) Electrical scheme of the two-qubit circuit operated and typical sequence during processor operation. (a) Two capacitively coupled transmon qubits have tunable frequencies controlled by the flux induced in their SQUID loop by a local current line. The coupling capacitance (center) yields a swapping evolution between the qubits when on resonance. Each transmon is embedded in a nonlinear resonator used for single-shot readout. Each reflected readout pulse is routed to a cryogenic amplifier through circulators, homodyned at room temperature, and acquired digitally, which yields a two-bit outcome. (b) Typical operation of the processor showing the resonant microwave pulses $a(t)$ applied to the qubits and to the readouts, on top of the dc pulses (polylines) that vary the transition frequencies of qubit I (solid) and II (dashed). With the qubits tuned at a first working point for single-qubit gates, resonant pulses are applied for performing X and Y rotations, as well as small flux pulses for Z rotations; qubits are then moved to the interaction point for two-qubit gate operations. Such sequences can be combined as needed by the algorithm. Qubits are then moved to their initial working points for applying tomography pulses as well as a $|1\rangle \rightarrow |2\rangle$ pulse $X_{12}(\pi)$ to increase the fidelity of the forthcoming readout. Finally, they are moved to better readout points and read.

searched state with a high probability. The implementation of Grover's algorithm in a two-qubit Hilbert space often proceeds in a simpler way[21–26] since the result is obtained with certainty after a single algorithm step. The algorithm then consists of an encoding sequence depending on the searched state, followed by a universal decoding sequence that retrieves it. Grover's algorithm thus provides a simple benchmark for two-qubit processors. Its implementation with our quantum processor is shown in Fig. 3(a). First, the superposed state $|\phi\rangle$ is obtained by applying $\pi/2$ rotations around the Y axis for the two qubits. The oracle operator O_{uv} tagging the two-qubit state $|uv\rangle \equiv |u\rangle_{\mathrm{I}} \otimes |v\rangle_{\mathrm{II}}$ to be searched is then applied to state $|\phi\rangle$. Each O_{uv} consists of an iSWAP gate followed by a $Z(\pm\pi/2)$ rotation on each qubit, with the four possible sign combinations $(-,-)$, $(+,-)$, $(-,+)$, and $(+,+)$ corresponding to $uv = 00$, 01, 10, and 11, respectively. In the algorithm we

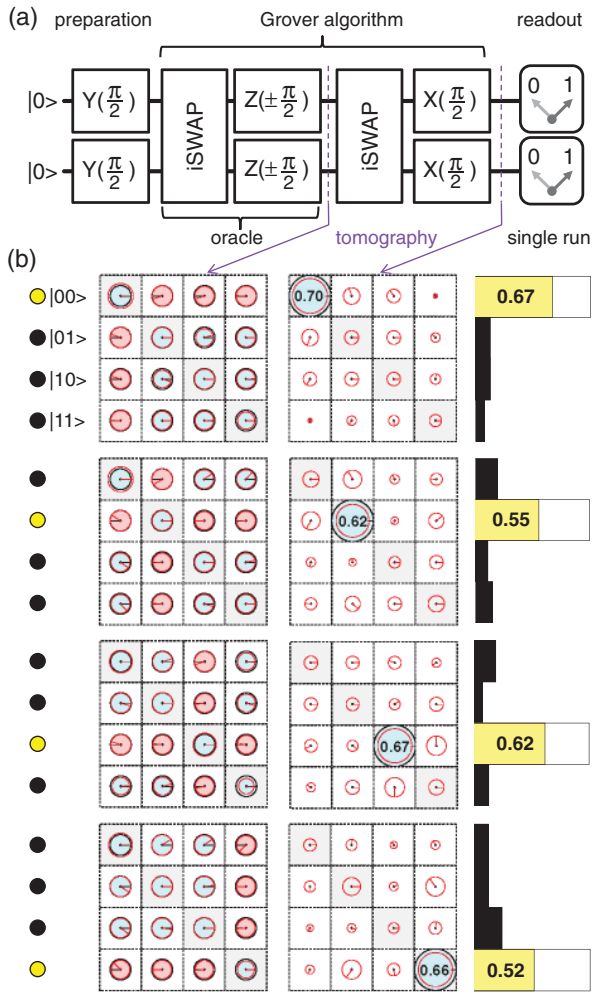

FIG. 3. (Color online) (a) Experimental sequence used for implementing the Grover search algorithm on four objects. First, $Y(\pi/2)$ rotations are applied to produce the superposition $|\phi\rangle = (1/2)\sum_{u,v}|uv\rangle$ of all basis states; then one of the four possible oracles (corresponding to the four sign combinations of the Z rotations) is applied. The tagged state is then decoded in all cases using an iSWAP operation followed by $X(\pi/2)$ rotations. (b) State tomography at two steps of the algorithm (ρ matrices) and success probability after a single run (histograms). The bright dots on the left-hand side mark the basis state tagged by each oracle operator used. The amplitude of each matrix element is represented by a disk [black for the ideal density matrix, red (gray) for the measured one] and its phase by an arrow (as well as a filling color for the ideal matrix). After applying the oracle, the information on the tagged state is encoded in the phase of six particular elements of ρ. After decoding, the tagged state should be the only matrix element present in ρ. The fidelity F_{final} actually obtained is indicated in this element. The probability distribution of the single-run readout outcomes is shown on the right-hand side (bright box for the correct answer, solid dark boxes for the wrong ones).

use, the encoding is a phase encoding as in Ref. 10. When applied to $|\phi\rangle$, each oracle operator inverts the sign of the component corresponding to the state it tags, respectively, to the other ones. The density matrix, after applying the oracle, ideally takes a simple form: The amplitude of all coefficients is $1/4$, and the phase of an element ρ_{rs} is $\varphi_{rs} = \pi(\delta_{rt} + \delta_{st})$, where t corresponds to the state tagged by the oracle operator. The state tomography performed after applying the oracle, shown in Fig. 3(b), is in good agreement with this prediction. More quantitatively, we find that after having applied the oracle operator, the intermediate fidelity is $F_{\text{int}} = 0.87$, 0.80, 0.84, and 0.82, respectively. The last part of the algorithm consists in transforming the obtained state in the searched state irrespectively of it, or equivalently to transform the phase information distributed over the elements of the density matrix in a weight information with the whole weight on the searched state. This operation is readily performed by applying an iSWAP gate followed by $X(\pi/2)$ rotations for both qubits. We find that the fidelity of the density matrix at the end of the algorithm is $F_{\text{final}} = 0.70$, 0.62, 0.67, and 0.66, respectively. We explain both F_{int} and F_{final} by gate errors at a 2% level, by errors in the tomography pulses at a 2% level, as well as by decoherence during the whole experimental sequence [at the coupling point, relaxation times are $T_1^{\text{I}} \simeq 450$ ns and $T_1^{\text{II}} \simeq 500$ ns, and the effective dephasing times $T_\varphi^{\text{I}} \simeq T_\varphi^{\text{II}} \simeq 2\ \mu$s (Ref. 15)].

We now consider the success probability obtained after a single run (with no tomography pulses), which probes the quantum speed-up actually achieved by the processor. We find (see Fig. 3) that our processor does yield the correct answer with a success probability $P_{\text{S}} = 0.67$, 0.55, 0.62, and 0.52 for the four basis states, which is smaller than the density matrix fidelity F_{final}. One notices that the difference between F_{final} and P_{S}, mostly due to readout errors, slightly depends on the searched state: The larger the energy of the searched state, the larger is the difference. This dependence is well explained by the effect of relaxation during the readout pulse, which is the main error source at readout, the second one being readout crosstalk. One also notices that the outcome errors are distributed over all the wrong answers. To summarize, the errors of our implementation of Grover's algorithm originate both from small unitary errors accumulated during the algorithm, and from decoherence during the whole sequence, in particular, during the final readout.

We finally discuss the significance of the obtained results in terms of quantum information processing. The achieved success probability is smaller than the theoretically achievable value 1, but nevertheless it is sizably larger than the value of 0.25 obtained by running once the classical algorithm that consists in making a random trial. From the point of view of a user who has to find out which unknown oracle has been given to him, the fidelity of the algorithm outcome is $f_{ab} = 0.57$, 0.63, 0.57, and 0.59 for the 00, 01, 10, and 11 outcomes, respectively, as explained in Sec. V of the Supplemental Material.[16] Despite the presence of errors, this result demonstrates the quantum speed-up for Grover's algorithm when searching in a Hilbert space with a small size $N = 4$.

In conclusion, we have demonstrated the operation of the Grover search algorithm in a superconducting two-qubit processor with a single-shot nondestructive readout. This result indicates that the quantum speed-up expected from quantum algorithms is within reach of superconducting quantum bit processors. Demonstrating the $\sqrt{N}$ speed-up for Grover's algorithm in larger Hilbert spaces requires a qubit architecture

more scalable than the present one, which presently is a major challenge in the field.

We gratefully acknowledge discussions with M. Devoret, D. DiVicenzo, L. DiCarlo, and within the Quantronics group, technical support from P. Orfila, P. Senat, and J. C. Tack, as well as financial support from the European research contract SOLID, from ANR Masquelspec and C'Nano, and from the German Ministry of Education and Research.

[1]L. K. Grover, in *Proceedings of the 28th Annual ACM Symposium on the Theory of Computing*, edited by G. L. Miller (ACM, New York, 1996), p. 212; Am. J. Phys. **69**, 769 (2001).

[2]P. W. Shor, *Proceedings of the 35th Annual Symposium on Foundations of Computer Science* (IEEE, Los Alamitos, CA, 1994); SIAM J. Comput. **26**, 1484 (1997).

[3]M. A. Nielsen and I. L. Chuang, *Quantum Computation and Quantum Information* (Cambridge University Press, Cambridge, UK, 2000).

[4]T. D. Ladd, F. Jelezko, R. Laflamme, Y. Nakamura, C. Monroe, and J. L. O'Brien, Nature (London) **464**, 45 (2010).

[5]D. P. DiVincenzo, Fortschr. Phys. **48**, 771 (2000).

[6]J. Koch, T. M. Yu, J. Gambetta, A. A. Houck, D. I. Schuster, J. Majer, A. Blais, M. H. Devoret, S. M. Girvin, and R. J. Schoelkopf, Phys. Rev. A **76**, 042319 (2007).

[7]J. A. Schreier, A. A. Houck, J. Koch, D. I. Schuster, B. R. Johnson, J. M. Chow, J. M. Gambetta, J. Majer, L. Frunzio, M. H. Devoret, S. M. Girvin, and R. J. Schoelkopf, Phys. Rev. B **77**, 180502 (2008).

[8]Y. Nakamura, Yu. A. Pashkin, and J. S. Tsai1, Nature (London) **398**, 786 (1999).

[9]D. Deutsch and R. Jozsa, Proc. R. Soc. London A**439**, 553 (1992).

[10]L. DiCarlo, J. M. Chow, J. M. Gambetta, L. S. Bishop, B. R. Johnson, D. I. Schuster, J. Majer, A. Blais, L. Frunzio, S. M. Girvin, and R. J. Schoelkopf, Nature (London) **460**, 240 (2009).

[11]M. D. Reed, L. DiCarlo, S. E. Nigg, L. Sun, L. Frunzio, S. M. Girvin, and R. J. Schoelkopf, Nature (London) **482**, 382 (2012).

[12]T. Yamamoto, M. Neeley, E. Lucero, R. C. Bialczak, J. Kelly, M. Lenander, M. Mariantoni, A. D. O'Connell, D. Sank, H. Wang, M. Weides, J. Wenner, Y. Yin, A. N. Cleland, and J. M. Martinis, Phys. Rev. B **82**, 184515 (2010).

[13]M. Mariantoni, H. Wang, T. Yamamoto, M. Neeley, R. C. Bialczak, Y. Chen, M. Lenander, E. Lucero, A. D. O'Connell, D. Sank, M. Weides, J. Wenner, Y. Yin, J. Zhao, A. N. Korotkov, A. N. Cleland, and J. M. Martinis, Science **334**, 6052 (2011).

[14]E. Lucero, R. Barends, Y. Chen, J. Kelly, M. Mariantoni, A. Megrant, P. O'Malley, D. Sank, A. Vainsencher, J. Wenner, T. White, Y. Yin, A. N. Cleland, and J. M. Martinis, e-print arXiv:1202.5707.

[15]A. Dewes, F. R. Ong, V. Schmitt, R. Lauro, N. Boulant, P. Bertet, D. Vion, and D. Esteve, Phys. Rev. Lett. **108**, 057002 (2012).

[16]See Supplemental Material at http://link.aps.org/supplemental/10.1103/PhysRevB.85.140503 for technical information about the sample preparation (I), sample parameters (II), and experimental setup (III), and for the detailed analysis of readout errors (IV) and algorithm fidelity (V).

[17]F. R. Ong, M. Boissonneault, F. Mallet, A. Palacios-Laloy, A. Dewes, A. C. Doherty, A. Blais, P. Bertet, D. Vion, and D. Esteve, Phys. Rev. Lett. **106**, 167002 (2011).

[18]F. Mallet, Florian R. Ong, A. Palacios-Laloy, F. Nguyen, P. Bertet, D. Vion, and D. Esteve, Nat. Phys. **5**, 791 (2009).

[19]I. Siddiqi, R. Vijay, F. Pierre, C. M. Wilson, M. Metcalfe, C. Rigetti, L. Frunzio, and M. H. Devoret, Phys. Rev. Lett. **93**, 207002 (2004).

[20]M. B. Metcalfe, E. Boaknin, V. Manucharyan, R. Vijay, I. Siddiqi, C. Rigetti, L. Frunzio, R. J. Schoelkopf, and M. H. Devoret, Phys. Rev. B **76**, 174516 (2007).

[21]J. A. Jones, M. Mosca, and R. H. Hansen, Nature (London) **393**, 344 (1998).

[22]I. L. Chuang, N. Gershenfeld, and M. Kubinec, Phys. Rev. Lett. **80**, 3408 (1998).

[23]K. A. Brickman, P. C. Haljan, P. J. Lee, M. Acton, L. Deslauriers, and C. Monroe, Phys. Rev. A **72**, 050306 (2005).

[24]N. Bhattacharya, H. B. van Linden van den Heuvell, and R. J. C. Spreeuw, Phys. Rev. Lett. **88**, 137901 (2002).

[25]P. Walther, K. J. Resch, T. Rudolph, E. Schenck, H. Weinfurter, V. Vedral, M. Aspelmeyer, and A. Zeilinger, Nature (London) **434**, 169 (2005).

[26]J. Ahn, T. C. Weinacht, and P. H. Bucksbaum, Science **287**, 463 (2000).

Supplemental material

Demonstrating quantum speed-up in a superconducting two-qubit processor

A. Dewes[1], R. Lauro[1], F.R. Ong[1], V. Schmitt[1],

P. Milman[2], P. Bertet[1], D. Vion[1], and D. Esteve[1]

[1]*Service de Physique de l'Etat Condensé/IRAMIS/DSM (CNRS URA 2464), CEA Saclay, F-91191 Gif-sur-Yvette, France and*

[2]*Laboratoire Matériaux et Phénomènes Quantiques, Université Paris Diderot, Bâtiment Condorcet, 10, rue Alice Domon et Léonie Duquet, F75205 Paris, France*

I. SAMPLE PREPARATION

The sample is fabricated on a silicon chip oxidized over 50 nm. A 150 nm thick niobium layer is first deposited by magnetron sputtering and then dry-etched in a SF_6 plasma to pattern the readout resonators, the current lines for frequency tuning, and their ports. Finally, the transmon qubit, the coupling capacitance and the Josephson junctions of the resonators are fabricated by double-angle evaporation of aluminum through a shadow mask patterned by e-beam lithography. The first layer of aluminum is oxidized in a $Ar - O_2$ mixture to form the oxide barrier of the junctions. The chip is glued with wax on a printed circuit board (PCB) and wire bonded to it. The PCB is then screwed in a copper box anchored to the cold plate of a dilution refrigerator.

II. SAMPLE PARAMETERS

The sample is first characterized by spectroscopy [15]. The incident power used is high enough to observe the resonator frequency $\nu_{\rm R}$, the qubit line ν_{01}, and the two-photon transition at frequency $\nu_{02}/2$ between the ground and second excited states of each transmon. A fit of the transmon model to the data yields the sample parameters, i.e. total Josephson energies of the transmons in zero magnetic field $E_{\rm J}^{\rm I}/h = 36.2\,{\rm GHz}$ and $E_{\rm J}^{\rm II}/h = 43.1\,{\rm GHz}$, total charging energies $E_{\rm C}^{\rm I}/h = 0.98\,{\rm GHz}$ and $E_{\rm C}^{\rm II}/h = 0.87\,{\rm GHz}$, assymetries between the two junctions of a transmon $d_I = 0.2$ and $d_{\rm II} = 0.35$. The measured resonance frequencies of the readout resonators are $\nu_{\rm R}^{\rm I} = 6.84\,{\rm GHz}$, and $\nu_{\rm R}^{\rm II} = 6.70\,{\rm GHz}$. The qubit-readout anticrossing at $\nu = \nu_{\rm R}$ yields the qubit-readout couplings $g_0^{\rm I} \simeq g_0^{\rm II} \simeq (2\pi)\,50\,{\rm MHz}$. Independent measurements of the resonator dynamics yield quality factors $Q_{\rm I} = Q_{\rm II} = 730$ and Kerr non linearities [15,17] $K_{\rm I}/\nu_{\rm R}^{\rm I} \simeq K_{\rm II}/\nu_{\rm R}^{II} \simeq -2.3 \pm 0.5 \times 10^{-5}$.

III. EXPERIMENTAL SETUP

- Qubit resonant microwave pulses: The qubit drive pulses are generated by two phase-locked microwave generators feeding a pair of I/Q-mixers. The IF inputs are provided by a 4-Channel1 GS/s arbitrary waveform generator (AWG Tektronix AWG5014). Single-sideband mixing in the frequency range of 50-300 MHz is used to generate

multi-tone drive pulses and to obtain a high ON/OFF ratio ($> 50\,\mathrm{dB}$). Phase and amplitude errors are corrected by applying suitable sideband and carrier frequency dependent corrections to the amplitude and offset of the IF signals.

- Qubit frequency control: Flux control pulses are generated by a second AWG and sent to the chip through a transmission line equipped with 40 dB total attenuation and a pair of 1 GHz dissipative low-pass filters at 4 K. The input signal of each flux line is returned to room temperature through an identical transmission line and measured, which allows to compensate the non-ideal frequency response of the line.

- Readout pulses: The driving pulses for the Josephson bifurcation amplifier (JBA) readouts are generated by mixing the continuous signals of a pair of microwave generators with IF pulses provided by a 1 GS/s arbitrary waveform generator (AWG Tektronix AWG5014). Each readout pulse consists of a measurement part with a rise time of 30 ns and a hold time of 100 ns, followed by a $2\,\mu s$ long latching part at 90 % of the pulse height.

- Drive and measurement lines: The drive and readout microwave signals of each qubit are combined and sent to the sample through a pair of transmission lines with total attenuation 70 dB and filtered at 4 K and 300 mK. A microwave circulator at 20 mK protects the chip from the amplifier noise. The signals are amplified by 36 dB at 4 K by two cryogenic HEMT amplifiers (CIT Cryo 1) with noise temperature 5 K. The reflected readout pulses are amplified and demodulated at room temperature. The IQ quadratures of the demodulated signals are sampled at 1 GS/s by a 4-channel data acquisition system (Acqiris DC282).

IV. READOUT ERRORS

Errors in our readout scheme are discussed in detail in Ref. [15] for a single qubit. First, incorrect mapping $|0\rangle \rightarrow 1$ or$|1\rangle \rightarrow 0$ of the projected state of the qubit to the dynamical state of the resonator can occur, due to the stochastic nature of the switching between the two dynamical states. As shown in Fig. 4.1, the probability p to obtain the outcome 1 varies continuously from 0 to 1 over a certain range of drive power P_d applied to the readout. When the shift in power between the two $p_{|0\rangle,|1\rangle}(P_\mathrm{d})$ curves is not much larger than

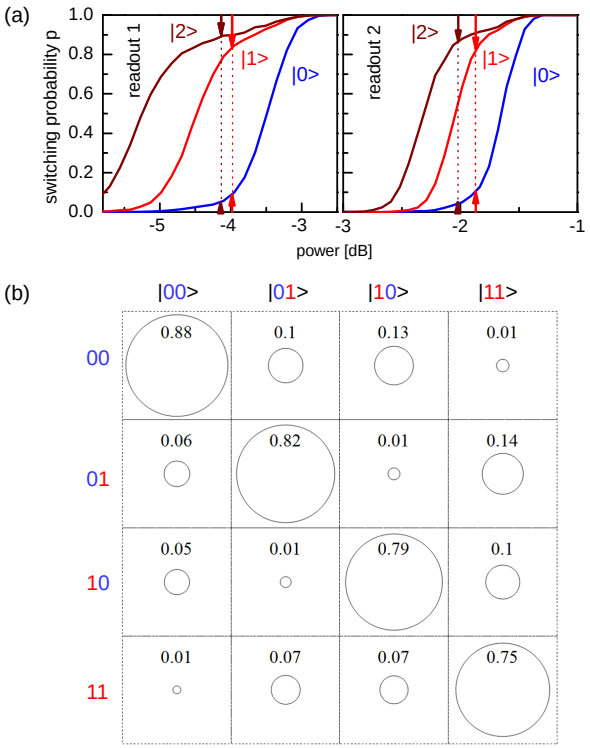

Figure IV.1:

(a) Switching probability p of each readout as a function of its peak driving power, when its qubit is prepared in state $|0\rangle$ (blue), $|1\rangle$ (red), or $|2\rangle$ (brown), with the other qubit being far detuned. The arrows indicate the readout errors where the contrast is optimal with (brown) and without (red) $|1\rangle \rightarrow |2\rangle$ shelving. (b) Readout matrix $\mathcal{R}$ giving the probabilities of the four ab outcomes, for the four computational input states $|uv\rangle$, when using $|1\rangle \rightarrow |2\rangle$ shelving. Each matrix elements is represented by a circle of area proportional to its value (a unit circle would touch the cell borders).

this range, the two curves overlap and errors are significant even at the optimal drive power where the difference in p is maximum. Second, even in the case of non overlapping $p_{|0\rangle,|1\rangle}(P_{\mathrm{d}})$ curves, the qubit initially projected in state$|1\rangle$ can relax down to $|0\rangle$ before the end of the measurement, yielding an outcome 0 instead of 1. The probability of these two types of errors vary in opposite directions as a function of the frequency detuning $\Delta = \nu_{\mathrm{R}} - \nu > 0$ between the resonator and the qubit, so that a compromise has to be found for Δ. As explained in the main text, we use a shelving method to the second excited state in order to improve the readout contrast $c = Max\left(p_{|1\rangle} - p_{|0\rangle}\right)$, with a microwave π pulse at frequency

ν_{12} bringing state $|1\rangle$ into state $|2\rangle$ just before the readout pulse. The smallest errors $e_0^{\mathrm{I,II}}$ and $e_1^{\mathrm{I,II}}$ when reading $|0\rangle$ and $|1\rangle$ are found for $\Delta_{\mathrm{I}} = 440\,\mathrm{MHz}$ and $\Delta_{\mathrm{II}} = 575\,\mathrm{MHz}$: $e_0^{\mathrm{I}} = 5\%$ and $e_1^{\mathrm{I}} = 13\%$ (contrast $c_{\mathrm{I}} = 1 - e_0^{\mathrm{I}} - e_1^{\mathrm{I}} = 82\%$), and $e_0^{\mathrm{II}} = 5.5\%$ and $e_1^{\mathrm{II}} = 12\%$ ($c_{\mathrm{II}} = 82\%$). When using the $|1\rangle \rightarrow |2\rangle$ shelving before readout, $e_0^{\mathrm{I}} = 2.5\%$ and $e_2^{\mathrm{I}} = 9.5\%$ (contrast $c_{\mathrm{I}} == 1 - e_0^{\mathrm{I}} - e_2^{\mathrm{I}} = 88\%$), and $e_0^{\mathrm{II}} = 3\%$ and $e_2^{\mathrm{II}} = 8\%$ ($c_{\mathrm{II}} = 89\%$). These best results are very close to those obtained in Ref. [15] of main text, but cannot however be exploited for simultaneous readout of the two qubits.

Indeed, when the two qubits are measured simultaneously, we find an influence of the projected state of each qubit on the outcome of the readout of the other one. In order to to minimize this spurious effect, we increase the detuning $\Delta_{\mathrm{I,II}}$ up to $\sim 1\,\mathrm{GHz}$ with respect to previous optimal values. An immediate consequence shown in Fig. S4.1(a) is a reduction of the $c_{\mathrm{I,II}}$ contrasts. The errors when reading $|0\rangle$ and $|1\rangle$ are then $e_0^{\mathrm{I}} = 10\,\%$ and $e_1^{\mathrm{I}} = 16\,\%$ (contrast $c_{\mathrm{I}} = 74\%$) and $e_0^{\mathrm{II}} = 12\,\%$ and $e_1^{\mathrm{II}} = 15\,\%$ (contrast $c_{\mathrm{II}} = 73\%$). When shelving the qubit in state $|2\rangle$, the errors are $e_0^{\mathrm{I}} = 5\,\%$, $e_2^{\mathrm{I}} = 11\,\%$ (contrast $c_{\mathrm{I}} = 84\%$), $e_0^{\mathrm{II}} = 5\,\%$, $e_2^{\mathrm{II}} = 12\,\%$ (contrast $c_{\mathrm{I}} = 83\%$). The readout errors are captured in the 4×4 readout matrix $\mathcal{R}$ shown in Fig. S4.1(c), that gives the probabilities p_{uv} of the four possible outcomes for the different input states using the $|1\rangle \rightarrow |2\rangle$ shelving technique. This matrix $\mathcal{R}$ is used to correct the readout errors only when doing state tomography, and not when the running the algorithm once. The cause of the readout crosstalk in our processor is discussed in Ref. [15].

V. ALGORITHM FIDELITY

From the point of view of a user that would search which unknown oracle has been given to him, the fidelity f_{ab} of the algorithm for each possible outcome ab is $f_{ab} = p_{ab/O_{ab}} / \left(p_{ab/O_{00}} + p_{ab/O_{01}} + p_{ab/O_{10}} + p_{ab/O_{11}}\right)$ with $p_{ab/O_{uv}}$ the probability of obtaining outcome ab knowing that O_{uv} has been used. These probabilities are shown in table V.1, yielding $f_{00,01,10,11} = 0.57$, 0.63, 0.57, and 0.59.

ab/O_{uv}	O_{00}	O_{01}	O_{10}	O_{11}	$\sum$	f_{ab}
00	0.666	0.192	0.188	0.122	1.168	57.0 %
01	0.127	0.554	0.071	0.122	0.874	63.4 %
10	0.128	0.106	0.615	0.239	1.088	56.5 %
11	0.079	0.148	0.126	0.517	0.870	59.4 %

Table V.1: Conditional probabilities $p_{ab/O_{uv}}$ and statistical fidelities f_{ab} for all possible outcomes ab, measured for our version of Grover's algorithm.